ASPECTS OF THE MORPHOLOGICAL, RADIOGRAPHIC AND ULTRASONOGRAPHIC ANATOMY OF THE RED PANDA (*AILURUS FULGENS*) AND RING-TAILED LEMUR (*LEMUR CATTA*)

by

Modesta L. J. Makungu

A thesis submitted in partial fulfilment of the requirements for the degree of Doctor of Philosophy in the Department of Anatomy and Physiology in the Faculty of Veterinary Science, University of Pretoria

July 2015

ASPECTS OF THE MORPHOLOGICAL, RADIOGRAPHIC AND ULTRASONOGRAPHIC ANATOMY OF THE RED PANDA (*AILURUS FULGENS*) AND RING-TAILED LEMUR (*LEMUR CATTA*)

By: Dr. Modesta L. J. Makungu
Department of Anatomy and Physiology
Faculty of Veterinary Science
University of Pretoria
South Africa

Supervisor: Prof. Hermanus B. Groenewald
Department of Anatomy and Physiology
Faculty of Veterinary Science
University of Pretoria
South Africa

Co-supervisor: Prof. Wencke M. du Plessis
Ross University School of Veterinary Medicine
Basseterre
St. Kitts, West Indies

Co-supervisor: Dr. Michelle Barrows
Bristol Zoo Gardens
United Kingdom

DECLARATION

I, Modesta L. J. Makungu, declare that the thesis, which I hereby submit for the degree of Doctor of Philosophy at the University of Pretoria, is my own work and has not previously been submitted by me for a degree at this or any other tertiary institution.

.....

Makungu M.L.J.

July 2015

ETHICS STATEMENT

The author, whose name appears on the title page of this thesis, has obtained, for the research described in this work, the applicable research ethics approval. The author declares that she has observed the ethical standards required in terms of the University of Pretoria's *Code of ethics for researchers* and the *Policy guidelines for responsible research.*

SUMMARY

The red panda and ring-tailed lemur are species, which are commonly kept in zoological gardens. The red panda and ring-tailed lemur are classified as vulnerable and endangered, respectively, by the International Union for Conservation of Nature and Natural Resources. The aim of this study was to describe the normal radiographic thoracic anatomy, radiographic and ultrasonographic abdominal anatomy as well as the normal morphology of the pelvis, thoracic and hind limb in captive red pandas and ring-tailed lemurs as a reference for clinical use. Radiography and ultrasonography were performed in adult captive red pandas and ring-tailed lemurs during annual health examinations. Bone specimens of adult red pandas and ring-tailed lemurs were used for gross osteological study. The morphology of the pelvis, thoracic and hind limb of the red panda and ring-tailed lemur supported the presence of strong flexor and supinator muscles and flexibility of limb joints, which are important in arboreal quadrupedal locomotion. However, the scapula of the ring-tailed lemur is modified for both arboreal and terrestrial quadrupedal locomotion. Additionally, the morphology of the pelvis and hind limb of the ring-tailed lemur showed locomotor adaptation for jumping. Normal radiographic and ultrasonographic reference ranges for thoracic structures and abdominal organs were established and ratios were calculated. Knowledge of the normal morphology, radiographic and ultrasonographic anatomy of the red panda and ring-tailed lemur should prove useful in the diagnosis of diseases and for routine health examinations.

ACKNOWLEDGEMENTS

I would like to thank the Organization for Women in Science for the Developing World (OWSD), Swedish International Development Cooperation Agency (SIDA), University of Pretoria, Johannesburg (JHB) and Bristol zoos for supporting this study. The JHB, Bristol and Lory Park zoos and Montecasino Bird Gardens for permission of using their animals and cadavers for this study. The National Museum of Scotland, Ditsong National Museum of South Africa and Dr. Shaw Badenhorst for supplying of bone specimens. Tecmed Africa-Midrand, South Africa for providing an ultrasound machine.

I am grateful to my supervisor Prof. Hermanus B. Groenewald, co-supervisors Prof. Wencke M. du Plessis and Dr. Michelle Barrows for their support, training, tireless encouragement and guidance throughout this study. I wish to thank Drs. Katja Koeppel, Georgina Cole, Brett Gardner and Kathryn Perrin, Ms. Katherine Visser, Ms. Fania Mohlala, sisters and animal handlers of the JHB and Bristol zoo for their assistance during health examinations, anaesthesia, radiographic and ultrasonographic examinations.

I wish to express my gratitude to Profs. Robert M. Kirberger and Ann Carstens, Drs. Nicky Cassel, Cheekin Lim and Nerissa Stander, and Sisters Bev Olivier and Melanie McClean of the diagnostic imaging section at the Onderstepoort Veterinary Academic Hospital for their training and assistance during radiographic and computed tomographic examinations. Mrs. Wilma Olivier and laboratory staff (Mr. A. Flinks, M. Mothemane and P. Mokoena) of

the Department of Anatomy and Physiology, Faculty of Veterinary Science, University of Pretoria for their assistance in administrative work and preparation of bone specimens, respectively. Mrs. Charmaine Vermeulen of the Department for Education Innovation of the University of Pretoria for her assistance in photography.

I also wish to thank Mr. Albert du Plessis and Mr. David Pilling and their families for their support and generosity during my stay in Bristol, United Kingdom and Pretoria, South Africa.

I acknowledge the Sokoine University of Agriculture, Tanzania for the study leave, which I was granted. Prof. Salvatory B. P. Bittegeko, former Head of the Department of Veterinary Surgery and Theriogenology, Faculty of Veterinary Medicine, Sokoine University of Agriculture for his co-operation throughout the duration of my study. To staff members Anatomy and Physiology Department, Tanzanian community in Gauteng, my colleagues' postgraduate students, and birthday club members who made me feel at home during my stay in Pretoria, not forgetting the Friday braais. Thank you all.

Last but not least, I am deeply indebted to my family for their support and encouragement throughout the study period.

DEDICATION

Dedicated to my father Mr. John Makungu and my mother Mrs. Salustia Makungu for their love, support and full commitment in my education, my young sister Nancy and my family for their support throughout the study period.

TABLE OF CONTENTS

LIST OF FIGURES

LIST OF TABLES

CHAPTER 1

GENERAL INTRODUCTION

1.1 INTRODUCTION

The red panda (*Ailurus fulgens*) is classified as a vulnerable species by the International Union for Conservation of Nature and Natural Resources (IUCN) (IUCN, 2014). It is primarily distributed in the Himalayas and southern China (Fisher et al., 2009). The red panda is a quadruped arboreal animal. It belongs to the order: Carnivora, suborder: Caniformia, family: Ailuridae and genus: *Ailurus* (Wei and Zhang, 2009). The red panda is related to procyonids, mustelids and skunks (Groves, 2011).

The ring-tailed lemur (*Lemur catta*) is classified as an endangered species according to IUCN (IUCN, 2014). It is a quadruped arboreal animal primarily distributed in south and south-western Madagascar (Budnitz and Dainis, 1975). The ring-tailed lemur belongs to the order: Primata, suborder: Strepsirrhini, family: Lemuridae and genus: *Lemur* (Nowak, 1999). Strepsirrhines are characterised by retaining primitive characteristics such as prominent scent glands, rhinarium and pointed muzzle (Jungle, 2003; Ankel-Simons, 2007). Most of them do not look like monkeys, but rather resemble more primitive animals such as domestic cats and dogs (Ankel-Simons, 2007).

Diagnostic imaging is important in humans, domestic animals and wildlife species. Depending on the chosen diagnostic imaging modality, it enables the visual evaluation of certain normal anatomy and potentially enables recognition and diagnosis of many diseases. Most veterinarians use radiology as their first choice diagnostic imaging modality. More advanced diagnostic imaging modalities such as ultrasound, endoscopy, fluoroscopy, computed tomography (CT), magnetic resonance imaging (MRI) and scintigraphy are increasingly being used by many veterinarians. They are non-invasive and provide an alternative to invasive procedures such as surgical exploration.

In captive red pandas, pneumonia and septicaemia are major causes of neonatal deaths (Philippa and Ramsay, 2011). The most common diseases of adult captive red pandas are gastric ulcers, enteritis, hepatic lipidosis, stomatitis and periodontitis (Philippa and Ramsay, 2011). Pulmonary diseases such as lung worm infestation (Preece, 2011), lung sarcoma and mycobacteriosis (Philippa and Ramsay, 2011) have been reported in this species. Cardiac diseases including right heart failure (Preece, 2011), dirofilariasis (Harwell and Craig, 1981), traumatic pericarditis (Zwart, 1989) and hypertrophic cardiomyopathy (Philippa and Ramsay, 2011) have been documented in this species.

Renal diseases like nephrosis, nephritis, glomerulonephrosis (Zwart, 1989) and polycystic kidneys (Makungu et al., 2013) occur in red pandas. Other diseases, which have been reported in the red panda include hepatitis (Zwart, 1989), hyperostotic bone disease (Lynch et al., 2002), avascular necrosis of

the femoral head (Delclaux et al., 2002) and osteoarthritis (Philippa and Ramsay, 2011).

Obesity is a major nutritional problem in captive ring-tailed lemurs (Jungle et al., 2009) as a result of change in their lifestyle particularly diet (Goodchild and Schwitzer, 2008). Haemochromatosis (iron storage disease) has been reported to be a common disease in captive ring-tailed lemurs (Taylor, 2009), although it has been disputed (Jungle et al., 2009). The likely causes of iron storage disease are excess intake of dietary iron, citrus fruits and insufficient tannins (Taylor, 2009). Other liver diseases such as hepatic lipidosis, fibrosis, capillariasis (Zordan et al., 2012) and neoplasia like cholangioma (Remick et al., 2009) and cholangiocarcinoma (Chang et al., 1979) have been reported in this species. Kidney conditions like renal aplasia/hypoplasia (Scott and Camb, 1925), infarcts and pyelonephritis (Burton et al., 1986) have also been documented.

Pulmonary diseases including pneumonia (Hamerton, 1944; Tuten et al., 2011), atelectasis (Palotay and Uno, 1975) and tuberculosis (Schmidt, 1975) and cardiac diseases like encephalomyocarditis virus infection (Canelli et al., 2010) and pericardial effusion (Zordan et al., 2012) occur in ring-tailed lemurs. Other diseases, which occur in ring-tailed lemurs include sudden acute respiratory distress syndrome (M. Barrows, personal communications), diabetes mellitus (Jungle et al., 2009), toxoplasmosis (Taylor, 2009), cystitis (Burton et al., 1986), periarticular hyperostosis (Jungle et al., 1994), nutritional secondary hyperparathyroidism (Tomson and Lotshaw, 1978), idiopathic

proliferative bone disease (Weber et al., 1995), osteosarcoma (Warwick, 1951) and hydatidosis (Palotay and Uno, 1975). In hydatidosis, cysts have been reported to involve the liver, spleen, kidneys, mesentery, urinary bladder, stomach, small intestines, omentum and lungs (Palotay and Uno, 1975; Shahar et al., 1995; Kondo et al., 1996).

Knowledge of the normal gross osteology, radiographic and ultrasonographic anatomy of the thorax, abdomen, pelvis, thoracic and pelvic limb is important for species identification and accurate interpretation and diagnosis of diseases involving various body systems. Normal gross osteology (Nickel et al., 1986), radiographic (Thrall and Robertson, 2011) and ultrasonographic (Nyland and Mattoon, 2002) anatomy of the thorax, abdomen, pelvis, thoracic and pelvic limb in small animals is well documented and serves as a reference for species identification and diagnosis of diseases.

Several authors have reported the normal gross osteology (Heinrich and Houde, 2006; Ankel-Simons, 2007), radiographic (Wagner and Kirberger, 2005a; Martini et al., 2013; Martins et al., 2013; Young et al., 2013) and ultrasonographic (Wagner and Kirberger, 2005b; Amory et al., 2013; Ribeiro et al., 2013) anatomy of wildlife species, which provide a reference for species identification and diagnosis of diseases. Knowledge of the normal gross osteology, radiographic and ultrasonographic anatomy of the thorax, abdomen, pelvis, thoracic and pelvic limb of the red panda and ring-tailed lemur is important for accurate diagnosis and treatment of diseases in order to

improve their chance of survival. This is particularly important given their value and conservation status.

1.2 HYPOTHESIS

Significant species specific differences exist in the gross osteology, radiographic and ultrasonographic anatomy of the thorax, abdomen, pelvis, thoracic and pelvic limb.

1.3 OBJECTIVES

The objectives of this study were:

- To describe the normal morphology of the thoracic limb of the ring-tailed lemur evidenced by gross osteology and radiography as a reference for species identification and clinical use
- To describe the normal morphology of the thoracic limb of the red panda evidenced by gross osteology and radiography as a reference for species identification and clinical use
- To describe the normal morphology of the pelvis and hind limb of the ring-tailed lemur evidenced by gross osteology and radiography as a reference for species identification and clinical use
- To describe the normal morphology of the pelvis and hind limb of the red panda evidenced by gross osteology and radiography as a reference for species identification and clinical use
- To describe the radiographic thoracic anatomy of the ring-tailed lemur as a reference for clinical use
- To describe the radiographic thoracic anatomy of the red panda as a reference for clinical use

- To describe the radiographic and ultrasonographic abdominal anatomy of the ring-tailed lemur as a reference for clinical use
- To describe the radiographic and ultrasonographic abdominal anatomy of the red panda as a reference for clinical use

1.4 REFERENCES

Amory, J. T., W. M. du Plessis, A. Beierschmitt, J. Beeler-Marfisi, R. M. Palmour, and T. Beths, 2013: Abdominal ultrasonography of the normal St. Kitts vervet monkey (*Chlorocebus sabaeus*). J. Med. Primatol. **42,** 28–38.

Ankel-Simons, F., 2007: Primate Anatomy: An Introduction. Boston: Academic Press.

Budnitz, N., and K. Dainis, 1975: *Lemur catta*: Ecology and behaviour. In: Lemur Biology (I. Tattersall and R. W. Sussman, eds). New York: Plenum Press. pp. 219–235.

Burton, M., R. J. Morton, E. Ramsay, and E. L. Stair, 1986: Coccidioidomycosis in a ring-tailed lemur. J. Am. Vet. Med. Assoc. **189,** 1209–1211.

Canelli, E., A. Luppi, A. Lavazza, D. Lelli, E. Sozzi, A. M. M. Martin, D. Gelmetti, E. Pascotto, C. Sandri, W. Magnone, and P. Cordioli, 2010: Encephalomyocarditis virus infection in an Italian zoo. Virol. J. **7,** 1–7.

Chang, J., J. L. Wagner, and R. W. Kornegay, 1979: Spontaneous cholangiocarcinoma in a ring-tailed lemur (*Lemur catta*). Lab. Anim. Sci. **29,** 374–376 (Abstract).

Delclaux, M., C. Talavera, M. López, J. M. Sánchez, and M. I. García, 2002: Avascular necrosis of the femoral heads in a red panda (*Ailurus fulgens*): Possible Legg-Calve-perthes disease. J. Zoo. Wildl. Med. **33,** 283–285.

Fisher, R. E., B. Adrian, M. Barton, J. Holmgren, and S. Y. Tang, 2009: The phylogeny of the red panda (*Ailurus fulgens*): evidence from the forelimb. J. Anat. **215,** 611–635.

Goodchild, S., and C. Schwitz, 2008: The problem of obesity in captive lemurs. Int. Zoo. News. **55,** 353–357.

Groves, C., 2011: The taxonomy and phylogeny of *Ailurus*. In: Red Panda Biology and Conservation of the First Panda (A. Glatston, ed.). London: Academic Press. pp. 101–124.

Hamerton, B. C. A. E., 1944: Report on the deaths occurring in the Society's Gardens during the year 1943. J. Zool. **114,** 307–321.

Harwell, G., and T. M. Craig, 1981: Dirofilariasis in a red panda. J. Am. Vet. Med. Assoc. **179,** 1258.

Heinrich, R. E., and P. Houde, 2006: Postcranial anatomy of viverravus (mammalian, carnivore) and implications for substrate use in basal carnivore. J. Vert. Paleontol. **26,** 422–435.

IUCN, 2014: IUCN Red list of threatened species. Version 2014. 3. Available at: http://www.iucnredlist.org, accessed on 18 November 2014.

Jungle, R. E., 2003: Prosimians. In: Zoo and Wild Animal Medicine (M. E. Fowler and R. E. Miller, eds). Missouri: Saunders. pp. 334–346.

Jungle, R. E., C. V. Williams, and J. Campbell, 2009: Nutrition and behavior of lemurs. Vet. Clin. Exot. **12,** 339–348.

Jungle, R. E., K. G. Mehren, T. P. Meehan, G. J. Crawshaw, M. C. Duncan, L. Gilula, F. Gannon, G. Finkel, and M. P. Whyte, 1994: Periarticular hyperostosis and renal disease in six black lemurs of two family groups. J. Am. Vet. Med. Assoc. **205,** 1024–1029.

Kondo, H., Y. Wada, G. Bando, M. Kosuge, K. Yagi, and Y. Oku, 1996: Alveolar hydatidosis in a gorilla and a ring-tailed lemur in Japan. J. Vet. Med. Sci. **58,** 447–449.

Lynch, M., H. McCracken, and R. Slocombe, 2002: Hyperostotic bone disease in red pandas (*Ailurus fulgens*). J. Zoo. Wildl. Med. **33,** 263–271.

Makungu, M., W. M. du Plessis, M. Barrows, K. N. Koeppel, and H. B. Groenewald, 2013: Polycystic kidneys in the red panda (*Ailurus fulgens*). J. Zoo. Wildl. Med. **44,** 777–780.

Martini, A. C., Y. S. Meireles, S. Monzem, L. P. Vanconcelos, N. C. M. R. Turbino, M. A. A. Dahroug, D. Farias, P. B. Néspoli, G. F. Gonçalves, R. L. Souza, and L. D. Guimarães, 2013: Radiographic evaluation of the cardiac silhouette using the VHS method (vertebral heart score) in young and adults coatis (*Nasua nasua*, Linneaus 1766) living in captivity. Semin Ciênc Agrár **34,** 3823–3830

Martins, G. S., E. R. Lopes, I. I. G. Taques, C. Y. Correia, Y. S. Meireles, N. C. M. R. Turbino, L. D. Guimarães, and P. B. Néspoli, 2013: Radiographic morphology of the skeleton, thorax and abdomen of coati (*Nasua nasua* Linnaeus, 1766). Pesq. Vet. Bras. **33,** 1137–1143.

Nickel, R., A. Schummer, E. Seiferle, J. Frewein, H. Wilkens, and K. H. Wille, 1986: The Anatomy of the Domestic Animals. Berlin: Springer-Verlag.

Nowak, R. M., 1999: Order Primate. In: Walker's Mammals of the World (R. M. Nowak, ed.). Baltimore: The Johns Hopkins University Press. pp. 490–631.

Nyland, T. G., and J. S. Mattoon, 2002: Small Animal Diagnostic Ultrasound. Philadelphia: Saunders.

Palotay, J. L., and H. Uno, 1975: Hydatid disease in four nonhuman primates. J. Am. Vet. Med. Assoc. **167,** 615–618.

Philippa, J. and E. Ramsay, 2011. Captive red panda medicine. In: Red Panda Biology and Conservation of the First Panda (A. Glatston, ed.). London: Academic Press. pp. 271–285.

Preece, B., 2011: Red panda pathology. In: Red Panda Biology and Conservation of the First Panda (A. Glatston, ed.). London: Academic Press. pp. 287–302.

Remick, A. K., A. J. Van Wettere, and C. V. Williams, 2009: Neoplasia in prosimians: case series from captive prosimians population and literature review. Vet. Pathol. **46,** 746–772.

Ribeiro, R. G., A. P. A. Costa, N. Bragato, A. M. Fonseca, J. C. M. Duque, T. D. Prado, A. C. R. Silva, and N. C. Borges, 2013: Normal sonographic anatomy of the abdomen of coatis (*Nasua nasua* Linnaeus 1766). BMC Vet. Res. **9,**124.

Schmidt, R. E., 1975: Tuberculosis in a ring-tailed lemur (*Lemur catta*). J. Zoo. Wildl. Med. **6,** 11–12.

Scott, H. H., and H. Camb, 1925: Congenital malformations of the kidney in reptiles, birds and mammals. Proc. Zool. Soc. Lond. **95,** 1259–1269.

Shahar, R., I. H. Horowitz, and I. Aizenberg, 1995: Disseminated hydatidosis in a ring-tailed lemur (*Lemur catta*): A case report. J. Zoo. Wildl. Med. **26,** 119–122.

Taylor, K., 2009: Ring-tailed Lemur Husbandry Manual. New South Wales: Taronga Western Plains Zoo.

Thrall, D. E., and I. D. Robertson, 2011: Atlas of Normal Radiographic Anatomy and Anatomic Variants in the Dog and Cat. Missouri: Elsevier Saunders.

Tomson, F. N., and R. R. Lotshaw, 1978: Hyperphosphataemia and hypocalcemia in lemurs. J. Am. Vet. Med. Assoc. **173,** 1103–1106.

Tuten, H. C., H. C. Miller, and A. E. Ellis, 2011: Cuterebrid myiasis (Diptera: Oestridae) in captive ring-tailed lemurs (*Lemur catta*) at a South Carolina Zoo. J. Zoo. Wildl. Med. **42,** 504–507.

Wagner, W. M., and R. M. Kirberger, 2005a: Radiographic anatomy of the thorax and abdomen of the common marmoset (*Callithrix jacchus*). Vet. Radiol. Ultrasound. **46,** 217–224.

Wagner, W. M., and R. M. Kirberger, 2005b: Transcutaneous ultrasonography of the abdomen in the normal common marmoset (Callithrix jacchus). Vet. Radiol. Ultrasound. **46,** 251–258.

Warwick, R., 1951: A sarcoma of bone in a ring-tailed lemur. J. Pathol. Bacteriol. **63,** 499–501.

Weber, M., N. Lamberski, and K. Heriot, 1995: An idiopathic proliferative disease of bone in two species of ruffed lemur (*Varecia variegata variegata* and *Varecia variegata rubra*). In: Proceedings of the joint conference of the American Association of Zoo Veterinarians, Wildlife Disease Association, American Association of Wildlife Veterinarians. Lansing, Michigan. pp. 268.

Wei, F., and Z. Zhang, 2009: Family Ailuridae (red panda). In: Handbook of the Mammals of the World Vol. 1 Carnivores (D. E. Wilson and R. A. Mittermeier, eds). Barcelona: Lynx Edicions. pp. 498–503.

Young, A. N., W. M. du Plessis, D. Rodriguez, and A. Beierschmitt, 2013: Thoracic radiographic anatomy in vervet monkeys (*Chlorocebus sabaeus*). J. Med. Primatol. **42,** 310–317.

Zordan, M., M. Tirado, and C. López, 2012: Hepatic capillariasis in captive ring-tailed lemurs (*Lemur catta*). J. Zoo. Wildl. Med. **43,** 430–433.

Zwart, P., 1989: Contribution to the pathology of the red panda (*Ailurus fulgens*). In: Red Panda Biology (A. R. Glatston, ed.). The Netherlands: SPB Academic Publishing. pp. 25–29.

CHAPTER 2

LITERATURE REVIEW

2.1 RED PANDA (*AILURUS FULGENS*)

2.1.1 Classification

The red panda (*Ailurus fulgens*) (Fig. 2.1) belongs to the order: Carnivora, suborder: Caniformia, family: Ailuridae and genus: *Ailurus* (Wei and Zhang, 2009). It is the only living species in the family Ailuridae (Wei and Zhang, 2009) and is related to procyonids, skunks and mustelids (Groves, 2011). The red panda is classified as a vulnerable species by the International Union for Conservation of Nature and Natural Resources (IUCN) (IUCN, 2014). Its population is threatened by loss and fragmentation of its habitat and poaching for the pet trade and skin (Srivastav et al., 2009).

Fig. 2.1 Photograph of an adult red panda (*Ailurus fulgens*)

2.1.2 Size

The head and body length ranges from 560 to 625 mm, whereas the tail length ranges from 370 to 472 mm (Roberts and Gittleman, 1984). In captivity the weight of adult males ranges from 3.7 to 6.2 kg, with a mean weight of 5.0 kg. The mean weight of females is 4.9 kg, with ranges from 4.2 to 6.0 kg (Roberts and Gittleman, 1984). Wild red pandas weigh between 4.0 to 5.0 kg (Preece, 2011). There is no sexual dimorphism in the colour and size (Roberts and Gittleman, 1984).

2.1.3 Distribution and habitat

The red panda is primarily distributed in Nepal, China, India and Bhutan (Ghose and Dutta, 2011). It is mainly an arboreal animal and lives in mountain forests with bamboo understory at an altitude of 1500–4800 m (Srivastav et al., 2009). The red panda is found in multiple vegetation types such as evergreen forests, deciduous forests, coniferous forests, evergreen and deciduous broad-leaf forests, and deciduous and coniferous mixed forests (Wei and Zhang, 2011). Its habitat contains a high density of shrubs, tree stumps and fallen logs that provide an easy access to bamboo leaves (Wei and Zhang, 2009).

2.1.4 Feeding

The red panda is largely vegetarian and feeds primarily on bamboo leaves [80–90%] (Wei and Zhang, 2009). Bamboo leaves of genera *Phyllostachys*, *Sinarundinaria*, *Thamnocalamus*, *Chimonobambusa* and *Qiongzhuea* form the main diet (Nijboer and Dierenfeld, 2011). It also feeds on berries, seeds, small

vertebrates, insects, flowers, eggs and bamboo shoots (Srivastav et al., 2009; Wei and Zhang, 2009, 2011).

2.1.5 Anatomy

Respiratory system

The trachea of the red panda consists of 38 cartilage rings and is 11.43 cm in length and 1.27 cm in average width (Flower, 1870). The cartilage rings are incomplete dorsally (Fig. 2.2). The trachea (Fig. 2.3), branches into two short principal bronchi (Flower, 1870). The right principal bronchus is shorter and wider than its left counterpart (Flower, 1870). Each principal bronchus divides into a cranial and caudal branch (Flower, 1870).

Fig. 2.2 Dorsal photographic view of the trachea of a 14.3-year-old male red panda. Note the incomplete cartilaginous rings of the trachea.

The right lung consists of four lobes; the cranial, medial, caudal and accessory lobes (Fig. 2.3). The latter is pointed and lies on the medial surface of the caudal lobe (Flower, 1870). The left lung consists of two triangular lobes; the cranial and caudal lobes (Fig. 2.3). The caudal lobe is larger than the cranial lobe (Flower, 1870). The cranial branch of each principal bronchus is confined to the cranial lobe of each lung (Flower, 1870). The caudal branch of the left principal bronchus is confined to the caudal lobe of the left lung, whereas the caudal branch of the right principal bronchus also sends bronchial branches to the middle and accessory lobes (Flower, 1870).

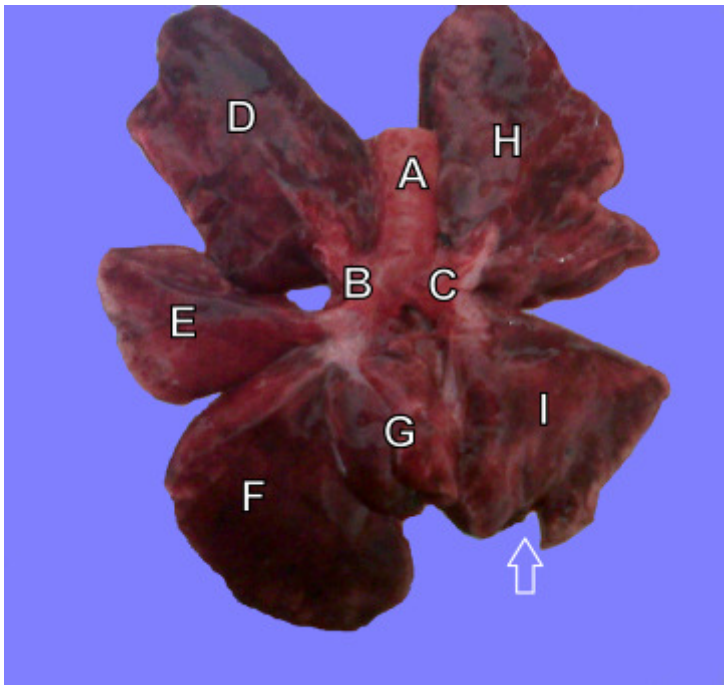

Fig. 2.3 Ventral photographic view of lungs of a 14.3-year-old male red panda. (A) Trachea, (B) right bronchus, (C) left bronchus, (D) right cranial lung lobe, (E) right medial lung lobe, (F) right caudal lung lobe, (G) right accessory lung lobe, (H) left cranial lung lobe and (I) left caudal lung lobe. Open white arrow indicates a site where tissue sample was taken for histopathology.

Digestive system

The liver (Fig. 2.4) of the red panda was seen by the author in one cadaver and consists of four lobes (left, quadrate, right and caudate), four sublobes (left medial, left lateral, right medial and right lateral) and two processes (caudate and papillary). The gall bladder (Fig. 2.4) was located between the quadrate and right medial lobes.

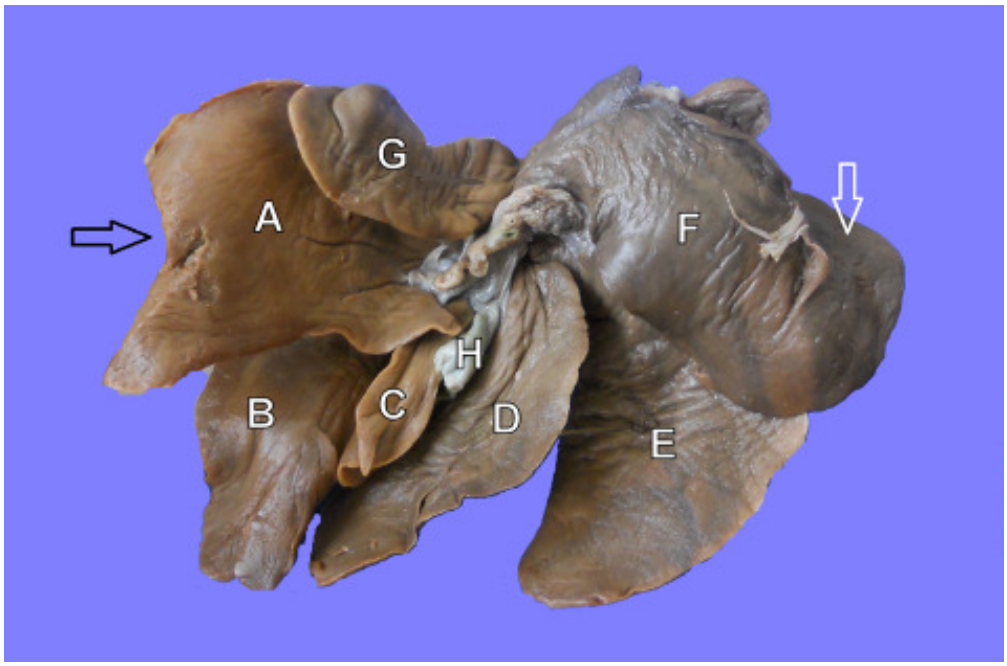

Fig. 2.4 Photograph of the visceral surface of a formalin-fixed liver of a 14.3-year-old male red panda. (A) Left lateral lobe, (B) left medial lobe, (C) quadrate lobe, (D) right medial lobe, (E) right lateral lobe, (F) caudate process of the caudate lobe, (G) papillary process of the caudate lobe and (H) gall bladder. Open white arrow indicates the renal fossa, whereas the open black arrow indicates the site where tissue sample was taken for histopathology.

The stomach of the red panda consists of a single chamber with a thick walled pylorus (Flower, 1870). The digestive tract (Fig. 2.5) is relatively short with a total length of 264.16 cm from the pylorus to the anus (Flower, 1870). The caecum is absent and externally there is no clear distinction between the ileum and colon (Flower, 1870). The lumen of the large intestine is slightly bigger than that of the small intestine (Carlsson, 1925). The ascending, transverse and descending colons are short (Carlsson, 1925). The total length of the colon and rectum is 18 cm (Carlsson, 1925).

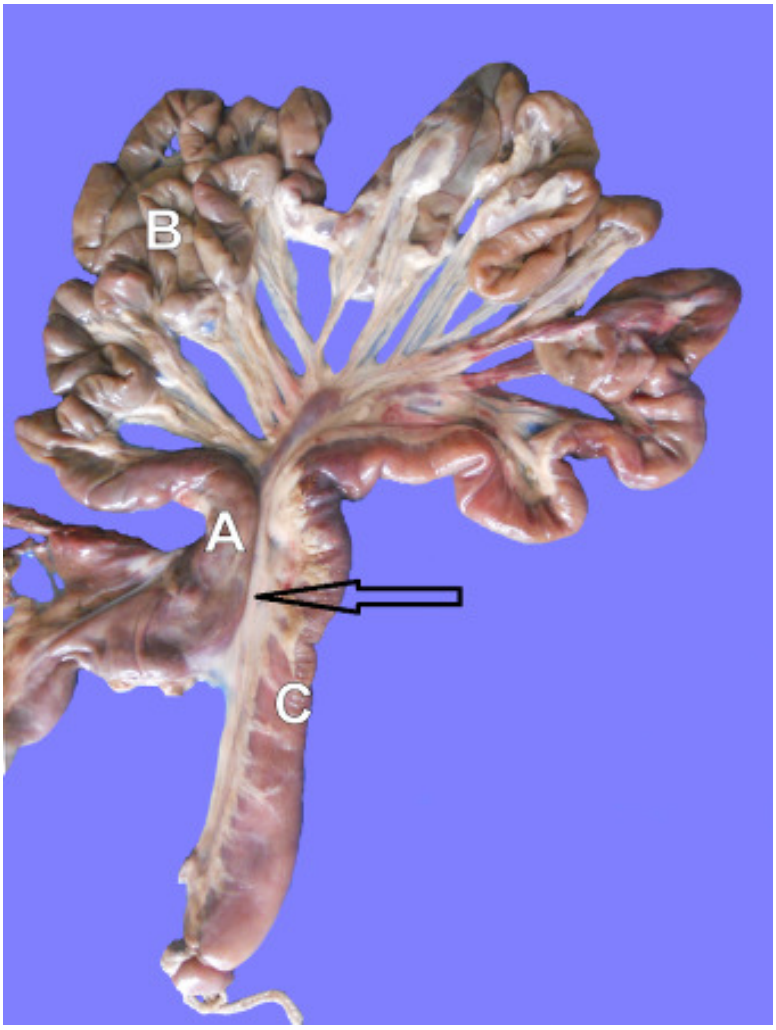

Fig. 2.5 Photograph of intestines of a 14.3-year-old male red panda. (A) Duodenum, (B) jejunum and (C) colon. Duodenocolic fold (open black arrow).

Lymphatic system

The spleen is elongated without a notch or fissure and is located on the left of the stomach (Flower, 1870). It is 14.5 cm in length (Flower, 1870).

Urogenital system

The kidneys lack lobules on the surface and the right kidney is slightly more cranial than the left kidney (Flower, 1870). The os penis is present.

2.1.6 Diseases

Musculoskeletal system

Musculoskeletal diseases like hyperostostic bone disease (Lynch et al., 2002), avascular necrosis of the femoral head (Delclaux et al., 2002), osteomyelitis (Kummerfeld et al., 2008; Preece, 2011), osteoarthrosis, traumatic injuries, ankylosing spondylitis and neoplasia such as squamous cell carcinoma (Philippa and Ramsay, 2011; Preece, 2011) have been reported in this species.

Cardiovascular system

Cardiovascular diseases like right heart failure (Preece, 2011), traumatic pericarditis (Zwart, 1989), dirofilariasis (Harwell and Craig, 1981; Preece, 2011), hypertrophic cardiomyopathy and left ventricular myohypertrophy (Philippa and Ramsay, 2011) have been documented in this species.

Respiratory system

Diseases involving the respiratory system such as infectious and non-infectious pneumonia e.g. aspiration pneumonia, chronic fibrosing interstitial pneumonia and verminous pneumonia (Patterson-Kane et al., 2009; Philippa and Ramsay, 2011; Preece, 2011; Zwart, 1989), lung sarcoma (Philippa and Ramsay, 2011), tracheal obstruction (Preece, 2011), pleuritis (Preece, 2011; Zwart, 1989), anthracosis (Zwart, 1989) and bovine tuberculosis (Philippa and Ramsay, 2011) have been reported in the red panda. Pneumonia is one of the major causes of death in captive neonates (Philippa and Ramsay, 2011).

Digestive system

Diseases of the digestive system such as pyloric ulcers, gastric torsion, enteritis, and intestinal obstruction have been observed in the red panda (Philippa and Ramsay, 2011; Preece, 2011; Zwart et al., 1989). Liver diseases like hepatic lipidosis (Montali et al., 1989), hepatitis, bile duct proliferation (Zwart, 1989) and neoplasia such as hepatocarcinoma (Philippa and Ramsay, 2011) have also been reported. Gastric ulcers, enteritis and hepatic lipidosis are the most common diseases in adult captive red pandas (Philippa and Ramsay, 2011).

Urogenital system

The red panda kidney resembles that of domestic cats since it is prone to physiological accumulation of fat and chronic renal disease (Zwart et al., 1989). Chronic renal disease occurs frequently in older animals and

histopathology shows end-stage renal lesions similar to those seen in domestic cats (Philippa and Ramsay, 2011; Preece, 2011). No aetiology has been identified and it is speculated to be a degenerative disease of old age (Philippa and Ramsay, 2011). Other urogenital diseases such as nephrosis, nephritis, cystic dilation of tubules, glomerulonephrosis (Zwart et al., 1989), polycystic kidneys (Makungu et al., 2013), pyometra (Preece, 2011) and neoplasia such as papillary renal adenoma (Kummerfeld et al., 2008) and ovarian granulosa cell tumour (Alton et al., 2004) have also been reported in this species.

Other diseases which have been seen in the red panda include splenitis (Zwart et al., 1989), feline infectious peritonitis (Preece, 2011) and neoplasia such as chronic lymphoid leukemia and myelogenous leukaemia (Philippa and Ramsay, 2011).

2.2 RING-TAILED LEMUR (*LEMUR CATTA*)

2.2.1 Classification

The ring-tailed lemur (*Lemur catta*) (Fig. 2.6) belongs to the order: Primata, suborder: Strepsirrhini, family: Lemuridae and genus: *Lemur* (Nowak, 1999). It is classified as an endangered species by the IUCN (IUCN, 2014). Most strepsirrhines do not look like monkeys but resemble more primitive animals (Ankel-Simons, 2007). They are characterized by retaining primitive features like prominent scent glands, rhinarium, pointed muzzle, tapetum lucidum, open eye sockets, small brain case, epitheliochorial placenta, and bicornuate uterus (Jungle, 2003; Ankel-Simons, 2007).

Fig. 2.6 Photograph of an adult ring-tailed lemur (*Lemur catta*)

2.2.2 Size

The head and body length ranges from 385 to 455 mm (mean; 423 mm) whereas the tail length ranges from 560 to 624 mm (mean; 595 mm) (Wilson and Hanlon, 2010). The cranium measures 78 to 88 mm (mean; 84) in length (Wilson and Hanlon, 2010). In the wild, the mean weight of the ring-tailed lemur has been reported to be 2.2 kg (Jungle, 2003; Goodchild and Schwitzer, 2008). In captivity, females weigh 2.678 kg whereas males weigh 2.705 kg (Kappeler, 1991).

2.2.3 Distribution and habitat

The ring-tailed lemur is primarily distributed in south and south-western Madagascar (Budnitz and Dainiz, 1975). Its habitat consists of continuous canopy forests, brush and scrub forests, and mixed forests (Budnitz and Dainiz, 1975). The latter occurs where continuous canopy forest merges into brush and scrub habitat (Budnitz and Dainiz, 1975). The continuous canopy forests are dominated by *Tamarindus indica* and *Celtis gomphophylla*, whereas the brush and scrub forests are dominated by *Azima tetracantha*, *Maerua filiformis*, *Salvadora angustifolia*, and *Guisivianthe papionaea* (Budnitz and Dainiz, 1975).

2.2.4 Feeding

The ring-tailed lemur is an opportunistic omnivore (Taylor, 2009) primarily eating fruits (Wilson and Hanlon, 2010). It also feeds on leaves (Wilson and Hanlon, 2010). Tamarind leaves and seed pods are commonly consumed (Wilson and Hanlon, 2010). Apart from fruits and leaves, it also feeds on small

vertebrates, arthropods, flowers, decayed wood and insect cocoons (Taylor, 2009).

2.2.5 Anatomy

Respiratory system

The trachea of *Lemurs* has complete cartilaginous rings (Fig. 2.7) with the thoracic part being very long (Patten, 1899). The principal bronchi are relatively short with the right principal bronchus being shorter than the left principal bronchus (Patten, 1899).

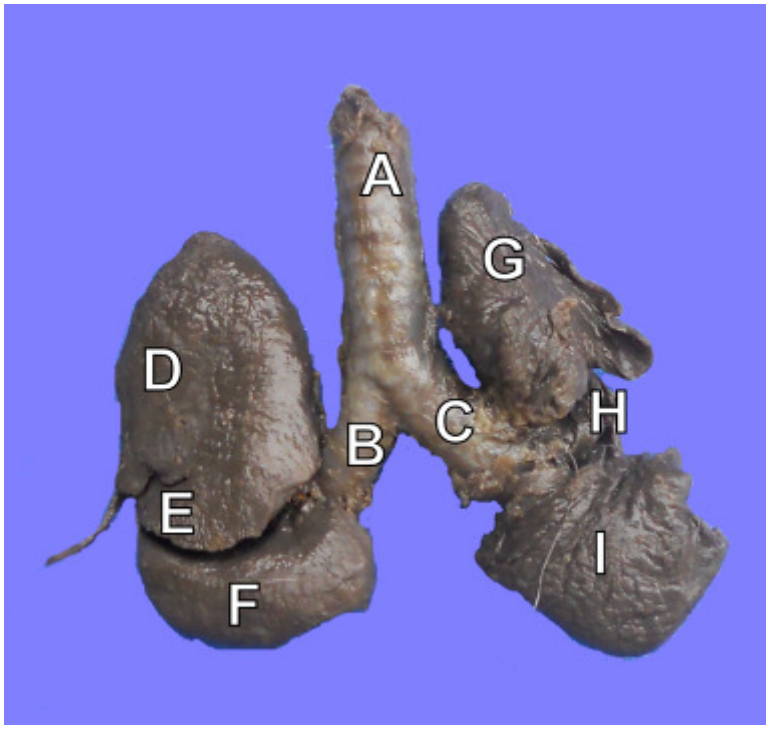

Fig. 2.7 Dorsal photographic view of formalin-fixed lungs of a 5-year-old female ring-tailed lemur. Note the complete cartilaginous rings of the trachea. (A) Trachea, (B) left bronchus, (C) right bronchus, (D) cranial part of the cranial lobe of the left lung, (E) caudal part of the cranial lobe of the left lung, (F) caudal lobe of the left lung, (G) cranial lobe of the right lung, (H) medial lobe of the right lung and (I) caudal lobe of the right lung

Each lung is conical with a pointed apex. The latter, is more pointed than in humans (Patten, 1899). The apex of the lungs does not protrude through the thoracic inlet into the root of the neck. It only reaches to the level of the caudal border of the first costal arch (Patten, 1899). The left lung consists of two lobes; the cranial and caudal lobes. The cranial lobe is larger than the caudal lobe. The cranial lobe is incompletely subdivided into cranial and caudal parts by a short fissure (Patten, 1899). The right lung consists of cranial, medial, caudal and accessory lobes (Patten, 1899) (Fig. 2.7). Osman Hill, (1953) reported the presence of three lobes in the left lung of genus *Lemur*.

Digestive system

The stomach of the ring-tailed lemur is simple and pyriform (Osman Hill, 1953). The greater part of the small intestine possesses a wide diameter especially the duodenum. The duodenum narrows considerably towards the ileum (Patten, 1902). It consists of a longer cranial portion and a shorter transverse portion which crosses the spine as far caudally as the fourth lumbar vertebra (Osman Hill, 1953). The caecum is large and very long with a conical appendix-like termination (Osman Hill, 1953).

The colon has a sigmoid arrangement (Fig. 2.8). From the right caudally located ileo-caecal junction, the ascending colon proceeds in an oblique direction cranially and to the left up to the hepatic flexure. From the hepatic flexure to the splenic flexure, the transverse colon pursues a curved course making a U-shaped ansa. The rest of the large intestine from the splenic flexure to the anus takes a straight course caudally (Patten, 1902; Osman Hill,

1953). Campbell et al., (2000) observed apparent teniae in the caecum of the ring-tailed lemur but no distinct teniae were observed in the colon.

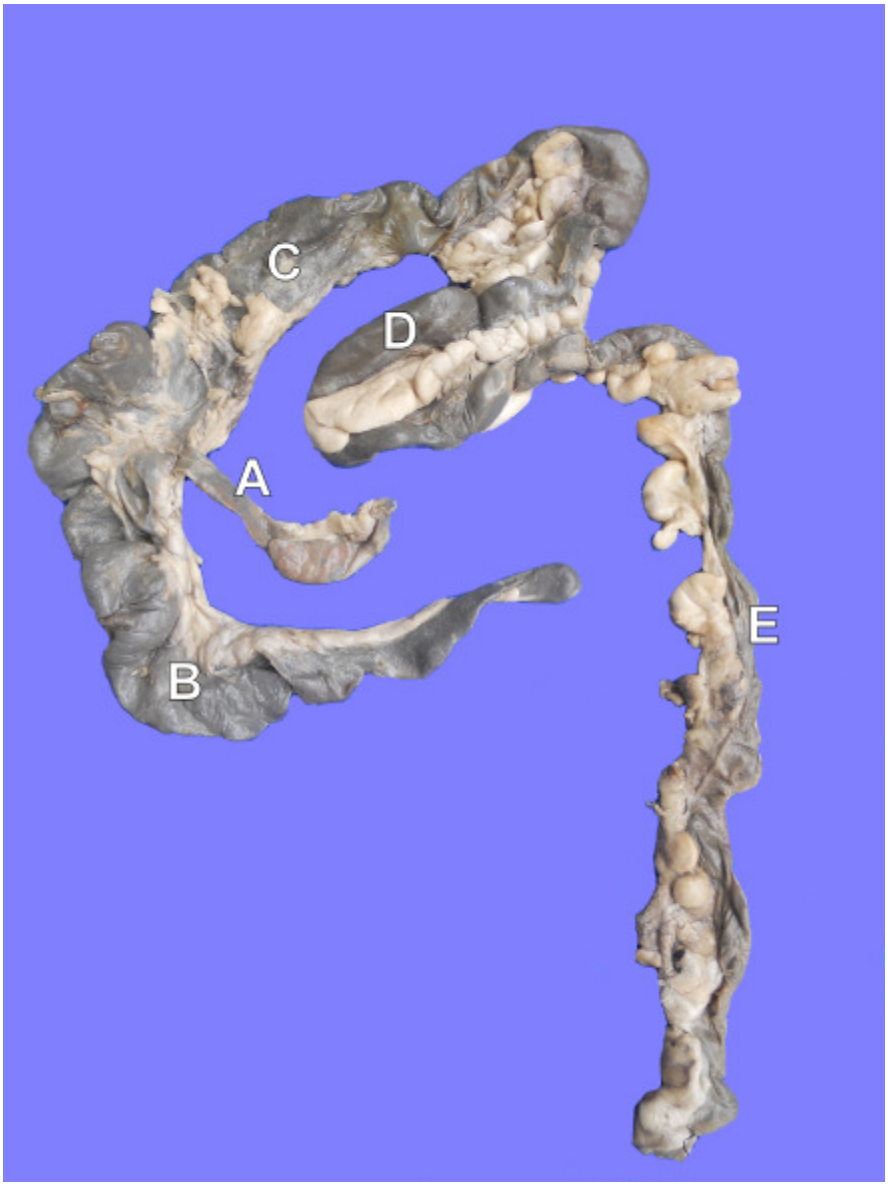

Fig. 2.8 Photograph of formalin-fixed intestines of a 5-year-old female ring-tailed lemur. Note the U-shaped ansa formed by the transverse colon (D). (A) Ileum, (B) cecum, (C) ascending colon and (E) descending colon.

In the ring-tailed lemur, the liver consists of four lobes; the right, left, quadrate and caudate lobes (Osman Hill, 1953). The left lobe is the largest (Osman Hill, 1953). The caudate process of the caudate lobe is large and bears a renal impression. The papillary process of the caudate lobe is very small (Osman Hill, 1953). The gall bladder lies in a deep fissure of the quadrate lobe near its right margin (Osman Hill, 1953) (Fig. 2.9).

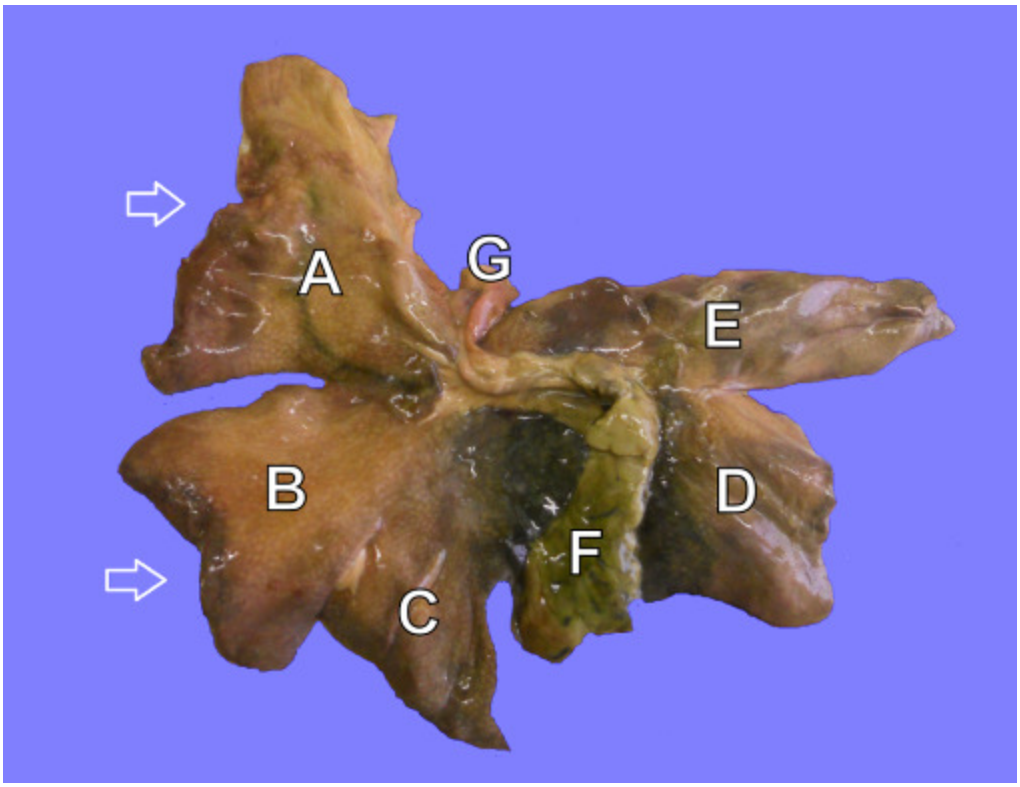

Fig. 2.9 Photograph of the visceral surface of the liver of a 5-year-old female ring-tailed lemur. (A) Left lateral lobe, (B) left medial lobe, (C) quadrate lobe, (D) right lobe, (E) caudate process of the caudate lobe, (F) gall bladder and (G) papillary process of the caudate lobe. Open white arrows indicate sites where tissue samples were taken for histopathology.

Lymphatic system

The spleen of the ring-tailed lemur is an elongated strap-like structure resembling that of lower mammals rather than the spleen of monkeys and apes (Osman Hill, 1953).

Urogenital system

The kidneys are located on the dorsal abdominal wall in the lumbar region (Osman Hill, 1953). The right kidney is located cranial to the left kidney (Osman Hill, 1953). The undivided medulla is located centrally surrounded by an even layer of cortex. The medulla ends medially in a single pyramid which projects into the renal sinus (Osman Hill, 1953). The pelves of the ureters are entirely intrarenal. The pyriform urinary bladder is intra-abdominal and is broader in males than in females (Osman Hill, 1953).

The os penis is roughly fusiform and lacks any hint of a urethral groove (Drea and Weil, 2008). The clitoris resembles the male penis superficially although the urethra opens on the ventral surface of the glans (Drea and Weil, 2008). An os clitoridis is present within the corpus cavernosum of the glans clitoridis. It lies dorsal and distal to the opening of the urethra, and is parallel with the urethra (Drea and Weil, 2008).

2.2.6 Diseases

Musculoskeletal system

Musculoskeletal diseases such as nutritional secondary hyperparathyroidism (Tomson and Lotshaw, 1978), idiopathic proliferative bone disease (Weber et al., 1995), multifocal pyogranulomatous osteomyelitis (Backues et al., 2001), periarticular hyperostosis (Jungle et al., 1994), traumatic injuries (Dank et al., 2012), and neoplasia like osteosarcoma (Warwick, 1951), mammary carcinomas (Wadsworth et al., 1980), lipoma and papilloma (Remick et al., 2009) have been reported in lemurs.

Respiratory system

Diseases of the respiratory system like pneumonia (Hamerton, 1944; Tuten et al., 2011), tuberculosis (Schmidt, 1975), pleural effusions (Burton et al., 1986; Jungle, 2003), lung atelectasis (Palotay and Uno, 1975), sudden acute respiratory distress syndrome (M. Barrows, personal communications) and neoplasia such as lymphoma (Pye et al., 2000) and myelolipoma (Remick et al., 2009) have been reported in the ring-tailed lemur.

Cardiovascular system

Cardiovascular diseases such as encephalomyocarditis virus infection (Canelli et al., 2010) and pericardial effusion (Zordan et al., 2012) have also been documented.

Digestive system

Diseases involving the digestive system such as tooth wear and loss (Cuozzo et al., 2010), intestinal ulcers (Scott and Camb, 1925) and neoplasia like colonic adenocarcinoma (Remick et al., 2009) have been reported in this species. Further, liver diseases like fibrosis, hepatic lipidosis, capillariasis (Zordan et al., 2012), haemochromatosis (Taylor, 2009) and neoplasia such as cholangioma (Remick et al., 2009) and cholangiocarcinoma (Chang et al., 1979) have also been documented.

Urogenital system

Urogenital diseases such as urinary tract obstruction (Jungle, 2003), renal aplasia/hypoplasia (Scott and Camb, 1925), pyelonephritis, kidney infarcts, cystitis (Burton et al., 1986) and neoplasia like mixed epithelial and stromal tumour of the kidney (Muller et al., 2007), renal adenoleiomyofibromatous harmatoma (Jones and Casey, 1981) and papillary adenoma of the prostate (Remick et al., 2009) have been reported in this species.

Other diseases which have been reported in the ring-tailed lemur include; hydatidosis (Kondo et al., 1996; Palotay and Uno, 1975; Shahar et al., 1995), cysticercosis (Luzón et al., 2010) and neoplasia such as adrenal gland phaechromocytoma (Remick et al., 2009).

2.3 RADIOGRAPHY

2.3.1 X-rays

X-rays were discovered on November 8, 1895 by a German physicist, Wilhelm Conrad Roentgen (Lavin, 2007). They are one form of electromagnetic radiation similar to visible light but with a shorter wavelength and high energy (Lavin, 2007). Although X-rays are useful in the diagnosis of diseases, they are dangerous if not used properly. Therefore understanding their physical properties ensures efficient and safe use of X-rays. The following are physical properties of X-rays (Lavin, 2007), which should be considered whenever using them for diagnosis of diseases:

- They travel in a straight line
- They have an ability to penetrate materials that absorb or reflect visible light
- The wavelength is variable and is related to the energy of radiation
- They produce an invisible image on photographic film, which can be converted into a visible image after film processing
- They have an ability to cause certain crystals to fluoresce
- They have an ability to ionize or excite atoms and molecules of substances through which they pass
- They can cause biologic changes in living tissues. The biologic changes may occur directly due to ionization or excitation of important molecules in cells or indirectly due to chemical changes occurring near the cell. The affected cells may be damaged or killed.

2.3.2 Electromagnetic radiation

Electromagnetic radiation is a combination of electric and magnetic energy travelling through a space at the speed of light, 3 x 10^8 m/s (Perry, 1993). It consists of oscillating electric and magnetic fields (Hendee and Russell Ritenour, 2002). Examples of electromagnetic radiation are visible light, ultraviolet light, infrared, radio and television waves, microwaves, X-rays and gamma rays (Perry, 1993). The different forms of electromagnetic radiation can be differentiated based on their wavelength (λ) (Perry, 1993).

The energy of electromagnetic radiation is inversely proportional to its wavelength (Thrall and Widmer, 2007). The shorter the wavelength the greater the energy of electromagnetic radiation, and vice versa (Lavin, 2007). Electromagnetic radiation with shorter wavelength has greater energy and higher penetration power than those with longer wavelength (Lavin, 2007). An electromagnetic wave does not require a medium for propagation. It can travel in a vacuum as well as through matter (Hendee and Russell Ritenour, 2002). Radiation with energy less than 13.6 eV is classified as non-ionizing radiation (Hendee and Russell Ritenour, 2002). X-rays, gamma rays and some ultraviolet rays are the only electromagnetic radiation with sufficient energy to ionize matter (Perry, 1993).

2.3.3 X-rays production

X-rays are produced in an X-ray tube when high-speed electrons strike a heavy metal like tungsten (Perry, 1993). The process of X-rays production is very inefficient. For X-ray tubes operated at conventional voltages, only 1% of the energy released at the impact of electrons is in the form of X-rays, whereas 99% is released in the form of heat (Lavin, 2007). When high speed electrons strike a heavy metal (target), X-rays are produced by two atomic processes, which are radiative and collisional interactions (Thrall and Widmer, 2007).

In collisional interaction (K-shell emission), the oncoming high speed electron from the cathode ejects an orbital electron from the K-shell of the target atom (Thrall and Widmer, 2007). A more peripheral (outer shell) electron from the higher energy level or a free electron will fill the void in the inner shell (Thrall and Widmer, 2007). The difference in the energy level is emitted as characteristic X-ray (Hendee and Russell Ritenour, 2002). The ejected electron and the oncoming electron from the cathode may produce additional collisional or radiative interactions, but the X-ray photons produced are of low energy and not useful for diagnostic imaging (Thrall and Widmer, 2007). Theoretically, any shell could contribute to collisional interaction. However, in practice, transition of electrons among shells beyond M-shell produce only low energy X-rays, visible light and ultraviolet light (Hendee and Russell Ritenour, 2002). These low energy X-rays are removed by inherent filtration and do not become part of the useful beam (Hendee and Russell Ritenour, 2002).

The characteristic X-rays produced by a target are usually dominated by one or two peaks with specific energies slightly less than the binding energy of the K-shell electrons (Hendee and Russell Ritenour, 2002). This is due to the fact that the most likely transition involves an L-shell electron dropping to fill a vacancy in the K-shell. This transition produces a characteristic X-ray photon, which is equal to the difference in electron binding energies of the K- and L-shells (Hendee and Russell Ritenour, 2002). A characteristic X-ray photon with an energy equal to the binding energy of the K-shell alone is produced only when the vacancy in a K-shell is filled with a free electron from outside the atom and the probability of this event is very small (Hendee and Russell Ritenour, 2002). A characteristic X-ray released during transition of an electron between adjacent shells is known as α X-ray e.g. K_{α}, whereas an X-ray produced by transition involving non-adjacent shells is known as β X-ray e.g. K_{β} (Hendee and Russell Ritenour, 2002).

In radiative (braking or bremsstrahlung) interaction, the oncoming high speed electron from the cathode is attracted by a positively charged nucleus of the target atom (Thrall and Widmer, 2007). It slows and bends around the nucleus of the target atom releasing X-ray photons. The oncoming electron may produce additional X-ray photons through radiative or collisional interactions (Thrall and Widmer, 2007). X-rays produced by collisional interactions account for only a small fraction of the total X-rays produced in an X-ray tube. When a peak kilovoltage (kVp) of 80–100 is applied across the X-ray tube, about 90% of the emitted X-rays are bremsstrahlung radiation and 10% are characteristic radiation (Perry, 1993).

The higher the potential voltage difference applied across the X-ray tube, the faster the electron will travel from the cathode to the anode, the greater the amount of energy released on impact and the shorter the wavelength of the X-ray produced (Douglas and Williamson, 1980). The shorter the wavelength of the X-rays, the greater the penetration power (quality) of the X-ray beam (Douglas and Williamson, 1980). The quality of the X-ray beam produced can be varied by varying the potential voltage difference across the tube (Douglas and Williamson, 1980). The potential voltage difference across the tube is adjusted with the kVp selector on the control panel (Thrall and Widmer, 2007). X-rays with longer wavelengths are referred to as “soft” X-rays, whereas those with shorter wavelengths are referred to as ‘hard’ X-rays (Douglas and Williamson, 1980).

The quantity of X-rays produced depends on the number of electrons available at the cathode. The number of electrons produced at the cathode is directly related to the amount of electric current passing through the filament of the cathode, which in turn is regulated by the milliamperage selector on the control panel of the X-ray machine (Thrall and Widmer, 2007). Therefore by regulating the current delivered to the filament, the operator controls the quantity (intensity) of X-rays produced (Douglas and Williamson, 1980). The higher the milliamperage, the greater the quantity of X-rays produced. However, the quantity of X-rays produced during a given exposure also depends on the duration of exposure (exposure time) (Douglas and Williamson, 1980). Therefore the quantity of X-rays produced depends on the milliamperage and exposure time (Douglas and Williamson, 1980).

2.3.4 X-ray machine

The main components of the X-ray machine are; the X-ray tube, transformers, control panel and tube stand (Douglas and Williamson, 1980). The X-ray tube consists of an anode and cathode encased in a glass envelope (Lavin, 2007). The glass envelope is evacuated and surrounds other components, which are required for X-ray production i.e. the anode and cathode (Hendee and Russell Ritenour, 2002). The vacuum environment eliminates air molecule obstacles from the electron stream (Lavin, 2007). Additionally, it reduces deterioration of the filament (cathode) by oxidation (Hendee and Russell Ritenour, 2002). The entire X-ray tube is mounted inside a metal housing (tube-housing), which is grounded electrically (earthed) and lined with lead (Hendee and Russell Ritenour, 2002). The tube-housing protects the glass envelope from physical damage (Lavin, 2007), attenuates X-rays emerging from the X-ray tube in an undesired direction (Hendee and Russell Ritenour, 2002; Lavin, 2007) and serves as a reservoir for oil, which absorbs heat generated from the anode and insulate the tube housing from high voltage applied to the X-ray tube (Hendee and Russell Ritenour, 2002).

The tube-housing is equipped with an aperture (window) through which an X-ray beam emerges (Douglas and Williamson, 1980). The glass envelope, the layer of insulating oil surrounding the tube and the window in the tube housing act as a filter, which absorbs the softest X-rays from the beam (Perry, 1993). This property of the tube head is known as inherent filtration (Perry, 1993; Hendee and Russell Ritenour, 2002). Additional filtration is achieved by

adding aluminium filters in the X-ray beam pathway between the X-ray tube and the collimator (Perry, 1993).

The total filtration used in diagnostic radiology is 2.5 mm of aluminium (0.5 mm: inherent filtration; 2 mm: added filtration) (Perry, 1993). Filters absorb low energy X-rays, therefore harden the X-ray beam and hence improve the penetrability (quality) of the X-ray beam (Perry, 1993). Low energy X-rays increase the radiation dose to the patient without contributing substantially to the image formation (Hendee and Russell Ritenour, 2002). Therefore, the primary function of the filters is to reduce the radiation dose to the patient (Perry, 1993).

The anode is a positively charged electrode inside the X-ray tube. It consists of a bevelled metal target placed on a cylindrical base (Lavin, 2007). The target is usually composed of tungsten, which can withstand and dissipate high temperatures (Lavin, 2007). The choice of a target material affects the energy at which characteristic X-rays appear and the efficiency of X-ray production (Hendee and Russell Ritenour, 2002). In fixed technical factors i.e. tube voltage, milliamperage and time, a target material with a higher atomic number will produce more X-rays per unit time by the process of bremsstrahlung (Hendee and Russell Ritenour, 2002). Molybdenum can produce K-characteristic X-rays at a lower voltage than tungsten (Hendee and Russell Ritenour, 2002). Therefore, for low voltage studies of soft tissue structures such as mammography, X-ray tubes with a molybdenum target are

more preferred than those with a tungsten target (Hendee and Russell Ritenour, 2002).

There are two main types of anodes; the stationary and rotating anodes. The stationary anode is found in dental and small portable radiography units (Lavin, 2007). The target area is made up of tungsten, which is embedded on a cylinder of copper. The face of the target is angled down towards the window (Lavin, 2007). The angle ranges from 6º–17º in most diagnostic X-ray tubes (Hendee and Russell Ritenour, 2002). The cooling mechanism in stationary anodes is achieved by the presence of a copper block, which is a good conductor of heat and hence draws heat away from the tungsten target. Additionally, oil which surrounds the glass tube within the tube housing absorbs heat radiated from the anode. However, the stationary anode cannot withstand large amounts of heat, which is its primary limitation. Repeated bombardment by electrons and subsequent heat production causes pitting of the target surface (Lavin, 2007). This limitation led to the development of a rotating anode, which is found in X-ray machines with high output.

The disk shaped rotating anode is mounted on a spindle, which is made of molybdenum, whereas the disk is composed of tungsten or some similar alloy that can withstand high temperatures (Lavin, 2007). It rotates on an axis through the centre of the tube and hence heat is distributed over a larger area, which provides a cooler surface for the electron stream. The target area within which the X-rays collide remains constant (Lavin, 2007).

The focal spot is the area on the target that is bombarded by the electron stream (Perry, 1993). The smaller the focal spot the sharper the radiographic image. Unfortunately a small focal spot is associated with a greater concentration of heat and increase the danger of overloading and melting the target (Perry, 1993). A large focal spot can tolerate more heat than a small focal spot but causes penumbra effect, which blurs the image (Lavin, 2007).

The bevelled edge of the anode angles the target, which makes the effective area of the target (effective focal spot) much smaller than the actual focal spot (Perry, 1993) and at the same time maintains a large area to be struck by electrons, which facilitates heat distribution (Thrall and Widmer, 2007). This phenomenon is known as the line-focus principle (Perry, 1993) and was devised by Goetze (Douglas and Williamson, 1980). The actual focal spot is the area of the target which is bombarded by the electron stream (Perry, 1993), whereas the effective (apparent) focal spot is the foreshortened appearance of the target seen from the window of the X-ray tube (Douglas and Williamson, 1963). The line-focus principle combines the image sharpness of a small focal spot with the ability of a large focal spot to tolerate heat (Perry, 1993).

The cathode is a negatively charged electrode for the high-tension circuit. It is also a source of electrons required for X-ray production (Douglas and Williamson, 1980). The cathode consists of a coiled wire filament made up of tungsten. Tungsten has a high melting point, therefore it can withstand the heat produced at the filament. Additionally, it has a high atomic number, which

corresponds to the potential electron availability (Lavin, 2007). The filament is mounted on rigid wires, which support it and carry the electric current that is used to heat the filament (Lavin, 2007). In most X-rays tubes, the filament measures 0.2 cm in diameter and 1 cm in length. A single filament is found in some X-ray tubes usually those used in small portable and mobile units, whereas most modern tubes have two filaments (Lavin, 2007). When a filament is heated by a low voltage current, a cloud of electrons is formed around the filament (Douglas and Williamson, 1980). The loose electrons are accelerated at a high speed to bombard with the anode (target), when the exposure button is pressed and high-tension is applied to the tube (Douglas and Williamson, 1980).

Variation in intensity across an X-ray beam is known as the heel effect (Hendee and Russell Ritenour, 2002). It is caused by the absorption of some of the X-rays by the target (Perry, 1993). For targets mounted at a small angle, the attenuation of X-rays emerging along the anode side of the X-ray beam is greater than for those emerging along the side of the beam nearest the cathode. Consequently, the X-ray intensity decreases from the cathode to the anode side of the beam (Hendee and Russell Ritenour, 2002). To compensate for the heel effect, thicker portions of a patient must always be positioned towards the cathode side of the X-ray beam (Hendee and Russell Ritenour, 2002). A wedge filter with a thickness increasing from the anode to the cathode side of the X-ray beam may also be installed in the tube housing near the tube window (Hendee and Russell Ritenour, 2002).

Transformers are an essential part of an X-ray machine (Douglas and Williamson, 1980). They convert the incoming voltage (110 V or 220 V) from a standard power source into a suitable form for the operation of an X-ray tube (Douglas and Williamson, 1980; Lavin, 2007). There are three types of transformers in an X-ray machine; step-down transformer, step-up transformer and autotransformer (Douglas and Williamson, 1980). A step-down transformer is placed between the X-ray machine input voltage and the cathode filament (Lavin, 2007). It reduces the voltage of the incoming line to approximately 10 V, which is required to heat the filament of the cathode (Lavin, 2007). The average incoming line voltage to most X-ray machines is 110 V or 220 V (Lavin, 2007). This voltage would cause the filament to vaporize instantly (Lavin, 2007).

The autotransformer allows fluctuations in the mains input voltage to be corrected before the current is fed to the step-up transformer (Douglas and Williamson, 1980). The step-up transformer produces sufficient high voltage current required for the production of X-rays i.e. from 40 kVp upwards (Douglas and Williamson, 1980). It increases the incoming line voltage from 110 V or 220 V to thousands of volts required for X-rays production (Lavin, 2007).

The control panel contains switches, meters and controls necessary for operating the X-ray machine (Douglas and Williamson, 1980). The closure of the On/Off switch permits the flow of current to the X-ray machine necessary for subsequent exposure (Douglas and Williamson, 1980). The On/Off switch

should only be left at 'On' when the machine is being used and returned to 'Off' at the completion of radiography (Douglas and Williamson, 1980). The actual voltage being supplied to the X-ray machine from the mains is indicated by the voltmeter. If there is any variation in the voltage supplied to the X-ray machine from the mains, the X-ray machine will not give a consistent output (Douglas and Williamson, 1980). Fluctuations in the voltage supplied to the X-ray machine are corrected by adjusting the autotransformer by means of the voltage compensator control (Douglas and Williamson, 1980). In newer X-ray units it occurs automatically (Lavin, 2007).

The kVp selector regulates the potential voltage difference across the tube (Douglas and Williamson, 1980). The higher the kVp setting, the greater the penetrating ability (quality) of the X-ray beam and vice versa. In most modern X-ray machines the kVp selector is directly calibrated so that the desired value can be easily selected. However, in some small X-ray machines it is automatically linked to a certain milliamperage value (Douglas and Williamson, 1980). Most portable X-ray machines have a kVp range of 60 to 90, whereas the average portable X-ray machine has a kVp range of 40 to 120 (Lavin, 2007). The milliamperage selector controls the current flowing to the cathode filament (Lavin, 2007), whereas the milliammeter records the current passing through the tube. The milliammeter records only during the actual X-ray exposure (Douglas and Williamson, 1980). The tube stand is the apparatus, which is used to support the X-ray tube during radiographic exposure (Douglas and Williamson, 1980). It includes different forms of

suspension, which vary from small table top stands to overhead ceiling mountings (Douglas and Williamson, 1980).

2.3.5 Interaction of X-rays with matter

X-ray photons interact with matter by the following mechanism; coherent scattering, photoelectric effect, Compton scattering, pair production and photodisintegration (Perry, 1993). Coherent scattering involves low energy X-rays below 10 keV (Perry, 1993) and an X-ray photon from the X-ray tube changes its direction after interaction with matter (Thrall and Widmer, 2007). The X-ray photon is not absorbed and its energy does not change (Thrall and Widmer, 2007). The fraction of X-rays striking a patient that undergoes coherent scattering is very small, approximately 5 % (Thrall and Widmer, 2007). The scattered photons may strike the X-ray film or radiographer thereby degrading the image quality (film fogging) or increasing personnel exposure, respectively (Thrall and Widmer, 2007). Therefore, coherent scattering is not useful in the production of the radiograph (Thrall and Widmer, 2007). Coherent scattering is the only mechanism of X-ray interaction with matter that does not cause ionization (Perry, 1993).

In Compton scattering, the incoming X-ray photon from the X-ray tube ejects a peripheral shell electron of a tissue atom (ionization) (Thrall and Widmer, 2007). The photon is scattered at a different angle with a lower energy level than the original photon, and may produce more ionization or degrade the image quality (film fogging) (Thrall and Widmer, 2007). Additionally, it is a radiation safety hazard (Thrall and Widmer, 2007). The ejected orbital electron

may produce additional ionizations but will be subsequently absorbed in the patient (Thrall and Widmer, 2007). Compton reaction is independent of the atomic number of the absorber, which is disadvantageous because it results in poor image contrast due to poor differential absorption (Thrall and Widmer, 2007).

In photoelectric effect the incoming photon from the X-ray tube ejects an inner (K) shell electron of a tissue atom (Thrall and Widmer, 2007). The incoming photon is completely absorbed, whereas the ejected orbital electron is capable of producing more tissue ionization but will eventually be absorbed in the patient (Thrall and Widmer, 2007). As the more peripheral or free electron fills the shell vacancy, it gives up energy in the form of a photon with characteristic radiation (Thrall and Widmer, 2007). The energy of a characteristic radiation is a function of the atomic number of the atom from which it originates. Therefore, the characteristic radiation released is of a low energy, which is absorbed locally and contributes to the absorbed dose in the patient being radiographed (Thrall and Widmer, 2007). The probability of a photoelectric interaction is directly proportional to the cube of the atomic number and inversely proportional to the cube of the photon energy (Thrall and Widmer, 2007). The dependence of the photoelectric absorption on the atomic number of the absorber leads to differential absorption, which results in good tissue contrast, between tissues (Thrall and Widmer, 2007). However, when very high energy photons are used for radiography, contrast between tissues of various type decreases (Thrall and Widmer, 2007).

In summary, Compton scattering and photoelectric effect are the interactions which are most important in diagnostic radiology (Perry, 1993). They occur with the photon energy range (30–140 kV) used in diagnostic radiology (Perry, 1993). Compton scattering dominates at the higher energy range, whereas the photoelectric effect occurs at the lower energy range (Perry, 1993). The photoelectric effect results in image formation (Thrall and Widmer, 2007). Further it lacks scattered photons, which if present result in radiation exposure of personnel and film fogging (Thrall and Widmer, 2007). However, due to absorption of the entire incoming photon, the patient dose associated with the photoelectric effect is high (Thrall and Widmer, 2007). Almost all scattered radiation that is encountered in diagnostic radiology results from Compton scattering (Thrall and Widmer, 2007). The pair production and photodisintegration do not occur in the diagnostic X-ray energy range; therefore have no importance in diagnostic radiology (Perry, 1993).

2.3.6 Image formation

A radiograph is an image of the number and distribution of X-rays that pass through the patient and strike the cassette (Thrall and Widmer, 2007). In conventional radiography the X-ray image is recorded on the X-ray film, which provides a permanent visible record of the image of the subject. The X-ray film consists of a flexible base of either cellulose acetate or polyester resin coated on one or both sides with a layer of emulsion (Hendee and Russell Ritenour, 2002). The latter, is attached to the base by an adhesive layer. The X-ray film emulsion contains silver halide granules, usually silver bromide, suspended in a gelatine matrix (Hendee and Russell Ritenour, 2002). It is sensitive to

ionizing radiation, visible and ultraviolet light (Hendee and Russell Ritenour, 2002), and is protected from physical damage by a layer of protective coating (T coat).

X-ray absorption by the body is not homogeneous but differs depending on the tissue composition (Thrall and Widmer, 2007). Therefore, when a patient is struck by an X-ray beam, the number of X-rays that reach the film is not uniform. X-ray photons that reach the film hit the silver halide crystals and cause complex interchange of electrons, which liberate halide atoms and leave metallic silver (Douglas and Williamson, 1980). The effect is still invisible and is referred to as the latent image (Douglas and Williamson, 1980). The latter becomes visible after film processing. During development the metallic silver precipitate forming neutral silver deposits, which appear black (Thrall and Widmer, 2007). Unexposed silver halide crystals are washed away during fixation leaving clear areas on the X-ray film (Thrall and Widmer, 2007). The amount of precipitated silver in any particular part of the film is directly related to the number of X-rays that reach that part of the film from the patient (Thrall and Widmer, 2007).

Generally, there are two types of digital radiography; the computed radiography (CR) and direct radiography (DR) (Körner et al., 2007). Each uses an X-ray generator similar to that used for conventional film-screen radiography (Armbrust, 2007). Additionally, the collimator and aluminium filters are similar to those of traditional film-screen radiography (Armbrust, 2007). Grids are also used; however they may be modified depending on the

digital equipment (Armbrust, 2007). Digital radiography differs from conventional film-screen radiography in the method by which the radiation is detected after the X-rays pass through the patient (Armbrust, 2007). In digital radiography, images are electronically captured, recorded and viewed at a computer terminal replacing the radiographic film and view box (Mattoon, 2006; Lavin, 2007).

Computed radiography was developed by Fuji (Tokyo, Japan) and has been in use since the 1980s (Widmer, 2008). Its main components are the imaging plate (detector), plate reader, analog to digital converter and a computer and software to process the digitized image (Widmer, 2008). The imaging plate is used to record the latent image (Armbrust, 2007). It is enclosed in a cassette for protection (Lavin, 2007). The CR cassette is almost similar to the conventional screen-film cassette but it holds an imaging plate instead of a film and an intensifying screen (Roberts and Graham, 2001). The design and physics of an imaging plate are very similar in concept to conventional phosphor screens (intensifying screens) used with film (Rowlands, 2002). It is mainly composed of a protective layer, phosphor layer, reflective layer, support layer/base and backing layer (Miyahara, 1987; Rowlands, 2002). The phosphor layer, which is an active component of the system (Lavin, 2007) consists of photostimulable phosphor crystals and a polymer (binder) deposited on a support layer (Rowlands, 2002). The binder can be nitrocellulose, polyester, acrylic, polyurethane or uretan (Miyahara, 1987; Rowlands, 2002). The commonly used photostimulable phosphor crystals are barium fluorohalides doped with an activator such as europium ($BaFX:Eu^{2+}$)

(Widmer, 2008). Chlorine (Cl), bromine (Br) or Iodine (I) or an arbitrary mixture of them are used as halogens (X) (Rowlands, 2002).

When X-rays strike the imaging plate, electrons in the crystals are excited to a higher energy level and stored in electron traps, thereby forming a latent image (Armbrust, 2007, Widmer, 2008). The latter, is analogous to the latent image acquired on conventional X-ray films but decays rapidly depending on the type of the crystal (Widmer, 2008). It is stable for only minutes to days (Widmer, 2008). This is because the amount of stored energy decreases over time (Körner et al., 2007).

The plate reader consists of a laser, optical scanner, photomultiplier tubes and motorized platform (Widmer, 2008). When an exposed cassette is placed in the plate reader, the plate reader automatically removes the imaging plate from the cassette and scans it with a red laser (helium-neon laser) (Armbrust, 2007). The laser beam scans the imaging plate in a series of horizontal lines (Widmer, 2008) and during the scanning process the trapped electrons are released into a lower energy state (Armbrust, 2007). The stored energy is released in the form of visible light by the process of photostimulable luminescence (Widmer, 2008). The emitted light at each point of the imaging plate is collected by the optical system (fiberoptics) to photomultiplier tubes (Lavin, 2007; Widmer, 2008). The various light intensities are converted into corresponding electric signals and amplified by the photomultiplier tubes (Widmer, 2008). At this stage the image data is in analog format (Widmer, 2008).

The analog to digital converter uses a binary system to convert the analog signal to digital data (numbers) (Armbrust, 2007). In this process the only integers which are used are 0 and 1 (Armbrust, 2007). Therefore each analog signal is assigned a binary value that corresponds to the brightness of each pixel and individual data points are sent to a specified pixel in the image matrix (Widmer, 2008). In computed radiography, a 2048 x 2048 matrix is often used (Widmer, 2008). The brightness of each pixel represents the degree of X-ray attenuation of the imaged structure and is assigned a corresponding shade of gray by the computer (Widmer, 2008).

A computer is required to handle the digital data that form a digital image. Each digital number is represented in a gray-scale image on a computer screen in the form of tiny squares, the pixels (picture elements) (Armbrust, 2007). Therefore, all digital images are composed of a grid of rows and columns of tiny pixels (Armbrust, 2007). The further imaging process is entirely digital and uses computer software programs (Widmer, 2008).

During the read out process not all the energy stored in the crystal is used (Widmer, 2008). Therefore the imaging plate must be erased for reuse (Widmer, 2008). This is achieved by flooding the imaging plate with high intensity white light, which releases residual energy (Widmer, 2008). After being erased, the imaging plate is returned to the cassette and ejected from the plate reader ready to reuse (Mattoon, 2007).

There are mainly two types of direct digital read out detectors; the flat panel detectors and charge coupled device (CCD) detectors (Widmer, 2008). The CCD detectors are not recognised by some medical physicists as true direct digital detectors (Widmer, 2008).

The flat panel detectors are rigid imaging plates, which have a similar appearance to cassettes used in conventional film-screen systems (Widmer, 2008). They can be direct or indirect converting (Widmer, 2008). Direct converting flat panel detectors convert X-ray energy directly into an electric charge (Chotas et al., 1999). They consist of thin film transistor arrays, which have been deposited onto a glass substrate in multiple layers, beginning with read out electronics at the lowest level, followed by charge collectors (storage capacitors) at higher level (Chotas et al., 1999; Kotter and Langer, 2002). The photoconductor layer is added on top of the electronic thin-film transistor arrays (Chotas et al., 1999). The latter covers the entire detector surface in a matrix that corresponds to pixels viewed on the computer screen (Widmer, 2008). Therefore, the pixel charge collection and read out electronics for each pixel are immediately adjacent to the site of the X-ray interactions (Chotas et al., 1999). The entire assembly is encased in a protective enclosure with external cabling for computer connection (Chotas et al., 1999). The thick photoconductor layer is nearest to the entry of the X-ray beam and directly converts X-rays to electrical charges (Widmer, 2008). It is composed of amorphous selenium, which is a semi-conductor with excellent photoconductor properties (Widmer, 2008).

Before an exposure is made, an electric field is applied across the photoconductive layer (amorphous selenium layer) through a bias electrode on the top surface of the selenium (Chotas et al., 1999). As the X-rays exiting from the patient are absorbed in the detector, electrons and holes are released within the selenium, and due to the electric field created, the electric charges migrate nearly perpendicularly to both surfaces of the selenium layer without much lateral diffusion (Chotas et al., 1999; Kotter and Langer, 2002). Therefore at the bottom of the amorphous selenium layer charges are drawn to the charge-collection electrodes where they are stored until read out (Kotter and Langer, 2002). The charge collected is proportional to the X-rays received by the detector (Kotter and Langer, 2002). The charges collected are read out one row at a time by the process of active matrix read out, whereby every data line transports the information for one pixel during the read out of one row (Kotter and Langer, 2002). The read out is send to the computer after analog to digital conversion (Widmer, 2008).

In indirect converting flat panel detectors, the scintillator and amorphous silicon photodiode circuitry are added as top layers on the thin-film transistor arrays replacing the photoconductor layer (Chotas et al., 1999). Therefore, indirect converting flat panel detectors consist (from top to bottom) of the scintillator layer, an amorphous silicon photodiode layer, and the thin-film transistor arrays (Kotter and Langer, 2002). The scintillator layer converts X-ray photons into visible light (Kotter and Langer, 2002). The scintillators can be structured or unstructured (Chotas et al., 1999).

Unstructured scintillators emit visible light, which can spread to adjacent pixels and thereby reduce the spatial resolution (Chotas et al., 1999). An example of an unstructured scintillator is a conventional fluorescent screen (Chotas et al., 1999). A structured scintillator consists of cesium iodide crystals that are grown perpendicularly on the detector (Chotas et al., 1999; Kotter and Langer, 2002). The crystalline structure consists of discrete parallel “needles” and behaves similar to fibre optics (Chotas et al., 1999). It channels most of the light directly to the photodiode layer (Chotas et al., 1999). Therefore, it significantly reduces lateral diffusion of the scintillator light (Kotter and Langer, 2002) and improves spatial resolution (Chotas et al., 1999). The single crystals have a diameter of approximately 5–10 µm (Kotter and Langer, 2002).

The amorphous silicon photodiode layer transforms visible light from the scintillator layer into electric charges (Kotter and Langer, 2002). When X-rays strike the scintillator layer visible light is emitted, which is proportional to the incident X-ray energy (Chotas et al., 1999). The emitted visible light is converted into an electric charge by the amorphous silicon photodiode layer (Chotas et al., 1999). The charge collector electrodes drain the electric charges generated by the photodiode array (Kotter and Langer, 2002). The charge collected at each photodiode is converted into a digital value by the underlying read out electronics (Chotas et al., 1999).

The main difference between CR and DR is in the imaging plate (Widmer, 2008). In DR, the imaging plate captures incident X-rays from the patient and

produces a digital signal that is sent directly to a computer for interpretation, which eliminates the need for plate reader as with a CR (Widmer, 2008).

2.3.7 Clinical use

Radiography is indicated for diagnosis, evaluation and monitoring the progression of various conditions such as those which affect the musculoskeletal system (Burk and Feeney, 2003).

Quality radiographs and knowledge of the normal radiographic anatomy of individual species are important in radiographic interpretation. Therefore the radiologist should be familiar with the basic principles underlying the production of radiographs (Kealy and McAllister, 2000) and different artefacts, which may hinder the interpretation of radiographs (Berry and Thrall, 2007). The normal radiographic anatomy of wildlife species has been documented by several authors (Silverman and Morgan, 1980; Baitchman and Kollias, 2000; Wagner and Kirberger, 2005a; Martins et al., 2013; Young et al., 2013), which serves as a reference for the diagnosis of various diseases.

Additionally, the use of radiography in the diagnosis of diseases in wildlife species has been reported by several authors (Palotay and Uno, 1975; Tomson and Lotshaw, 1978; Wallach and Boever, 1983; Jungle et al., 1994; Delclaux et al., 2002; Lynch et al., 2002; Neilsen et al., 2014). Despite the usefulness of radiography in the diagnosis of various diseases, X-rays are capable of causing ionizing radiation, which may lead to lethal damage to

tissues. Therefore, radiation safety procedures should be followed during radiography.

2.4 ULTRASONOGRAPHY

2.4.1 Sound wave

A sound wave is a longitudinal wave in which the motion of the molecules in the medium within the wave is parallel to the direction of the wave propagation (Hendee and Russell Ritenour, 2002). Sound waves require a medium through which to travel. They cannot travel in a vacuum (Tod Drost, 2007). In the body there are different media such as gas and semisolids (Gorgas, 2011).

Frequency of a sound wave is the number of cycles per second introduced into the medium. It is usually expressed in Hertz (Hz). One Hz equals one cycle per second. The maximum height of the cycle is the amplitude of the sound wave, whereas the distance covered by one cycle of a sound wave is the wavelength. The wavelength (λ) of the sound wave is expressed in metres (m). The speed (velocity) of sound in soft tissues is 1 540 m/s and is considered to be constant (Gorgas, 2011). The relationship between frequency, wavelength and velocity of the sound wave can be expressed by the following formula:

$$f = v/\lambda$$

Where: f = frequency; λ = wavelength; v = velocity.

Therefore, the frequency of a sound wave is inversely proportional to its wavelength. Sound waves with higher frequency have shorter wavelength and vice versa. The shorter the wavelength, the better the resolution. However, sound waves with shorter wavelength have poor penetrating ability.

Ultrasound is a sound wave with a frequency above the upper range of human hearing (Nyland et al., 2002). The human ear can detect sound waves within a frequency range of 16 000–20 000 Hz (Gorgas, 2011). Diagnostic ultrasound uses sound waves with frequency well above 20 000 Hz, normally 2–10 MHz (Mannion, 2006). Infrasound is a sound with lower frequencies (Gorgas, 2011).

2.4.2 Acoustic impedance

The velocity of an ultrasound wave through a medium depends on the physical properties of the medium (Hendee and Russell Ritenour, 2002). In low density media such as air the ultrasound wave travels with lower velocity, whereas in high density media like solids the ultrasound wave travels with higher velocity. The velocity of ultrasound wave in liquids is intermediate between those of solids and gases (Hendee and Russell Ritenour, 2002). In biologic tissues the velocity of ultrasound waves is similar to the velocity of ultrasound waves in liquids with the exception of bone and lung (Hendee and Russell Ritenour, 2002).

Acoustic impedance is the product of the tissue density and velocity of sound within that tissue (Nyland et al., 2002). The percentage of the sound beam

reflected or transmitted as it passes from one tissue to another depends on the tissue's density and the velocity of sound within each tissue. Therefore, the difference in acoustic impedance between tissues determines the percentage of ultrasound beam reflected or transmitted (Nyland et al., 2002). Since the velocity of ultrasound wave in soft tissues is assumed to be constant, tissue density can be used to estimate the acoustic impedances in soft tissues (Nyland et al., 2002).

2.4.3 Transducer

A transducer is any device that converts one form of energy into another (Hendee and Russell Ritenour, 2002). An ultrasound transducer converts electrical energy into ultrasound energy and vice versa during transmission and reception, respectively, of sound waves (Hendee and Russell Ritenour, 2002). The transducer cannot transmit ultrasound waves and receive echoes at the same time. It alternates between sending and receiving mode (Gorgas, 2011). A greater proportion of time (99%) is spent in receiving echoes and the remaining (1%) in transmitting ultrasound waves (Gorgas, 2011).

The transducer of an ultrasound wave contains piezoelectric crystals such as lead-zirconate-titanate (PZT) (Gorgas, 2011). The frequency emitted by a transducer depends on the thickness of the piezoelectric crystal i.e. the dimension of the crystal along the axis of an ultrasound beam (Hendee and Russell Ritenour, 2002). Thick crystals produce low frequencies, whereas thin crystals produce high frequencies (Hendee and Russell Ritenour, 2002). The frequency of the crystals cannot be changed by scanner's controls, it is

inherent (Nyland et al., 2002). Changing the frequency requires selection of a different transducer except for multifrequency transducers (Nyland et al., 2002). In multifrequency transducers the frequency can be electronically altered within a certain range e.g. 5–10MHz (Kircher, 2011).

The efficiency of transmission and reception of an ultrasound beam between the transducer and medium depends on how well the transducer is coupled to the medium (Hendee and Russell Ritenour, 2002). Transmission and reception of an ultrasound beam with minimum energy loss occurs when the acoustic impedance of the coupling medium is intermediate between the acoustic impedances of the crystal and the medium and if the thickness of the coupling medium is much less that the ultrasound wave length (Hendee and Russell Ritenour, 2002). Acoustic gel, which consists mostly of water is a common acoustic coupling medium used.

Ultrasound transducers are available in many sizes and shapes. The selection of the transducer depends on the characteristics of the anatomical region to be imaged and the physical properties of the transducer (Tod Drost, 2007). Electronic or array transducers are composed of multiple piezoelectric crystals that can change the direction or degree of focus of the ultrasound beam by timing the excitation of the crystals (Hendee and Russell Ritenour, 2002). The crystals may be arranged in a line, curved line or concentric rings (Hendee and Russell Ritenour, 2002; Tod Drost, 2007). There are four main types of array transducers which are in use; the linear array, curvilinear array, phased array and annular array.

In linear and curvilinear array transducers an image composed of scan lines is formed by sequentially exciting the crystals in the entire array (Hendee and Russell Ritenour, 2002). The crystals may be as many as 60–240 or more and are excited electronically in groups of 3–20 or more. Excitation of each group of crystals forms a scan line (Hendee and Russell Ritenour, 2002). The succeeding scan line is obtained by excitation of the next group of crystals, which is made to overlap the first group (Hendee and Russell Ritenour, 2002).

In linear array transducers, the crystals are linearly arranged and form a rectangular image with parallel scan lines. Crystals are curvilinearly arranged and form a fan-shaped image with radiating scan lines in curvilinear array transducers (Mannion, 2006). The curvilinear array transducer produces an image with a wider field of view than the linear array transducer (Nyland et al., 2002). However, for imaging superficial structures the latter is preferred since it provides a wide near field of view with good definition of structures (Mannion, 2006).

In a phased array transducer each scan line is obtained by excitation of all crystals (usually 128) in an array and beam steering is possible by using slight delays between excitation of elements (Hendee and Russell Ritenour, 2002). Phased array transducers produce a fan-shaped image with radiating scan lines and the crystals are linearly arranged. It has a small footprint, which allows access to small windows (Mannion, 2006). The annular array is not commonly used.

2.4.4 Production of ultrasound waves

Ultrasound waves are produced in the transducer by a converse piezoelectric effect (Hendee and Russell Ritenour, 2002). The piezoelectric effect was first discovered in 1880 by Pierre and Jacques Curie (Hendee and Russell Ritenour, 2002). 'Piezein' is a Greek world meaning 'to press' (Gorgas, 2011). Therefore, the piezoelectric effect is the ability of a crystal to convert pressure into an electric energy (Gorgas, 2011). The piezoelectric effect is used to produce an electrical signal (image) in response to ultrasound waves (Hendee and Russell Ritenour, 2002).

When sound waves are applied to the transducer, piezoelectric crystals transmit their energy to the transducer resulting in mechanical compression (pressure) of the piezoelectric crystal (Gorgas, 2011). The compression of the piezoelectric crystal produces an electric voltage, which is amplified and converted for a display (Gorgas, 2011). This phenomenon is the piezoelectric effect (Hendee and Russell Ritenour, 2002).

On the other side, when an electric impulse is applied across the piezoelectric crystal it causes mechanical deformation of the crystal i.e. expansion or compression depending on the polarity of the voltage applied (Hendee and Russell Ritenour, 2002). This is followed by vibration of the piezoelectric crystal and ultrasound waves are generated (Kealy and McAllister, 2000). This phenomenon is the converse piezoelectric effect i.e. conversion of the electrical energy to mechanical (sound) energy (Hendee and Russell Ritenour, 2002). Sound is not produced continuously by the transducer. It is

produced in pulses and each pulse consists of two or three waves (Nyland et al., 2002). An image is formed from echoes returning to the transducer after each pulse (Nyland et al., 2002).

2.4.5 Interaction of ultrasound waves with tissues

Sound can be attenuated, refracted or diffracted when it interacts with tissues (Nyland et al., 2002; Gorgas, 2011). Attenuation is any mechanism that removes energy from the ultrasound wave (Hendee and Russell Ritenour, 2002). The amount of attenuation depends on the frequency and the distance travelled by the ultrasound wave (Tod Drost, 2007). The attenuation of the ultrasound wave is directly proportional to the frequency of the sound (Nyland et al., 2002). The higher the frequency of the ultrasound wave, the higher the attenuation. Attenuation is the result of absorption, reflection and scattering of an ultrasound wave (Nyland et al., 2002).

When sound waves interact with tissues, their mechanical energy is converted to heat, which is absorbed by body tissues (Nyland et al., 2002). Therefore absorption is the conversion of a sound wave's mechanical energy to heat and it is a major component of sound attenuation in soft tissues (Tod Drost, 2007). The heat is produced as a result of frictional forces caused by back and forth movements of the molecules of the transmitting medium in response to the ultrasound wave passage (Nyland et al., 2002). In diagnostic ultrasonography the amount of sound absorbed is low and the temperature change produced is insignificant (Tod Drost, 2007).

Reflection occurs when a sound wave encounters tissue interfaces of different acoustic impedance (Tod Drost, 2007). It is assumed to occur at relatively smooth interfaces, which have dimensions greater than the ultrasound wavelength i.e. 'specular reflectors' (Hendee and Russell Ritenour, 2002). Specular reflection permits visualization of the boundaries between organs (Hendee and Russell Ritenour, 2002).

The percentage of the ultrasound wave reflected from an interface depends on the acoustic impedance of the media on opposite sides of the interface (Hendee and Russell Ritenour, 2002). The higher the acoustic impedance mismatch (difference) at an interface the higher the energy of an ultrasound wave reflected, and the lower the amount of the ultrasound wave transmitted across the interface (Hendee and Russell Ritenour, 2002). Body tissues have small differences in acoustic impedance, which is ideal for diagnostic imaging. This is because only a small fraction of the ultrasound wave will be reflected at the interfaces and a greater proportion will be transmitted and available for imaging deeper structures (Nyland et al., 2002). If high acoustic impedance mismatch is present, for example at a soft tissue-air interface in the lungs, a greater proportion of the ultrasound wave will be reflected and not available for imaging deeper structures. In such interfaces acoustic shadowing occurs distal to the interface (Nyland et al., 2002).

Echo is the reflected sound wave (Gorgas, 2011). Only echoes reflected back to the transducer are used for image formation (Tod Drost, 2007). The ultrasound wave strikes body interfaces at different angles and the angle of

incidence is equal to the angle of reflection (Hendee and Russell Ritenour, 2002). When an ultrasound wave strikes an interface at an angle more than 3 degrees from the perpendicular, very few echoes from the interface will be detected by the transducer (Hendee and Russell Ritenour, 2002). Therefore for optimal visualization of the interface, the ultrasound wave must strike the interface perpendicularly. Image quality may be improved by scanning at different angles in order to align different interfaces perpendicular to the ultrasound wave (Nyland et al., 2002).

Scattering occurs when a sound wave encounters uneven interfaces, which are smaller than the wavelength of the ultrasound wave i.e. 'nonspecular reflectors' (Hendee and Russell Ritenour, 2002). It is independent of the beam angle and the incidence increases with an increase in the frequency of the sound wave (Nyland et al., 2002). Nonspecular reflectors have low acoustic impedance mismatch therefore they return as weak echoes. The echoes can be imaged since they are abundant and also tend to reinforce each other (Nyland et al., 2002). Scattering (nonspecular reflection) occurs mainly in parenchyma organs and permits visualization of tissue parenchyma i.e. texture of the organs (Tod Drost, 2007).

Refraction is the change in the direction of the ultrasound wave (Nyland et al., 2002). It occurs when the ultrasound wave strikes an interface at an angle other than 90 degrees and if the speed of the ultrasound wave is different on the opposite sides of the interface (Hendee and Russell Ritenour, 2002). Ultrasound waves travel with various velocities in different body tissues

(Gorgas, 2011). If the velocity of the sound in the second medium is less than in the first medium, the angle of refraction is less than the angle of incidence, whereas if the velocity of the sound in the second medium is higher than in the first medium, the angle of refraction is greater than the angle of incidence (Gorgas, 2011). Refraction is the principal cause of artefacts in diagnostic ultrasonography. It results in displacement errors in positioning reflective interfaces in the image (Hendee and Russell Ritenour, 2002). This is because the ultrasound machine assumes that the ultrasound travels in a straight line (Hendee and Russell Ritenour, 2002).

Diffraction is the change in the direction of the ultrasound waves as they pass through an opening or obstacle (Gorgas, 2011). It increases with lower frequency sound waves i.e. longer wavelengths (Gorgas, 2011).

2.4.6 Resolution

Spatial resolution is the ability of a modality to discriminate objects in close contact (Gorgas, 2011). In diagnostic ultrasonography spatial resolution depends on the frequency of the transducer and the distance from the transducer (Nyland et al., 2002). The ability to separate objects along the axis of the ultrasound beam is the axial resolution. It is determined by the pulse length, which in turn depends on the frequency of the transducer (Nyland et al., 2002). The higher the frequency of the transducer, the shorter the wavelength and the spatial pulse length, the better the axial resolution (Gorgas, 2011). The spatial pulse length is commonly two or three pulse

length (0.1 to 1.0 mm) and the axial resolution cannot be more than half the pulse length due to overlapping of the returning echoes (Nyland et al., 2002).

The ability to separate two objects perpendicular to the axis of the ultrasound beam along the plane of the scan is the lateral resolution (Nyland et al., 2002). It depends on the beam's width, which in turn depends on the distance from the transducer and the frequency of the transducer (Nyland et al., 2002). The narrower the width of the ultrasound beam the greater the lateral resolution (Fischetti and Scott, 2007).

Lateral resolution is achieved when the beam width is narrower than the distance separating the objects (Gorgas, 2011). The best lateral resolution occurs at the focal point and decreases as one moves away from the focal point; however acceptable lateral resolution is obtained when imaging within the focal zone (Nyland et al., 2002). Higher frequency transducers have high lateral resolution (Mannion, 2006). With advanced technology, modern transducers have more than one focal zone and are capable of adjusting it (Mannion, 2006). All ultrasonographic measurements if possible should be taken along the beam axis since in most ultrasound machines the axial resolution is better than the lateral or elevated resolution (Nyland et al., 2002).

2.4.7 Echo display modes

In diagnostic ultrasonography echoes returning to the transducer can be displayed as brightness (B) or motion (M) (Hendee and Russell Ritenour,

2002). The time it takes for the echo to return to the transducer after pulse transmission is recorded as the depth.

Brightness mode (B-mode) displays the returning echoes as dots on the screen (Nyland et al., 2002). The amplitude of the returning echoes is represented by the brightness of the dots and hence the 'brightness' mode (Hendee and Russell Ritenour, 2002). The greater the amplitude of the returning echo, the brighter the dot on the image (Gorgas, 2011). The location of the reflecting interface from the transducer is displayed in two dimensions (*x* and *y*). The position of the dot on the image along the beam's axis corresponds to the depth from the transducer at which the echo originated (Nyland et al., 2002).

Motion or time-motion mode (M-mode or TM-mode) is commonly used in echocardiography to evaluate the heart (Nyland et al., 2002). In the M-mode, the position of the transducer is represented at the top of the image and time is displayed on the horizontal axis, whereas the depth is displayed on the vertical axis (Nyland et al., 2002). A single line of B-mode dots is swept horizontally across the monitor (Nyland et al., 2002). The brightness of the dots represents the amplitude of the echo. The depth represents the distance of the reflecting interface from the transducer.

2.4.8 Clinical use

Compared to radiography, diagnostic ultrasonography produces cross sectional images without superimposition of structures and has a superior

tissue contrast (Kinns, 2011). It allows evaluation of organ parenchyma and enables accurate sampling at specific sites (Kinns, 2011). Dynamic motion of organs such as the heart can be evaluated (Szabo, 2004). Surgical planning is enhanced by greater specificity in localization of the lesion and it provides detail on vascularisation and vascular and lymph node involvement (Kinns, 2011). There is no ionising radiation therefore it is safe (Kinns, 2011).

A high skill level is needed for ultrasonography in order to obtain good quality images due to differences in anatomy, number of access windows and many possible planes of view (Szabo, 2004). Experience is also required to optimize instrumentation and to find relevant planes of view and targets of diagnostic significance. Additionally, recognition, interpretation and measurement of images for diagnosis requires experience (Szabo, 2004).

Knowledge of the normal ultrasonographic abdominal anatomy of individual species is important in the diagnosis of abdominal diseases. The normal ultrasonographic abdominal anatomy of dogs and cats has been documented (Nyland and Mattoon, 2002; Barr and Gaschen, 2011), which provides a reference for clinical use. Several authors (Wagner and Kirberger, 2005b; Alves et al., 2007; Makungu et al., 2012; Amory et al., 2013; Ribeiro et al., 2013) have also reported the normal ultrasonographic abdominal anatomy of wildlife species, which provides a reference for routine health examinations and diagnosis of diseases.

Ultrasonography is commonly used in small animals in the diagnosis of abdominal diseases (Nyland and Mattoon, 2002; Barr and Gaschen, 2011). In wildlife species abdominal ultrasonography has been used in the diagnosis of various diseases (Shahar et al., 1995; Chittick et al., 2001; Tordiffe, et al., 2012; Neilsen et al., 2014).

2.5 REFERENCES

Alton, K., H. Vielgrader, T. Voracek, and W. Zenker, 2004: Endocrine dermatosis and granulosa cell tumour in a red panda. Vet. Dermatol. **15 (Suppl. 1),** 69.

Alves, F. R., F. B. Costa, M. M. S. Arouche, A. C. E. Barros, M. A. Miglino, L. C. Vulcano, and P. C. Guerra, 2007: Ultrasonographic evaluation of the urinary system, liver and uterus of *Cebus apella* monkey. Pesq. Vet. Bras. **27,** 377–382.

Amory, J. T., W. M. du Plessis, A. Beierschmitt, J. Beeler-Marfisi, R. M. Palmour, and T. Beths, 2013: Abdominal ultrasonography of the normal St. Kitts vervet monkey (*Chlorocebus sabaeus*). J. Med. Primatol. **42,** 28–38.

Ankel-Simons, F., 2007: Primate Anatomy: An Introduction. Boston: Academic Press.

Armbrust, L. J., 2007: Digital images and digital radiographic image capture. In: Textbook of Veterinary Diagnostic Radiology (D. E. Thrall, ed.). St. Louis: Saunders Elsevier. pp. 22–37.

Backues, K. A., J. P. Hoover, R. J. Bahr, A. W. Confer, J. A. Chalman, and M. L. Larry, 2001: Multifocal pyogranulomatous osteomyelitis resembling chronic recurrent multifocal osteomyelitis in a lemur. J. Am. Vet. Med. Assoc. **218,** 250–253.

Baitchman, E. J., and G. V. Kollias, 2000: Clinical anatomy of the North American river otter (*Lontra Canadensis*). J. Zoo. Wildl. Med. **31,** 473–483.

Barr, F., and L. Gaschen, 2011: BSAVA Manual of Canine and Feline Ultrasonography. Gloucester: BSAVA.

Berry, C. R., and D. E. Thrall, 2007: Introduction to radiographic interpretation. In: Textbook of Veterinary Diagnostic Radiology (D. E. Thrall, ed.). St. Louis: Saunders Elsevier. pp. 78–93.

Budnitz, N., and K. Dainis, 1975: Lemur catta: ecology and behaviour. In: Lemur Biology (I. Tattersall and R. W. Sussman, eds). New York: Plenum Press. pp. 219–236.

Burk, R. L., and D. A. Feeney, 2003: Small Animal Radiology and Ultrasonography: A Diagnostic Atlas and Text. Philadelphia: Saunders.

Burton, M., R. J. Morton, E. Ramsay, and E. L. Stair, 1986: Coccidioidomycosis in a ring-tailed lemur. J. Am. Vet. Med. Assoc. **189,** 1209–1211.

Campbell, J. L., J. H. Eisemann, C. V. Williams, and K. M. Glenn, 2000: Description of the gastrointestinal tract of five lemur species: *Propithecus tattersalli*, *Propithecus verreauxi coquereli*, *Varecia variegata*, *Hapalemur griseus* and *Lemur catta*. Am. J. Primatol. **52,** 133–142.

Canelli, E., A. Luppi, A. Lavazza, D. Lelli, E. Sozzi, A. M. M. Martin, D. Gelmetti, E. Pascotto, C. Sandri, W. Magnone, and P. Cordioli, 2010: Encephalomyocarditis virus infection in an Italian zoo. Virol. J. **7,** 1–7.

Carlsson, A., 1925: Über *Ailurus fulgens*. Acta. Zool. **6,** 269–305.

Chang, J., J. L. Wagner, and R. W. Kornegay, 1979: Spontaneous cholangiocarcinoma in a ring-tailed lemur (*Lemur catta*). Lab. Anim. Sci. **29,** 374–376.

Chittick, E., D. Rotstein, T. Brown, and B. Wolfe, 2001: Pyometra and uterine adenocarcinoma in a melengestrol acetate-implanted captive coati (*Nasua nasua*). J. Zoo Wildl. Med. **32,** 245–251.

Chotas, H. G., J. T. Dobbins, and C. E. Ravin, 1999: Principles of digital radiography with large-area, electronically readable detectors: a review of the basics. Radiology. **210,** 595–599.

Cuozzo, F. P., M. L. Sauther, L. Gould, R. W. Sussman, L. M. Villers, and C. Lent, 2010: Variation in dental wear and tooth loss among known aged, older ring-tailed lemurs (Lemur catta): A comparison between wild and captive individuals. Am. J. Primatol. **72,** 1026–1037.

Dank, G., I. Horowitz, and I. Aroch, 2012: Treatment of chronic lymphocytic leukemia in a ring-tailed lemur (*Lemur catta*). Isr. J. Vet. Med. **67,** 186–189.

Delclaux, M., C. Talavera, M. López, J. M. Sánchez, and M. I. García, 2002: Avascular necrosis of the femoral heads in a red panda (*Ailurus fulgens fulgens*): possible Legg-Calve-Perthes disease. J. Zoo. Wildl. Med. **33,** 283–285.

Douglas, S. W., and H. D. Williamson, 1963: Principles of Veterinary Radiography. London: Baillière Tindall and Cox.

Douglas, S. W., and H. D. Williamson, 1980: Principles of Veterinary Radiography. London: Baillière Tindall.

Drea, C. M., and A. Weil, 2008: External genital morphology of the ring-tailed lemur (*Lemur catta*): Females are naturally “masculinised”. J. Morphol. **269,** 451–463.

Fischetti, A. J., and R. C. Scott, 2007: Basic ultrasound beam formation and instrumentation. Clin. Tech. Small. Anim. Pract. **22,** 90–92.

Flower, W. H., 1870: On the anatomy of *Ailurus fulgens*. Proc. Zool. Soc. London. **1870,** 752–769.

Ghose, D., and P. K. Dutta, 2011: Status and distribution of Red Panda *Ailurus fulgens fulgens* in India. In: Red Panda Biology and Conservation of the First Panda (A. Glatson, ed.). London: Academic Press. pp. 357–373.

Goodchild, S., and C. Schwitzer, 2008: The problem of obesity in captive lemurs. Int. Zoo. News. **55,** 353–357.

Gorgas, D., 2011: Physical principles. In: BSAVA Manual of Canine and Feline Ultrasonography (F. Barr and L. Gaschen, eds). Gloucester: BSAVA. pp. 1–14.

Groves, C., 2011: The taxonomy and phylogeny of *Ailurus*. In: Red Panda Biology and Conservation of the First Panda (A. Glatston, ed.). London: Academic Press. pp. 101–124.

Hamerton, B. C. A. E., 1944: Report on the deaths occurring in the Society's Gardens during the year 1943. J. Zool. **114,** 307–321.

Harwell, G., and T. M. Craig, 1981: Dirofilariasis in a red panda. J. Am. Vet. Med. Assoc. **179,** 1258.

Hendee, W. R., and E. Russell Ritenour, 2002: Medical Imaging Physics. New York: John Wiley & Sons, Inc.

IUCN, 2014: IUCN Red list of threatened species. Version 2014. 3. Available at: http://www.iucnredlist.org, accessed on 18 November 2014.

Jones, S. R. and H. W. Casey, 1981: Primary renal tumors in nonhuman primates. Vet. Pathol. **18,** 89–104.

Jungle, R. E., 2003: Prosimians. In: Zoo and Wild Animal Medicine, 5th Edition (M. E. Fowler and R. E. Miller, eds). Missouri: Saunders. pp. 334–346.

Jungle, R. E., K. G. Mehren, T. P. Meehan, G. J. Crawshaw, M. C. Duncan, L. Gilula, F. Gannon, G. Finkel, and M. P. Whyte, 1994: Periarticular hyperostosis and renal disease in six black lemurs of two family groups. J. Am. Vet. Med. Assoc. **205,** 1024–1029.

Kappeler, P. M., 1991: Patterns of sexual; dimorphism in body weight among prosimians primates. Folia. Primatol. **57,** 132–146.

Kealy, J. K., and H. McAllister, 2000: Diagnostic Radiology and Ultrasonography of the Dog and Cat. Philadelphia: W. B. Saunders Company.

Kinns, J., 2011: Abdomen. In: BSAVA Manual of Canine and Feline Ultrasonography (F. Barr and L. Gaschen, eds). Gloucester: BSAVA. pp. 72–84.

Kircher, P. R., 2011: Equipment. In: BSAVA Manual of Canine and Feline Ultrasonography (F. Barr and L. Gaschen, eds). Gloucester: BSAVA. pp. 15–20.

Kondo, H., Y. Wada, G. Bando, M. Kosuge, K. Yagi, and Y. Oku, 1996: Alveolar hydatidosis in a gorilla and ring-tailed lemur in Japan. J. Vet. Med. Sci. **58,** 447–449.

Körner, M., C. H. Weber, S. Wirth, K. F. Pfeifer, M. F. Reiser, and M. Treitl, 2007: Advances in digital radiography: physical principles and system overview. Radiographics. **27,** 675–686.

Kotter, E., and M. Langer, 2002: Digital radiography with large-area flat-panel detectors. Eur. Radiol. **12,** 2562–2570.

Kummerfeld, M., A. Knieriem, P. Wohlsein, M. Verlag, and H. Schaper, 2008: Osteomyelitis and papillary renal adenoma in a red panda (*Ailurus fulgens fulgens*). Dtsch. Tierarztl. Wochenchr. **115,** 421–425.

Lavin, L. M., 2007: Radiography in Veterinary Technology. Philadelphia: Saunders Elsevier.

Luzón, M., C. de la Fuente-López, E. Martínez-Nevado, J. Fernández-Morán, and F. Ponce-Gordo, 2010: Taenia crassiceps cysticercosis in a ring-tailed lemur (*Lemur catta*). J. Zoo. Wildl. Med. **41,** 327–330.

Lynch, M., H. McCracken, and R. Slocombe, 2002: Hyperostotic bone disease in red pandas (*Ailurus fulgens*). J. Zoo. Wildl. Med. **33,** 263–271.

Makungu, M., W. M. du Plessis, M. Barrows, K. N. Koeppel, and H. B. Groenewald, 2012: Ultrasonographic abdominal anatomy of healthy captive caracals (*Caracal caracal*). J. Zoo. Wildl. Med. **43,** 522–529.

Makungu, M., W. M. du Plessis, M. Barrows, K. N. Koeppel, and H. B. Groenewald, 2013: Polycystic kidneys in the red panda (*Ailurus fulgens*). J. Zoo. Wildl. Med. **44,** 777–780.

Mannion, P., 2006: Principles of diagnostic ultrasound. In: Diagnostic Ultrasound in Small Animal Practice (P. Mannion, ed.). Oxford: Blackwell Science Ltd. pp. 1–19.

Martins, G. S., E. R. Lopez, I. I. G. Taques, C. Y. Correia, Y. S. Meireles, N. C. M. R. Turbino, L. D. Guimarães, and P. B. Néspoli, 2013: Radiographic morphology of the skeleton, thorax, and abdomen of coati (*Nasua nasua* Linnaeus, 1766). Pesq. Vet. Bras. **33,** 1137–1143).

Mattoon, J. S., 2006: Digital radiography. Vet. Comp. Orthop. Traumatol. **19,** 123–132.

Miyahara, J., 1987: Imaging plate. In: Computed Radiography (Y. Tateno, T. Linuma and M. Takano, eds). Tokyo: Springer. pp. 7–15.

Montali, R. J., R. Wallace, L. G. Phillips Jr., M. Bush, M. Roberts, S. D. Crissey, K. J. Warnell, O. T. Oftedal, M. Edwards, and L. Rabin, 1989: Hepatopathy and hypercholesterolemia in red pandas associated with a diet change. In: Red Panda Biology (A. R. Glatston, ed.). The Netherlands: SPB Academic Publishing. pp. 31–40.

Muller, S., A. Oevermann, C. Wenker, H. J. Altermatt, and N. Robert, 2007: A mixed epithelial and stromal tumor of the kidney in a ring-tailed lemur (*Lemur catta*). Vet. Pathol. **44,** 243–246.

Neilsen, C., C. Mans, and S. A. Colopy, 2014: Gastric dilatation and volvulus in a red panda (*Ailurus fulgens*). Vet. Surg. 1–2.

Nijboer, J., and E. S. Dierenfeld, 2011: Red panda nutrition: How to feed a vegetarian carnivore. In: Red Panda Biology and Conservation of the First Panda (A. Glatston, ed.). London: Academic Press. pp. 257–270.

Nowak, R. M., 1999: Order Primate. In: Walker's Mammals of the World. Baltimore: Johns Hopkins University Press. pp. 490–631.

Nyland, T. G., and J. S. Mattoon, 2002: Small Animal Diagnostic Ultrasound. Philadelphia: Saunders.

Nyland, T. G., J. S. Mattoon, E. J. Herrgesell, and E. R. Wisner, 2002: Physical principles, instrumentation, and safety of diagnostic ultrasound. In: Small Animal Diagnostic Ultrasound (T. G. Nyland and J. S. Mattoon, eds). Philadelphia: Saunders. pp. 1–18.

Osman Hill, W. C., 1953: Primates Comparative Anatomy and Taxonomy Vol. 1. Strepsirhini. United Kingdom: Edinburgh at the University Press. pp. 50–388.

Palotay, J. L., and H. Uno, 1975: Hydatid disease in four nonhuman primates. J. Am. Vet. Med. Assoc. **167,** 615–618.

Patten, C. J., 1899: The form and position of the thoracic and abdominal viscera of the ruffed lemur (*Lemur varius*). Trans. Royal. Acad. Med. Ireland. **17,** 652–677.

Patten, C. J., 1902: The form and position of the thoracic and abdominal viscera of the ruffed lemur (*Lemur varius*). Trans. Royal. Acad. Med. Ireland. **20,** 441–473.

Patterson-Kane, J. C., L. M. Gibbons, R. Jefferies, E. R. Morgan, N. Wenzlow, and S. P. Redrobe, 2009: Pneumonia from *Angiostrongylus vasorum* infection in a red panda (*Ailurus fulgens fulgens*). J. Vet. Diagn. Invest. **21,** 270–273.

Perry, R. L., 1993: Principles of conventional radiography and fluoroscopy. Vet. Clin. North. Am. Small. Anim. Pract. **23,** 235–252.

Philippa, J., and E. Ramsay, 2011: Captive red panda medicine. In: Red panda Biology and Conservation of the First Panda (A. R. Glatston, ed.). London: Academic Press. pp. 271–285.

Preece, B., 2011: Red panda pathology. In: Red panda Biology and Conservation of the First Panda (A. R. Glatston, ed.). London: Academic Press. pp. 287–302.

Pye G. W., R. A. Bennette, S. P., Terrell, P. E. Ginn, L. J. McSherry, L. J. Herry, and A. R. Alleman, 2000: T-cell-Rich B-cell lymphoma in a ring-tailed lemur (*Lemur catta*). J. Zoo. Wildl. Med. **31,** 388–393.

Remick, A. K., A. J. Van Wettere, and C. V. Williams, 2009: Neoplasia in prosimians: case series from captive prosimians population and literature review. Vet. Pathol. **46,** 746–772.

Ribeiro, R. G., A. P. A. Costa, N. Bragato, A. M. Fonseca, J. C. M. Duque, T. D. Prado, A. C. R. Silva, and N. C. Borges, 2013: Normal sonographic anatomy of the abdomen of coatis (*Nasua nasua* Linnaeus 1766). BMC Vet. Res. **9,**124

Roberts, G. D., and J. P. Graham, 2001: Computed radiography. Vet. Clin. North. Am. Equine. Pract. **17,** 47–61.

Roberts, M. S., and J. L. Gittleman, 1984: *Ailurus fulgens*. Mamm. Species. **222,** 1–8.

Rowlands, J. A., 2002: The physics of computed radiography. Phys. Med. Biol. **47,** 123–166.

Schmidt, R. E., 1975: Tuberculosis in a ring-tailed lemur (*Lemur catta*). J. Zoo. Wildl. Med. **6,** 11–12.

Scott, H. H., and H. Camb, 1925: Congenital malformations of the kidney in reptiles, birds and mammals. Proc. Zool. Soc. Lond. **95,** 1259–1269.

Shahar, R., I. H. Horowitz, and I. Aizenberg, 1995: Disseminated hydatidosis in a ring-tailed lemur (*Lemur catta*). J. Zoo. Wildl. Med. **26,** 119–122.

Silverman, S., and J. P. Morgan, 1980: Thoracic radiography of the normal rhesus macaque (*Macaca mulatta*). Am. J. Vet. Res. **41,** 1704–1719.

Srivastav, A., P. Nigam, D. Chakraborty, and A. K. Nayak, 2009: The National Studbook of Red Panda (*Ailurus fulgens*). New Delhi: Wildlife Institute of India, Dehradum and Central Zoo Authority.

Szabo, T. L., 2004: Diagnostic Ultrasound Imaging inside out. USA: Elsevier Academic Press. pp. 1–28.

Taylor, K., 2009: Ring-tailed Lemur Husbandry Manual. New South Wales: Taronga Western Plains Zoo.

Thrall, D. E., and W. R. Widmer, 2007: Physics of diagnostic radiology, radiation protection, and darkroom theory. In: Textbook of Veterinary Diagnostic Radiology (D. E. Thrall, ed.). St. Louis: Saunders Elsevier. pp. 2–21.

Tod Drost, Wm., 2007: Basic ultrasound physics. In: Textbook of Veterinary Diagnostic Radiology (D. E. Thrall, ed.). St. Louis: Saunders Elsevier. pp. 38–49.

Tomson, F. N., and R. R. Lotshaw, 1978: Hyperphosphatemia and hypocalcemia in lemurs. J. Am. Vet. Med. Assoc. **173,** 1103–1106.

Tordiffe, A. S. W., G. F. van der Watt, and F. Reyers, 2012: Cystine urolithiasis in a caracal (*Caracal caracal*). J. Zoo Wildl. Med. **43,** 649–651.

Tuten, H. C., H. C. Miller, and A. E. Ellis, 2011: Cuterebrid myiasis (Diptera: Oestridae) in captive ring-tailed lemurs (*Lemur catta*) at a South Carolina Zoo. J. Zoo. Wildl. Med. **42,** 504–507.

Wadsworth, P. F., C. Gopinath, and D. M. Jones, 1980: Mammary neoplasia in ring-tailed lemurs (*Lemur catta*). Vet. Pathol. **17,** 386–388.

Wagner, W. M., and R. M. Kirberger, 2005a: Radiographic anatomy of the thorax and abdomen of the common marmoset (*Callithrix jacchus*). Vet. Radiol. Ultrasound. **46,** 217–224.

Wagner, W. M., and R. M. Kirberger, 2005b: Transcutaneous ultrasonography of the abdomen in the normal common marmoset (*Callithrix jacchus*). Vet. Radiol. Ultrasound. **46,** 251–258.

Wallach, J. D., and W. J. Boever, 1983: Diseases of Exotic Animals: Medical and Surgical Management. Philadelphia: W. B. Saunders Company.

Warwick, R., 1951: A sarcoma of bone in a ring-tailed lemur. J. Pathol. Bacteriol. **63,** 499–501.

Weber, M., N. Lamberski, and K. Heriot, 1995: An idiopathic proliferative disease of bone in two species of ruffed lemur (*Varecia variegata variegata* and *Varecia variegata rubra*). In: Proceedings of the joint conference of the American Association of Zoo Veterinarians, Wildlife Disease Association, American Association of Wildlife Veterinarians. Lansing, Michigan. pp. 268.

Wei, F., and Z. Zhang, 2009: Family Ailuridae (red panda). In: Handbook of the Mammals of the World Vol. 1 Carnivores (D. E. Wilson and R. A. Mittermeier, eds). Barcelona: Lynx Edicions. pp. 498–503.

Wei, F., and Z. Zhang, 2011: Red panda ecology. In: Red Panda Biology and Conservation of the First Panda (A. Glatson, ed.). London: Academic Press. pp. 193–212.

Widmer, W. R., 2008: Acquisition hardware for digital imaging. Vet. Radiol. Ultrasound. **49,** S2–S8.

Wilson, D. E., and E. Hanlon, 2010: *Lemur catta* (Primate: Lemuridae). Mamm. Species. **42,** 58–74.

Young, A. N., W. M. du Plessis, D. Rodriguez, and A. Beierschmitt, 2013: Thoracic radiographic anatomy in vervet monkeys (*Chorocebus sabaeus*). J. Med. Primatol. **42,** 310–317.

Zordan, M., M. Tirado, and C. López, 2012: Hepatic capillariasis in captive ring-tailed lemurs (*Lemur catta*). J. Zoo. Wildl. Med. **43,** 430–433.

Zwart, P., 1989: Contribution to the pathology of the red panda (*Ailurus fulgens*). In: Red Panda Biology (A. R. Glatston, ed.). The Netherlands: SPB Academic Publishing. pp. 25–29.

CHAPTER 3

THORACIC LIMB MORPHOLOGY OF THE RING-TAILED LEMUR (*LEMUR CATTA*) EVIDENCED BY GROSS OSTEOLOGY AND RADIOGRAPHY

3.1 INTRODUCTION

The ring-tailed lemur (*Lemur catta*) is classified as an endangered species by the International Union for Conservation of Nature and Natural Resources (IUCN) (IUCN, 2014). It is primarily distributed in south and south-western Madagascar (Budnitz and Dainis, 1975). The ring-tailed lemur belongs to the suborder strepsirrhini (Nowak, 1999). Most strepsirrhines resemble more primitive animals such as domestic cats and dogs by retaining characteristics like prominent scent glands, the rhinarium and a pointed muzzle (Jungle, 2003; Ankel-Simons, 2007).

Radiography is a non-invasive diagnostic imaging modality (Owens and Biery, 1999a), which is indicated for the diagnosis, evaluation and monitoring the progression of various conditions affecting the musculoskeletal system (Burk and Feeney, 2003). It is commonly used as the first diagnostic imaging modality for the musculoskeletal system in exotic animal practice. Diseases of lemurs involving the musculoskeletal system, where radiography was used as the first diagnostic imaging modality, include idiopathic proliferative bone disease characterized by irregular enlargement of bones of the distal limbs as

a result of periosteal proliferation (Weber et al., 1995), nutritional secondary hyperparathyroidism (Tomson and Lotshaw, 1978), multifocal pyogranulomatous osteomyelitis (Backues et al., 2001), periarticular hyperostosis (Jungle et al., 1994) and neoplasia such as osteosarcoma (Warwick, 1951). However, limited information is available about the normal gross osteology and radiographic anatomy of the appendicular skeleton of lemurs (Jouffroy, 1975; Roberts and Davidson, 1975).

Knowledge of the normal gross osteology and radiographic anatomy is important for accurate interpretation and diagnosis of various conditions, which involve the musculoskeletal system (Owens and Biery, 1999b; Smallwood and Spaulding, 2013; Thrall, 2013). Normal gross osteology and radiographic anatomy of the thoracic limb in companion animals is well documented and serves as a guide for diagnosis of various musculoskeletal diseases (Nickel et al., 1986; Thrall and Robertson, 2011; Smallwood and Spaulding, 2013). This study describes the morphology of the thoracic limb of captive ring-tailed lemurs evidenced by gross osteology and radiography.

3.2 MATERIALS AND METHODS

3.2.1 Sample population

Twelve (11 live and one dead) adult, intact, skeletally mature captive ring-tailed lemurs were used for the radiographic study. Live animals were clinically healthy, and radiography was performed during their annual health examination under general anaesthesia. Of the 11 live animals, eight were

females and three were males and their age ranged from 2.8 to 25.7 years (mean: 10.8 ± 7.6 years). Their minimum and maximum weights were 2.4 kg and 3.4 kg, respectively, (mean: 3.0 ± 0.3 kg). Of the 11 live animals, one female (7.3 year old; 2.8 kg) died during the course of the study and was included in the gross osteological study. One dead female animal (5 year old; 2.8 kg), which had died from a cause unrelated to disease of the musculoskeletal system was included in the study.

Bone specimens of the thoracic limb of three adult skeletally mature animals, one from the Ditsong National Museum (male of unknown age) and two dead females mentioned above, were used for gross osteological study. The study was approved by the Animal Use and Care Committee (AUCC) of the University of Pretoria.

3.2.2 Radiography

Radiography of the right thoracic limb was performed using a tabletop technique. In six animals, a Roentgen 703 X-ray machine (GEC Medical Equipment Ltd, Middlesex, UK) was used at a source to image distance (SID) of 105 cm with 60 kVp and 3 mAs. Images were obtained using a computed radiography (CR) unit (Regius Model 110, Konica Minolta Medical and Graphic, INC., Tokyo, Japan).

In five animals, a EVA-HF525 X-ray machine (Comed Medical System Co. Ltd, Kyunggi, Korea) was used at a SID of 95 cm with 46 kVp and 5 mAs. Mammography films (UM-MA, Fujifilm Corporation, Tokyo, Japan) were used

in combination with mamoray screens (Fujifilm Europe GmbH, Duesseldorf, Germany), and an automatic X-ray film processor model CP-345 (ELK Corporation, Tokyo, Japan) was used.

In the remaining animal, radiography was performed using a Siemens Polymat 50 (Siemens, Munich, Germany) X-ray machine at a SID of 100 cm, kVp range of 48–58 and mAs range of 4–5. Images were obtained using a CR unit (Fuji Axim FCR Capsula XL, Fujifilm Corporation, Tokyo, Japan).

A mediolateral (ML) view of the right thoracic limb was taken with the animal in right lateral recumbency. The radiograph included the right front leg from the shoulder joint to the distal aspect of the digits. To obtain a true ML view of the thoracic limb, tape was applied around the carpus and secured on the cassette to maintain the antebrachium and manus in a pronated position to prevent supination. To avoid the superimposition of the clavicle over the scapula on the ML view, the cranial margin of the right scapula was positioned at the level of the cranial margin of the *manubrium sterni* or slightly caudally.

Additionally, a caudocranial (CdCr) view of the right shoulder, a craniocaudal (CrCd) view of the right elbow and a dorsopalmar (DPa) view of the right manus were taken. A CdCr view of the shoulder joint was taken with the animal in dorsal recumbency and collimation included the distal half of the scapula and the proximal half of the humerus. The CrCd view of the elbow joint and DPa view of the manus were obtained with the animal in sternal recumbency. Collimation of the elbow joint included the distal humerus and

proximal radius and ulna. For the manus, collimation included the distal radius and ulna and distal aspect of the digits.

3.2.3 Gross osteology

The gross osteology of the thoracic limb was described. Radiographic findings were correlated with the gross osteologic findings. Digital photographs of the clavicle, humerus, radius, ulna and carpus were taken with CANON 5DMARK2 (Canon Inc., Tokyo, Japan) for illustration. The clavicle, scapula, humerus, radius and ulna were photographed in cranial and lateral views, and the carpus was photographed in a dorsal view. In addition, caudal (clavicle, scapula and humerus), medial (clavicle and humerus) and distal (scapula) photographic views were also taken.

3.2.4 Bone measurements

Bone measurements of the right thoracic limb were performed on the radiographic images with the exception of the scapula, which was performed on bone specimens. The maximum lengths of bones were measured from the proximal to the distal extremities. The maximum lengths of the humerus, radius and ulna were measured on the ML radiographic view.

For the metacarpal bones and phalanges, the maximum lengths were measured on the DPa radiographic view of the manus. The craniocaudal diameter of the scapula was measured as the maximum distance perpendicular to the maximum length. Radiographic measurements were not compensated for magnification.

3.2.5 Statistical analysis

Statistical analysis was performed using Stat View© (SAS Institute Inc., Cary, NC, USA) statistical package. A descriptive statistical analysis was performed for the age and weight of the animal, and the length and craniocaudal diameter of the bones. Data were expressed as mean ± standard deviation (SD) and the range.

3.3 RESULTS

3.3.1 Clavicle

The clavicle is well developed (Figs 3.1 and 3.2). The sternal extremity has an almost semicircular articular facet for articulation with the *Manubrium sterni* (Fig. 3.1c). The acromial extremity bears a fusiform facet for articulation with the hamate process of the scapula (Fig. 3.1d).

On the ML radiographic view of the shoulder joint, the clavicle projects cranially to the craniodistal aspect of the scapula, whereas on the CdCr radiographic view of the shoulder joint, it is seen distal to the scapula with its acromial extremity superimposed on the medial half of the proximal aspect of the humerus (Fig. 3.2). A distinct articulation between the hamate process of the scapula and acromial extremity of the clavicle is seen on both the ML and CdCr radiographic views of the shoulder joint (Fig. 3.2). Measurements of bones of the thoracic limb are shown in Tables 3.1 and 3.2.

3.3.2 Scapula

The scapula is narrow craniocaudally and elongated proximodistally (Fig. 3.3a). The dorsal margin is longer than the cranial margin (Fig. 3.3a). The coracoid process is well developed, mediolaterally flattened and directed caudodistally (Fig. 3.3). On the ML radiographic view of the shoulder joint, the coracoid process projects distally beyond the shoulder joint superimposed on the humeral head (Fig. 3.2a). On the CdCr radiographic view of the shoulder joint, it is better visualized and projects distally on the medial side of the shoulder joint (Fig. 3.2b). The articular surface of the glenoid cavity is peanut-shaped and narrow with a shallow concavity (Fig. 3.3c). The cranial articular surface of the glenoid cavity is elongated distally (Fig. 3.3c). The infraglenoid tubercle is represented by a rough surface (Fig. 3.3c). The supraglenoid tubercle is less prominent (Fig. 3.3b).

The infraspinous fossa is deeply concave, whereas the supraspinous fossa is fairly flat and smaller (Fig. 3.3a). The area for the origin of the *M. teres major* is large (Fig. 3.3a). The spine of the scapula is slanted towards the infraspinous fossa (Fig. 3.3a). The hamate process is large, long and well developed, extending beyond the glenoid cavity (Figs 3.2 and 3.3). It is flattened mediolaterally and directed craniodistally. On the ML radiographic view of the shoulder joint, the hamate process projects cranially beyond the shoulder joint (Fig. 3.2a). On the CdCr radiographic view of the shoulder joint, it is superimposed on the lateral half of the proximal aspect of the humerus (Fig. 3.2b). The distal extremity of the hamate process bears a facet for

articulation with the acromial end of the clavicle (Fig. 3.3b). The suprahamate process is absent (Fig. 3.3a).

3.3.3 Humerus

The humeral head is oval facing caudally (Fig. 3.4a). The proximal extremity of the major tubercle is flat and does not extend higher than the humeral head (Fig. 3.4a,b,c). Proximally, the major tubercle has a flat area for the insertion of the *M. supraspinatus*. Laterally, it presents with an oval depression for the insertion of the *M. infraspinatus*, which is at the same level as the humeral head (Fig. 3.4b,c). Just distocaudal to the area of the insertion of the *M. infraspinatus*, there is a small depression for the insertion of the *M. teres minor* (Fig. 3.4c). The minor tubercle is convex and further distal than the humeral head (Fig. 3.4a,b,d). It presents with a prominent area for the attachment of the *M. subscapularis*, which faces caudomedially (Fig. 3.4d). On the ML and CdCr radiographic views of the shoulder joint, the major and minor tubercles are further distal than the humeral head (Fig. 3.2). The humeral neck is well defined caudally (Fig. 3.4a).

The body of the humerus is slender (Fig. 3.5). On the ML radiographic view of the humerus, the cranial and caudal cortices of the distal half of the humerus are almost of the same thickness (Fig. 3.5). An area of soft tissue opacity is superimposed over the proximal half of the humeral diaphysis in male (Fig. 3.5a,b), but not female animals (Fig. 3.5c), which is secondary to the brachial scent gland. The crests of the major and minor tubercles are very pronounced located on the cranial and medial surfaces, respectively, of the body of the

humerus (Fig. 3.4b,d). The crest of the major tubercle is thin and slanted towards the medial side (Fig. 3.4d). Distally, it is continuous with the deltoid tuberosity.

On the ML radiographic view of the shoulder joint, the crest of the minor tubercle is seen as a thin radiopaque longitudinal line superimposed on the proximal half of the humerus (Fig. 3.2). On the CdCr radiographic view of the shoulder joint, the crest of the major tubercle is seen as a thin longitudinal radiopaque line superimposed on the body of the humerus (Fig. 3.2b). The deltoid (Fig. 3.4b,c,d) and teres major (Fig. 3.4a,b,d) tuberosities are very pronounced. The deltoid tuberosity projects cranially on the ML radiographic view of the humerus (Fig. 3.5).

The proximal third of the lateral surface of the body of the humerus is marked by the triceps muscle line (Fig. 3.4c), which extends from the caudodistal aspect of the major tubercle to the distal aspect of the cranially located deltoid tuberosity. Cranial to the triceps muscle line and caudal to the crest of the major tubercle, the proximal third of the lateral surface of the body bears a shallow longitudinal groove (Fig. 3.4c).

The lateral supracondylar crest is well developed (Figs. 3.4e,f and 3.6b). The medial epicondyle is larger and better developed than its lateral counterpart (Fig. 3.4e,f). The medially located supracondylar foramen slopes from medial to craniodistal (Fig. 3.4e,f). On the CrCd radiographic view of the elbow joint, the supracondylar foramen is seen as two ovoid radiolucent areas just

proximal to the medial epicondyle (Fig. 3.6b). The articular surface of the humeral condyle is fairly symmetrical (flat) and presents with a distinct medially located trochlea humeri and a laterally located capitulum humeri (Fig. 3.4e,f). The capitulum humeri are grooved, whereas the trochlea humeri, are not grooved (Fig. 3.4e).

The radial and coronoid fossae are well defined (Fig. 3.4e). The radial fossa is more prominent than the coronoid fossa. The horizontally aligned olecranon fossa is shallow and fairly triangular with rounded angles (Fig. 3.4f). On the CrCd radiographic view of the elbow joint, the olecranon fossa has an ovoid shape and is elongated in a mediolateral direction (Fig. 3.6b). The supratrochlear foramen is absent.

3.3.4 Radius and ulna

Radius and ulna are separate bones of similar width with a wide inter-osseous space. The ulna is longer than the radius (Fig. 3.7). The radial head is distinct and fairly elliptical in shape sloping from lateral to medial (Fig. 3.8a). It has a concave articular fovea proximally and is well demarcated from the body by a long distinct neck (Figs 3.6 and 3.8a,c).

The body of the radius curves cranially along the longitudinal axis of the bone when viewed from lateral or medial (Fig. 3.7). The distal third of the bone is rotated towards the lateral side. Distal to the neck, the caudal surface of the body bears a prominent radial tuberosity, which is relatively distally located (Figs 3.6 and 3.8a,c). The radial tuberosity is marked by a short groove (Fig.

3.8a). The body of the radius bears a deep longitudinal groove distal to the radial tuberosity. Further, it presents with longitudinal grooves craniolaterally and craniomedially. The caudal surface of the distal aspect of the body of the radius bears a broad flat surface.

The radial trochlea is broader than the head and is flared on the ML and DPa radiographic views of the carpus (Fig. 3.9). The radial trochlea has three cranial grooves for the passage of tendons (Fig. 3.8b). The middle and lateral grooves are separated by a wide tubercle. The medially located styloid process is pointed (Fig. 3.8b,d). The ulnar notch is fairly flat (Fig. 3.8d).

The ulna bears a proximally directed square-shaped tuber olecrani (Figs 3.6 and 3.10a,c). A small osseous spur is seen radiographically on the caudoproximal aspect of the tuber olecrani in two animals (Figs 3.6c and 3.7b). The anconeal process is short and wide (Fig. 3.10a). The prominent and rounded medial coronoid process (Fig. 3.10a) appears pointed on the ML radiographic view of the elbow joint (Fig. 3.6a,c). The craniolaterally located radial notch is a fairly rounded projection with a single articular facet sloping from medially to laterally (Fig. 3.10a,c). The radial notch projects cranially from the surface of the ulna (Fig. 3.10a,c).

The body of the ulna is slightly curved with the lateral and medial surfaces marked by prominent longitudinal grooves. Just distal to the medial coronoid process, the body of the ulna bears a groove for the insertion of the m. brachialis (Fig. 3.10a).

The ulnar head is well developed (Figs 3.9 and 3.10). The styloid process is bulbous with a convex articular surface for articulation with the ulnar and accessory carpal bones (Figs 3.9 and 3.10). The articular circumference slopes in a craniocaudal direction and is increased from the surface of the body of the ulna (Fig. 3.10d). It forms an approximately ninety degree angle with the styloid process (Fig. 3.10d). Just proximal to the articular circumference, the cranial surface of the body of the ulna presents with a flat surface for the origin for the *M. pronator quadratus* and is bordered medially by a crest (Fig. 3.10b). The radial and ulnar physeal scars are linear-shaped (Fig. 3.9). On the ML radiographic view of the antebrachium, areas of soft tissue opacity are noted summating with the distal half of the antebrachium in male animals as a result of the antebrachial scent glands (Fig. 3.7b).

3.3.5 Carpus

The carpal bones form a convex dorsal outline. There are nine carpal bones arranged in three rows. The proximal row comprises the radial, intermediate, ulnar and accessory carpal bone. The central carpal bone is the only bone situated in the middle row. The distal row comprises the first, second, third and fourth carpal bones (Fig. 3.9).

The radial carpal bone is the most medial carpal bone in the proximal row (Fig. 3.9a,b) and reveals a palmaromedial prominent tuberosity. The tuberosity on the palmaromedial aspect of the radial carpal bone is seen as an ovoid area of increased bone opacity on the medial aspect of the radial carpal bone on the DPa radiographic view of the carpus (Fig. 3.9b). The ulnar carpal

bone (Fig. 3.9b) presents with a small palmarly directed process. Proximally, the bone bears two articular facets for the accessory carpal bone and styloid process of the ulna. The intermediate carpal bone is the smallest bone in the proximal row situated between the radial and ulnar carpal bones (Fig. 3.9). The palmarolaterally directed accessory carpal bone is Y-shaped when viewed from proximal. The dorsal surface of the bone has two articular facets, one for the styloid process of the ulna and the other for the ulnar carpal bone.

The central carpal bone is crescent-shaped and situated in the middle row (Fig. 3.9). The fourth carpal bone is the largest carpal bone located on the lateral side of the distal row (Fig. 3.9). It is wedge-shaped when viewed from dorsally and articulates both with the fourth and fifth metacarpal bones. The first to third carpal bones in the distal carpal row articulate with their corresponding metacarpal bones (Fig. 3.9). A sesamoid bone for the *M. abductor pollicis longus* is always seen on the medial aspect of the carpus (Fig. 3.9b).

3.3.6 Metacarpus and digits

There are five metacarpal bones (Fig. 3.11), namely (mediolateral sequence): metacarpal (MC) bones I–V. The MC bones are widely spread and equally developed in terms of width. They are relatively shorter in relation to the length of their corresponding digits. The first MC bone diverges further medial from the rest of the MC bones, with the dorsal and palmar surfaces facing almost medially and laterally, respectively, (Fig. 3.11). There are five digits. Digits II–V each have three phalanges: the proximal (P1), middle (P2) and

distal (P3) phalanges. Digit I has only phalanges P1 and P3 (Fig. 3.11). The P1 phalanx is the longest, whereas the P3 phalanx is the shortest (Fig. 3.11).

Each metacarpophalangeal joint has paired proximal sesamoid bones on the palmar aspect. The abaxial proximal sesamoid bones of digits II and III are longer than their counterparts, whereas the axial proximal sesamoid bones of digits IV and V are longer than their counterparts. An ovoid ossicle was always seen on the palmar aspect at the inter-phalangeal joint of digit I (Fig. 3.11). The soft tissue opacity surrounding the MC bones, including the carpus and metacarpophalangeal joints, is prominent (Fig. 3.11).

3.4 DISCUSSION

Strepsirrhines are predominantly arboreal animals with the exception of the ring-tailed lemur, which spends up to one-third of its time on the ground (Ankel-Simons, 2007). The ring-tailed lemur is a quadruped with its locomotor activity involving climbing, jumping and running (Ankel-Simons, 2007).

Strong flexor muscles and flexibility of the thoracic limb joints are important in arboreal quadrupeds. The long and well-developed clavicle and small and shallow glenoid cavity observed in this study indicate that the shoulder joint in this species is freely and highly mobile (Ankel-Simons, 2007) and capable of a large range of movements. The clavicle, which attaches to the *manubrium sterni* and acromion of the scapula in this species, keeps the scapula in a lateral position, which provides the shoulder joint with high mobility (Ankel-

Simons, 2007). The distal elongation of the cranial articular surface of the glenoid cavity is believed to prevent luxation of the humeral head in extreme retraction of the humerus.

The narrow scapula with a long dorsal margin and a short cranial margin allows rapid movement of the thoracic limb and at the same time provides an adequate area for insertion of the scapulovertebral muscles, which support the body weight and absorb the shock of the footfall at the end of a quadrupedal leap. This is probably an adaptation to both arboreal and terrestrial lifestyles.

The abduction ability of the shoulder joint is supported by the presence of a broad and long acromion process and the location of the insertion of the *M. infraspinatus* at the same level as the head of the humerus. The broad and long acromion process increases the power of the *M. deltoideus* in the abduction of the humerus (Taylor, 1974). In some African mammals, it was found that the insertion of the *M. infraspinatus* above the level of the humeral head diminishes its abduction function (Hopwood, 1947).

The fairly symmetrical (flat) distal articular surface of the humerus observed in this species provides a suitable surface for a rocking movement of the ulna aiding in supination (Taylor, 1974). Further, the well-developed lateral supracondylar crest is the origin of the *M. brachioradialis*, a supinator of the antebrachium. The craniolaterally located radial notch with a single articular facet that projects cranially from the surface of the ulna allows greater rotation

of the radius (Taylor, 1974; Gonyea, 1978). The elliptically shaped radial head acts as a cam that transmits the radius' eccentric motion and hence permits rotation of the radius without stretching of the inter-osseous ligament (Gonyea, 1978). Additionally, the increase of the ulnar articular circumference from the body, well-developed body and ulnar head act as a pivot, which supports the radius during rotation movement.

The presence of strong flexor muscles of the thoracic limb is supported by the presence of the following features: a large area and prominent tuberosity, which provides the origin and insertion, respectively, of the *M. teres major*, which flexes the humerus, a prominent medial epicondyle, which provides the origin of the flexor muscles of the manus and a relatively distally located and prominent radial tuberosity, which provides the insertion for the *M. biceps brachii*, which flexes the elbow joint. Additionally, the presence of a well defined radial fossa indicates that the thoracic limb in this species is adapted for elbow flexion (Fleagle and Simons, 1995).

The oval caudally facing humeral head, lack of extension of the greater tubercle proximal to the humeral head and the proximally directed tuber olecrani are characteristic features of arboreal quadrupedal primates (Fleagle and Simons, 1995; Ankel-Simons, 2007). A slightly curved body of the ulna has been observed in other small arboreal quadrupedal primates (Fleagle and Simons, 1995). Large arboreal quadrupedal primates have a greater curvature of the body of the ulna as a result of regular use of the thoracic limb in a more flexed position (Fleagle and Simons, 1995).

The presence of the central carpal bone in skeletally mature ring-tailed lemurs is different from humans, domestic cats and dogs (Nickel et al., 1986). The central carpal bone has also been reported in other strepsirrhines (Osman Hill, 1953; Jouffroy, 1975). The medial divergence of the first MC bone from the rest of the MC bones observed in ring-tailed lemurs is associated with the manus being an efficient grasping tool during feeding and locomotion (Ankel-Simons, 2007). The widely spread and short MC bones provide a large space and allow greater effectiveness of the muscles responsible for small movements of the digits (Taylor, 1974). The palmarolaterally directed accessory carpal bone is associated with ulnar deviation (Taylor, 1974).

The presence of two proximal sesamoid bones palmar to the metacarpophalangeal joint of all digits observed in ring-tailed lemurs is similar to wild feline species (Kirberger et al., 2000; 2005) but different from humans (Msamati and Igbigbi, 2001; Dharap et al., 2007). In humans, two proximal sesamoid bones are always present palmar to the metacarpophalangeal joint of the thumb and less frequently to rarely in other fingers (Msamati and Igbigbi, 2001; Dharap et al., 2007). Variation in the length between abaxial and axial proximal sesamoid bones of the same digit has also been observed in wild feline species (Kirberger et al., 2000; 2005). The ovoid ossicle seen at the inter-phalangeal joint of digit I in all animals suggests that the ossicle is a normal anatomical finding in this species. It is most likely that the ossicle is intra-articular as described for the great toe in humans (Suwannahoy et al., 2012) and should be differentiated from an avulsion fracture or intra-articular mineralized body.

Areas of increased soft tissue opacity seen superimposed over the proximal half of the humerus and the distal half of the antebrachium in male animals are a result of scent gland and should not be mistaken with soft tissue masses such as neoplasia, hematomas, seromas, granulomas, cellulitis, abscesses and cysts. In this study, scent glands (brachial and antebrachial) were seen only in male animals on radiographic examination. Wilson and Hanlon (2010) reported that the brachial scent gland is barely developed in female ring-tailed lemurs, whereas the antebrachial scent gland is present in both sexes.

The thick soft tissue opacity seen around the carpus, MC bones and metacarpophalangeal joints on the DPa radiographic view of the manus is different from domestic cats and dogs (Thrall and Robertson, 2011) and should not be mistaken as soft tissue swelling as a result of cellulitis, neoplasia, abscesses or inflammation due to trauma or a foreign body.

The radiographic measurements of bones obtained in this study might be slightly increased due to the effect of magnification (Thrall, 2013). However, we hope the length measurements might provide useful information for future studies.

In summary, the thoracic limb morphology of the ring-tailed lemur supports the presence of strong flexor muscles and flexibility of the thoracic limb joints, which is important in arboreal quadrupedal locomotion. However, the proximal part of the thoracic limb is modified for both arboreal and terrestrial quadrupedal locomotion. The osteology and radiographic anatomy of the

thoracic limb of the ring-tailed lemur is important for accurate interpretation and diagnosis of musculoskeletal diseases involving the thoracic limb. Further, studies are needed to determine the importance of the inter-phalangeal ossicle in the first digit for the biomechanics of the first digit.

3.5 ACKNOWLEDGEMENTS

The authors would like to thank the Organisation for Women in Science for the Developing World (OWSD), Swedish International Development Cooperation Agency (SIDA), University of Pretoria, Johannesburg (JHB) and Bristol zoos for supporting this study. The Ditsong National Museum and Dr. Shaw Badenhorst for supplying bone specimens. Dr. Brett Gardner, Dr. Kathryn Perrin, Ms. Fania Mohlala, sisters and animal handlers of Onderstepoort Veterinary Academic Hospital, Bristol and JHB zoos for their assistance during radiographic examination. Mrs. Wilma Olivier and Mrs. Charmaine Vermeulen of University of Pretoria for their assistance in administrative work and photography, respectively.

3.6 REFERENCES

Ankel-Simons, F., 2007: Primate Anatomy: An Introduction. Boston: Academic Press.

Backues, K. A., J. P. Hoover, R. J. Bahr, A. W. Confer, J. A. Chalman, and M. L. Larry, 2001: Multifocal pyogranulomatous osteomyelitis resembling chronic recurrent multifocal osteomyelitis in a lemur. J. Am. Vet. Med. Assoc. **218,** 250–253.

Budnitz, N., and K. Dainis, 1975: *Lemur catta*: Ecology and Behaviour. In: Lemur Biology (I. Tattersall and R. W. Sussman, eds). New York: Plenum Press, pp. 219–235.

Burk, R. L., and D. A. Feeney, 2003: Small animal radiology and ultrasonography. A Diagnostic Atlas and Text. Philadelphia: Saunders.

Dharap, A. S., H. Al-Hashimi, S. Kassab, and M. F. Abu-Hijleh, 2007: Incidence and ossification of sesamoid bones in the hands and feet: A radiographic study in an Arab population. Clin. Anat. **20,** 416–423.

Fleagle, J. G., and E. L. Simons, 1995: Limb skeleton and locomotor adaptations of *Apidium phiomense*, an Oligocene Anthropoid from Egypt. Am. J. Phys. Anthropol. **97,** 235–289.

Gonyea, W. J., 1978: Functional implications of felid forelimb anatomy. Acta. Anat. **102,** 111–121.

Hopwood, A. T., 1947: Contributions to the study of some African Mammals-III. Adaptations of the bones of the forelimb of the lion, leopard and cheetah. J. Linn. Soc. Zool. **41,** 259–271.

IUCN, 2014: IUCN Red List of Threatened Species. Version 2014.3. Available at: http://www.iucnredlist.org (accessed on 18 November 2014).

Jouffroy, F. K., 1975: Osteology and Myology of the Lemuriform Postcranial Skeleton. In: Lemur Biology (I. Tattersall and R. W. Sussman, eds). New York: Plenum Press. pp. 149–192.

Jungle, R. E., 2003: Prosimians. In: Zoo and Wild Animal Medicine (M. E. Fowler and R. E. Miller, eds). Missouri: Saunders. pp. 334–346.

Jungle, R. E., K. G. Mehren, T. P. Meehan, G. J. Crawshaw, M. C. Duncan, L. Gilula, F. Gannon, G. Finkel, and M. P. Whyte, 1994: Periarticular hyperostosis and renal disease in six black lemurs of two family groups. J. Am. Vet. Med. Assoc. **205,** 1024–1029.

Kirberger, R. M., H. B. Groenewald, and W. M. Wagner, 2000: A radiological study of the sesamoid bones and Os meniscus of the cheetah (*Actinonyx jubatus*). Vet. Comp. Orthopaed. **13,** 172–177.

Kirberger, R. M., W. M. du Plessis, and P. H. Turner, 2005: Radiologic Anatomy of the normal appendicular skeleton of the lion (*Panthera leo*). Part 2: Pelvic limb. J. Zoo. Wildl. Med. **36,** 29–35.

Msamati, B. C., and P. S. Igbigbi, 2001: Radiographic appearance of sesamoid bones in the hands and feet of Malawian subjects. Clin. Anat. **14,** 248–253.

Nickel, R., A. Schummer, E. Seiferle, J. Frewein, H. Wilkens, and K. H. Wille, 1986: The Anatomy of the Domestic Animals. Berlin: Springer-Verlag.

Nowak, R. M., 1999: Order Primate. In: Walker's Mammals of the World (R. M. Nowak, ed.). Baltimore: The Johns Hopkins University Press. pp. 490–631.

Osman Hill, W. C., 1953: Primates (Comparative Anatomy and Taxonomy). I. Strepsirhini. Edinburgh: University Press. pp. 50–380.

Owens, J. M., and D. N. Biery, 1999a: The scope of diagnostic imaging. In: Radiographic Interpretation for the Small Animal Clinician (J. M. Owens and D. N. Biery, eds). Baltimore: Williams and Wilkins. pp. 1–8.

Owens, J. M., and D. N. Biery, 1999b: Principles of radiographic interpretation. In: Radiographic Interpretation for the Small Animal Clinician (J. M. Owens and D. N. Biery, eds). Baltimore: Williams and Wilkins. pp. 9–13.

Roberts, D., and I. Davidson, 1975: The lemur scapula. In: Lemur Biology (I. Tattersall and R. W. Sussman, eds). New York: Plenum Press. pp. 125–147.

Smallwood, J. E., and K. A. Spaulding, 2013: Radiographic anatomy of the appendicular skeleton. In: Textbook of Veterinary Diagnostic Radiology (D. E. Thrall, ed.). Missouri: Saunders Elsevier. pp. 224–251.

Suwannahoy, P., T. Srisuwan, N. Pattamapaspong, and P. Mahakkanukrauh, 2012: Intra-articular ossicle in interphalangeal joint of the great toe and clinical implication. Surg. Radiol. Anat. **34,** 39–42.

Taylor, M. E., 1974: The functional anatomy of the forelimb of some African Viverridae (Carnivora). J. Morph. **143,** 307–335.

Thrall, D. E., 2013: Introduction to radiographic interpretation. In: Textbook of Veterinary Diagnostic Radiology (D. E. Thrall, ed.). Missouri: Saunders Elsevier. pp. 74–86.

Thrall, D. E., and I. D. Robertson, 2011: The thoracic limb. In: Atlas of Normal Radiographic Anatomy and Anatomic Variants in the Dog and Cat (D.

E. Thrall and I. D. Robertson, eds). Missouri: Elsevier Saunders. pp. 69–98.

Tomson, F. N., and R. R. Lotshaw, 1978: Hyperphosphatemia and hypocalcemia in lemurs. J. Am. Vet. Med. Assoc. **173,** 1103–1106.

Warwick, R., 1951: A sarcoma of bone in a ring-tailed lemur. J. Pathol. Bacteriol. **63,** 499–501.

Weber, M., N. Lamberski, and K. Heriot, 1995: An idiopathic proliferative disease of bone in two species of ruffed lemur (*Varecia variegata variegata* and *Varecia variegata rubra*). In: Proceedings of the joint conference of the American Association of Zoo Veterinarians, Wildlife Disease Association, American Association of Wildlife Veterinarians. Lansing, Michigan. pp. 268.

Wilson, D. N., and E. Hanlon, 2010: *Lemur catta* (Primates: Lemuridae). Mamm. Species. **42,** 58–74.

3.7 TABLES

Table 3.1 Measurements (cm) of the scapula, humerus, radius and ulna of the right thoracic limb in captive ring-tailed lemurs

Bone	Variable	Number of animals	Mean ± SD (cm)	Range (cm)
Scapula	Length[a]	3	5.40 ± 0.10	5.30 – 5.50
	Craniocaudal diameter[a]	3	2.60 ± 0.30	2.30 – 2.90
Humerus	Length[b]	12	9.29 ± 0.15	8.97 – 9.53
Radius	Length[b]	12	9.75 ± 0.22	9.46 – 10.10
Ulna	Length[b]	12	11.05 ± 0.28	10.69 – 11.50

[a]Measurements done on bone specimens

[b]Radiographic measurements not compensated for magnification

Table 3.2 Radiographic measurements (cm)[a] of metacarpal bones and phalanges of the right thoracic limb in captive ring-tailed lemurs

Bone	Number of animals	Length (Mean ± SD) cm	Range (cm)
MC I	12	1.23 ± 0.12	0.90 – 1.34
MC II	12	1.99 ± 0.27	1.20 – 2.22
MC III	12	2.30 ± 0.09	2.12 – 2.40
MC IV	12	2.22 ± 0.09	2.08 – 2.40
MC V	12	2.05 ± 0.11	1.90 – 2.30
P1 of digit I	12	1.10 ± 0.10	0.90 – 1.21
P1 of digit II	12	1.50 ± 0.08	1.39 – 1.60
P1 of digit III	12	1.81 ± 0.08	1.68 – 1.90
P1 of digit IV	12	1.92 ± 0.07	1.82 – 2.00
P1 of digit V	12	1.54 ± 0.16	1.04 – 1.66
P2 of digit II	12	0.96 ± 0.04	0.90 – 1.00
P2 of digit III	12	1.22 ± 0.05	1.15 – 1.30
P2 of digit IV	11	1.31 ± 0.07	1.20 – 1.40
P2 of digit V	11	1.05 ± 0.05	0.97 – 1.10
P3 of digit I	12	0.62 ± 0.30	0.40 – 1.55
P3 of digit II	10	0.38 ± 0.04	0.30 – 0.43
P3 of digit III	10	0.42 ± 0.04	0.36 – 0.50
P3 of digit IV	10	0.43 ± 0.06	0.30 – 0.50
P3 of digit V	10	0.39 ± 0.03	0.30 – 0.40

[a]Radiographic measurements not compensated for magnification

MC, metacarpal; P1, proximal phalanx; P2, middle phalanx; P3, distal phalanx

3.8 FIGURES

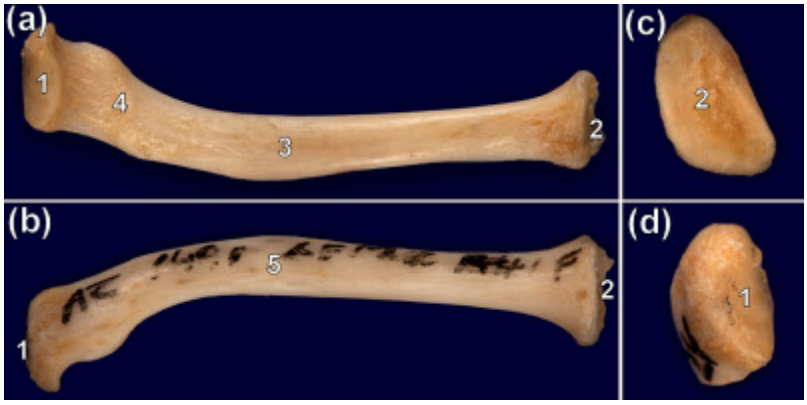

Fig. 3.1 Caudal (a), cranial (b), medial (c) and lateral (d) views of a bone specimen of the clavicle of an adult male ring-tailed lemur. (1) Acromial facet, (2) sternal facet, (3) caudal surface, (4) trapezoid line and (5) cranial surface.

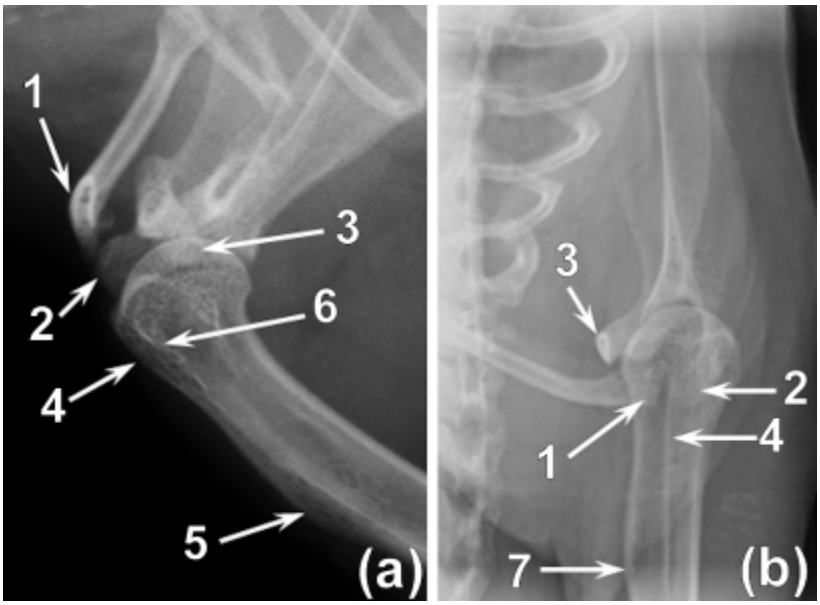

Fig. 3.2 Mediolateral (a) and CdCr (b) radiographic views of the right shoulder joint of a 5-year-old female ring-tailed lemur. (1) Acromial end of the clavicle, (2) hamate process, (3) distal end of the coracoid process, (4) major tubercular crest, (5) deltoid tuberosity, (6) minor tubercular crest and (7) tuberosity for the *M. teres major*.

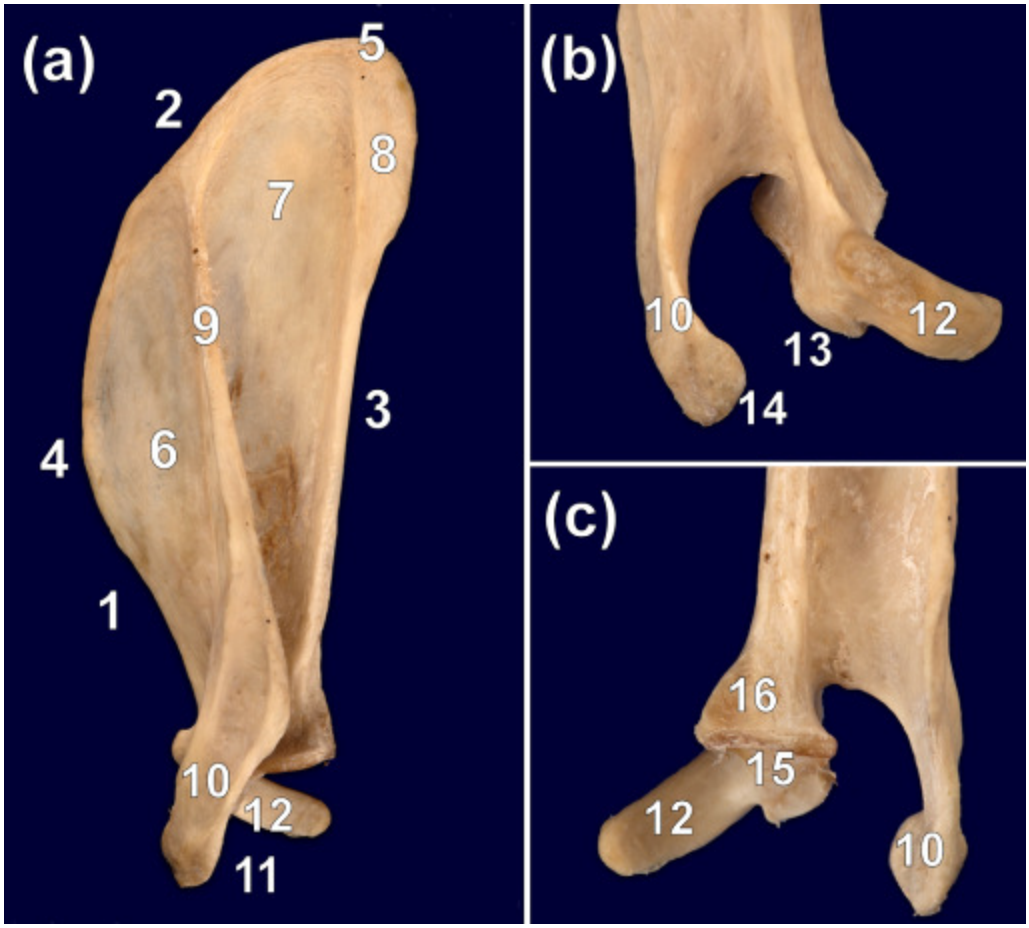

Fig. 3.3 Lateral (a) and distal aspect of the cranial (b) and caudal (c) views of a bone specimen of the scapula of a 5-year-old female ring-tailed lemur. (1) Cranial margin, (2) dorsal margin, (3) caudal margin, (4) cranial angle, (5) caudal angle, (6) supraspinous fossa, (7) infraspinous fossa, (8) area for the origin of *M. teres major*, (9) scapular spine, (10) hamate process, (11) ventral angle, (12) coracoid process, (13) supraglenoid tubercle, (14) facet for articulation with the acromial end of the clavicle, (15) glenoid cavity and (16) infraglenoid tubercle.

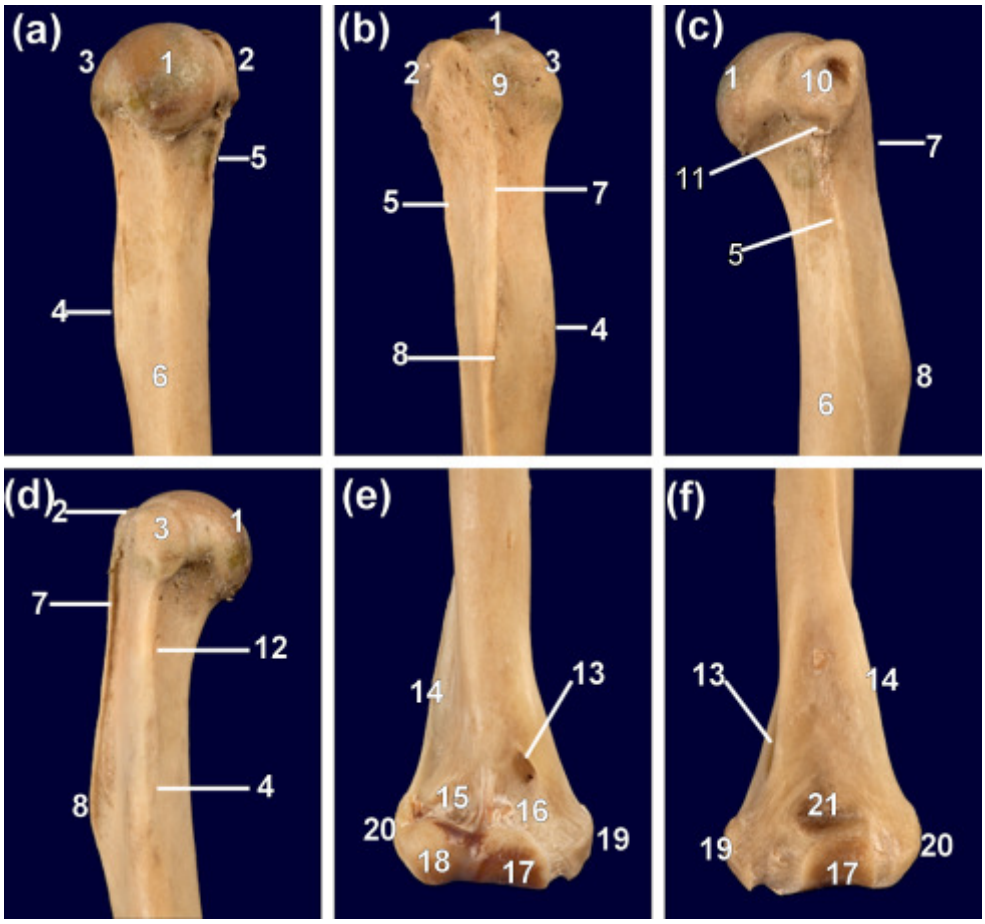

Fig. 3.4 Caudal (a), cranial (b), lateral (c), medial (d) and cranial (e), caudal (f) views of the proximal and distal, respectively, of a bone specimen of the humerus of a 7-year-old female ring-tailed lemur. (1) Humeral head, (2) major tubercle, (3) minor tubercle, (4) tuberosity for the *M. teres major*, (5) triceps muscle line, (6) body, (7) major tubercular crest, (8) deltoid tuberosity, (9) intertubercular groove, (10) *Facies m. infraspinatus*, (11) area for the insertion of the *M. teres minor*, (12) minor tubercular crest, (13) supracondylar foramen, (14) lateral supracondylar crest, (15) radial fossa, (16) coronoid fossa, (17) trochlea humeri, (18) capitulum humeri, (19) medial epicondyle, (20) lateral epicondyle and (21) olecranon fossa.

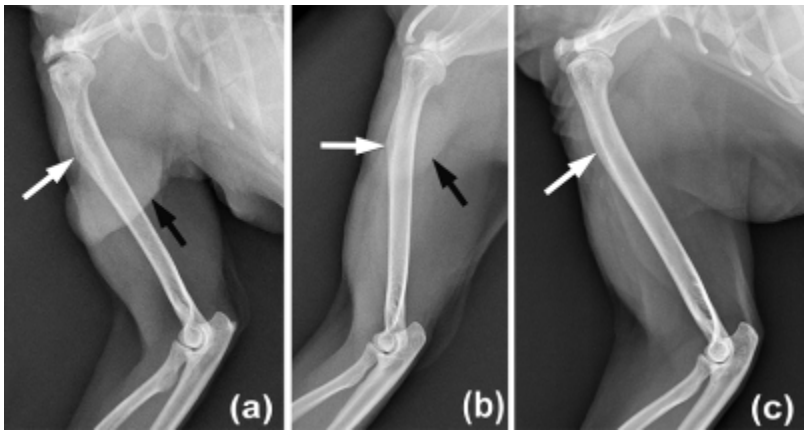

Fig. 3.5 Mediolateral radiographic view of the humerus of 22.8-year-old (a), 4.8-year-old (b) and 3.7-year-old (c), male (a, b) and female (c) ring-tailed lemur. Note the superimposition of the clavicle (a, c) on the scapula which prevents accurate evaluation of the shoulder joint. Deltoid tuberosity (white arrows) and brachial scent glands (black arrows).

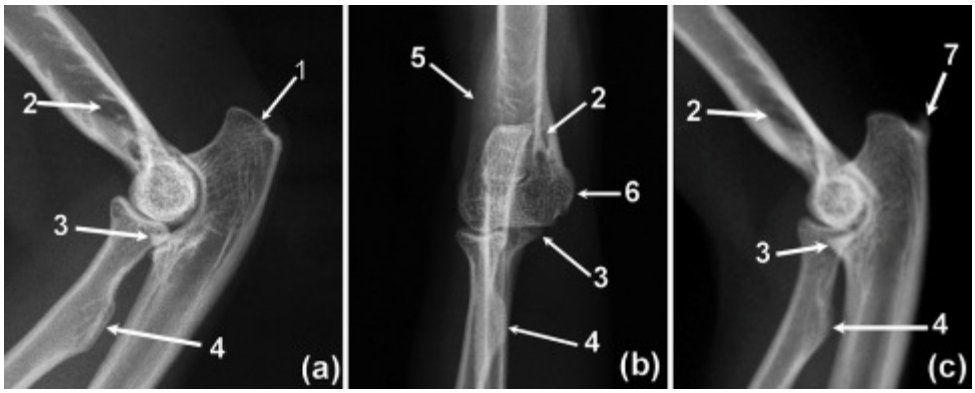

Fig. 3.6 Mediolateral (a, c) and CrCd (b) radiographic views of the right elbow joints of a 5-year-old (a, b) and 9.3-year-old (c) female ring-tailed lemur. (1) Tuber olecrani, (2) supracondylar foramen, (3) medial coronoid process, (4) radial tuberosity, (5) lateral supracondylar crest, (6) medial epicondyle and (7) olecranon spur.

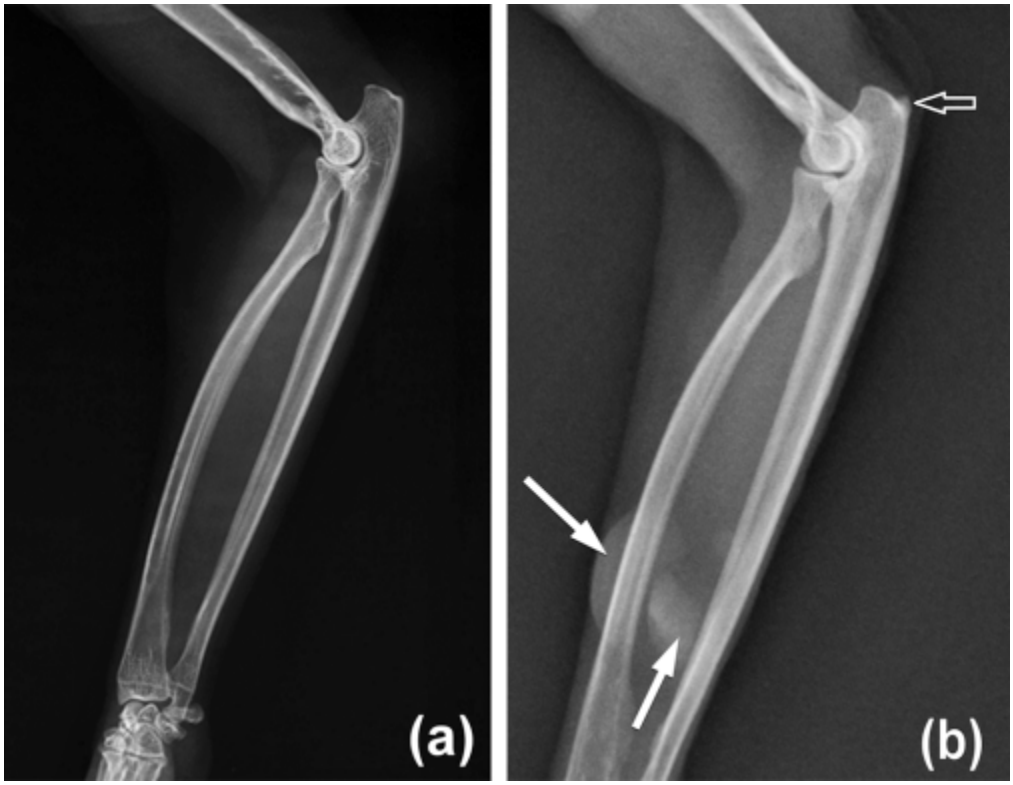

Fig. 3.7 Mediolateral radiographic view of the right antebrachium of a 5-year-old female (a) and 22.8-year-old male (b) ring-tailed lemur. (a, b) Note the wide interosseous space. (b) Note also the olecranon spur (open white arrow) and areas of increased soft tissue opacity (white arrows) in the distal half of the antebrachium due to superimposition of prominent antebrachial scent gland in the male animal.

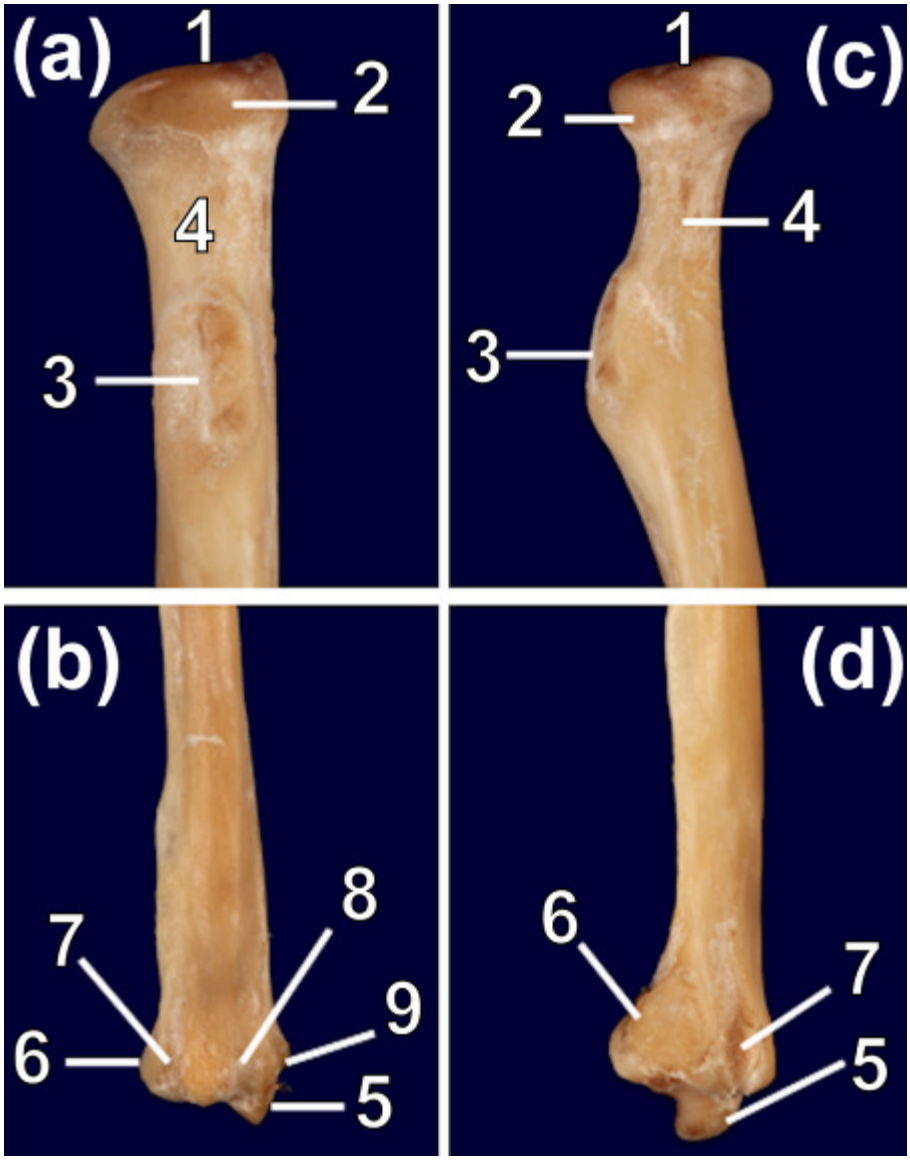

Fig. 3.8 Caudal (a), cranial (b) and lateral (c, d) views of the proximal (a, c) and distal (b, d) aspects of a bone specimen of the radius of a 7-year-old female ring-tailed lemur. (1) Radial head fovea, (2) articular circumference, (3) radial tuberosity, (4) radial neck, (5) styloid process, (6) ulnar notch, (7) lateral tendon groove, (8) middle tendon groove and (9) medial tendon groove.

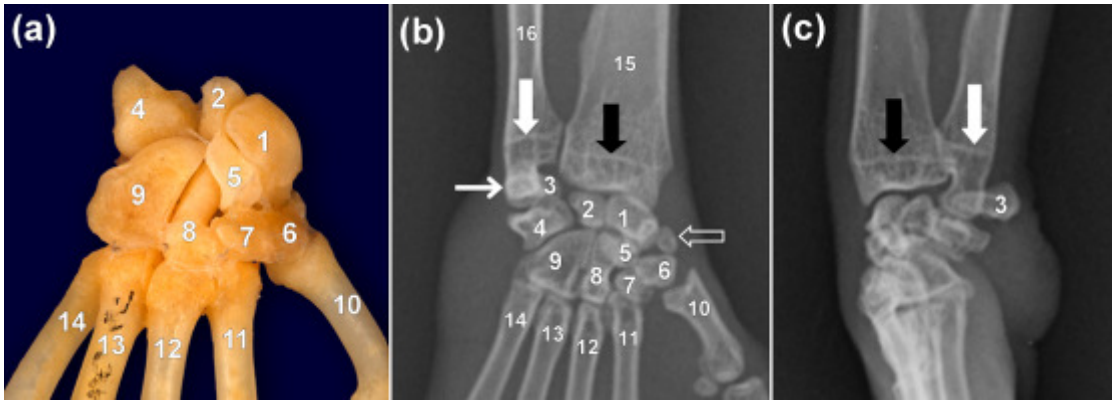

Fig. 3.9 Dorsal (a), DPa (b) and ML (c) views of a bone specimen (a) and radiographs (b, c) of the carpus of an adult male (a) and 5-year-old female (b, c) ring-tailed lemur. Note the medial divergence of the first MC bone from the rest of the MC bones (a, b). Note also the radial (thick black arrow) and ulnar (thick white arrow) transverse physeal scars (b, c). The increased mineral opacity (thin white arrow) is a result of superimposition of the styloid process of the ulna and accessory carpal bone. Note the presence of a sesamoid bone of the *M. abductor pollicis longus* on the medial aspect of the carpus (open white arrow). (1) Radial carpal bone, (2) intermediate carpal bone, (3) accessory carpal bone, (4) ulnar carpal bone, (5) central carpal bone, (6) first carpal bone, (7) second carpal bone, (8) third carpal bone, (9) fourth carpal bone, (10) first MC bone, (11) second MC bone, (12) third MC bone, (13) fourth MC bone, (14) fifth MC bone, (15) radius and (16) ulna.

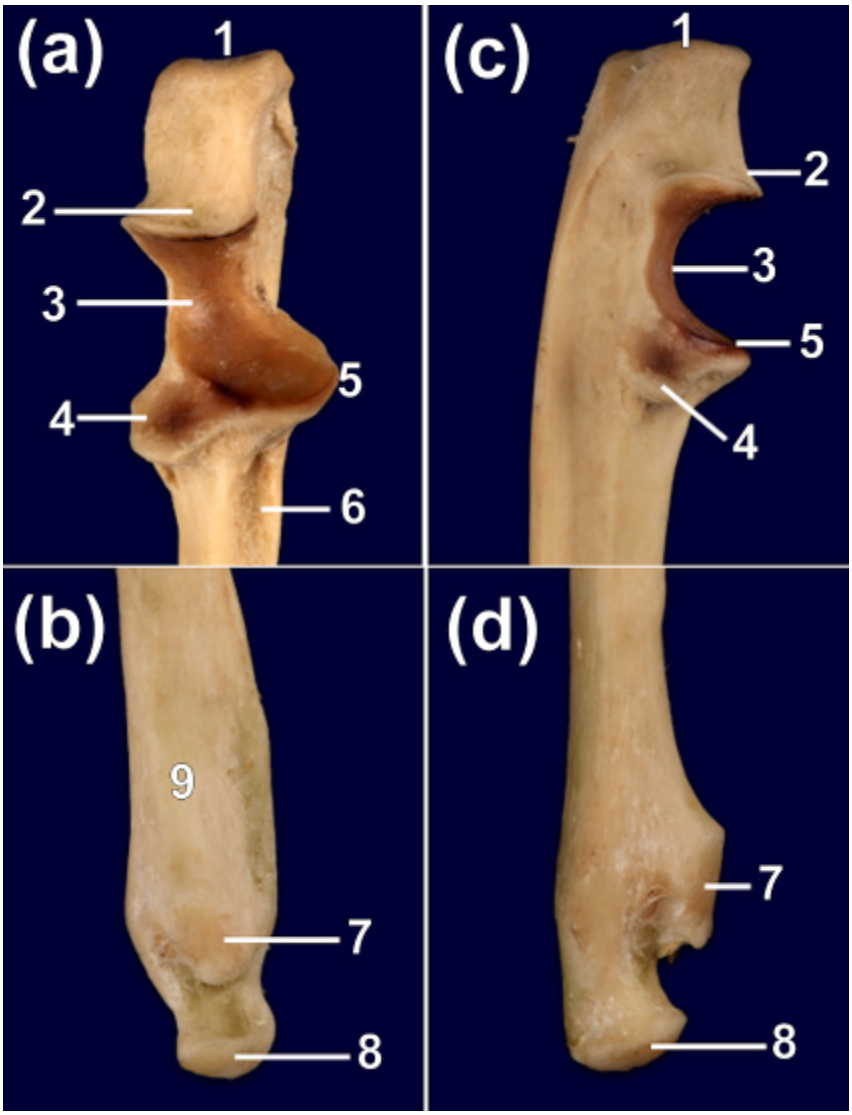

Fig. 3.10 Cranial (a, b) and lateral (c, d) views of the proximal (a, c) and distal (b, d) aspect of a bone specimen of the ulna of a 5-year-old female ring-tailed lemur. (1) Tuber olecrani, (2) anconeal process, (3) trochlear notch, (4) radial notch, (5) medial coronoid process, (6) groove for the insertion of *M. brachialis*, (7) articular circumference, (8) styloid process and (9) area for the origin of the *M. pronator quadratus*.

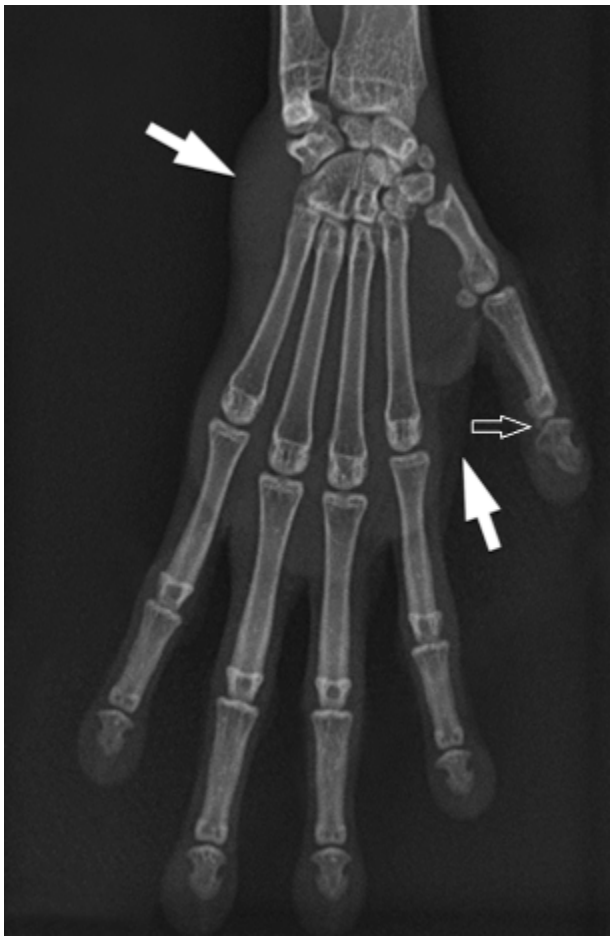

Fig. 3.11 Dorsopalmar radiographic view of the right manus of a 5-year-old female ring-tailed lemur. Note the widely spread metacarpal (MC) bones and digits. Note also the medial divergence of the first MC bone as well as the thick soft tissues around the carpus, MC bones and metacarpophalangeal joints (white arrows) and an ovoid shaped ossicle (open white arrow) at the inter-phalangeal joint of the first digit.

CHAPTER 4

MORPHOLOGY OF THE PELVIS AND HIND LIMB OF THE RING-TAILED LEMUR (*LEMUR CATTA*) EVIDENCED BY GROSS OSTEOLOGY, RADIOGRAPHY AND COMPUTED TOMOGRAPHY

4.1 INTRODUCTION

The ring-tailed lemur (*Lemur catta*) is primarily distributed in south and south-western Madagascar (Budnitz and Dainis, 1975). It is classified as an endangered species by the International Union for Conservation of Nature and Natural Resources (IUCN) (IUCN, 2014).

It belongs to the order: Primata, suborder: Strepsirrhini, family: Lemuridae and genus: *Lemur* (Nowak, 1999). Strepsirrhines are characterized by retaining primitive characteristics such as a pointed muzzle, rhinarium, tapetum lucidum, bicornuate uterus, small brain case, epitheliochorial placenta, open eye sockets and prominent scent glands (Jungle, 2003; Ankel-Simons, 2007). Most of them do not look like monkeys, but rather resemble more primitive animals such as domestic cats and dogs (Ankel-Simons, 2007). Like other primates, strepsirrhines have flat nails in most of the digits, the hindlimbs are longer than the forelimbs and they have a high degree of orbital frontality (Ankel-Simons, 2007). Anatomical variations have been reported in the family

Lemuridae (Jungle, 2003). For example, the bamboo lemur (*Hapalemur*) is having a flat face, shorter muzzle and more vertical in locomotion compared to other members in the family Lemuridae (Jungle, 2003).

Due to the presence of similarities between strepsirrhines and primitive animals and anatomical variations within the family Lemuridae, it was thought to be beneficial to describe the morphology of the pelvis and hind limb of the ring-tailed lemur evidenced by gross osteology, radiography and computed tomography (CT) as a reference for clinical use and species identification.

4.2 MATERIALS AND METHODS

4.2.1 Animals

In total, 14 captive adult healthy ring-tailed lemurs from the Bristol zoo (6), UK, Johannesburg (JHB) zoo (7) and Montecasino Bird Gardens (1), Republic of South Africa (RSA) were radiographed in this study during their annual health examinations. This study was approved by the Animal Use and Care Committee (AUCC) of the University of Pretoria. Of the 14 animals, 10 were females and four were males. The age of the animals ranged from 1.4 years to 25.7 years (mean: 10.87 ± 7.6 years). The minimum weight of the animals was 2.1 kg and the maximum weight was 3.4 kg (mean: 2.97 ± 0.4 kg). There was no significant difference ($P > 0.05$) in the mean age and weight of the animals between males and females.

4.2.2 Radiography

Radiography of the pelvis and right hind limb was performed under general anaesthesia and a tabletop technique was used. In eight animals, X-ray machine EVA-HF525 (Comed Medical Systems Co. Ltd, Kyunggi, Korea) was used at a source to image distance (SID) of 95 cm. Regular speed screen type Fuji medical X-ray films (Fujifilm Corporation, Tokyo, Japan) were used in combination with RAREX green regular intensifying screens (Okamoto manufacturing Co. LTD, Tokyo, Japan). X-ray film processor model CP-345 (ELK Corporation, Tokyo, Japan) was used. All radiographs were obtained with 42 kVp and mAs ranging from 1.25–2.5 except that in one animal radiographs of the stifle and tarsus were taken using mammography films (UM-MA, Fujifilm Corporation) in combination with mamoray screens (Fujifilm Europe GmbH, Duesseldorf, Germany) at 46 kVp and 5 mAs.

In the remaining six animals, X-ray machine Roentgen 703 (GEC Medical Equipment Ltd, Middlesex, UK) was used, and images were obtained using a computed radiography (CR) unit (Regius Model 110, Konica Minolta Medical and Graphic, INC., Tokyo, Japan). All radiographs were obtained with 60 kVp and 3 mAs at a SID of 105 cm. Previous radiographs of two animals, which were taken before skeletal maturity were retrieved and examined for the location of the physes.

4.2.3 Computed tomography

Computed tomography of the hind limbs was performed in one animal, which died during the course of the study. The animal was positioned in sternal

recumbency with the hind limbs extended caudally. Computed tomography was performed using a Siemens Emotion Duo CT scanner (Siemens Medical Systems, Forchheim, Germany) at 130 kVp and 30 mAs. Transverse slices (2 mm thickness) of the right and left hind limbs from the mid-diaphysis of the right and the left femur to the distal phalanges were obtained at a pitch of 1.35 with a sharp kernel (B80s). Images were viewed using a bone window (WW=2000, WL=400) at a slice thickness of 1.25 mm. The right stifle joint was dissected after CT examination, and radiographs of the lateral meniscus and tissues in the cranial aspect of the joint (joint capsule and infrapatellar fat pad) were obtained.

4.2.4 Gross osteology

Radiographic findings were correlated with osteology specimens of an adult male ring-tailed lemur from the Ditsong National Museum, RSA, and an adult female ring-tailed lemur, which died during the course of the study.

4.2.5 Bone measurements

Bone measurements were performed on radiographic images. Maximum length was measured from proximal to distal extremities. Maximum length of long bones, sesamoids and ossicles was measured on the mediolateral (ML) view. For the lateral meniscal ossicle, maximum length was measured on the craniocaudal (CrCd) view. The CrCd and ML diameters were taken on the ML and CrCd views, respectively. For the long bones, CrCd and ML diameters were taken at the mid-diaphysis. The ML and CrCd diameters of sesamoids and ossicles were measured as a maximum diameter perpendicular to the

length. The maximum length of the phalanges, tarsal and metatarsal bones was measured on the dorsoplantar (DPl) view.

The transverse diameter of the pelvis was measured from one iliopectineal line to the other on the ventrodorsal (VD) view (O'Brien, 1978). The maximum length was measured on the VD view between two lines drawn transversely just caudal and cranial to the margins of the right ischiatic tuberosity and right cranial dorsal iliac spine, respectively. The conjugate diameter was measured from the cranial end of the pelvic symphysis to the sacral promontory on the right lateral (RL) view of the pelvis. For the os penis and os clitoridis, the length was measured as a maximum distance on either the ML view of the femur, VD or right lateral (RL) views of the pelvis. Measurements were not compensated for magnification.

4.2.6 Statistical analysis

Data were analysed using Stat View© (SAS Institute Inc., Cary, NC, USA) statistical package. The mean, range and standard deviation (SD) were calculated. The unpaired *t*-test was used to compare the difference in age, weight and pelvic measurements between males and females. Statistical significance was accepted at $P \leq 0.05$. Data are expressed as mean ± SD.

4.3 RESULTS

Radiographic measurements of bones, sesamoids and ossicles are shown in Tables 4.1–4.3.

4.3.1 Pelvis

The pelvic bone has a prominent short pelvic symphysis (Figs 4.1, 4.2, 4.3 and 4.4), and the obturator foramen is equilateral triangular with rounded angles when viewed from dorsally. The iliac crest is almost straight and thin (Figs 4.1, 4.2, 4.3 and 4.4). The caudal ventral iliac spine is well developed and prominent located just cranial to the cranial acetabular edge (Figs 4.1, 4.2, 4.3 and 4.4). The gluteal surface is more or less directed laterally (Fig. 4.2).

The ventral border of the ilium bears a flat surface just cranial to the auricular surface sloping from medial to lateral and extending to the cranial ventral iliac spine (Fig. 4.1). The middle third of the cranial half of the wing is markedly thinner than the dorsal and ventral thirds (Figs 4.1, 4.2, and 4.3). The arcuate line is more prominent (Fig. 4.1) and divides the sacropelvic surface of the body of the ilium into two almost equal medial and ventromedial surfaces. The medial surface is almost flat, while the ventromedial surface is concave (Fig. 4.1).

The pubis appears L-shaped (Fig. 4.1), and the ramus and table of the ischium are markedly narrow (Figs 4.1, 4.2, 4.3 and 4.4). The iliopubic eminence is not prominent (Figs 4.1 and 4.2). When viewed from dorsally or ventrally, the body of the ischium converges medially towards the ischiatic tuberosity (Figs 4.1 and 4.3). Each ischiatic tuberosity bears a concave depression caudolaterally (Figs 4.2 and 4.3) and the ischiatic arc is narrow

(Figs 4.1 and 4.3). The pelvic measurements were higher in females compared to males although not statistically significant ($P > 0.05$).

4.3.2 Femur

The femur is generally long and straight (Fig. 4.5). The cranial and ventral articular margins of the femoral head are more pronounced and elevated from the femoral neck (Fig. 4.6a) than dorsal and caudal articular margins (Fig. 4.6b). The caudolaterally located third trochanter is well developed and positioned slightly more distally than the minor trochanter (Fig. 4.6a,b). The major trochanter extends proximal to the femoral head (Fig. 4.6a,b). The caudomedially located minor trochanter is prominent and not connected to the major trochanter by the inter-trochanteric crest (Fig. 4.6b). The inter-trochanteric crest connects the major and third trochanters (Fig. 4.6b).

The lateral and medial ridges of the femoral trochlea converge proximally, with the lateral ridge being thicker and more elevated compared to its medial counterpart (Fig. 4.6c). The popliteal fossa is prominent, while the extensor fossa is absent (Fig. 4.6d). The lateral supracondylar tuberosity is larger and located more proximally than its medial counterpart. Articular facets for the lateral and medial sesamoids of the *M. gastrocnemius* (lateral and medial fabellae) are located just distal to the proximal border of the caudal surface of the condyles (Fig. 4.6e). A teardrop-shaped area of fat opacity is seen caudal to the distal femoral metaphysis just proximal to the lateral and medial fabellae (Fig. 4.5).

4.3.3 Stifle joint

On the ML view, the patella is similar to that of a feline species with an elongated and pointed apex. There is a tuberosity on the cranial surface of the patella (Fig. 4.7). The caudal surface of the apex slopes from caudoproximal to craniodistal (Fig. 4.7). The lateral fabella appears bulbous and elongated craniocaudally, whereas the medial fabella appears almost semicircular and rarely pentagonal or triangular (Fig. 4.7). The popliteal sesamoid bone is seen as angular or ovoid (Fig. 4.7). The distal physis of the femur and the proximal physis of the tibia appear similar to those seen in domestic cats and dogs, while the proximal physis of the fibula appears s-shaped (Fig. 4.7b).

On the CrCd view, the lateral and medial fabellae appear ovoid with the former elongated mediolaterally and the latter proximodistally (Fig. 4.8). The popliteal sesamoid bone appears ovoid (Fig. 4.8). The location of the popliteal sesamoid bone varies; on the CrCd view, it is seen superimposed on the lateral tibial condyle where it is poorly visualized (Figs 4.8 and 4.12a). On the ML view, it is mostly seen caudoproximal to the tibial condyles with its distal extremity superimposed on the tibial condyles (Figs 4.5 and 4.7a) and rarely just caudal to the inter-condylar eminence (Fig. 4.7b) or superimposed on the tibial condyles (Fig. 4.12b).

In four animals with an age range from 7.3 years to 9.3 years (mean: 8.69 ± 0.9 years), a lateral meniscal ossicle was seen (Figs 4.8, 4.9 and 4.10a). The meniscal ossicle appeared ovoid with a sclerotic margin laterally within the lateral joint space on the CrCd view (Fig. 4.8). It was not visualized on the ML

view (Fig. 4.7a). Another ossicle located laterally in the infrapatellar fat pad was seen in five animals (Figs 4.5b, 4.7a, 4.8, 4.9 and 4.10b) with an age range from 7.3 years to 22.8 years (mean: 11.51 ± 6.4 years). On the ML view, the former was mostly seen as an ovoid and rarely bean-shaped bone with a sclerotic margin in the cranial aspect of the joint (Figs 4.5b and 4.7a). On the CrCd view, it was poorly visualized due to its superimposition on the lateral femoral and tibial condyles (Fig. 4.8).

4.3.4 Tibia and fibula

The proximal extremity of the tibia bears an undivided inter-condylar eminence (Figs 4.11a and 4.12a). The facies articularis fibularis is prominent and ovoid with a convex articular surface (Fig. 4.11a). The cochlea tibia presents with an almost flat surface without an intermediate ridge (Fig. 4.11b). When viewed from distally, the facies articularis malleoli medialis is convex and nearly straight (Fig. 4.11b).

The head of the fibula bears a concave facies articularis capitis fibularis on its proximal surface. The proximal and distal thirds of the body are almost circular in cross-section, while the middle third is semicircular in cross-section. The distal end of the fibula (lateral malleolus) presents with a medial articular facet and a distomedial articular surface (Fig. 4.11c). The medial articular facet is almost flat and articulates with the fibular notch of the tibia. The distomedial articular surface, facies articularis malleoli lateralis, which articulates with the lateral surface of the talus, is slightly concave sloping from medial to lateral (Fig. 4.11c).

4.3.5 Tarsus

The tarsus consists of seven tarsal bones, namely calcaneus, talus, central tarsal bone, fourth tarsal bone (T IV), third tarsal bone (T III), second tarsal bone (T II) and first tarsal bone (T I) (Fig. 4.13). The distal row of the tarsal bones is arranged in such a manner that it is almost semicircular in transverse section (Fig. 4.13).

The trochlea of the talus presents with almost equal-sized medial and lateral ridges separated by a shallow groove. The central tarsal bone is elongated longitudinally and positioned obliquely such that the plantar surface faces plantaromedial. T III is elongated longitudinally. The height of T II is almost half that of T III. The first tarsal bone is roughly L-shaped with the distal half of the bone being elongated in a dorsoplantar direction and almost cylindrical in shape (Fig. 4.13).

4.3.6 Metatarsus and digits

There are five metatarsal bones, namely (mediolateral sequence); metatarsal (MT) bones I–V (Fig. 4.14). The first metatarsal bone is markedly stouter compared to others with a greater medial divergence from the rest of the metatarsal bones. It is positioned in such a way that the dorsal and plantar surfaces face almost medial and lateral, respectively (Fig. 4.14). There are five digits. Digit I has only proximal (P1) and distal (P3) phalanges, the middle phalanx (P2) is absent. It is shorter and stouter compared with the others (Fig. 4.14b).

4.3.7 Metatarsophalangeal and inter-phalangeal joints

Each metatarsophalangeal joint has paired ovoid (axial and abaxial) plantar proximal sesamoid bones. The axial proximal sesamoid bones of digits I, IV and V are longer than their counterparts, whereas in digits II and III, the abaxial proximal sesamoid bones are longer than their counterparts (Fig. 4.14). An inter-phalangeal ossicle was seen in digit I in all animals. The former was seen as either ovoid or crescent shaped on the DPl view of the *pes* (Fig. 4.14b).

4.3.8 Other findings

An area of mineral opacity was seen within the soft tissue of the external genitalia in female and male animals, believed to be the os clitoridis (Fig. 4.5a) and os penis (Fig. 4.5b), respectively. Spondylosis deformans was seen in two animals; in one animal between the third sacral (S3) and the first caudal (Cd1) vertebrae and between Cd1 and the second caudal vertebrae (Cd2). In the second animal it was between Cd1 and Cd2.

4.4 DISCUSSION

A well developed and prominent caudal ventral iliac spine in ring-tailed lemurs is related to the locomotor adaptation of jumping in this species (Sigmon and Farslow, 1986). The former provides attachment for a well developed and powerful *M. rectus femoris*, which is an important extensor of the stifle joint during jumping (Sigmon and Farslow, 1986). The caudal ventral iliac spine is also well developed in humans as an adaptation to erect posture whereby it

provides an attachment for powerfully developed *M. rectus femoris* aiding in balancing (Sigmon and Farslow, 1986). *M. rectus femoris* is not powerfully developed in monkeys and apes, and the caudal ventral iliac spine is not as prominent as in ring-tailed lemurs and humans (Sigmon and Farslow, 1986).

The markedly thinner area of the middle third of the cranial half of the wing of the ilium observed in this species might be a result of the presence of a stretching ligament, *Ligamentum interspinosum* (Jouffroy, 1975; Sigmon and Farslow, 1986). The latter increases the surface of the ilial wings without increasing the weight of the bone (Jouffroy, 1975) probably as an adaptation for jumping. The *Ligamentum interspinosum* attaches to the cranial ventral and caudal ventral iliac spines (Jouffroy, 1975).

An almost laterally directed gluteal surface observed in this species is similar to domestic cats and dogs (Nickel et al., 1986) but different from higher primates (Sigmon and Farslow, 1986). In the latter, the gluteal surface is directed more towards a dorsal direction as an adaptation to a postural habit of sitting or squatting (Sigmon and Farslow, 1986). The latter can be observed in ring-tailed lemurs (Rand, 1935) but not as frequently as in higher primates.

The *M. iliopsoas* is double in this species (Sigmon and Farslow, 1986) consisting of *M. psoas major* and *M. iliacus*, which inserts to the minor trochanter as in domestic cats and dogs (Nickel et al., 1986). The presence of a concave and wide ventromedial sacropelvic surface of the body of the ilium in this species is different from domestic cats and dogs. In domestic cats and

dogs, the ventromedial sacropelvic surface of the body of the ilium is smaller compared to the medial one. The *M. iliacus*, which is being accommodated in the ventromedial sacropelvic surface of the body of the ilium is powerful in this species and functions mainly as a thigh flexor (Sigmon and Farslow, 1986). The strength of this muscle is further supported by the presence of a prominent minor trochanter.

The presence of a third trochanter in this species is similar to most strepsirrhines and callitrichids (Sigmon and Farslow, 1986). The former provides insertion for *M. gluteus superficialis*. A straight femoral shaft observed in this species is a characteristic feature in strepsirrhines and monkeys (Sigmon and Farslow, 1986).

In domestic cats and dogs the extensor fossa provides the origin for the *M. extensor digitorum longus* (Nickel et al., 1986). The latter originates from the cranial border of the lateral tibial condyle, inter-osseous membrane and cranial surface of the head of the fibula in this species (Sigmon and Farslow, 1986), which explains the absence of the extensor fossa on the lateral condyle of the femur in this study. In domestic cats and dogs, the extensor fossa is a useful landmark in distinguishing the lateral and medial condyles of the femur on the ML view of the stifle joint (Comerford, 2006).

The visibility of the cranial articular margin of the femoral head on the VD view of the pelvis and CrCd view of the femur in all animals is the result of an almost perpendicular elevation of the margin from the femoral neck in this

species. The visibility of the cranial articular margin of the femoral head should not be misinterpreted as a caudolateral curvilinear osteophyte (Morgan's line) (Mayhew et al., 2002) or physeal scar (Thrall and Robertson, 2011). The cranial articular margin of the femoral head has also been observed in domestic dogs when it is presented en face to the primary beam (Gibbs, 1997).

The presence of a tuberosity on the cranial surface of the patella and the extent of its mineral opacity indicates the high strength of the *M. quadriceps femoris*. The latter is large and powerful in this species and is related to locomotor adaptation of jumping (Sigmon and Farslow, 1986).

The radiographic evidence of both medial and lateral fabellae in all animals is different from humans and domestic cats. In domestic cats, the medial fabella may not be visualised radiographically (Arnbjerg and Heje, 1993) whereas in humans, both the lateral and medial fabellae may not be visualised radiographically (Zeng et al., 2012). The medial and lateral fabellae provide the origin for the medial and lateral heads, respectively, of the *M. gastrocnemius* (Sigmon and Farslow, 1986). The two heads of the *M. gastrocnemius* are equally well developed in the ring-tailed lemur (Sigmon and Farslow, 1986). The popliteal sesamoid bone provides the origin for the *M. popliteus*.

Several functions have been postulated for sesamoid bones and cartilages such as they alter the direction of pull of certain muscles, diminish friction and

withstand pressure (Mottershead, 1988). However, the reason for their existence and exact function is debatable (Mottershead, 1988). It is most likely that sesamoid bones enable tendons in which they are associated with to become fixed to an adjacent bony area, thus allowing the particular muscle involved to act in a specialized manner at certain times and for a specific purpose (Mottershead, 1988).

The two types of ossicles seen in the stifle joint of the healthy ring-tailed lemur are normal anatomical findings in this species and should be differentiated from intra-articular calcified or ossified lesions and bone fragments from avulsion of the lateral collateral ligament and cranial cruciate ligament in the stifle joint. The presence of the sclerotic rim surrounding the ossicles in our study is similar to the radiographic appearance of the ossicle of the meniscus in humans (Bernstein et al., 1976). The sclerotic rim represents a cortical bone surrounding a trabecular bone (Bernstein et al., 1976) although this was not proven histologically in our study.

The ossicle of the meniscus has been reported to occur in species of domestic (Thrall and Robertson, 2011) and non-domestic cats (Ganey et al., 1994; Kirberger et al., 2000; Walker et al., 2002). In the Bengal tiger, the ossicle of the meniscus has been associated with running and jumping whereby the ossicle probably provides a mechanical fulcrum to accommodate the dynamic change in the shape of the meniscus during extension of the stifle (Ganey et al., 1994). The dynamic change of the shape of the meniscus distributes the load of the articulation through the meniscus, which reduces

wear and fatigue of the articular surfaces of the femur and tibia (Ganey et al., 1994). This might also be true for the ring-tailed lemur since their locomotor habit involves springing and branch running (Ankel-Simons, 2007).

The occurrence of the ossicle in the lateral meniscus and its location, observed in this study, is different from domestic cats (Whiting and Pool, 1984) in which the cranial horn of the medial meniscus is involved. The ossicle may involve the medial, lateral or both medial and lateral menisci in primates (Ganey et al., 1994). In man, intrameniscal ossicles are very unusual, and are frequently positioned in the medial meniscus compared to the lateral meniscus (Le Minor, 1990). The cause of variation in the location of the ossicle within the different species cannot be ascertained properly and warrants further research.

The presence of the ossicle in the lateral meniscus of the ring-tailed lemur has also been observed previously (Le Minor, 1990). In a study involving the morphology of the lateral meniscus, Le Minor, (1990) found that in the genus *Lemur* where 32 subjects were studied, 13 had one ossicle located at the junction of the body and the cranial horn (usual level), 11 had two ossicles, one located at the usual level and the second in the caudal horn and eight had no ossicles. However, in this study only one ossicle was seen located in the body of the lateral meniscus. To the best of our knowledge, the occurrence of an ossicle in the infrapatellar fat pad has not yet been described in healthy domestic and non-domestic animals.

The elongated appearance of the central tarsal bone in a longitudinal direction is related to the locomotor adaptation for jumping in this species. In strepsirrhines, higher values of tarsal length as a percentage of total foot length are found in *Galago*, which has an elongated calcaneus and central tarsal bones, which increase the tarsal leverage for jumping (Sigmon and Farslow, 1986). The oblique orientation of the central tarsal bone and the dorsoplantar elongation of the distal half of T I is a result of the rotation of MT I and digit I. The stoutness and medial divergence of MT I and digit I away from the rest of the digits and metatarsal bones is related to the feet being an efficient grasping tool in non-human primates (Ankel-Simons, 2007).

Variation in the longitudinal length between axial and abaxial metatarsophalangeal plantar proximal sesamoid bones of the same digit has also been observed in non-domestic cats (Kirberger et al., 2000, 2005). In non-domestic cats, the axial proximal sesamoid bones were longer than their counter parts (Kirberger et al., 2000, 2005).

In the human, the location of the inter-phalangeal ossicle directly plantar to the inter-phalangeal joint of digit I is associated with the development of anatomical, biomechanical and clinical pathologies (Roukis and Hurless, 1996). They are usually single and bilateral (Roukis and Hurless, 1996) although the presence of double ossicles has also been reported (Davies et al., 2003; Suwannahoy et al., 2012). In humans, they can be located plantarmedial, plantarlateral or plantar to the inter-phalangeal joint of the hallux and their shape varies from spherical, oval, elliptical, rectangular or

triangular (Roukins and Hurless, 1996). The frequency of inter-phalangeal ossicle in human varies greatly where it can be as high as 91% and as low as 0% (Masaki, 1984; Roukis and Hurless, 1996; Msamati and Igbigbi, 2001; Dharap et al., 2007). The presence of the inter-phalangeal ossicle in all healthy animals in this study suggests that the ossicle is a normal anatomical finding in this species. Further, studies are needed to determine the importance of the inter-phalangeal ossicle for the biomechanics of the first digit.

It was difficult in this study to obtain a true DPl view of the metatarsals and digits as a result of the curved arrangement in a transverse direction of the distal row of the tarsal bones and rotation and abduction of digit I and MT I from the rest of the digits and metatarsal bones. Further, the bone measurements obtained in this study will be slightly higher than the actual values as a result of the effect of magnification (Berry and Thrall, 2007). Spondylosis deformans, which has been observed at the sacrococcygeal and between the cranial coccygeal vertebrae in this species is most likely related to more strain exerted in this area as a result of the standing position of the tail during jumping, running and walking.

Although the pelvis and hind limb of the ring-tailed lemur shares more anatomical features with domestic cats than with dogs, it also possesses some unique anatomical features. Variations exist in the normal morphology of the pelvis and hind limb of different animal species. Knowledge of the normal morphology of the pelvis and hind limb of individual species is

important for species identification and interpretative purposes. The use of only atlases from domestic cats and dogs for interpretative purposes may be misleading.

4.5 ACKNOWLEDGEMENTS

The authors would like to thank the Organization for Women in Science for the Developing World (OWSD), Swedish International Development Cooperation Agency (SIDA), University of Pretoria, Johannesburg (JHB) and Bristol Zoos for supporting this study. Dr. Shaw Badenhorst and the Ditsong National Museum for supplying the bone specimens. Dr. Brett Gardner, Dr. Kathryn Perrin, Dr. Cheekin Lim, Ms. Fania Mohlala, sisters and animal handlers of Onderstepoort Veterinary Academic Hospital, Bristol and JHB Zoos for their assistance during CT and radiographic examinations. Montecasino Bird Gardens for permission to use their animal. Mrs. Charmaine Vermeulen and Mrs. Wilma Olivier of University of Pretoria for their assistance in preparation of figures and administrative work, respectively.

4.6 REFERENCES

Ankel-Simons, F., 2007: Primate Anatomy: An Introduction. Boston: Academic Press.

Arnbjerg, J., and N. I. Heje, 1993: Fabellae and popliteal sesamoid bones in cats. J. Small. Anim. Pract. **34,** 95–98.

Bernstein, R. M., H. E. Olsson, R. M. Spitzer, K. E. Robinson, and M. W. Korn, 1976: Ossicle of the Meniscus. Am. J. Roentgenol. **127,** 785–788.

Berry, C. R., and D. E. Thrall, 2007: Introduction to radiographic interpretation. In: Textbook of Veterinary Diagnostic Radiology (D. E. Thrall, ed.). Missouri: Saunders Elsevier. pp. 78–92.

Budnitz, N., and K. Dainis, 1975: *Lemur catta*: Ecology and behaviour. In: Lemur Biology (I. Tattersall and R. W. Sussman, eds). New York: Plenum Press. pp. 219–235.

Comerford, E. J., 2006: The stifle joint. In: BSAVA Manual of Canine and Feline Musculoskeletal Imaging (F. J. Barr and R. M. Kirberger, eds). Gloucester: BSAVA. pp. 135–149.

Davies, M. B., K. Abdlslam, and R. J. Gibson, 2003: Interphalangeal sesamoid bones of the great toe: An anatomic variant demanding careful scrutiny of radiographs. Clin. Anat. **16,** 520–521.

Dharap, A. S., H. Al-Hashimi, S. Kassab, and M. F. Abu-Hijleh, 2007: Incidence and ossification of sesamoid bones in the hands and feet: A radiographic study in an Arab population. Clin. Anat. **20,** 416–423.

Ganey, T. M., J. A. Ogden, N. Abou-Madi, B. Colville, J. M. Zdyziarski, and J. H. Olsen, 1994: Meniscal ossification II. The normal pattern in the tiger knee. Skeletal. Radiol. **23,** 173–179.

Gibbs, C., 1997: The BVA/KC scoring scheme for control of hip dysplasia: interpretation of criteria. Vet. Rec. **141,** 275–284.

IUCN, 2014: IUCN Red List of Threatened Species. Version 2014.3. Available at: http://www.iucnredlist.org (accessed on 18 November 2014).

Jouffroy, F. K., 1975: Osteology and Myology of the Lemuriform Postcranial Skeleton. In: Lemur Biology (I. Tattersall and R. W. Sussman, eds). New York: Plenum Press. pp. 149–192.

Jungle, R. E., 2003: Prosimians. In: Zoo and Wild Animal Medicine (M. E. Fowler and R. E. Miller, eds). Missouri: Saunders. pp. 334–346.

Kirberger, R. M., W. M. du Plessis, and P. H. Turner, 2005: Radiologic anatomy of the normal appendicular skeleton of the lion (*Panthera leo*). Part 2: Pelvic limb. J. Zoo. Wildl. Med. **36,** 29–35.

Kirberger, R. M., H. B. Groenewald, and W. M. Wagner, 2000: A radiological study of the sesamoid bones and Os meniscus of the cheetah (*Actinonyx jubatus*). Vet. Comp. Orthopaed. **13,** 172–177.

Le Minor, J. M., 1990: Comparative morphology of the lateral meniscus of the knee in primates. J. Anat. **170,** 161–171.

Masaki, T., 1984: An anatomical study of the interphalangeal sesamoid bone of the hallux. Nihon. Seikeigeka. Gakkai. Zasshi. **58,** 419–-27.

Mayhew, P. D., P. J. McKelvie, D. N. Biery, F. S. Shofer, and G. K. Smith, 2002: Evaluation of a radiographic caudolateral curvilinear osteophyte

on the femoral neck and its relationship to degenerative joint disease and distraction index in dogs. J. Am. Vet. Med. Assoc. **220,** 472–476.

Mottershead, S., 1988: Sesamoid bones and cartilages: An enquiry into their function. Clin. Anat. **1,** 59–62.

Msamati, B. C., and P. S. Igbigbi, 2001: Radiographic appearance of sesamoid bones in the hands and feet of Malawian subjects. Clin. Anat. **14,** 248–253.

Nickel, R., A. Schummer, E. Seiferle, J. Frewein, H. Wilkens, and K. H. Wille, 1986: The Anatomy of the Domestic Animals Vol. 1. Berlin: Springer-Verlag.

Nowak, R. M., 1999: Order Primate. In: Walker's Mammals of the World (R. M. Nowak, ed.). Baltimore: The Johns Hopkins University Press. pp. 490–631.

O'Brien, T., 1978: Normal radiographic anatomy of the abdomen. In: Radiographic Diagnosis of Abdominal Disorders in the Dog and Cat (T. O' Brien, ed.). Philadelphia: W. B. Saunders Company. pp. 9–47.

Rand, A. L., 1935: On the habits of some Madagascar Mammals. J. Mammal. **16,** 89–104.

Roukis, T. S., and J. S. Hurless, 1996: The hallucal interphalangeal sesamoid. J. Foot. Ankle. Surg. **35,** 303–308.

Sigmon, B. A., and D. L. Farslow, 1986: The Primate Hind limb. In: Comparative Primate Biology Vol. 1: Systematics, Evolution, and Anatomy (D. R. Swindler and J. Erwin, eds). New York: Alan R. Liss, Inc. pp. 671–718.

Suwannahoy, P., T. Srisuwan, N. Pattamapaspong, and P. Mahakkanukrauh, 2012: Intra-articular ossicle in interphalangeal joint of the great toe and clinical implication. Surg. Radiol. Anat. **34,** 39–42.

Thrall, D. E., and I. D. Robertson, 2011: Atlas of Normal Radiographic Anatomy and Anatomic Variants in the Dog and Cat. Missouri: Elsevier Saunders.

Walker, M., D. Phalan, J. Jensen, J. Johnson, M. Drew, V. Samii, G. Henry, and J. McCauley, 2002: Meniscal ossicles in large non-domestic cats. Vet. Radiol. Ultrasound. **43,** 249–254.

Whiting, P. G., and R. R. Pool, 1984: Intrameniscal calcification and ossification in the stifle joints of three domestic cats. J. Am. Anim. Hosp. Assoc. **21,** 579–584.

Zeng, S., X. Dong, R. Dang, G. Wu, J. Wang, D. Wang, H. Huang, X. Guo, X. Dong, and R. Dang, 2012: Anatomic study of fabella and its surrounding structures in a Chinese population. Surg. Radiol. Anat. **34,** 65–75.

4.7 TABLES

Table 4.1 Radiographic measurements (cm) not compensated for magnification of the pelvis, os penis, os clitoris and long bones of the right hind limb in healthy captive ring-tailed lemurs

Bone	Variable	Number of animals	Mean ± SD (cm)	Range (cm)
Pelvis	Length	12	9.07 ± 0.27	8.38 – 9.40
	Conjugate diameter	13	4.84 ± 0.24	4.25 – 5.22
	Transverse diameter	13	3.36 ± 0.11	3.20 – 3.50
Os penis	Length	4	1.40 ± 0.14	1.22 – 1.56
Os clitoridis	Length	6	0.38 ± 0.06	0.29 – 0.48
Femur	Length	10	14.46 ± 0.28	14.02 – 14.90
	ML diameter	12	0.88 ± 0.03	0.85 – 0.94
	CrCd diameter	10	0.92 ± 0.03	0.87 – 0.98
Tibia	Length	11	13.73 ± 0.32	13.25 – 14.20
	ML diameter	9	0.70 ± 0.03	0.65 – 0.74
	CrCd diameter	11	0.91 ± 0.05	0.85 – 1.00
Fibula	Length	11	12.84 ± 0.42	12.10 – 13.30
	ML diameter	10	0.34 ± 0.04	0.30 – 0.42
	CrCd diameter	11	0.37 ± 0.04	0.32 – 0.40

ML, mediolateral

CrCd, craniocaudal

Table 4.2 Radiographic measurements (cm) not compensated for magnification of sesamoid bones and ossicles of the right hind limb in healthy captive ring-tailed lemurs

Sesamoid/ossicle	Variable	Number of animals	Mean ± SD (cm)	Range (cm)
Patella	Length	11	1.71 ± 0.07	1.63 – 1.80
	ML diameter	7	0.90 ± 0.06	0.81 – 0.98
	CrCd diameter	11	0.59 ± 0.05	0.51 – 0.66
Lateral fabella	Length	11	0.34 ± 0.03	0.30 – 0.40
	ML diameter	8	0.47 ± 0.03	0.42 – 0.50
	CrCd diameter	11	0.44 ± 0.07	0.35 – 0.55
Medial fabella	Length	11	0.47 ± 0.05	0.41 – 0.60
	ML diameter	11	0.38 ± 0.03	0.33 – 0.45
	CrCd diameter	11	0.35 ± 0.03	0.30 – 0.40
Popliteal	Length	8	0.28 ± 0.09	0.17 – 0.40
	ML diameter	6	0.33 ± 0.03	0.30 – 0.37
	CrCd diameter	7	0.22 ± 0.03	0.19 – 0.25
Meniscal ossicle	Length	4	0.25 ± 0.04	0.20 – 0.30
	ML diameter	4	0.16 ± 0.05	0.10 – 0.20
Infrapatella fat pad ossicle	Length	5	0.23 ± 0.04	0.20 – 0.30
	ML diameter	3	0.32 ± 0.1	0.20 – 0.40
	CrCd diameter	5	0.17 ± 0.03	0.15 – 0.20
Inter-phalangeal ossicle	Length	12	0.21 ± 0.04	0.16 – 0.30
	ML diameter	12	0.43 ± 0.05	0.33 – 0.50

ML, mediolateral

CrCd, craniocaudal

Table 4.3 Radiographic measurement (cm) not compensated for magnification of short bones of the right hind limb in healthy captive ring-tailed lemurs

Bone	Number of animals	Length (Mean ± SD) cm	Range (cm)
Calcaneus	12	2.67 ± 0.13	2.50 – 2.90
Talus	12	1.69 ± 0.05	1.60 – 1.77
Central tarsal bone	12	1.19 ± 0.08	1.08 – 1.30
T I	12	0.84 ± 0.09	0.70 – 0.96
T II	12	0.46 ± 0.04	0.40 – 0.50
T III	12	0.93 ± 0.11	0.80 – 1.1800
T IV	12	0.99 ± 0.07	0.87 – 1.10
MT I	12	2.83 ± 0.12	2.70 – 3.04
MT II	12	3.09 ± 0.15	2.90 – 3.37
MT III	12	3.10 ± 0.14	2.90 – 3.32
MT IV	12	3.13 ± 0.12	2.90 – 3.30
MT V	12	3.10 ± 0.16	2.80 – 3.32
P1 of digit I	12	1.50 ± 0.08	1.30 – 1.63
P1 of digit II	11	1.82 ± 0.10	1.62 – 1.92
P1 of digit III	10	1.97 ± 0.09	1.76 – 2.11
P1 of digit IV	10	2.12 ± 0.11	1.92 – 2.28
P1 of digit V	11	1.76 ± 0.08	1.60 – 1.91
P2 of digit II	10	1.01 ± 0.08	0.90 – 1.10
P2 of digit III	10	1.24 ± 0.08	1.11 – 1.32
P2 of digit IV	10	1.36 ± 0.08	1.24 – 1.46
P2 of digit V	11	1.11 ± 0.06	1.03 – 1.20
P3 of digit I	11	0.91 ± 0.03	0.87 – 0.97
P3 of digit II	9	0.59 ± 0.07	0.50 – 0.70
P3 of digit III	8	0.57 ± 0.04	0.50 – 0.60
P3 of digit IV	8	0.54 ± 0.03	0.50 – 0.60
P3 of digit V	10	0.49 ± 0.06	0.40 – 0.59

T, tarsal; M, metatarsal; P1, proximal phalanx; P2, middle phalanx; P3, distal phalanx

4.8 FIGURES

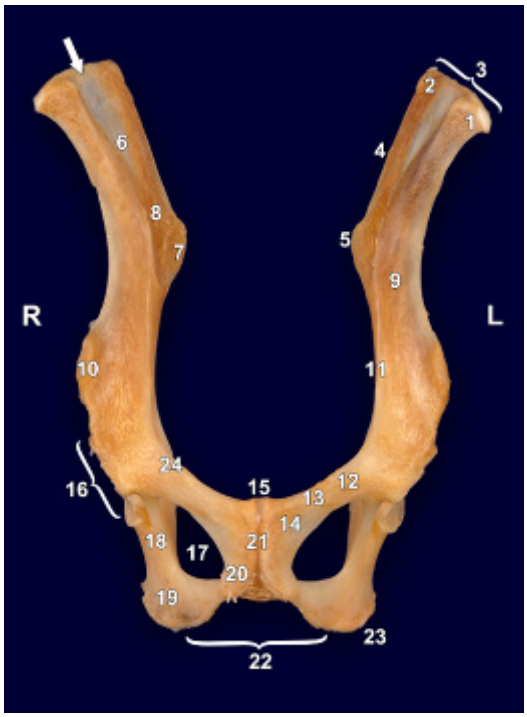

Fig. 4.1 Ventral view of an anatomical specimen of the pelvic bone of an adult male ring-tailed lemur. Note the presence of the thinner area in the middle third of the cranial half of the wing (arrow). (1) Cranial ventral iliac spine, (2) cranial dorsal iliac spine, (3) crest of ilium, (4) wing of ilium, (5) caudal dorsal iliac spine, (6) iliac surface, (7) auricular surface, (8) iliac tuberosity, (9) body of ilium, (10) caudal ventral iliac spine, (11) arcuate line, (12) pubic body, (13) cranial branch of pubis, (14) caudal branch of pubis, (15) pecten of pubic bone (16) acetabulum, (17) obturator foramen, (18) ischiatic body, (19) ischiatic table, (20) ischiatic branch, (21) symphysis pelvis, (22) ischiatic arch, (23) ischiatic tuberosity and (24) iliopubic eminence, (R) right, (L) left.

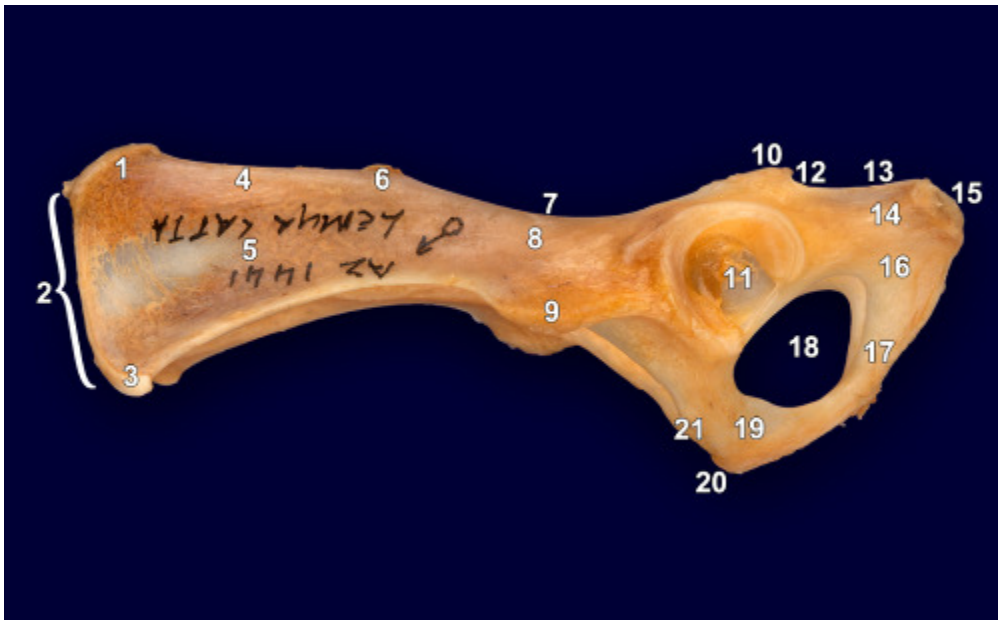

Fig. 4.2 Left lateral view of an anatomical specimen of the pelvic bone of an adult male ring-tailed lemur. Note the straight appearance of the iliac crest, ventral projection of the caudal ventral iliac spine from the body of ilium, prominent groove for the *M. obturatorius internus*, absence of psoas minor tubercle and the presence of the thinner area in the middle third of the cranial half of the wing. (1) Cranial dorsal iliac spine, (2) crest of ilium, (3) cranial ventral iliac spine, (4) wing of ilium, (5) gluteal surface, (6) caudal dorsal iliac spine, (7) greater ischiatic notch, (8) body of ilium, (9) caudal ventral iliac spine, (10) ischiatic spine, (11) acetabulum, (12) groove for the tendon of the *M. obturatorius internus*, (13) lesser ischiatic notch, (14) ischiatic body, (15) ischiatic tuberosity, (16) ischiatic table, (17) ischiatic branch, (18) obturator foramen, (19) pubic bone, (20) pecten of pubic bone and (21) iliopubic eminence.

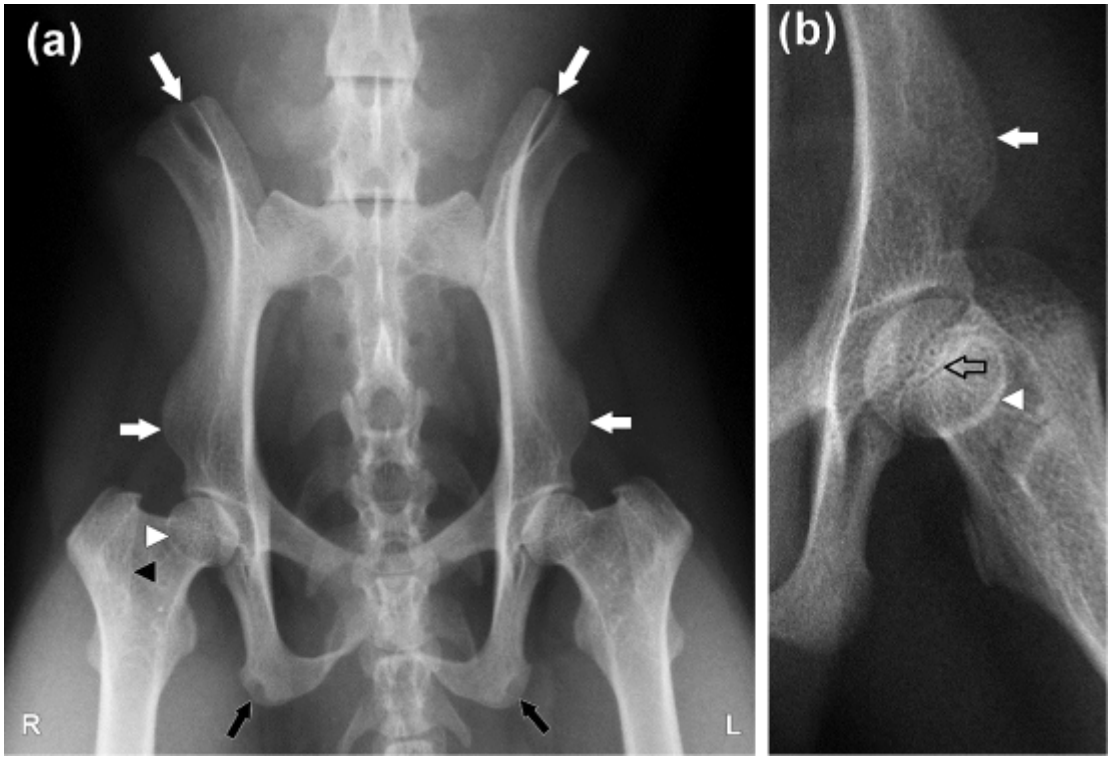

Fig. 4.3 Ventrodorsal radiographs of the pelvis (a) and left hip joint (b) of 9-year-old female (a) and 9-month-old male (b) ring-tailed lemurs. Note the presence of the wedge and ovoid radiolucent areas on each ilial wing (long white arrows) and ischial tuberosity (black arrows), respectively (a). The minor and third trochanters are prominent (a). The inter-arcuate spaces between caudal lumbar vertebrae, lumbosacral, sacrococcygeal and cranial coccygeal vertebrae are wide and ovoid (a). Note the visualisation of the cranial articular margin of the femoral head (white arrow heads), edge of the major trochanter (black arrow head), caudal ventral iliac spine (short white arrows) and zigzag appearance of the physis of the femoral head (open black arrow). (L) left, (R) right.

Fig. 4.4 Right lateral radiograph of the pelvis of a 3.7-year-old female ring-tailed lemur. Crests of the ilia are straight (arrow heads) and caudal ventral iliac spine project ventrally from the body of each ilium (arrow). Note the ovoid superimposed obturator foramina and very short ventral pelvic floor.

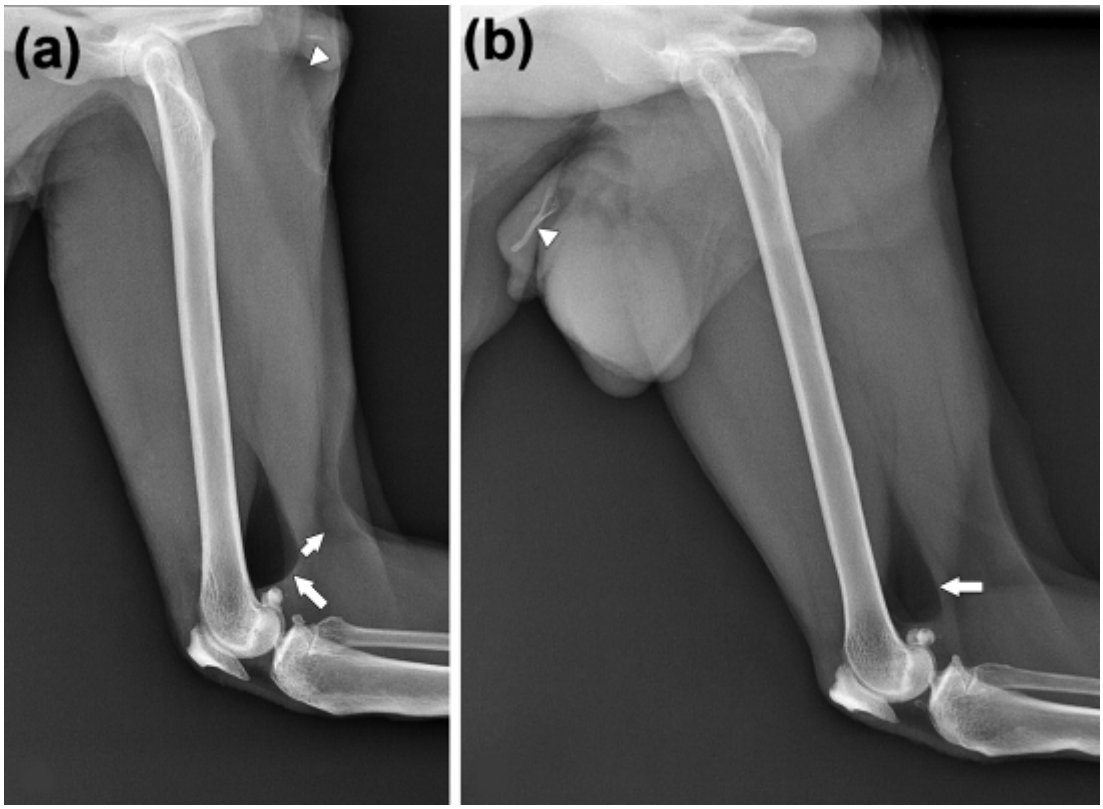

Fig. 4.5 Mediolateral radiographs of the right femur of a 25.7 (a) and 22.8 (b) year-old female and male ring-tailed lemur, respectively. The femur appears long, straight and slender similar to the domestic cat. A prominent teardrop-shaped (long white arrow) area of fat opacity is seen caudal to the femur just proximal to the lateral and medial fabellae (a, b). Areas of mineral opacity (arrow heads) seen in external genital organs are believed to be os clitoridis (a) and os penis (b). The visualization of the popliteal lymph node is indicated by a short white arrow (a). Note the variations in thickness of the cranial and caudal diaphyseal cortices between (a) and (b) which may be related to differences in activity level.

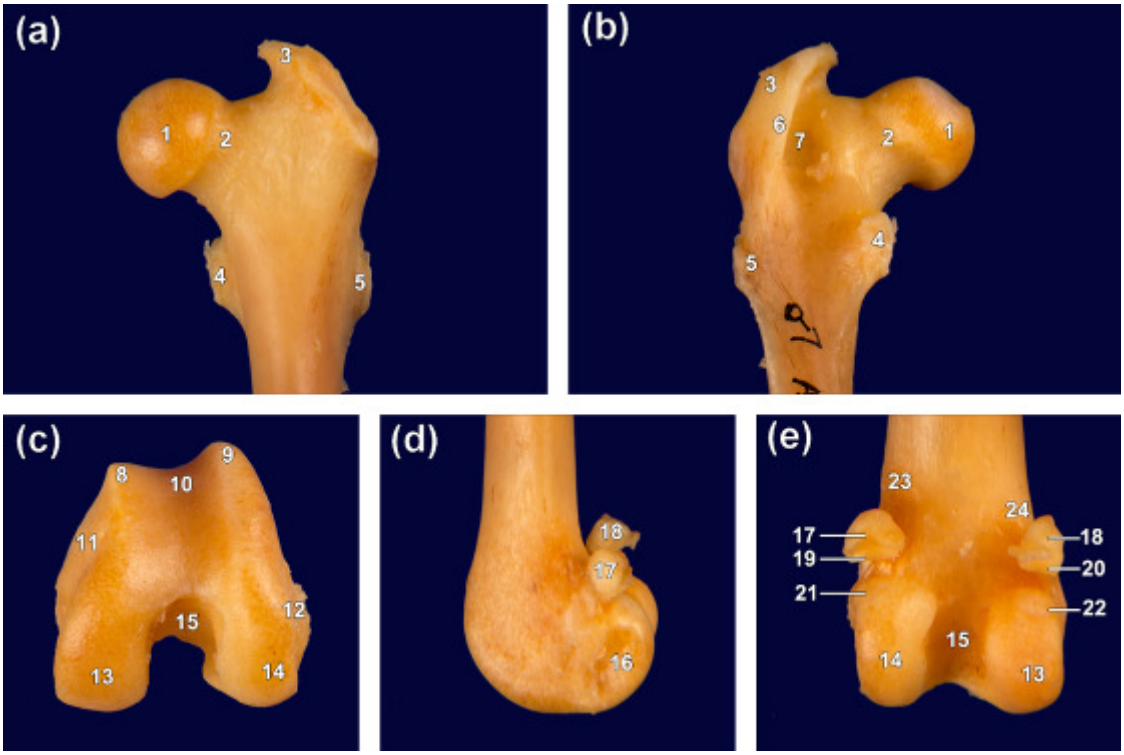

Fig. 4.6 Cranial (a), caudal (b) and distal (c), lateral (d), caudal (e) views of the proximal and distal anatomical specimen of left femur of an adult male ring-tailed lemur, respectively. (1) Head, (2) neck, (3) major trochanter, (4) minor trochanter, (5) third trochanter, (6) inter-trochanteric crest, (7) trochanteric fossa, (8) medial ridge, (9) lateral ridge, (10) trochlea, (11) medial epicondyle, (12) lateral epicondyle, (13) medial condyle, (14) lateral condyle, (15) inter-condylar fossa, (16) popliteal fossa, (17) lateral fabella, (18) medial fabella, (19) articular surface of the lateral fabella, (20) articular surface of the medial fabella, (21) facies articularis sesamoidea lateralis, (22) facies articularis sesamoidea medialis, (23) lateral supracondylar tuberosity and (24) medial supracondylar tuberosity.

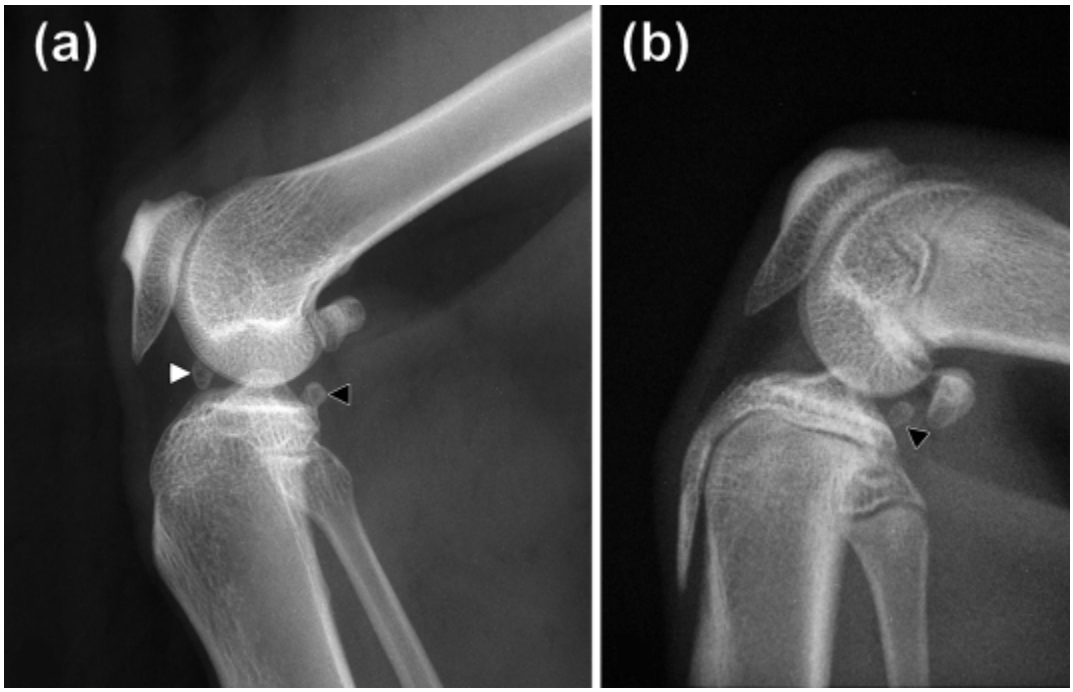

Fig. 4.7 Mediolateral radiographs of the right stifle joint of 7.3-year-old-female (a) and 9-month-old male (b) ring-tailed lemurs. Note the presence of a tuberosity on the cranial surface of the patella and the sloping of the caudal surface of the apex from proximocaudal to craniodistal (a, b). Note the presence of a popliteal sesamoid bone (black arrow heads) and a bean-shaped ossicle in the infrapatellar fat pad (white arrow head). Note the bulbous and semicircular superimposed lateral and medial fabellae, respectively. Note also a concave facies articularis capitis fibulae (a). Note the location further distally of the fibular head (a), which is almost similar to domestic cats. Note also the similar zig-zag-shaped appearance of the distal femoral and tibial physes as in domestic cats and dogs and the s-shaped proximal fibula physis (b).

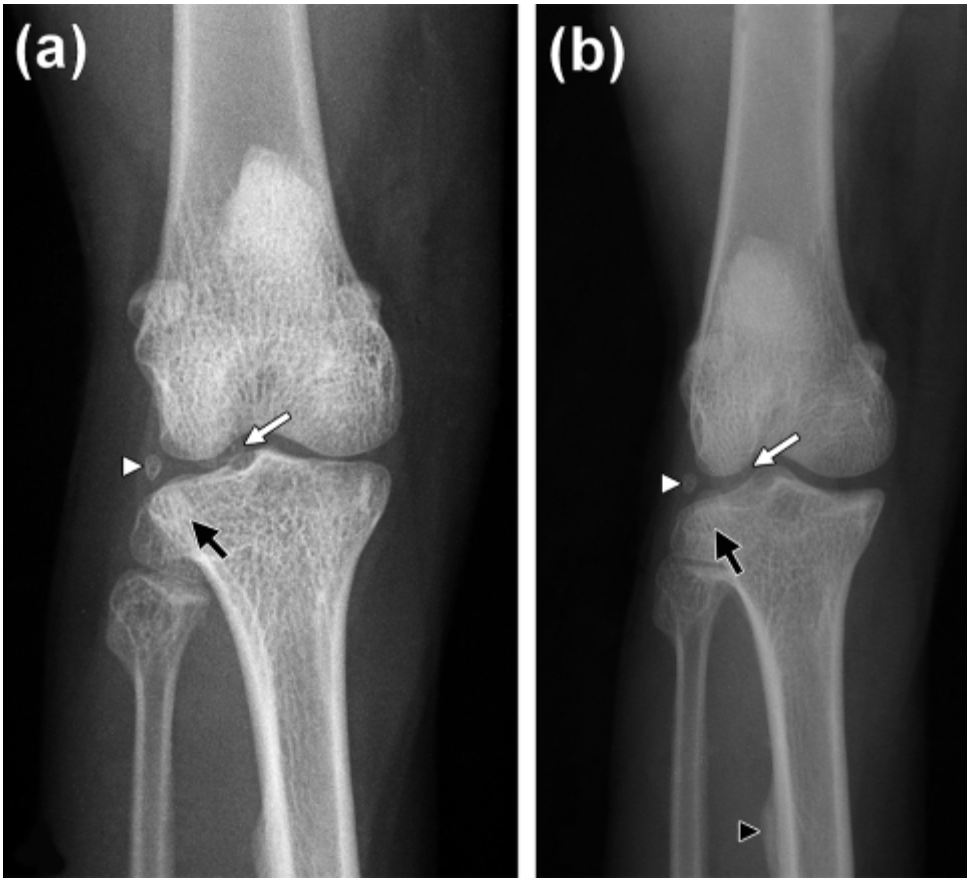

Fig. 4.8 Craniocaudal radiographs (a, b) of the right stifle joint of a 7.3-year-old-female ring-tailed lemur. (b) Exposure factors have been reduced. An ovoid ossicle in the infrapatellar fat pad (white arrow) is poorly visualized due to its superimposition on the lateral femoral and tibial condyles (a, b). Note the presence of an ovoid lateral meniscal ossicle (white arrow head) laterally within the lateral joint space and the poorly visualized ovoid popliteal sesamoid bone (black arrow) superimposed on the lateral tibia subchondral bone (a, b). Note also the lateral projection of the area for attachment of the semitendinosus muscle (b) indicated by a black arrow head. The concavity seen on the lateral aspect of the lateral condyle represents the popliteal fossa (a, b).

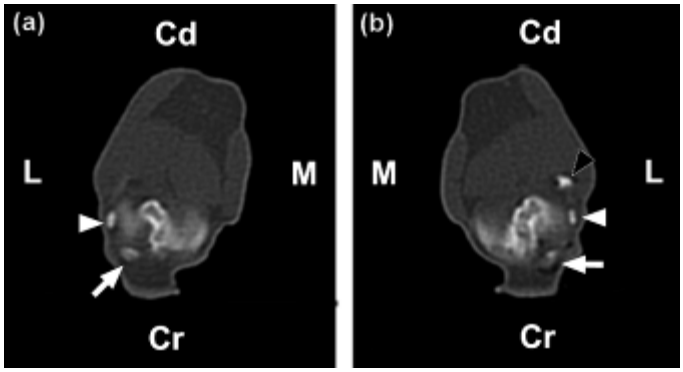

Fig. 4.9 Transverse CT images of the left (a) and right (b) stifle joints of the same animal as in Figs 7a and 8 at the level of the joint space displayed at a WW 2000, WL 400 using a sharp kernel (B80s). Note the visualisation of the lateral meniscal ossicle (white arrow head), popliteal sesamoid bone (black arrow head) and an ossicle in the infrapatellar fat pad (white arrow). (Cr) Cranial, (Cd) caudal, (M) medial, (L) lateral.

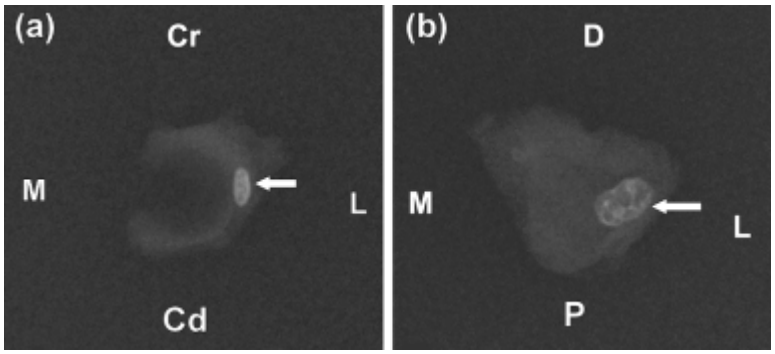

Fig. 4.10 Proximodistal (a) and CrCd (b) radiographs of the right lateral meniscus (a) and tissues in the cranial aspect of the right stifle joint (joint capsule and infrapatellar fat pad) (b) of the same animal as in Figs 7a and 8. Note the presence of ovoid ossicles (arrow) with a trabecular pattern surrounded by a sclerotic margin (a, b). Note also the location of the ossicle in the body of the lateral meniscus (a). (Cr) Cranial, (Cd) caudal, (D) distal, (P) proximal, (M) medial, (L) lateral.

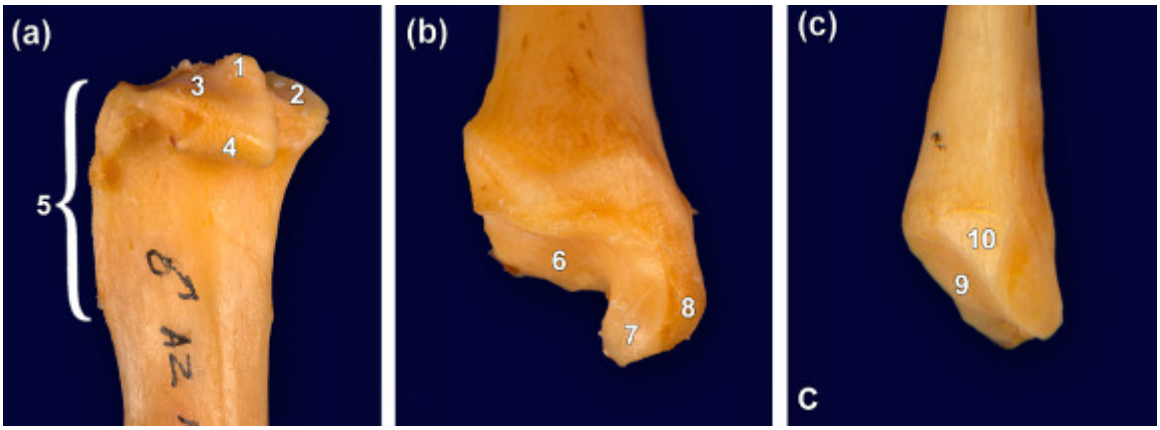

Fig. 4.11 (a) Caudolateral (b) cranial and (c) craniomedial views of an anatomical specimen of the left proximal tibia, right distal tibia and left distal fibula, respectively, of an adult ring-tailed lemur. (1) Intercondylar eminence, (2) medial condyle, (3) lateral condyle, (4) facies articularis fibularis, (5) tibial tuberosity, (6) cochlea tibia, (7) facies articularis malleoli medialis, (8) medial malleolus, (9) facies articularis malleoli lateralis and (10) articular surface for the fibular notch of the tibia.

Fig. 4.12 Craniocaudal (a) and mediolateral (b) radiographs of the right tibia and fibula of 4.8-year-old male and 3.7-year-old-female ring-tailed lemurs, respectively. Note the straight appearance of the bones and wide inter-osseous space, which is similar to domestic cats (a, b). The lateral projection of the area for attachment of the *M. semitendinosus* (white arrow head) is different from domestic cats and dogs (a). Similar to domestic cats the tibial tuberosity is not prominent (b). Note also the location of the popliteal sesamoid (black arrow head) in the area of the lateral joint space (a) and its superimposition on the caudo-proximal aspect of tibial condyles (b). Note the uniform thickness of the fibular diaphysis (a, b).

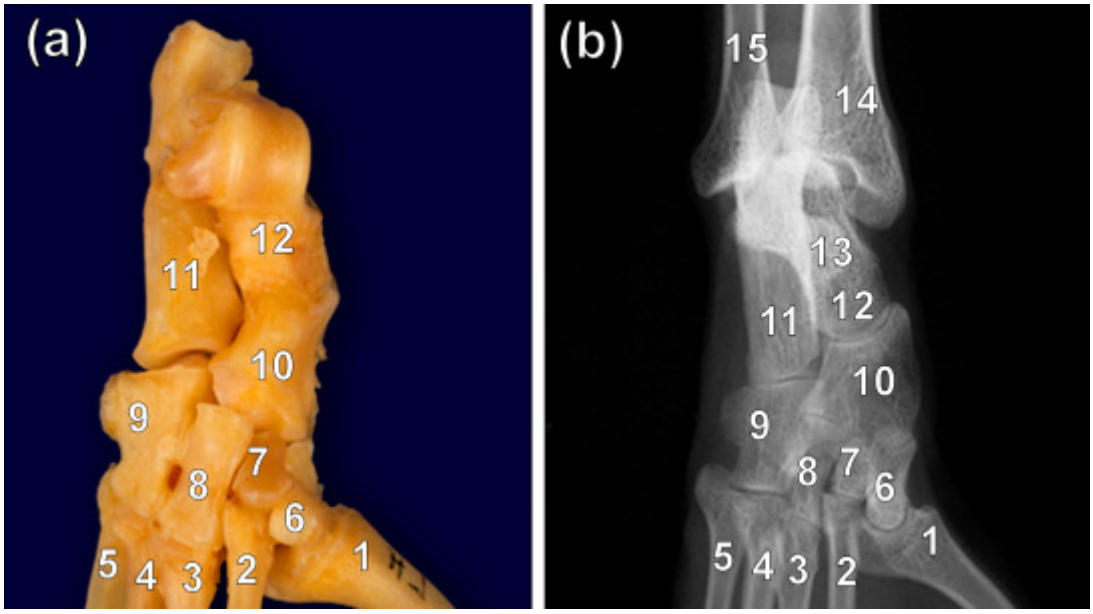

Fig. 4.13 Dorsal view of an anatomical specimen of the left tarsus of an adult ring-tailed lemur (a). Dorsoplantar radiograph of the right tarsus of a 7.3-year-old female ring-tailed lemur (b). The tarso-crural joint is flat and facies articularis malleoli lateralis slopes from medial to lateral (b). Note also the appearance of the tarsocrural joint (b), which is very similar to domestic cats. Note the proximodistal elongation of the central tarsal bone (a, b). (1) MT I, (2) MT II, (3) MT III, (4) MT IV, (5) MT V, (6) T I, (7) T II, (8) T III, (9) T IV, (10) central tarsal bone, (11) calcaneus, (12) talus, (13) *Sustentaculum tali* superimposed on the talus, (14) tibia and (15) fibula.

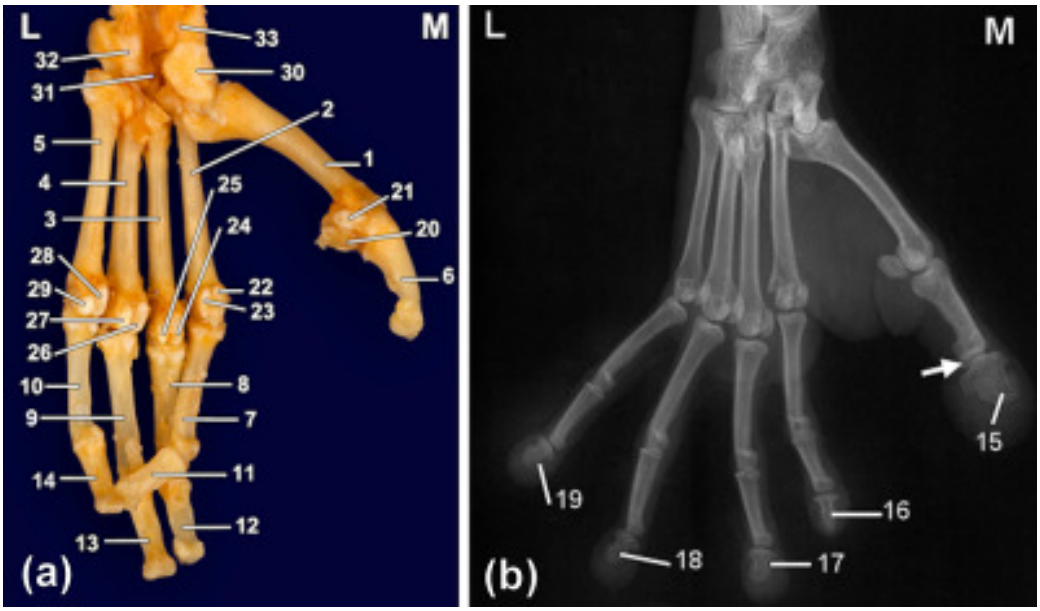

Fig. 4.14 (a) Plantar view of an anatomical specimen of the left MT and digits of an adult ring-tailed lemur. (b) Oblique radiograph of the right MT and digits of a 7.3-year-old female ring-tailed lemur obtained from the DPI view of the tarsus. Note the stoutness and medial divergence of the MT I and digit I from the rest of the MT and digits. The shorter abaxial and axial plantar proximal sesamoid bones of digit I, IV, V and digit II, III, respectively, compared to their counterparts. An inter-phalangeal ossicle on the plantar aspect of the inter-phalangeal joint of digit I is indicated by an arrow (b). (1) MT I, (2) MT II, (3) MT III, (4) MT IV, (5) MT V, (6) P1 of digit I, (7) P1 of digit II, (8) P1 of digit III, (9) P1 of digit IV, (10) P1 of digit V, (11) P2 of digit II, (12) P2 of digit III, (13) P2 of digit IV, (14) P2 of digit V, (15) P3 of digit I, (16) P3 of digit II, (17) P3 of digit III, (18) P3 of digit IV, (19) P3 of digit V, (20) axial sesamoid bone of digit I, (21) abaxial sesamoid bone of digit I, (22) abaxial sesamoid bone of digit II, (23) axial sesamoid bone of digit II, (24) abaxial sesamoid bone of digit III, (25) axial sesamoid bone of digit III, (26) axial sesamoid bone of digit IV, (27) abaxial sesamoid bone of digit IV, (28) axial sesamoid bone of digit V, (29) abaxial sesamoid bone of digit V, (30) T I, (31) T III, (32) T IV and (33) central tarsal bone.

CHAPTER 5

RADIOGRAPHIC THORACIC ANATOMY OF THE RING-TAILED LEMUR (*LEMUR CATTA*)

5.1 INTRODUCTION

The ring-tailed lemur (*Lemur catta*) is classified as an endangered species by the International Union for Conservation of Nature and Natural Resources (IUCN) (IUCN, 2014). It belongs to the suborder Strepsirrhini (Nowak, 1999). Strepsirrhines are characterised by retaining primitive characteristics such as bicornuate uterus, pointed muzzle, rhinarium, small brain case, tapetum lucidum, epitheliochorial placenta, prominent scent glands and open eye sockets (Jungle, 2003; Ankel-Simons, 2007).

In *Lemurs*, the trachea has complete cartilaginous rings and the principal bronchi are relatively short with the right being shorter than the left (Patten, 1899). Each lung is conical in shape with the apex being more pointed than that of the human lungs (Patten, 1899). The apex does not protrude past the thoracic inlet into the root of the neck. It only reaches to the level of the caudal border of the first costal arch (Patten, 1899). The left lung is divided into two lobes i.e. cranial and caudal lobes. The cranial lobe is larger than the caudal lobe. The former is incompletely subdivided by a short fissure into cranial and caudal parts (Patten, 1899). The right lung consists of four lobes; cranial, middle, caudal and accessory lobes (Patten, 1899).

Radiography is commonly performed on primates and several authors have documented the normal radiographic anatomy of the thorax in primates, which provides a reference for diagnosis of disease (Silverman and Morgan, 1980; Wagner and Kirberger, 2005; Schillaci et al., 2008; 2009; Brining et al., 2010; Alves et al., 2012; Young et al., 2013). Various thoracic diseases have been reported in ring-tailed lemurs such as pneumonia (Hamerton, 1943; Tuten et al., 2011), tuberculosis (Schmidt, 1975), hydatidosis (Kondo et al., 1996), neoplasia (Pye et al., 2000), pleural effusions (Jungle, 2003), lung atelectasis (Palotay and Uno, 1975), encephalomyocarditis virus infection (Canelli et al., 2010) and sudden acute respiratory distress syndrome (MB personal communication).

This study was performed to describe the normal radiographic thoracic anatomy of the ring-tailed lemur as a species specific reference. To the best of the authors' knowledge, this has not been published previously.

5.2 MATERIALS AND METHODS

5.2.1 Animals

A total of 15 captive ring-tailed lemurs from the Bristol zoo (6), United Kingdom (UK), Johannesburg zoo (8) and Montecasino Bird Gardens (1), South Africa (SA) were radiographed during their annual health examinations. Animals were considered healthy based on history, physical and clinical examinations, haematological evaluation, faecal examination and kidney and liver function tests. The age of the animals ranged from 1.40 years to 25.70

years (mean: 10.34 ± 7.63 years). The minimum and maximum weights of the animals were 2.10 kg and 3.44 kg respectively, (mean: 2.92 ± 0.42 kg). Of the 15 animals, 10 were females and five were males. There was no significant difference in the mean age (P = 0.39) and weight (P = 0.08) between males and females. This study was approved by the Bristol Zoo Gardens Research Committee and Animal Use and Care Committee (AUCC) of the University of Pretoria.

5.2.2 Radiography

Radiography of the thorax was performed under general anaesthesia. Animals were fasted for 8 to 12 hours but water was given *ad libitum* until shortly before general anaesthesia. Anaesthesia was induced either by isoflurane (IsoFlo, Abbott Laboratories Ltd., Berkshire, UK) via a mask or by intramuscular injection of medetomidine hydrochloride (Domitor, Pfizer Laboratories Ltd., Sandton, SA) and ketamine hydrochloride (Kyron Laboratories Ltd., Benrose, SA) combination. All animals were intubated and anaesthesia maintained with isoflurane (IsoFlo, Abbott Laboratories Ltd., Berkshire, UK: Isofor, Safe Line Pharmaceuticals Ltd., Roodepoort, SA).

Right lateral (RL) and dorsoventral (DV) radiographic views of the thorax were taken at the end of inspiration using a table-top technique. The forelimbs were positioned cranially for the RL view. For the DV view, the forelimbs were pulled cranially in 4/15 animals, whereas in 11/15 animals the elbows were positioned to either side of the thorax.

Radiographs were made using either a Roentgen 703 (GEC Medical Equipment Ltd., Middlesex, UK) or EVA-HF525 (Comed Medical System Co. Ltd., Kyunggi, Korea). In the former, a source to image distance (SID) of 105 cm was used with 60 kVp and 3 mAs (100 mA and 0.03 s). Images were obtained using a computed radiography (CR) unit Regius Model 110 (Konica Minolta Medical and Graphic INC., Tokyo, Japan).

With the EVA-HF525, a SID of 95 cm was used. Medium speed screen type films (Fujifilm Corporation, Tokyo, Japan) were used in combination with RAREX green regular intensifying screens (Okamoto manufacturing Co. Ltd., Tokyo, Japan). An exposure of 46 kVp and 1.25 mAs (25 mA and 0.05 s) was used with an automatic x-ray film processor model CP-345 (ELK Corporation, Tokyo, Japan).

5.2.3 Evaluation

The height (Fig. 5.1) of the thoracic vertebrae and sternebrae was measured on the RL view along a line that extended between the cranioventral and craniodorsal borders of the vertebral bodies and sternebrae (Nelson et al., 2011). The length (Fig. 5.1) of the thoracic vertebrae and sternebrae was measured on the RL view from the mid-point of the cranial end plate to the mid-point of the caudal end plate (Nelson et al., 2011). The depth of the thorax (TDp) (Fig. 5.1) was measured on the RL view from the dorsocaudal border of the last sternebra (sternebra four or five) to the closest edge of the vertebral column (Litster and Buchanan, 2000). The width of the thorax (TW)

(Fig. 5.2) was measured on the DV view as the maximum distance between the left and right pleural surfaces of the seventh ribs.

The visibility, shape and location of thoracic organs were recorded. The vertebral heart score (VHS) was measured on the DV and RL views (Figs 5.1 and 5.2) as previously described in dogs (Buchanan and Bücheler, 1995). The angle of cardiac inclination (ACI) was measured as the angle formed between the right cardiac border and the sternum (Fig. 5.1) on the RL view (Alves et al., 2012). The maximum diameter of the caudal vena cava (CVC) and aorta was measured on the RL view caudal to the cardiac silhouette and cranial to the diaphragm. The diameter of the CVC was also compared to that of the aorta and the length of the thoracic vertebral body (VL) above the tracheal bifurcation (Lehmkuhl et al., 1997).

The ratio of the tracheal diameter (TD) to thoracic inlet diameter (TID) was calculated on the RL view (Hayward et al., 2008). The TID was measured from the ventral aspect of the vertebral column at the midpoint of the most cranial rib to the dorsal surface of the manubrium at its point of minimal thickness (Fig. 5.1). The TD (Fig. 5.1) was measured between the internal surfaces of the tracheal wall perpendicular to the tracheal long axis at the point where the thoracic inlet distance crosses the midpoint of the tracheal lumen (Hayward et al., 2008).

The location of the carina with respect to thoracic vertebra was determined on the RL and DV views. In cases where the carina was not visible on the RL

view, the crossing point of the mainstem bronchi was used to locate its position. The angle between the mainstem bronchi (MSB) was measured on the DV view as the angle of divergence between the caudal borders of the left and right mainstem bronchi (Haskin and Goodman, 1982). The crossing point of the diaphragmatic crura/crus to the thoracic or lumbar vertebra on the RL view was recorded in relationship to the cranial thoracic vertebrae during inspiration.

5.2.4 Data analysis

Data was analysed using STAT VIEW® statistical package (SAS Institute, Cary, NC, USA). Mean, range and standard deviation were calculated. Student t-test was used to compare the mean age and weight between male and female animals as well as means of VHS on RL view versus DV view. Statistical significance was accepted at $P \leq 0.05$. Data is expressed as mean ± SD.

5.3 RESULTS

Patient positioning was better with forelimbs adjacent to the thorax compared to cranially on the DV view. Radiographic measurements and findings are summarised in Tables 5.1–5.3.

5.3.1 Musculoskeletal system

Out of 15 animals, 14 had 12 thoracic vertebrae (Fig. 5.3) whereas one animal (female) had 13 thoracic vertebrae. The anticlinal vertebra was thoracic

vertebra 10 (T10) in 12/15 animals (Fig. 5.3) and T11 in 3/15. The thoracic spine was fairly horizontally aligned (Figs 5.3 and 5.4). The height and length of thoracic vertebral bodies increased from cranial to caudal (Fig. 5.3). The spinous processes were almost of the same height (Fig. 5.3). Spondylosis deformans of thoracic vertebrae was seen in two animals aged 19 and 22 years.

Of the 15 animals, 14 had 12 pairs of ribs of which the last pair was floating (not connected to the costal arch) (Fig. 5.3). The animal with 13 thoracic vertebrae had 13 pairs of ribs of which the last two pairs were floating. The sternum was fairly straight and slender. It consisted of a manubrium sterni, four (6/15) or five (9/15) (Fig. 5.4) sternebrae and a xiphoid process. The cranial extremity of the manubrium sterni was wider than the caudal extremity. The last two (Fig. 5.4) or three sternebrae were fused in six and two animals, respectively. The thoracic inlet was very narrow (Figs 5.3 and 5.4) and the clavicles were well developed (Figs 5.3 and 5.5).

5.3.2 Cardiovascular system

In all animals the cardiac silhouette was in contact with the diaphragm (Fig. 5.3). The cardiodiaphragmatic contact increased in heavier (Figs 5.4 and 5.6) compared to lighter (Figs 5.3 and 5.5) animals. On the RL view, the ovoid heart was aligned almost parallel to the ribs and was positioned upright (Figs 5.3 and 5.4). The cranial border of the cardiac silhouette was poorly seen (Fig. 5.4) except in lighter animals (Fig. 5.3). The caudal vena cava (CVC) was clearly seen in nine animals (Fig. 5.3) and was not clearly visible in six

animals. The visibility of the CVC was better in light (Fig. 5.3) versus heavy animals (Fig. 5.4). In the majority of the animals (11/15) the aorta was not clearly seen or not seen at all (Figs 5.3 and 5.4). The size of the cardiac silhouette was wider than two intercostal spaces but did not exceed three intercostal spaces (Figs 5.3 and 5.4) on the RL view.

On the DV view, the ovoid cardiac silhouette was more diagonal in position (Figs 5.5 and 5.6). The apex was positioned to the left and there was extensive cardiodiaphragmatic contact (Figs 5.5 and 5.6), which increased in heavy animals (Fig. 5.6) compared to lighter animals (Fig. 5.5). The caudal lobar pulmonary veins and arteries were not clearly visible. There was a significant difference ($P = 0.003$) in the mean VHS obtained on the RL and DV views. Pericardial fat was seen in three heavier animals (3.3 kg and above). On the RL view, pericardial fat was seen along the cranial border of the heart (Fig. 5.7). On the DV view, it was seen around the cardiac apex (Fig. 5.8) and at 8-11 o'clock.

5.3.3 Respiratory system

On the RL view, the trachea with its mineralised cartilage rings was seen in all animals (Fig. 5.3). It was parallel (8/15) (Figs 5.3 and 5.4) or deviated dorsally to the spine (6/15). In only one animal did it diverge from the spine. The carina was frequently (12/15) not clearly visible or not visible at all (Fig. 5.3) on the RL view. It was clearly visible in only three animals (Fig. 5.4). On the DV view, the carina was clearly visible in 14/15 animals. There was no significant

difference ($P = 0.16$) in the mean position of the carina with respect to thoracic vertebra on the DV and RL views.

On the DV view, in 12/13 animals the trachea was running slightly to the right of the spine (Fig. 5.5). In one animal it was superimposed on the spine (Fig. 5.6). In 7/15 animals, interstitial, bronchointerstitial and alveolar patterns were observed in the right hemithorax with severe changes seen adjacent to the right margin of the cardiac silhouette, which was partially being obscured (Fig. 5.8). The caudoventral mediastinal reflection was seen in 3/15 animals. The craniodorsal mediastinum exceeded the width of the superimposed spine and appeared prominent in heavy animals (Fig. 5.6).

5.3.4 Other findings

The thoracic lymph nodes were not identified in any view. A pair of mammary glands was seen in female animals as increased soft tissue opacity ventral to the thorax partly superimposed over the triceps brachii muscle on the RL view. An area of increased soft tissue opacity in the proximal half of the humerus was seen in male animals representing the brachial scent glands (Fig. 5.4).

5.4 DISCUSSION

The mean weight of the animals observed in this study (2.92 kg) was higher than the reported mean weight of ring-tailed lemurs in the wild (2.2 kg) (Jungle, 2003; Goodchild and Schwitzer, 2008) and previously reported (male:

2.705 kg; female: 2.678 kg) in captivity (Kappeler, 1991). In captivity lemurs are commonly observed to be overweight or even obese mainly as a result of change in their lifestyle (Goodchild and Schwitzer, 2008).

In primates, variations in the number of thoracic vertebrae occur within a species (Wagner and Kirberger, 2005; Alves et al., 2012). The number of thoracic vertebrae observed in this species (12 to 13) is similar to the common marmoset (*Callithrix jacchus*) (Wagner and Kirberger, 2005). However, the mean number of thoracic vertebrae (12.1) is different from that reported in common marmoset (12.59) (Wagner and Kirberger, 2005) and indicates that there is very little variation in the number of thoracic vertebrae in this species when compared to the common marmoset. The increase in size of the thoracic vertebral bodies from cranial to caudal observed in this species has also been reported in the vervet monkey (*Chlorocebus sabaeus*) (Young et al., 2013) and in other primate species (Ankel-Simons, 2007).

Variation in the number and fusion of sternebrae has also been reported in the common marmoset (Wagner and Kirberger, 2005). Further, the mean number of sternebrae observed in this study (4.6) is similar to that reported in the common marmoset (4.5) (Wagner and Kirberger, 2005). The spondylosis deformans observed in this study was characterised by osteophyte formation at the vertebral body end plates similar to dogs although cranial thoracic vertebrae were also involved. In dogs the thoracolumbar and lumbosacral regions are commonly affected (Widmer and Thrall, 2013).

Measurement of thoracic width in this study was performed between the left and right pleural surfaces of the seventh ribs, rather than the eighth as in domestic cats and dogs (Buchanan and Bücheler, 1995; Litster and Buchanan, 2000) due to lack of visibility of the thoracic pleura at rib 8 in some of the animals. The lack of visibility of the thoracic pleura at rib 8 in some of the animals is the result of abdominal dominance in this species.

The mean VHS obtained in this study lies between the values reported in domestic cats (Litster and Buchanan, 2000) and dogs (Buchanan and Bücheler, 1995). The higher VHS value obtained from DV view than RL view has also been observed in domestic cats (Litster and Buchanan, 2000) and dogs (Buchanan and Bücheler, 1995). For VHS measurements, pericardial fat must be distinguished from the actual cardiac silhouette to avoid exaggerated VHS and misdiagnosis of cardiomegaly. Pericardial fat has also been seen in domestic cats and dogs (Litster and Buchanan, 2000; Johnson et al., 2008; Rudorf et al., 2008; Thrall and Robertson, 2011). The mean ACI obtained in this study (34.13º) is intermediate between the domestic cat (25–30º) and dog (40º) (Nickel et al., 1986).

The poorly defined cranial border of the cardiac silhouette observed in this study on the RL view is believed to be due to the deposition of fat in the pericardial sac. In obese domestic cats the cardiac silhouette margins may not be clearly seen due to pericardial fat (Litster and Buchanan, 2000). Pericardial fat in domestic cats was distinguished more readily on lateral radiographs and radiographic contrast between the true cardiac silhouette and fat was

sometimes enhanced by decreasing kVp and increasing mAs (Litster and Buchanan, 2000). The extensive cardiodiaphragmatic contact in this species is similar to that reported in the common marmoset (Wagner and Kirberger, 2005) and is due to abdominal dominance in these species.

The parallel or dorsal deviation of the trachea to the thoracic spine, which was observed in this species on the RL view, is normal and should not be misinterpreted as dorsal displacement of the trachea due to cardiac enlargement, cranial mediastinal mass, pleural effusion (Hayward et al., 2008) or substernal fat (Litster and Buchanan, 2000). Parallel alignment of the trachea to the thoracic spine has also been observed in dogs with a dorsoventrally compressed thorax such as the Dachshund and Welsh corgi (Thrall and Robertson, 2011).

The animal in which the trachea diverged from the spine had also kyphosis and spondylosis deformans of the entire thoracic spine. The position of the trachea slightly to the right of the spine which was observed in the majority of the animals on the DV view is similar to dogs (Hayward et al., 2008; Thrall and Robertson, 2011). The presence of mineralised tracheal cartilage rings in all animals in this study suggests that it is a normal feature in this species and not an incidental finding or ageing change.

The poor visibility of the carina on the RL view in the majority of the animals in this study is similar to the common marmoset (Wagner and Kirberger, 2005) but contrary to the vervet monkey (Young et al., 2013). The observed

interstitial, brochointerstitial and alveolar patterns are believed to be due to RL recumbency during radiography causing gravity dependent atelectasis, which would be consistent with their location in the right hemithorax. This would be also supported by the fact that heavier animals were prone to more severe atelectasis. None of the animals with these lung patterns revealed respiratory disease on clinical examination. In domestic cats and dogs the right middle lung lobe collapses before the other lobes because of a high pleural surface area: lung volume ratio, leading to less collateral ventilation. The same may hold true for the ring-tailed lemur evidenced by severe changes adjacent to the right margin of the cardiac silhouette, which was partially obscured.

The radiographic thoracic anatomy of the ring-tailed lemur more closely resembles the common marmoset (Wagner and Kirberger, 2005) than other reported New and Old World monkeys (Silverman and Morgan, 1980; Alves et al., 2012; Young et al., 2013). Variations exist in the normal radiographic thoracic anatomy of primates (Silverman and Morgan, 1980; Wagner and Kirberger, 2005; Alves et al., 2012; Young et al., 2013). Knowledge of the normal radiographic thoracic anatomy of individual species is important and fundamental for accurate diagnosis of diseases.

5.5 ACKNOWLEDGEMENTS

The authors would like to thank the Organisation for Women in Science for the Developing World (OWSD), Swedish International Development Cooperation Agency (SIDA), University of Pretoria, Johannesburg (JHB) and Bristol zoos

for supporting this study. Montecasino Bird Gardens for permission to use their animal for this study. Drs Brett Gardner and Kathryn Perrin, Ms. Fania Mohlala, sisters and animal handlers of the JHB and Bristol zoos for their assistance during radiography. Mrs. Charmaine Vermeulen and Mrs. Wilma Olivier of the University of Pretoria for their assistance in photography and administrative work respectively.

5.6 REFERENCES

Alves, F. R., F. B. Costa, P. P. Machado, A. N. Diniz, A. V. C. Araújo, C. E. Ambrósio, and P. C. Guerra, 2012: Anatomical and radiographic appearance of the capuchin monkey thoracic cavity (*Cebus apella*). Pesq. Vet. Bra. **32,** 1345–1350.

Ankel-Simons, F., 2007: Primate Anatomy: An Introduction. Boston: Academic Press.

Brining, D. L., J. S. Mattoon, L. Kercher, R. A. LaCasse, D. Safronetz, H. Feldmann, and M. J. Parnell, 2010: Thoracic radiography as a refinement methodology for the study of H1N1 influenza in cynomologus macaques (*Macaca fascicularis*). Comparative. Med. **60,** 389–395.

Buchanan, J. W., and J. Bücheler, 1995: Vertebral scale system to measure canine heart size in radiographs. J. Am. Vet. Med. Assoc. **206,** 194–199.

Canelli, E., A. Luppi, A. Lavazza, D. Lelli, E. Sozzi, A. M. M. Martin, D. Gelmetti, E. Pascotto, C. Sandri, W. Magnone, and P. Cordioli, 2010: Encephalomyocarditis virus infection in an Italian zoo. Virol. J. **7 (64),** 1–7.

Goodchild, S., and C. Schwitzer, 2008: The problem of Obesity in Captive lemurs. Int. Zoo. News. **55,** 353–357.

Hamerton, B. C. A. E., 1944: Report on the deaths occurring in the Society's Gardens during the year 1943. J. Zool. **114,** 307–321.

Haskin, P. H., and L. R. Goodman, 1982: Normal tracheal bifurcation angle: a reassessment. Am. J. Roentgenol. **139,** 879–882.

Hayward, N., T. Schwarz, and C. Weisse, 2008: The trachea. In: BSVA Manual of Canine and Feline Thoracic Imaging (T. Schwarz and V. Johnson, eds). Gloucester: BSAVA. pp. 213–227.

IUCN, 2014: IUCN Red list of threatened species, Version 2014.3. Available at: http://www.iucnredlist.org (accessed on 18 November 2014).

Johnson, V., K. Hansson, W. Maï, J. Dukes-McEwan, N. Lester, T. Schwarz, P. Chapman, and F. Morandi, 2008: The heart and major vessels. In: BSVA Manual of Canine and Feline Thoracic Imaging (T. Schwarz and V. Johnson, eds). Gloucester: BSAVA. pp. 86–176.

Jungle RE: Prosimians. In: Zoo and Wild Animal Medicine, 5th Edition. Fowler & Miller (eds). Missouri: Saunders, 2003, 334–346.

Kappeler, P. M., 1991: Patterns of sexual; dimorphism in body weight among prosimians primates. Folia. Primatol. **57,** 132–146.

Kondo, H., Y. Wada, G. Bando, M. Kosuge, K. Yagi, and Y. Oku, 1996: Alveolar hydatidosis in a gorilla and ring-tailed lemur in Japan. J. Vet. Med. Sci. **58,** 447–449.

Lehmkuhl, L. B., J. D. Bonagura, D. S. Biller, and W. M. Hartman, 1997: Radiographic evaluation of caudal vena cava size in dogs. Vet. Radiol. Ultrasound. **38,** 94–100.

Litster, A. L., and J. W. Buchanan, 2000: Radiographic and echocardiographic measurement of the heart in obese cats. Vet. Radiol. Ultrasound. **41,** 320–325.

Litster, A. L., and J. W. Buchanan, 2000: Vertebral scale system to measure heart size in radiographs of cats. J. Am. Vet. Med. Assoc. **216,** 210–214.

Nelson, N. C., J. S. Mattoon, and D. E. Anderson, 2011: Radiographic appearance of the thorax of clinically normal alpaca crias. Am. J. Vet. Res. **72,** 1439–1448.

Nickel, R., A. Schummer, E. Seiferle, J. Frewein, H. Wilkens, and K. H. Wille, 1986: The Anatomy of the Domestic Animals Vol.3. Berlin: Springer–Verlag.

Nowak, R. M., 1999: Order Primate. In: Walker's Mammals of the World (R. M. Nowak, ed.). Baltimore: The Johns Hopkins University Press. pp. 490–631.

Palotay, J. L., and H. Uno, 1975: Hydatid disease in four nonhuman primates. Am. Vet. Med. Assoc. **167,** 615–618.

Patten, C. J., 1899: The form and position of the thoracic and abdominal viscera of the ruffed lemur (*Lemur varius*). Trans. Royal. Acad. Med. Ireland. **17,** 652–677.

Pye, G. W., R. A. Bennette, S. P. Terrell, P. E. Ginn, L. J. McSherry, L. J. Herry, and A. R. Alleman, 2000: T-cell-Rich B-cell lymphoma in a ring-tailed lemur (*Lemur catta*). J. Zoo. Wildl. Med. **31,** 388–393.

Rudorf, H., O. Taeymans, and V. Johnson, 2008: Basics of thoracic radiography and radiology. In: BSAVA Manual of Canine and Feline Thoracic Imaging (T. Schwarz and V. Johnson, eds). Gloucester: BSAVA. pp. 1–19.

Schillaci, M. A., L. Jones-Engel, J. E. Heidrich, R. Benamore, A. Pereira, and N. Paul, 2008: Thoracic radiography of pet macaques in Sulawesi, Indonesia. J. Med. Primatol. **37,** 141–145.

Schillaci, M. A., S. Parish, and L. Jones-Engel, 2009: Radiographic measurement of the cardiothoracic ratio in pet macaques from Sulawesi, Indonesia. Radiography. **15,** 29–33.

Schmidt, R. E., 1975: Tuberculosis in a ring-tailed lemur (*Lemur catta*). J. Zoo. Wildl. Med. **6,** 11–12.

Silverman, S., and' J. P. Morgan, 1980: Thoracic radiography of the normal rhesus macaque (*Macaca mulatta*). Am. J. Vet. Res. **41,** 1704–1719.

Thrall, D. E., and I. D. Robertson, 2011: Atlas of Normal Radiographic Anatomy and Anatomic Variants in the Dog and Cat. St. Louis: Elsevier.

Tuten, H. C., H. C. Miller, and A. E. Ellis, 2011: Cuterebrid myiasis (Diptera: Oestridae) in captive ring-tailed lemurs (*Lemur catta*) at a South Carolina Zoo. J. Zoo. Wildl. Med. **42,** 504–507.

Wagner, W. M., and R. M. Kirberger, 2005: Radiographic anatomy of the thorax and abdomen of the common marmoset (*Callithrix jacchus*). Vet. Radiol. Ultrasound. **46,** 217–224.

Widmer, W. R., and D. E. Thrall, 2013: The canine and feline vertebrae. In: Textbook of Veterinary Diagnostic Radiology (D. E. Thrall, ed.). Louis: Saunders Elsevier. pp. 172–193.

Young, A. N., W. M. du Plessis, D. Rodriguez, and A. Beierschmidt, 2013: Thoracic radiographic anatomy in vervet monkeys (*Chlorocebus sabaeus*). J. Med. Primatol. **42,** 310–317.

5.7 TABLES

Table 5.1 Radiographic measurements (cm) of thoracic vertebrae in captive ring-tailed lemurs not compensated for magnification

Vertebra	Variable	Number	Mean ± SD (cm)	Range (cm)
T1	Length	14	0.68 ± 0.06	0.52 – 0.80
	Height	14	0.28 ± 0.03	0.25 – 0.30
T2	Length	14	0.74 ± 0.05	0.68 – 0.80
	Height	14	0.31 ± 0.04	0.25 – 0.40
T3	Length	14	0.77 ± 0.04	0.70 – 0.85
	Height	14	0.33 ± 0.02	0.30 – 0.35
T4	Length	14	0.80 ± 0.04	0.75 – 0.85
	Height	14	0.36 ± 0.03	0.30 – 0.40
T5	Length	14	0.80 ± 0.03	0.75 – 0.85
	Height	14	0.37 ± 0.04	0.30 – 0.40
T6	Length	14	0.83 ± 0.03	0.78 – 0.86
	Height	14	0.40 ± 0.02	0.35 – 0.45
T7	Length	14	0.86 ± 0.05	0.79 – 0.90
	Height	14	0.44 ± 0.04	0.39 – 0.50
T8	Length	14	0.91 ± 0.05	0.83 – 0.96
	Height	14	0.48 ± 0.05	0.40 – 0.55
T9	Length	14	0.97 ± 0.04	0.90 – 1.03
	Height	14	0.53 ± 0.04	0.49 – 0.60
T10	Length	14	1.06 ± 0.05	1.00 – 1.17
	Height	14	0.58 ± 0.05	0.50 – 0.65
T11	Length	14	1.16 ± 0.04	1.10 – 1.24
	Height	14	0.61 ± 0.04	0.50 – 0.66
T12	Length	14	1.26 ± 0.05	1.20 – 1.34
	Height	14	0.66 ± 0.04	0.59 – 0.70
T13	Length	1	1.35 ± 0.00	1.35 – 1.35
	Height	1	0.70 ± 0.00	0.70 – 0.70

T, thoracic

Table 5.2 Radiographic measurements (cm) of the manubrium sterni, sternebrae and xiphoid process not compensated for magnification in captive ring-tailed lemurs

	Variable	Number	Mean ± SD (cm)	Range (cm)
MS	Length	15	1.37 ± 0.14	1.16 – 1.61
	Height	15	0.71 ± 0.10	0.50 – 0.90
S1	Length	15	1.03 ± 0.10	0.90 – 1.20
	Height	15	0.43 ± 0.06	0.30 – 0.50
S2	Length	15	1.07 ± 0.07	0.99 – 1.20
	Height	15	0.42 ± 0.07	0.30 – 0.50
S3	Length	11	1.07 ± 0.10	0.95 – 1.30
	Height	11	0.39 ± 0.07	0.30 – 0.50
S4	Length	7	1.21 ± 0.24	0.95 – 1.60
	Height	7	0.37 ± 0.04	0.30 – 0.40
S5	Length	3	1.18 ± 0.14	1.10 – 1.35
	Height	3	0.35 ± 0.05	0.30 – 0.40
XP	Length	15	1.86 ± 0.28	1.50 – 2.71
	Height	15	0.21 ± 0.07	0.12 – 0.32

MS, manubrium sterni; S, sternebra; XP, xiphoid process

Table 5.3 Radiographic findings and measurements of the thorax not compensated for magnification in captive ring-tailed lemurs

Variable	Number	Mean ± SD	Range
TDp [cm]	15	5.43 ± 0.46	4.72 – 6.20
TW [cm]	15	7.28 ± 0.49	6.41 – 8.20
TDp: TW	15	0.75 ± 0.07	0.63 – 0.86
Sternebrae	15	4.60 ± 0.51	4.00 – 5.00
Anticlinal vertebra	15	10.20 ± 0.41	10.00 – 11.00
ACI [º]	15	34.13 ± 3.77	30.00 – 45.00
VHS [RL]	15	8.92 ± 0.47	8.00 – 9.60
VHS [DV]	13	9.42 ± 0.52	8.60 – 10.20
CVC diameter [cm]	9	0.70 ± 0.13	0.60 – 0.97
CVC: Aorta	4	0.88 ± 0.06	0.81 – 0.95
CVC: VL	8	0.85 ± 0.22	0.63 – 1.21
Aorta diameter [cm]	4	0.73 ± 0.06	0.67 – 0.80
Carina			
Vertebra [RL]	15	6.73 ± 0.70	6.00 – 8.00
Vertebra [DV]	14	6.50 ± 0.65	6.00 – 8.00
Angle between MSB [º]	14	82.60 ± 8.26	70.00 – 95.00
TD [cm]	14	0.71 ± 0.04	0.65 – 0.79
TID [cm]	14	1.99 ± 0.07	1.80 – 2.09
TD: TID	14	0.36 ± 0.02	0.33 – 0.40
Cranial crus			
Inspiration	15	12.49 ± 0.86	11.00 – 13.60

TDp, thoracic depth; TW, thoracic width; ACI, angle of cardiac inclination; VHS, vertebral heart score; RL, right lateral; DV, dorsoventral; CVC, caudal vena cava; TD, tracheal diameter; TID, thoracic inlet diameter; MSB, mainstem bronchi

5.8 FIGURES

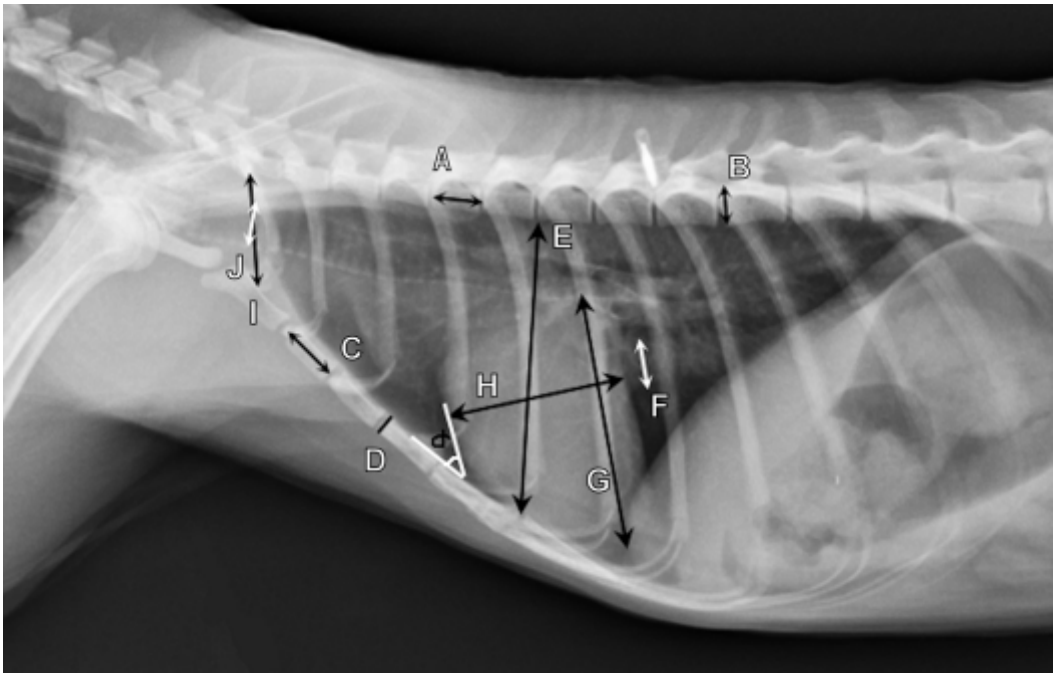

Fig. 5.1 Right lateral thoracic radiograph of a 2.8-year-old female ring-tailed lemur illustrating selected radiographic measurements. (A) Vertebral body length, (B) vertebral body height, (C) length of sternebra, (D) height of sternebra, (E) thoracic depth, (F) caudal vena cava diameter, (G) cardiac silhouette long axis measurement, (H) cardiac silhouette short axis measurement, (I) thoracic inlet diameter, (J) trachea diameter and α = angle of cardiac inclination.

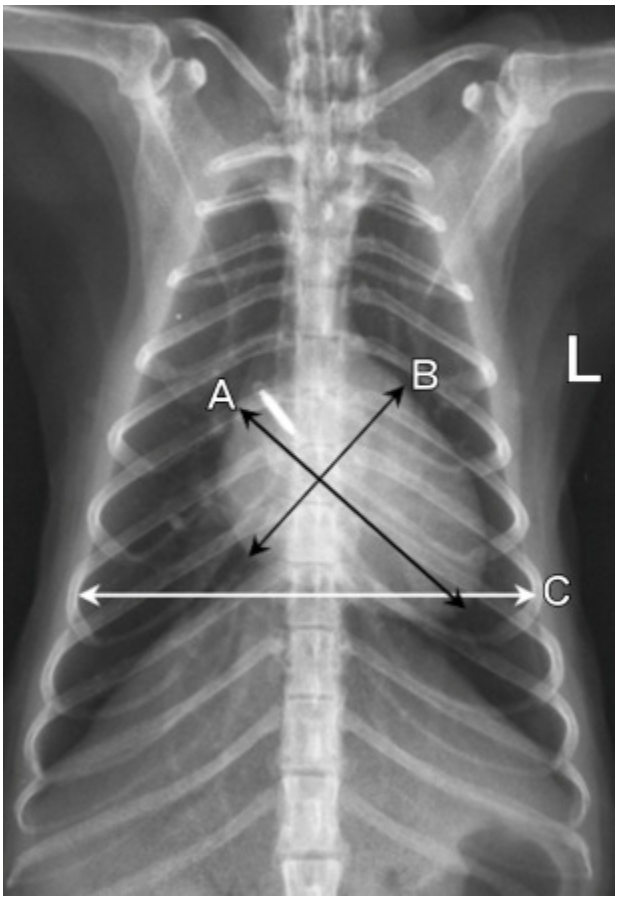

Fig. 5.2 Dorsoventral thoracic radiograph of a 3-year-old male ring-tailed lemur illustrating selected radiographic measurements. (A) Cardiac silhouette long axis measurement, (B) cardiac silhouette short axis measurement and (C) width of the thorax. L, left.

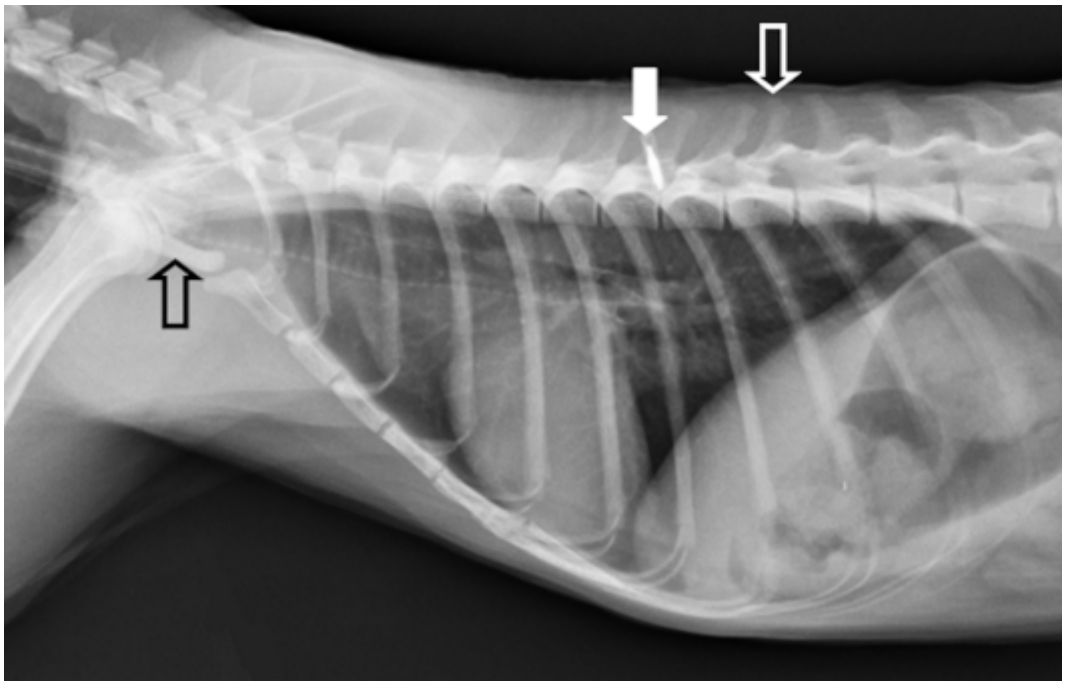

Fig. 5.3 Right lateral thoracic radiograph of a 2.8-year-old (2.44 kg) female ring-tailed lemur. Note the increase in length and height of the thoracic vertebral bodies from cranial to caudal, well developed clavicles (open black arrow) and a very narrow thoracic inlet. The trachea with mineralized cartilage rings is aligned almost parallel to the thoracic spine. Note also the almost parallel alignment of the heart with the ribs. The upright positioned cardiac silhouette is wider than two intercostal spaces but does not exceed three intercostal spaces. Note the anticlinal thoracic vertebra number 10 (open white arrow) and lack of visibility of the carina. The metal opacity (white arrow) represents a microchip.

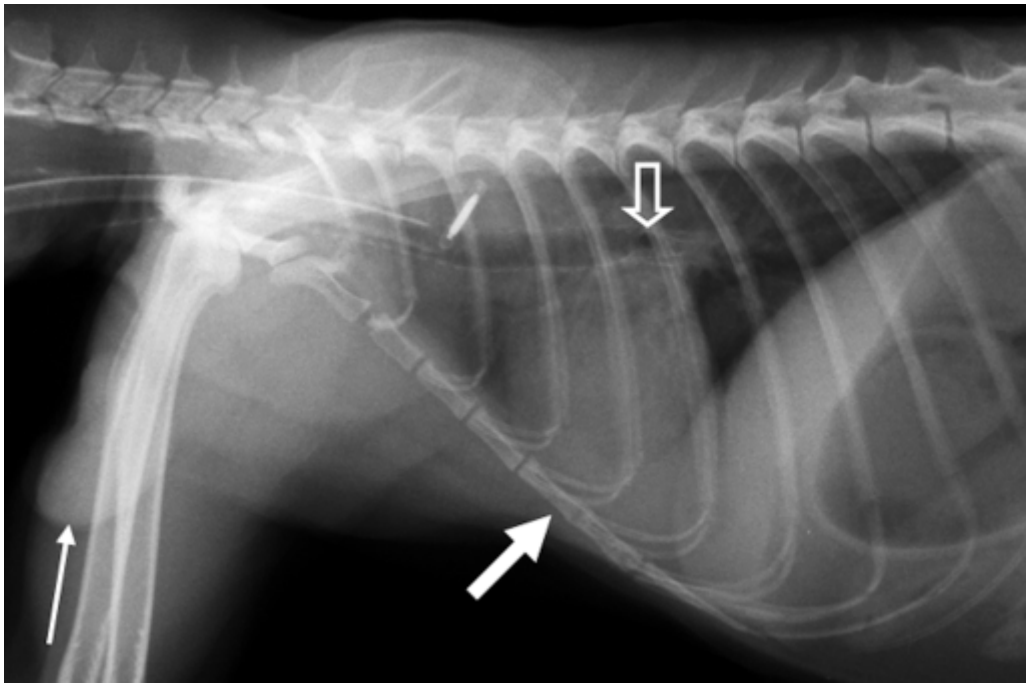

Fig. 5.4 Right lateral thoracic radiograph of a 7.3-year-old (3.02 kg) male ring-tailed lemur. Note the fusion of the last two sternebrae (thick white arrow) and extensive cardiodiaphragmatic contact. Note also an almost parallel alignment of the trachea with the thoracic spine, clearly visible carina (open white arrow) and the presence of scent glands (thin white arrow).

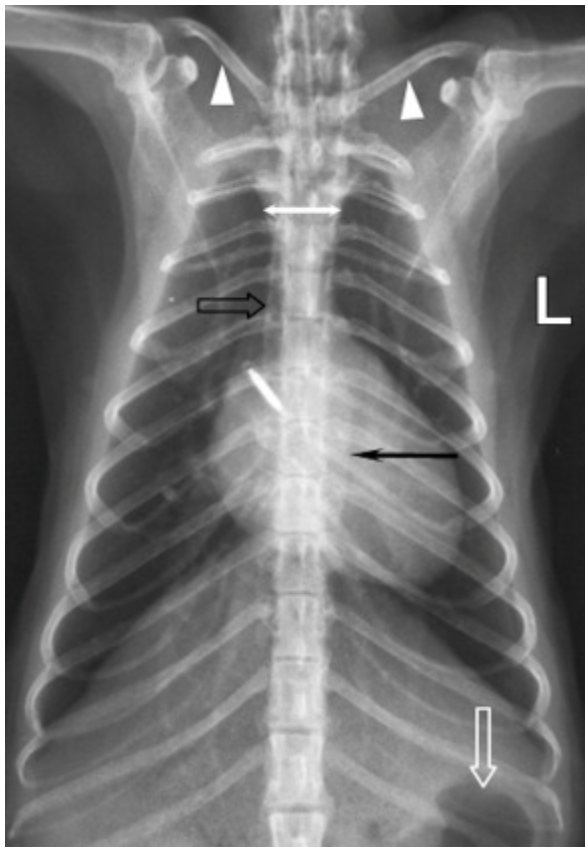

Fig. 5.5 Dorsoventral thoracic radiograph of a 3-year-old (2.31 kg) male ring-tailed lemur. The cardiac silhouette is more diagonally positioned and there is extensive cardiodiaphragmatic contact. Note the visualization of the left margin of the aorta (black arrow). The trachea is positioned slightly to the right of the spine (open black arrow). Note also the concentration of gastric gas in the gastric fundus (open white arrow), well developed clavicles (white arrow heads) and an almost similar thickness of the craniodorsal mediastinum and thoracic spine (white arrow). L, left.

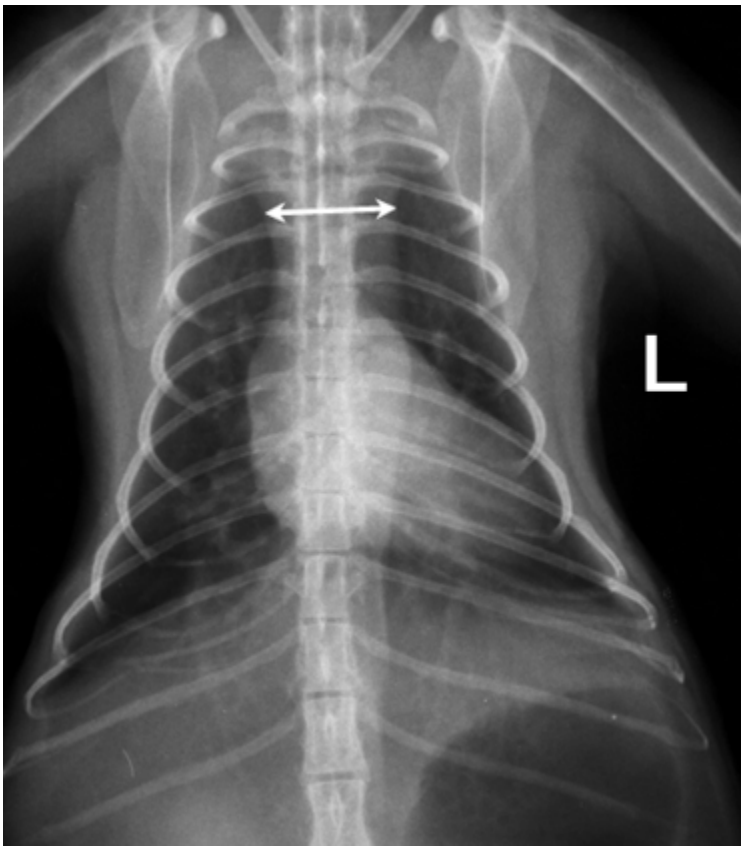

Fig. 5.6 Dorsoventral thoracic radiograph of a 12.3-year-old (3.24 kg) female ring-tailed lemur. Note the more extensive cardiodiaphragmatic contact when compared to Fig. 5.5. The trachea is poorly visible superimposed on the spine and sternum. Note also the more prominent craniodorsal mediastinum (white arrow) when compared to Fig. 5.5. L, left.

Fig. 5.7 Close-up of right lateral thoracic radiograph of the cranioventral aspect of the cardiac silhouette of a 4.8-year-old (3.3 kg) male ring-tailed lemur. Note the presence of fat opacity along the cranial border of the heart (white arrow).

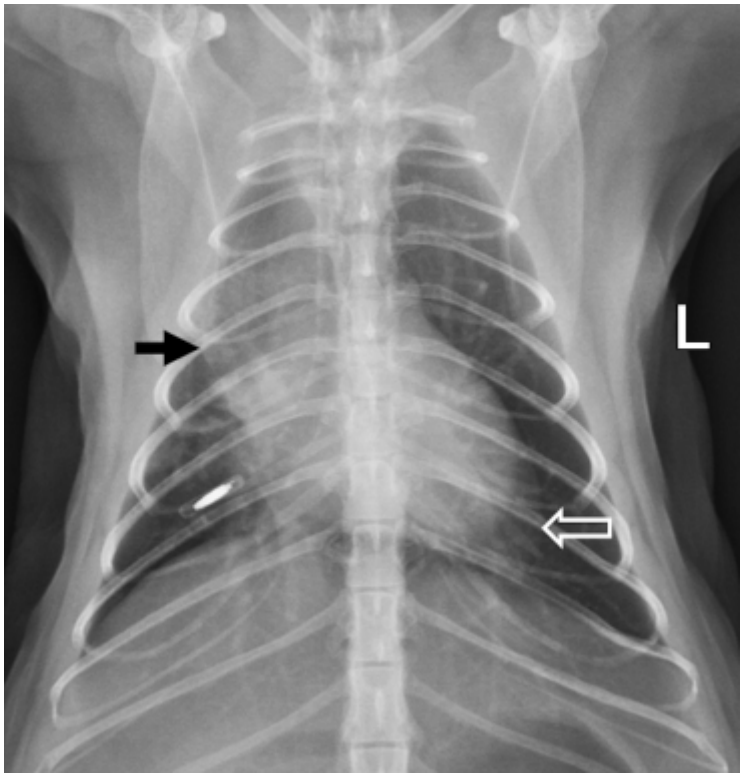

Fig. 5.8 Dorsoventral thoracic radiograph of a 4.8-year-old (3.3 kg) male ring-tailed lemur. Note the presence of fat opacity (open white arrow) around the apex of the heart. An alveolar lung pattern (black arrow) in the right hemithorax causes border effacement of the right aspect of the cardiac silhouette. L, left.

CHAPTER 6

RADIOGRAPHIC AND ULTRASONOGRAPHIC ABDOMINAL ANATOMY IN CAPTIVE RING-TAILED LEMURS (*LEMUR CATTA*)

6.1 INTRODUCTION

The ring-tailed lemur (*Lemur catta*) is primarily distributed in south and south-western Madagascar (Budnitz and Dainis, 1975). It is a species commonly kept in zoological gardens. The ring-tailed lemur is classified as an endangered species by the International Union for Conservation of Nature and Natural Resources (IUCN) (IUCN, 2014).

The ring-tailed lemur possesses a simple stomach, which is pyriform in shape (Osman Hill, 1953). The greater part of the small intestine possesses a wide diameter especially the duodenum, which narrows considerably towards the ileum (Patten, 1902). The duodenum consists of a longer cranial portion and a shorter transverse portion, which crosses the spine as far caudally as the fourth lumbar vertebra (Osman Hill, 1953). The caecum is very long and large with a conical appendix-like termination (Osman Hill, 1953). The colon has a characteristic sigmoid arrangement. From the right caudally placed ileo-caecal junction, the ascending colon proceeds obliquely forwards and to the left up to the hepatic flexure. From the hepatic to splenic flexure, the transverse colon pursues a curved course making a U-shaped ansa. The remainder of the

large intestine from the splenic flexure to the anus takes a straight course downwards (Patten, 1902; Osman Hill, 1953).

The spleen is an elongated strap-like structure resembling that of lower mammals rather than the spleen of monkeys and apes (Osman Hill, 1953). The kidneys are asymmetrically located on the dorsal abdominal wall in the lumbar region with the right kidney situated cranial to the left kidney (Osman Hill, 1953). The centrally located medulla is undivided and surrounded by an even layer of cortex. It ends medially in a single pyramid, which projects into the renal sinus (Osman Hill, 1953). The intra-abdominal urinary bladder is pyriform and broader in males than females (Osman Hill, 1953). The os penis is roughly fusiform and an os clitoridis is present within the corpus cavernosum of the glans clitoridis (Drea and Weil, 2008).

Diseases involving the digestive system such as intestinal ulcers (Scott and Camb, 1925) and neoplasia like colonic adenocarcinoma (Remick et al., 2009) have been documented in this species. Liver diseases like hepatic lipidosis, fibrosis, capillariasis (Zordan et al., 2012), haemochromatosis (Taylor, 2009), and neoplasia such as cholangiocarcinoma (Chang et al., 1979) and cholangioma (Remick et al., 2009) have also been reported.

Urogenital diseases like kidney infarcts, pyelonephritis, cystitis (Burton et al., 1986), renal aplasia/hypoplasia (Scott and Camb, 1925), urinary tract obstruction (Jungle, 2003), and neoplasia such as renal adenoleiomyofibromatous harmatoma (Jones and Casey, 1981), mixed

epithelial and stromal tumour of the kidney (Muller et al., 2007) and papillary adenoma of the prostate (Remick et al., 2009) have been documented in the ring-tailed lemur. Other abdominal diseases, which have been reported in this species are; cysticercosis (Luzón et al., 2010), hydatidosis (Palotay and Uno, 1975; Shahar et al., 1995) and neoplasia such as adrenal gland phaechromocytoma (Remick et al., 2009).

Radiography and ultrasonography are non-invasive diagnostic imaging techniques, which are used for diagnosis, staging and evaluation of various diseases involving the abdomen. Several authors have reported the normal radiographic (Wagner and Kirberger, 2005a) and ultrasonographic (Gaschen et al., 2000; Wagner and Kirberger, 2005b; Alves et al., 2007; Raharison et al., 2009; Takeshita et al., 2011; Amory et al., 2013) abdominal anatomy of primates, which provides a reference for the diagnosis of abdominal diseases. To the best of the authors' knowledge the normal radiographic and ultrasonographic abdominal anatomy of the ring-tailed lemur has not yet been published. The aim of this study was to report the normal radiographic and ultrasonographic abdominal anatomy in captive ring-tailed lemurs as guidance for clinical use.

6.2 MATERIALS AND METHODS

6.2.1 Animals

A total of 16 captive ring-tailed lemurs (*Lemur catta*) from the Johannesburg zoo, South Africa (SA) and Bristol zoo, United Kingdom (UK) were used in this

study. Ten were females and six were males. Of the 16 animals, six were used for both radiographic and ultrasonographic studies. Radiography and ultrasonography were performed in 13 and nine animals, respectively, during annual health examinations. Of the 13 animals used for radiographic study, seven were females and six were males. Their age ranged from 2.8 years to 19.8 years (mean: 8.21 ± 4.54 years). Their minimum and maximum weights were 2.31 kg and 3.44 kg, respectively, (mean: 2.99 ± 0.35 kg). There was no significant difference in the mean age (P = 0.44) and weight (P = 0.44) between male and female animals. For ultrasonographic study, the age of the animals ranged from 2.8 years to 25.7 years (mean: 12.88 ± 7.55 years). Their minimum and maximum weights were 2.31 kg and 3.37 kg, respectively, (mean: 2.88 ± 0.39 kg). Of the nine animals, eight were females and one was a male.

Radiographic and ultrasonographic examinations were performed under general anaesthesia. Animals were fasted for 8 to 12 hours but water was given *ad libitum* until shortly before general anaesthesia. Anaesthesia was induced either by intramuscular injection of medetomidine hydrochloride (Domitor, Pfizer Laboratories Ltd., Sandton, SA) and ketamine hydrochloride (Kyron Laboratories Ltd., Benrose, SA) combination or by isoflurane (IsoFlo, Abbott Laboratories Ltd., Berkshire, UK) via a mask. All animals were intubated and anaesthesia maintained with isoflurane (IsoFlo, Abbott Laboratories Ltd., Berkshire, UK: Isofor, Safe Line Pharmaceuticals Ltd., Roodepoort, SA).

Animals were considered healthy based on history, physical and clinical examination, haematological evaluation, faecal examination, and liver and kidney function tests. This study was approved by the Bristol Zoo Gardens Research Committee, Animal Use and Care Committee (AUCC) of the University of Pretoria and the Johannesburg Zoo Ethics and Research Committee.

6.2.2 Radiography

Right lateral (RL) and ventrodorsal (VD) views of the abdomen were taken at the end of expiration using a table-top technique. Radiographs were made by either an EVA-HF525 (Comed Medical System Co. Ltd., Kyunggi, Korea) or a Roentgen 703 (GEC Medical Equipment Ltd., Middlesex, UK) x-ray machine.

For the EVA-HF525 a source to image distance (SID) of 95 cm was used with 42 kVp and 2.5 mAs (25 mA and 0.1 s). Medium speed screen type films (Fujifilm Corporation, Tokyo, Japan) were used with RAREX green regular intensifying screens (Okamoto manufacturing Co. LTD, Tokyo, Japan). Radiographs were obtained with x-ray film processor model CP–345 (ELK Corporation, Tokyo, Japan). Radiographic images were digitalized using a digital camera (CANON 5DMARK2, Canon Inc., Tokyo, Japan).

With the Roentgen 703 an exposure of 60 kVp and 3 mAs (100 mA and 0.03) was used with a SID of 105 cm. Images were obtained with computed radiography unit Regius Model 110 (Konica Minolta Medical and Graphic, INC., Tokyo, Japan).

The dorsoventral height (Fig. 6.1) of lumbar vertebral bodies was measured on the RL view at the cranial end-plate (Adams et al., 2010). The craniocaudal length (Fig. 6.1) of lumbar vertebral bodies was measured on the RL view at the dorsal margin of the lumbar vertebral bodies from the cranial end-plate to the caudal end-plate. Additionally, for the second lumbar vertebra the craniocaudal length (Fig. 6.2) of the vertebral body was also measured on the VD view from the cranial end-plate to the caudal end-plate along the sagittal plane of the vertebra (Eshar et al., 2013).

Visibility, shape and location of the abdominal organs were recorded. The angle of the gastric axis (Fig. 6.1) was measured on the RL view between the gastric axis and a line drawn along the ventral aspect of the last thoracic vertebra to the first or the first two lumbar vertebrae (Wagner and Kirberger, 2005a). The gastric axis is an imaginary line from the fundus through the body and pylorus (Seiler and Maï, 2009). Maximum external diameters of small and large intestines (Fig. 6.1) were measured in cm and also compared with the height of the second lumbar vertebral body on the RL view (Adams et al., 2010). Additionally, the maximum external diameter of the large intestine was also compared with the length of the second lumbar vertebral body on the RL view (Wagner and Kirberger, 2005a). In cases where the large intestine could not be distinguished from the small intestine, the intestine with the largest external diameter was considered to be the large intestine (Wagner and Kirberger, 2005a).

Kidney length and width were measured on the VD view (Fig. 6.2) and compared with the length of the second lumbar vertebral body on the VD view (Wagner and Kirberger, 2005a; Eshar et al., 2013). Positions of the cranial and caudal poles of the kidneys with respect to the lumbar vertebrae were recorded on both RL and VD views.

6.2.3 Ultrasonography

Animals were positioned in dorsal recumbency, the ventral abdominal area was clipped and ultrasound coupling gel (Ultra Sound Gel, Portfolio Pharmaceuticals Ltd, Johannesburg, SA: Ultrasound gel, Henley's medical, Hertfordshire, UK) was applied. Abdominal ultrasonography was performed using either a LogicScan 128 EXT-1Z (Telemed Ltd., Vilnius, Lithuania) with a 7–10 MHz multifrequency linear transducer or a Landwind C40 (Shenzhen Landwind Industry Co Ltd, Shenzhen, China) with a 7.5 MHz linear transducer.

The length of the kidneys and wall thickness of the urinary bladder were measured on sagittal images. The width and height of the kidneys were measured on transverse images. The maximum splenic thickness was measured on parasagittal images of the left abdomen. All measurements were performed on frozen images with electronic callipers. For the urinary bladder, wall thickness was measured at the midventral location. Echogenicity of the renal cortex was compared to that of the splenic and liver parenchyma in 9/9 and 5/9 animals, respectively.

6.2.4 Data analysis

Data was analysed using Stat View® statistical package (SAS Institute, Cary, NC, USA). Mean, range and standard deviation (SD) were calculated. Paired t-test was used to compare the mean length of lumbar vertebral bodies, position of the cranial and caudal poles of the right and left kidneys on the VD versus (vs.) RL views, dimensions of the left vs. right kidneys and length of the second lumbar vertebral body on the VD vs. RL views. Unpaired t-test was used to compare the mean age, weight and dimensions of the vertebral bodies and kidneys between gender groups. Statistical significance was accepted at $P \leq 0.05$. Data is expressed as mean ± SD.

6.3 RESULTS

6.3.1 Musculoskeletal system

Of the 13 animals, 12 had seven lumbar vertebrae and one animal (male) had six lumbar vertebrae (Fig. 6.3). The mean length of the lumbar vertebral bodies increased significantly ($P < 0.0001$) from cranial to caudal up to the fifth lumbar vertebra. There was no significant ($P = 0.47$) difference in the mean length of the fifth and sixth lumbar vertebral bodies. The mean length of the seventh lumbar vertebral body was significantly ($P < 0.0001$) lower than that of the sixth lumbar vertebral body. The first lumbar vertebral body was the shortest (Table 6.1). There was a significant ($P = 0.03$) difference in the mean lengths of the second lumbar vertebral body obtained on the RL and VD views. There was no significant ($P > 0.05$) difference in the mean lengths and heights of lumbar vertebral bodies between male and female animals.

The sacrum consisted of three segments (12/13) (Figs 6.3 and 6.4) except in one animal (female: 2.8-year-old) where it consisted of two segments. The body of the sacrum was not fused in one and two animals with two and three sacral vertebrae, respectively. In the latter, it was seen between the last two sacral vertebrae. The os penis was seen in all male animals. The os clitoridis was not seen. Radiographic measurements of the lumbar vertebral bodies are shown in Tables 6.1 and 6.2.

Abdominal serosal detail was excellent in all animals and the majority of animals had a generous amount of abdominal fat (Fig. 6.4). On the RL view, accumulation of a large amount of abdominal fat was seen in the retroperitoneal space and cranioventral abdomen ventral to the stomach and caudal to the liver. Of the 13 animals, seven had a sagging ventral abdominal wall with fat opacity. Animals aged three years and less (2/13) had less abdominal fat.

On the VD view, hypaxial muscles were conspicuous (Fig. 6.4) except in the two lightest (< 2.5 kg) animals. Abdominal fat was seen between the lateral margin of the hypaxial muscles and the lateral body wall (Fig. 6.4). Abdominal organs were partially obscured by superimposition of the sagging ventral abdominal wall (Fig. 6.3). The lateral margins of the soft tissue opacity created by the conspicuous hypaxial muscles ended caudally at the level of the crest of the ilium (Fig. 6.4) whereas the sagging ventral abdominal wall ended either cranial or caudal to the crest of the ilium (Fig. 6.3).

6.3.2 Lymphatic system

On the VD view, the spleen was seen in the majority (12/13) of animals (Figs 6.3 and 6.4). It was either triangular (5/12) or fusiform (7/12) (Figs 6.3 and 6.4). The spleen was frequently (9/12) located adjacent to the left body wall lateral to the left kidney (Fig. 6.3). In three animals (3/12) less than 8-years, the spleen was smaller and located adjacent to the left body wall between the gastric fundus and the left kidney. On the RL view, the head of the spleen was seen in 3/13 animals.

On ultrasonography the spleen was initially difficulty to find. It was either triangular (7/9) (Fig. 6.5a) or sausage shaped (2/9) on parasagittal scans of the left abdomen. The splenic parenchyma was iso- (8/9) to hypoechoic (1/9) to renal cortex (Fig. 6.5a). The mean splenic thickness was 7.56 ± 1.68 mm (Table 6.5).

6.3.3 Glandular system

The liver was less prominent and well contained within the ribcage (Fig. 6.1). On the RL view, the caudoventral end of the liver was seen in all animals and extended caudally beyond the costal arch in only 3/13 animals. The visibility of the caudoventral margin of the liver was facilitated by the presence of a generous amount of fat in the cranioventral abdomen.

6.3.4 Digestive system

On the RL view, the mean angle of the gastric axis was 119.77 ± 6.97º. On the VD view, the pylorus was mostly (11/13) located to the right (Fig. 6.3) and

rarely (2/13) at the midline. The abdominal serosal detail was good (Fig. 6.4). The large intestine could be distinguished from the small intestine in 9/13 animals. The mean diameter of the small intestine and ratio compared to the height of the second lumbar vertebral body were 0.87 ± 0.21 cm and 1.11 ± 0.26, respectively. For the large intestine the mean diameter and ratio compared to the length and height of the second lumbar vertebral body were 1.68 ± 0.49 cm, 1.09 ± 0.30 and 2.18 ± 0.60, respectively. Radiographic measurements of the gastrointestinal tract are shown in Table 6.3.

6.3.5 Urinary system

Both kidneys were visible on the RL and VD views. On the VD view, the right and left kidneys were bean-shaped (Fig. 6.4). The left kidney was located caudal to the gastric fundus, whereas the right kidney's cranial pole was in close contact with the right liver (Fig. 6.4). On the RL view, the left kidney was frequently bean-shaped (11/13) and rarely ovoid (2/13) whereas the right kidney was either ovoid (7/13) or bean-shaped (6/13). The right kidney was positioned more cranial (Fig. 6.4) and dorsal (Fig. 1) to the left kidney.

The right kidney's mean length in cm ($P = 0.0032$) and ratio compared to the length of the second lumbar vertebral body ($P < 0.0036$) were significantly larger than for the left kidney. The left kidney's mean width in cm ($P < 0.0307$) and ratio compared to the length of the second lumbar vertebral body ($P < 0.0377$) were significantly larger than for the right kidney. The mean length and width of the right and left kidneys and ratio compared to the length of the

second lumbar vertebral body were not significantly different ($P > 0.05$) between gender groups.

On the RL and VD views of animals with seven lumbar vertebrae (12/13) the cranial pole of the right kidney was located at the level of either the first (RL: 8/12; VD: 10/12) or second (RL: 4/12; VD: 2/12) lumbar vertebra, whereas the caudal pole was located at the level of the third (RL: 10/12; VD: 10/12) or fourth (RL: 2/12; VD: 2/12) lumbar vertebra. For the left kidney the cranial pole was located at the level of either the second (RL: 4/12; VD: 11/12) or third (RL: 8/12; VD: 1/12) lumbar vertebra, whereas the caudal pole was located at the level of the third (RL: 1/12; VD: 1/12), fourth (RL: 6/12; VD: 10/12) or fifth (RL: 5/12; VD: 1/12). There was a significant difference in the mean position of the cranial ($P = 0.0024$) and caudal ($P = 0.0388$) poles of the left kidney on the VD and RL views. In an animal with six lumbar vertebrae the cranial poles of the right and left kidneys were located at the level of the 13th thoracic vertebra and first lumbar vertebra, respectively, on the RL and VD views (Fig. 6.3).

The urinary bladder was identified in 11/13 animals and was positioned intra-abdominal. It was oblong in nine and ovoid in two animals, respectively. Radiographic measurements of the kidneys are shown in Table 6.4.

On ultrasonography, the kidneys appeared ovoid on both transverse and sagittal images (Fig. 6.6). In all nine animals, the renal medulla was hypoechoic to the cortex with good corticomedullary distinction (Fig. 6.6). The

renal cortex was iso- (8/9) to hyperechoic (1/9) to the splenic parenchyma (Fig. 6.5a) and hyperechoic (5/5) to the liver parenchyma (Fig. 6.5b). The right kidney's mean width was significantly ($P = 0.03$) larger compared to that of the left kidney. Furthermore, the mean length ($P = 0.24$) and height ($P = 0.97$) of the right kidney were larger than the ones of the left kidney although this was not statistically significant. The urinary bladder contained anechoic urine. The mean thickness of the urinary bladder wall was 0.82 ± 0.34 mm. Ultrasonographic measurements of the kidneys and urinary bladder wall are shown in Table 6.5.

6.3.6 Other findings

Interarcuate spaces between caudal thoracic to cranial coccygeal vertebrae were wide (Fig. 6.4). Incidental spondylosis deformans of sacrococcygeal and coccygeal vertebrae was observed in a 19.8-year-old female ring-tailed lemur.

6.4 DISCUSSION

In primates, the number of lumbar vertebrae varies from three to ten with low numbers of lumbar vertebrae found in hominoids (Swindler, 1998). The presence of seven lumbar vertebrae in the majority of animals (12/13) observed in this study is very similar to catarrhine monkeys (Silverman and Morgan, 1980; Swindler, 1998), which is different from reported studies in the capuchin monkey (*Cebus apella*) (6) (Alves et al., 2012) and common marmoset (*Callithrix jacchus*) (6.35) (Wagner and Kirberger, 2005a). The

increase in size of the lumbar vertebral bodies from cranial to caudal observed in this species has also been reported in other primate species (Ankel-Simons, 2007). In this study, the first lumbar vertebral body was consistently shorter than other lumbar vertebrae, which is different to the common marmoset (Wagner and Kirberger, 2005a). In the common marmoset the last lumbar vertebra was the shortest compared to other lumbar vertebrae (Wagner and Kirberger, 2005a).

The presence of two sacral vertebrae observed in the female ring-tailed lemur has also been reported in the female common marmoset (Wagner and Kirberger, 2005a). Further, variation in the number of sacral vertebrae has also been reported in the capuchin monkey (three to four) (Alves et al., 2012). The wide interarcuate spaces observed in this species is different from domestic cats and dogs (Kirberger, 2006) and most likely allows flexibility of the spine as an adaptation to jumping. The radiographic visualisation of the os penis in the male was previously reported (Drea and Weil, 2008). The os clitoridis was not seen radiographically in female animals in this study due to the glans clitoridis not being collimated on abdominal radiographs as a result of its caudal location (Drea and Weil, 2008).

The excellent abdominal detail observed in this study is different from the reported study in the common marmoset (Wagner and Kirberger, 2005a) but similar to the domestic cat (Thrall and Robertson, 2011). Abdominal contrast in this species was enhanced by the presence of abdominal fat. The conspicuous hypaxial muscles and superimposition of the sagging ventral

abdominal skin on the VD view, should not be misdiagnosed as an abdominal mass. The former has also been observed in the domestic cat and is the result of pronounced retroperitoneal fat, which provides contrast to the margins of the hypaxial muscles (Thrall and Robertson, 2011).

On the RL view, fat in the cranioventral abdomen was seen between the ventral border of the stomach and the dorsal border of the caudoventral extension of the liver, which is different from the domestic cat. In the domestic cat it accumulates mostly ventral to the liver, which may result in dorsal displacement of the liver margins and give a false indication of a small liver (Thrall and Robertson, 2011).

The radiographic visualisation of the spleen in the ring-tailed lemur is similar to domestic cats and dogs (Thrall and Robertson, 2011). The identification of the spleen mainly on the VD view is similar to domestic cats (Thrall and Robertson, 2011) but different from dogs in which the spleen is commonly seen on the lateral and VD views (Thrall and Robertson, 2011). Further, in domestic cats the spleen occasionally can be seen on lateral radiographs or not at all (Thrall and Robertson, 2011), which is similar to the ring-tailed lemur.

The difficulty in identification of the spleen on ultrasonography, which was encountered initially, is attributed to the small size and different echogenicity of the spleen in this species. The mean splenic thickness of the ring-tailed lemur (7.56 mm) is intermediate between the common marmoset (6.65 mm) (Wagner and Kirberger, 2005b) and vervet monkey (*Chlorocebus sabaeus*)

(13.9 mm) (Amory et al., 2013). The liver in the ring-tailed lemur is less prominent compared to domestic cats and dogs (Thrall and Robertson, 2011) and common marmosets (Wagner and Kirberger, 2005a).

The mean diameter of the small intestine observed in this study (0.87 ± 0.21 cm) is within the reported small intestinal diameter (<1.2 cm) (Morgan, 1981) and close to the median value (1.1 cm) reported in normal domestic cats (Adams et al., 2010). Further, the mean ratio of the small intestinal diameter to the height of the second lumbar vertebral body obtained in this study (1.11 ± 0.26) is close to the median value (1.28) reported in domestic cats with no signs of gastrointestinal tract (GIT) disease (Adams et al., 2010). The mean diameter of the large intestine (1.68 ± 0.49 cm) and ratio compared to the height of the second lumbar vertebral body (2.18 ± 0.60) obtained in this study are lower than the median values 2.4 cm and 2.79, respectively, reported in domestic cats without signs of GIT disease (Adams et al., 2010).

The visibility of both kidneys on the VD and RL views in this species was enhanced by the presence of retroperitoneal fat. The cranial location of the right kidney compared to the left kidney is similar to the brown lemur (*Eulemur fulvus*) (Raharison et al., 2009), domestic cats and dogs (Feeney and Johnston, 2007) but different from the common marmoset (Wagner and Kirberger, 2005a). In the latter the right kidney is positioned caudal to the left kidney as a result of a large sized liver (Wagner and Kirberger, 2005a).

The mean lengths of the left (3.08 ± 0.25 cm) and right (3.22 ± 0.26) kidneys obtained from radiographic measurements in this study are within the reported range (3.0–4.5 cm) in domestic cats (Graham, 2011). Further, the mean ratio of the kidney's length to the length of the second lumbar vertebral body (left: 2.03 ± 0.20; right: 2.13 ± 0.20) obtained in this study is within the reported range (2.1 to 3.2) in domestic cats (Larson, 2009). The mean length of the left and right kidneys obtained from ultrasonographic measurement in ring-tailed lemurs (left: 3.00 cm; right: 3.13 cm) are similar to the reported means in brown lemurs (left: 3.00 cm; right: 3.05 cm) (Raharison et al., 2009) and are within the reported range (3.0-4.3 cm) in domestic cats (Larson 2009).

The ultrasonographic appearance of the ring-tailed lemur kidney i.e. ovoid, surrounded by a thin echogenic capsule with an outer hyperechoic cortex compared to inner medulla and the visualisation of the C-shaped hyperechoic renal sinus on the transverse images is similar to domestic cats and dogs (Nyland et al., 2002). In non-human primates (Gaschen et al., 2000; Wagner and Kirberger, 2005b; Amory et al., 2013) the echogenicity of the renal cortex has been reported to be either isoechoic or hyperechoic when compared to that of the spleen, which is similar to this study.

Further, the echogenicity of the renal cortex in non-human primates (Gaschen et al., 2000; Wagner and Kirberger, 2005b; Alves et al., 2007; Amory et al., 2013) has been reported to be isoechoic or hyperechoic when compared to the liver parenchyma, which is also similar to this study. The ultrasonographic appearance of the ring-tailed lemur urinary bladder is similar to that of

domestic cats and dogs (Nyland et al., 2002). The mean wall thickness of the urinary bladder obtained in this study (0.82 ± 0.34 mm) is lower than the reported range in domestic cats (1.3–1.7 mm) (Finn-Bodner, 1995). However, the thickness of the urinary bladder wall depends on the degree of the urinary bladder distension (Geisse et al., 1997).

Species-specific differences exist in radiographic and ultrasonographic abdominal anatomy. Knowledge of the normal radiographic and ultrasonographic abdominal anatomy of the ring-tailed lemur may prove to be a valuable diagnostic tool.

6.5 ACKNOWLEDGEMENTS

The authors would like to thank the Organisation for Women in Science for the Developing World (OWSD), Swedish International Development Cooperation Agency (SIDA), University of Pretoria, Johannesburg and Bristol zoos for supporting this study. Drs Brett Gardner and Kathryn Perrin, Ms. Fania Mohlala, sisters and animal handlers of the Bristol and Johannesburg zoos for their assistance during radiography and ultrasonography. Mrs. Charmaine Vermeulen and Mrs. Wilma Olivier of the University of Pretoria for their assistance in photography and administrative work, respectively.

6.6 REFERENCES

Adams, W. M., L. A. Sisterman, J. M. Klauer, B. M. Kirby, and T. L. Lin, 2010: Association of intestinal disorders in cats with findings of abdominal radiography. J. Am. Vet. Med. Assoc. **236,** 880–886.

Alves, F. R., F. B. Costa, M. M. S. Arouche, A. C. E. Barros, M. A. Miglino, L. C. Vulcano, and P. C. Guerra, 2007: Ultrasonographic evaluation of the urinary system, liver and uterus of *Cebus apella* monkey. Pesq. Vet. Bras. **27,** 377–382.

Alves, F. R., F. B. Costa, P. P. Machado, A. N. Diniz, A. V. C. Araújo, C. E. Ambrósio, and P. C. Guerra, 2012: Anatomical and radiographic appearance of the capuchin monkey thoracic cavity (*Cebus apella*). Pesq. Vet. Bras. **32,** 1345–1350.

Amory, J. T., W. M. du Plessis, A. Beierschmitt, J. Beeler-Marfisi, R. M. Palmour, and T. Beths, 2013: Abdominal ultrasonography of the normal St. Kitts vervet monkey (*Chlorocebus sabaeus*). J. Med. Primatol. **42,** 28–38.

Ankel-Simons, F., 2007: Primate Anatomy: An Introduction. Boston: Academic Press.

Budnitz, N., and K. Dainis, 1975: *Lemur catta*: ecology and behaviour. In: Lemur Biology (I. Tattersall and R. W. Sussman, eds). New York: Plenum Press, pp. 219–235.

Burton, M., R. J. Morton, E. Ramsay, and E. L. Stair, 1986: Coccidioidomycosis in a ring-tailed lemur. J. Am. Vet. Med. Assoc. **189,** 1209–1211.

Chang, J., J. L. Wagner, and R. M. Kornegay, 1979: Spontaneous cholangiocarcinoma in a ring-tailed lemur (*Lemur catta*). Lab. Anim. Sci. **29,** 374–376.

Drea, C. M., and A. Weil, 2008: External genital morphology of the ring-tailed lemur (*Lemur catta*): Females are naturally “masculinised”. J. Morphol. **269,** 451–463.

Eshar, D., J. A. Briscore, and W. Mai, 2013: Radiographic kidney measurements in North American pet ferrets (*Mustela furo*). J. Small. Anim. Pract. **54,** 15–19.

Feeney, D. A., and G. R. Johnston, 2007: The kidneys and ureters. In: Textbook of Veterinary Diagnostic Radiology (D. E. Thrall, ed). St. Louis: Saunders Elsevier, pp. 693–707.

Finn-Bodner, S. T., 1995: The urinary bladder. In: Practical Veterinary Ultrasound (R. E. Cartee, B. A. Selcer, J. A. Hudson, S. T. Finn-Bodner, M. B. Mahaffey, P. L. Johnson and K. W. Marich, eds). Philadelphia: William & Wilkins, pp. 200–235.

Gaschen, L., K. Menninger, and H. J. Schuurman, 2000: Ultrasonography of the normal kidney in the cynomolgus monkey (*Macaca fascicularis*): morphologic and Doppler findings. J. Med. Primatol. **29,** 76–84.

Geisse, A. L., J. E. Lowry, D. J. Schaeffer, and C. W. Smith, 1997: Sonographic evaluation of urinary bladder wall thickness in normal dogs. Vet. Radiol. Ultrasound. **38,** 132–137.

Graham, J. P., 2011: Kidneys and proximal ureters. In: BSAVA Manual of Canine and Feline Ultrasonography (F. Barr and L. Gaschen, eds). Gloucester: BSAVA, pp. 110–123.

IUCN, 2014: IUCN Red list of threatened species. Version 2014.3. Available at: http://www.iucnredlist.org (accessed on 18 November 2014).

Jones, S. R., and H. W. Casey, 1981: Primary renal tumors in nonhuman primates. Vet. Pathol. **18,** 89–104.

Jungle, R. E., 2003: Prosimians. In: Zoo and Wild Animal Medicine (M. E. Fowler and R. E. Miller, eds). Missouri: Saunders, pp. 334–346.

Kirberger, R. M., 2006: Spine-general. In: BSAVA manual of canine and feline musculoskeletal imaging (F. Barr and R. M. Kirberger, eds). Gloucester: BSAVA, pp. 220–232.

Larson, M. M., 2009: The kidneys and ureters. In: BSAVA Manual of Canine and Feline Abdominal Imaging (R. O'Brien, and F. Barr, eds). BSAVA, Gloucester, pp. 185–204.

Luzón, M., C. de la Fuente-López, E. Martínez-Nevado, J. Fernández-Morán, and F. Ponce-Gordo, 2010: Taenia crassiceps cysticercosis in a ring-tailed lemur (*Lemur catta*). J. Zoo. Wildl. Med. **41,** 327–330.

Morgan, J. P., 1981: The upper gastrointestinal examination in the cat: normal radiographic appearance using positive contrast medium. Vet. Radiol. Ultrasound. **22,** 159–169.

Muller, S., A. Oevermann, C. Wenker, H. J. Altermatt, and N. Robert, 2007: A mixed epithelial and stromal tumor of the kidney in a ring-tailed lemur (*Lemur catta*). Vet. Pathol. **44,** 243–246.

Nyland, T. G., J. S. Mattoon, E. J. Herrgesell, and E. R. Wisner, 2002: Urinary tract. In: Small Animal Diagnostic Ultrasound (T. G. Nyland and J. S. Mattoon, eds). Philadelphia: Saunders, pp. 158–195.

Osman Hill, W. C., 1953: Primates (Comparative Anatomy and Taxonomy). I. Strepsirhini. Edinburgh: University Press.

Palotay, J. L., and H. Uno, 1975: Hydatid disease in four nonhuman primates. J. Am. Vet. Med. Assoc. **167,** 615–618.

Patten, C. J., 1902: The form and position of the thoracic and abdominal viscera of the ruffed lemur (*Lemur varius*). Trans. Royal. Acad. Med. Ireland. **20,** 441–473.

Raharison, F., G. Mogicato, and J. Sautet, 2009: Anatomy and ultrasonography of the normal kidney in brown lemurs: *Eulemur fulvus*. Am. J. Primatol. **71,** 647–653.

Remick, A. K., A. J. Van Wettere, and C. V. Williams, 2009: Neoplasia in prosimians: case series from captive prosimians population and literature review. Vet. Pathol. **46,** 746–772.

Scott, H. H., and H. Camb, 1925: Congenital malformations of the kidney in reptiles, birds and mammals. Proc. Zool. Soc. Lond. **95,** 1259–1269.

Seiler, G., and W. Maï, 2009: The stomach. In: BSAVA Manual of Canine and Feline Abdominal Imaging (R. O'Brien, and F. Barr, eds). BSAVA, Gloucester, pp. 87–109.

Shahar, R., I. H. Horowitz, and I. Aizenberg, 1995: Disseminated hydatidosis in a ring-tailed lemur (*Lemur catta*). J. Zoo. Wildl. Med. **26,** 119–122.

Silverman, S., and J. P. Morgan, 1980: Thoracic radiography of the normal rhesus macaque (*Macaca mulatta*). Am. J. Vet. Res. **41,** 1704–1719.

Swindler, D. R., 1998: Introduction to the Primates. Seattle: University of Washington Press.

Takeshita, R. S. C., F. O. B. Monteiro, F. L. de Miranda Lins e Lins, G. A. da Silva, C. Faturi, L. N. Coutinho, M. V. B. Monteiro, T. Kugelmeier, P. H. G. de Castro, and J. A. P. C. Muniz, 2011: Haematological, hepatic and renal evaluation in *Aotus azarai infulatus*. J. Med. Primatol. **40,** 104–110.

Taylor, K., 2009: Ring-tailed Lemur Husbandry Manual. New South Wales: Taronga Western Plains Zoo.

Thrall, D. E., and I. D. Robertson, 2011: The abdomen. In: Atlas of Normal Radiographic Anatomy and Anatomic Variants in the Dog and Cat. St. Louis: Elsevier, pp. 169–206.

Wagner, W. M., and R. M. Kirberger, 2005a: Radiographic anatomy of the thorax and abdomen of the common marmoset (*Callithrix jacchus*). Vet. Radiol. Ultrasound. **46,** 217–224.

Wagner, W. M., and R. M. Kirberger, 2005b: Transcutaneous ultrasonography of the abdomen in the normal common marmoset (*Callithrix jacchus*). Vet. Radiol. Ultrasound. **46,** 251–258.

Zordan, M., M. Tirado, and C. López, 2012: Hepatic capillariasis in captive ring-tailed lemurs (*Lemur catta*). J. Zoo. Wildl. Med. **43,** 430–433.

6.7 TABLES

Table 6.1 Radiographic measurement of the length (cm) of lumbar vertebral bodies not compensated for magnification in captive ring-tailed lemurs

Vertebra	Variable	Number	Mean ± SD (cm)	Range (cm)
L1	Length RL	13	1.45 ± 0.04	1.38 – 1.50
L2	Length RL	13	1.55 ± 0.06	1.44 – 1.60
	Length VD	13	1.51 ± 0.07	1.40 – 1.60
L3	Length RL	13	1.66 ± 0.06	1.50 – 1.73
L4	Length RL	13	1.75 ± 0.06	1.60 – 1.81
L5	Length RL	13	1.84 ± 0.07	1.70 – 1.93
L6	Length RL	13	1.82 ± 0.12	1.54 – 2.00
L7	Length RL	12	1.57 ± 0.09	1.42 – 1.70

L, lumbar vertebra; RL, right lateral; VD, ventrodorsal

Table 6.2 Radiographic measurement of the height (cm) of lumbar vertebral bodies not compensated for magnification in captive ring-tailed lemurs

Vertebra	Variable	Number	Mean ± SD (cm)	Range (cm)
L1	Height RL	13	0.68 ± 0.05	0.60 – 0.78
L2	Height RL	13	0.77 ± 0.04	0.69 – 0.80
L3	Height RL	13	0.80 ± 0.06	0.70 – 0.90
L4	Height RL	13	0.79 ± 0.09	0.67 – 0.90
L5	Height RL	13	0.79 ± 0.06	0.64 – 0.90
L6	Height RL	13	0.85 ± 0.07	0.76 – 1.00
L7	Height RL	12	0.88 ± 0.06	0.80 – 1.00

L, lumbar vertebra; RL, right lateral

Table 6.3 Radiographic measurements of the gastrointestinal tract not compensated for magnification in captive ring-tailed lemurs

Variable	Number	Mean ± SD	Range
Angle of gastric axis [º]	13	119.77 ± 7.00	103.00 – 130.00
Small intestinal diameter (SID) [cm]	13	0.87 ± 0.21	0.50 – 1.20
SID: HL2[a]	13	1.11 ± 0.26	0.63 – 1.50
Large intestinal diameter (LID) [cm]	13	1.68 ± 0.49	1.14 – 2.50
LID: HL2	13	2.18 ± 0.60	1.44 – 3.13
LID: LL2[b]	13	1.09 ± 0.30	0.75 – 1.56

[a]Height of the second lumbar vertebral body

[b]Length of the second lumbar vertebral body

Table 6.4 Radiographic measurements of kidneys not compensated for magnification in captive ring-tailed lemurs

Variable	Number	Mean ± SD	Range
Left kidney			
Length [cm]	13	3.08 ± 0.25	2.80 – 3.59
L: LL2[a]	13	2.03 ± 0.20	1.75 – 2.49
Width [cm]	13	2.33 ± 0.21	2.00 – 2.72
W: LL2[b]	13	1.53 ± 0.15	1.35 – 1.80
Right kidney			
Length [cm]	13	3.22 ± 0.26	2.87 – 3.70
L: LL2	13	2.13 ± 0.20	1.85 – 2.57
Width [cm]	13	2.24 ± 0.19	1.98 – 2.53
W: LL2	13	1.48 ± 0.14	1.29 – 1.72

[a]Ratio of the kidney's length to length of the second lumbar vertebral body

[b]Ratio of the kidney's width to the length of the second lumbar vertebral body

Table 6.5 Ultrasonographic measurements of the spleen, kidneys and urinary bladder in captive ring-tailed lemurs

Variable	Number	Mean ± SD	Range
Left kidney [cm]			
Length	9	3.00 ± 0.23	2.60 – 3.31
Width	9	2.26 ± 0.24	1.87 – 2.71
Height	9	1.69 ± 0.45	1.26 – 2.79
Right kidney [cm]			
Length	9	3.13 ± 0.20	2.73 – 3.43
Width	9	2.54 ± 0.13	2.34 – 2.78
Height	9	1.69 ± 0.33	1.25 – 2.25
Urinary bladder wall thickness [mm]	5	0.82 ± 0.34	0.60 – 1.40
Splenic thickness [mm]	9	7.56 ± 1.68	4.2 – 10

6.8 FIGURES

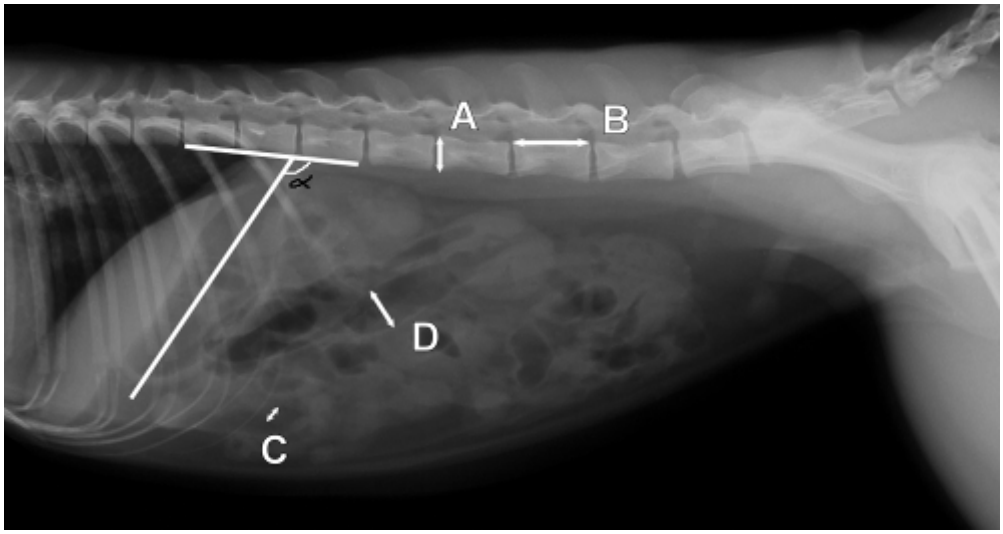

Fig. 6.1 Right lateral abdominal radiograph of an adult ring-tailed lemur illustrating radiographic measurements. (A) Vertebral body height, (B) vertebral body length, (C) external diameter of small intestine, (D) external diameter of large intestine and α = angle of gastric axis.

Fig. 6.2 Ventrodorsal abdominal radiograph of an adult ring-tailed lemur illustrating radiographic measurements. (A) Vertebral body length, (B) length of the kidney and (C) width of the kidney.

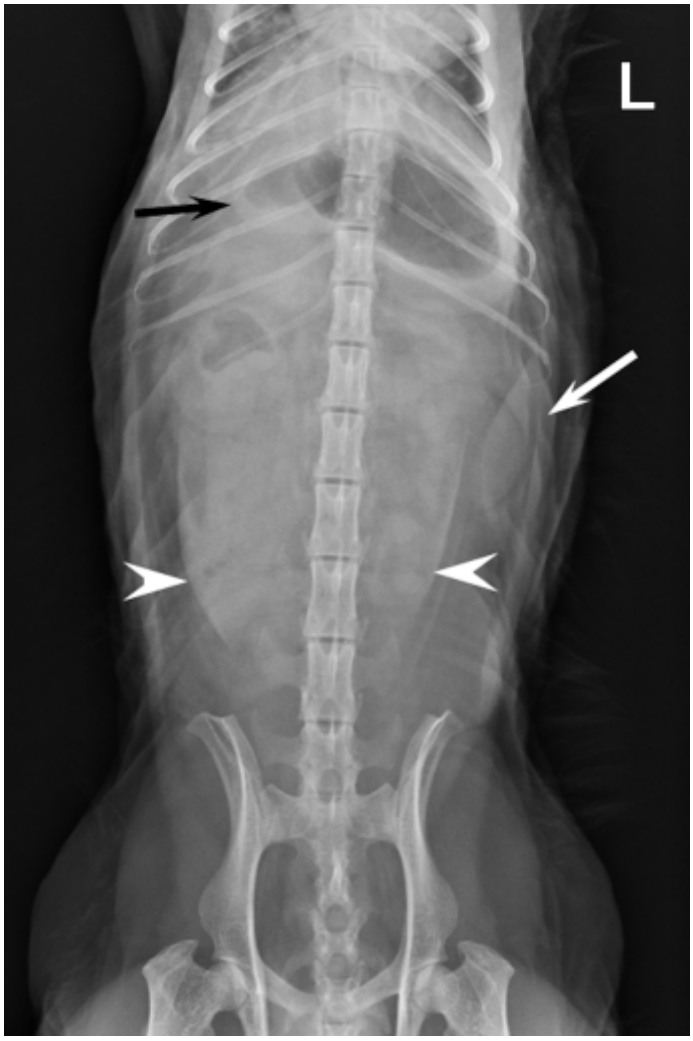

Fig. 6.3 Ventrodorsal abdominal radiograph of a 10.3-year-old (2.99 kg) male ring-tailed lemur. Note the presence of six lumbar vertebrae as well as the increase in soft tissue opacity as a result of superimposition of the sagging ventral abdominal wall partially obscuring abdominal organs (white arrow heads). The pylorus is located to the right of the midline (black arrow). The fusiform spleen is indicated by the white arrow. L = left.

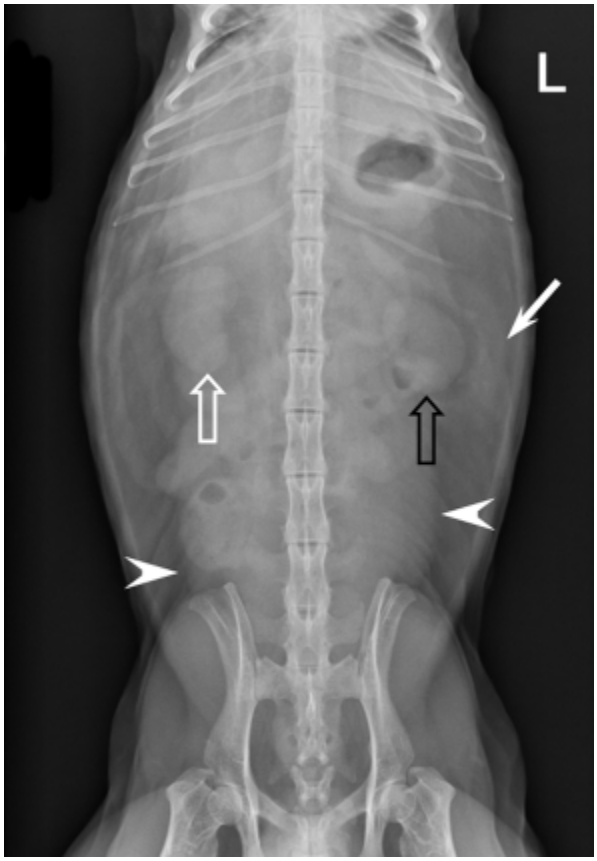

Fig. 6.4 Ventrodorsal abdominal radiograph of an 8.6-year-old (2.98 kg) male ring-tailed lemur. Note the wide interarcuate spaces from the caudal thoracic to cranial coccygeal vertebrae. The right kidney (open white arrow) is located more cranial than the left kidney (open black arrow). Note also the conspicuousness of the hypaxial muscles (white arrow heads) and the visualization of abdominal fat between the lateral margin of hypaxial muscles and the lateral body wall. The fusiform spleen is indicated by a white arrow. L = left.

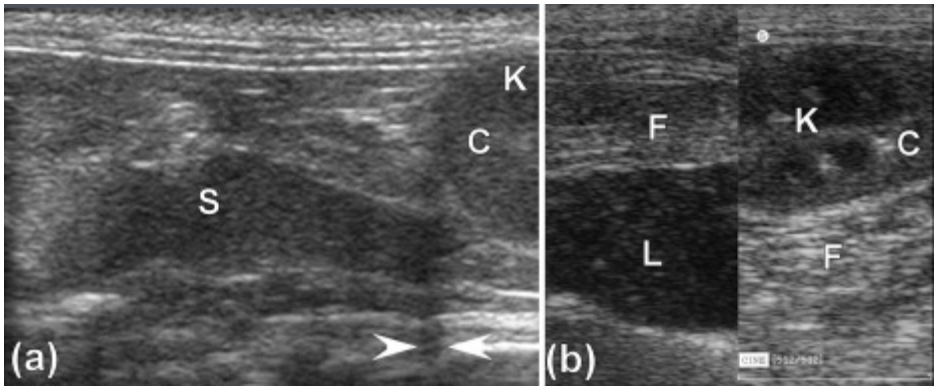

Fig. 6.5 (a) Sagittal sonographic image of the left kidney (K) of a 16.8-year-old (3.14 kg) female ring-tailed lemur. The renal cortex (C) is hyperechoic to the splenic parenchyma (S). Note the presence of an edge shadowing artefact (white arrow heads) from the kidney. (b) A split screen of sagittal sonographic images of the kidney (K) and Liver (L) of a 10.67-year-old (3.3 kg) female ring tailed lemur. The renal cortex (C) is hyperechoic to the liver parenchyma (L). F = fat.

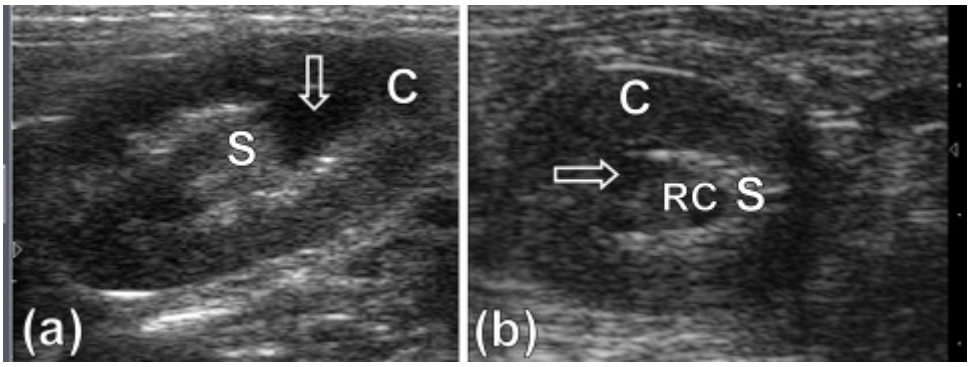

Fig. 6.6 Sagittal (a) and transverse (b) sonographic images of the right kidney of a 2.8-year-old (2.44 kg) and 13.8-year-old (3.12 kg) female ring-tailed lemur. Note the oval kidneys, hypoechoic medulla (open white arrow) when compared to cortex (C). (RC) Renal crest and (S) renal sinus.

CHAPTER 7

THORACIC LIMB MORPHOLOGY OF THE RED PANDA (*AILURUS FULGENS*) EVIDENCED BY GROSS OSTEOLOGY AND RADIOGRAPHY

7.1 INTRODUCTION

The red panda (*Ailurus fulgens*) is classified as a vulnerable species by the International Union for Conservation of Nature and Natural Resources (IUCN) (IUCN, 2014). It is a species commonly kept in zoological gardens. The red panda is an arboreal animal spending most of its time in trees. Although the red panda spends most of its time in trees it forages primarily on the ground (Roberts and Gittleman, 1984).

The red panda is affected by diseases involving the musculoskeletal system similar to those reported in domestic cats and dogs and radiography is commonly used as the first diagnostic imaging modality. Diseases involving the musculoskeletal system of the thoracic limb such as osteoarthritis and hyperostostic bone disease have been reported in the red panda (Lynch et al., 2002; Philippa and Ramsay, 2011; Preece, 2011).

Knowledge of the normal gross osteology and radiographic anatomy of the thoracic limb is important for accurate interpretation and diagnosis of musculoskeletal diseases involving the thoracic limb. The normal gross

osteology and radiographic anatomy of the thoracic limb in companion animals is well documented (Nickel et al., 1986; Thrall and Robertson, 2011; Smallwood and Spaulding, 2013), which serves as a reference for diagnosis of musculoskeletal diseases.

To the author's knowledge little information is available on the gross osteology of the thoracic limb of the red panda (Carlsson, 1925) and description of normal radiographic anatomy is missing. The aim of this study was to describe the morphology of the thoracic limb of the red panda evidenced by gross osteology and radiography as a reference for clinical use.

7.2 MATERIALS AND METHODS

7.2.1 Radiography

Radiography of the right thoracic limb was performed in seven adult, intact, skeletally mature captive red pandas (*Ailurus fulgens*) belonging to the Johannesburg zoo (JHB). Of the seven animals, five were males and two were females. The age of the animals ranged from 1.4 years to 14.3 years (mean: 7.3 ± 5.4 years). The mean weight of the animals was 4.5 ± 0.7 kg (range: 3.7 kg–5.6 kg). Radiography was performed under general anaesthesia during annual health examinations and a table top technique was used.

In six animals, an x-ray machine EVA-HF525 (Comed Medical System Co. Ltd, Kyunggi, Korea) was used at a source to image distance (SID) of 95 cm.

An automatic X-ray film processor model CP-345 (ELK Corporation, Tokyo, Japan) was used. Mammography films (UM-MA, Fujifilm Corporation, Tokyo, Japan) were used in combination with mamoray screens (Fujifilm Europe GmbH, Duesseldorf, Germany). All radiographs were obtained using a kVp range of 46–50 and 5 mAs. Radiographic images were digitalized using a digital camera (CANON 5DMARK2, Canon Inc., Tokyo, Japan).

In one animal, radiography was performed using a Siemens Polymat 50 x-ray machine (Siemens, Munich, Germany) and images were obtained using a computed radiography system, Fuji Axim FCR Capsula XL (Fujifilm Corporation, Tokyo, Japan) at a SID of 100 cm. A kVp range of 48–60 and mAs range of 4–5 was used.

Previous radiographs of the right thoracic limb of two red pandas, which were taken before skeletal maturity for clinical evaluation (one at the age of 10 months and the other at the age of 7 months) at the Bristol zoo were retrieved and evaluated for the location of physes. This study was approved by the Animal Use and Care Committee (AUCC) of the University of Pretoria.

7.2.2 Gross osteology

Bone specimens of adult skeletally mature animals from the National Museum of Scotland (one) and two euthanased animals from the JHB zoo were used for gross osteology study. Photographs of bone specimens were obtained using a digital camera (CANON 5DMARK2, Canon Inc., Tokyo, Japan). A report on the myology of the thoracic limb of the red panda (Fisher et al.,

2009) was used to locate the sites for the origins and insertions of different muscles of the thoracic limb on bone specimens and their functions.

7.2.3 Bone measurements

Bone measurements of the right thoracic limb were performed on radiographic images of skeletally mature captive red pandas with the exception of the scapula measurements of which were performed on bone specimens. The maximum lengths of bones were measured from the proximal to the distal extremities. The maximum lengths of the humerus, radius and ulna were measured on the mediolateral (ML) view whereas those of the metacarpals, phalanges and sesamoid bones were measured on the dorsopalmar (DPa) view of the manus.

The craniocaudal (CrCd) diameters of the humerus, radius and ulna were measured on the ML view at mid-diaphysis. The ML diameter of the sesamoid bone for the *M. abductor digiti I longus* was measured on the DPa view of the manus as the maximum diameter perpendicular to the maximum length. Radiographic measurements were not compensated for magnification.

7.2.4 Statistical analysis

Statistical analysis was performed using Stat View© (SAS Institute Inc., Carry, NC, USA) statistical package. Mean, range and standard deviation (SD) were calculated. Data are expressed as mean ± SD.

7.3 RESULTS

7.3.1 Clavicle

A rudimentary clavicle was seen in two animals aged 14.3 years and 1.4 years as an area of mineral opacity in the soft tissues just cranial to the supraglenoid tubercle on the ML view of the shoulder joint (Fig. 7.1a). On the caudocranial (CdCr) view of the shoulder joint, it was seen distomedial to the minor tubercle (Fig. 7.1b). Measurements of bones and sesamoid bones are shown in Tables 7.1–7.3.

7.3.2 Scapula

The scapula was wider craniocaudally and shorter proximodistally with a convex cranial margin (Fig. 7.2a). The proximal half of the caudal margin was almost convex, whereas the distal half was fairly straight with a rough surface (Fig. 7.2a). The mediodistally directed coracoid process was stouter (Fig. 7.2b,c) and the infraglenoid tubercle was well developed (Fig. 7.2b). On the ML view of the shoulder joint, the coracoid process was seen as a curvilinear area of increased mineral opacity caudal to the supraglenoid tubercle (Fig. 7.1a). The articular surface of the glenoid cavity was concave and extended proximal to the lateral area of the supraglenoid tubercle (Fig. 7.2c).

The infraspinous fossa was deep and concave, whereas the supraspinous fossa was convex (Fig. 7.2a). Caudal to the proximal half of the infraspinous fossa, the lateral surface presented with a large area for the origin of the *M. teres major* (Fig. 7.2a). The spine of the scapula was slightly slanted towards

the infraspinous fossa (Fig. 7.2a). The craniodistally directed hamate process was prominently large and flattened mediolaterally (Fig. 7.2a,b,c). On the ML view of the shoulder joint, the hamate process projected cranially beyond the cranial margin of the supraglenoid tubercle (Fig. 7.1a). On the CdCr view, it projected distally beyond the level of the glenoid cavity (Fig. 7.1b). The medial surface of the scapula presented with a triangular facies serrata.

7.3.3 Humerus

The humerus was the longest bone of the thoracic limb (Table 7.1). The proximal extremity of the humerus appeared smaller (Fig. 7.3a). The major and minor tubercles did not extend higher than the head of the humerus (Fig. 7.4a,b,c). The major tubercle was almost square and presented with a flat proximal margin (Fig. 7.4a). When viewed medially, the proximal and cranial margins of the minor tubercle formed approximately a right angle (Fig. 7.4c). On the ML view of the shoulder joint, the major and minor tubercles were further distal than the head of the humerus (Fig. 7.1a). The cranial and proximal margins of the minor tubercle appeared as a square area of increased mineral opacity caudal to the intertubercular groove (Fig. 7.1a). On the CdCr view of the shoulder joint, the major and minor tubercles were fairly flattened (Fig. 7.1b).

The area for the insertion of the *M. infraspinatus* (*Facies m. infraspinati*) was prominent, ovoid, elongated in a proximodistal direction and presented as a shallow fossa (Fig. 7.4b). It was at the same level as the head of the humerus (Fig. 7.4b). The area for the insertion of the *M. subscapularis* faced

caudomedially and was wider and prominent (Fig. 7.4c). The tuberosity for the *M. teres minor* was not seen.

The medial epicondyle was well developed and larger than the lateral epicondyle (Fig. 7.4d,f). The medial and lateral epicondyles presented with shallow depressions for the origin of the flexors and extensors of the carpus and digits, respectively. On the ML view of the elbow joint, the medial epicondyle was square, whereas the lateral epicondyle formed an obtuse angle (Fig. 7.5a). On the CrCd view of the elbow joint, the medial and lateral margins of the medial and lateral epicondyles, respectively, appeared undulating (Fig. 7.5b).

The lateral supracondylar crest was prominent (Fig. 7.4d,e,f) and projected caudally beyond the cortical bone on the ML view of the elbow joint (Fig. 7.5a). The medially located supracondylar foramen sloped from caudomedial to craniodistal (Fig. 7.4d,f). On the CrCd view of the elbow joint, the supracondylar foramen was represented by two ovoid radiolucent areas just proximal to the medial epicondyle (Fig. 7.5b) The ovoid olecranon fossa sloped from proximolateral to distomedial (Figs 7.4f and 7.5b). It was moderately deep and elongated mediolaterally (Fig. 7.4f).

The cranial surface of the condyle of the humerus had well defined radial and coronoid fossae (Fig. 7.4d). The articular surface of the condyle of the humerus presented with a larger grooved and medially located trochlea humeri and a small laterally located capitulum humeri (Fig. 7.4d). The cranial

surface of the trochlea humeri had a prominent medial trochlea lip (Fig. 7.4d), whereas the caudal surface was concave (Fig. 7.4f). The proximal and distal physes of the humerus were similar to those of the domestic cat and dog (Figs 7.1c and 7.5c).

7.3.4 Radius and ulna

The ulna was longer and relatively larger than the radius (Fig. 7.3b and Table 7.1). The head of the radius sloped from lateral to medial and was elliptical in outline (Fig. 7.6a,b). It had a concave articular fovea (Fig. 7.6a,b) and was demarcated from the body by a distinct neck (Figs 7.5a,b and 7.6a,b). The medial half of the cranial surface of the head of the radius was flat, whereas its lateral counterpart was convex (Fig. 7.6a). The caudal surface of the head of the radius presented with a smooth band, the articular circumference, for articulation with the radial notch of the ulna (Fig. 7.6b).

The body of the radius curved cranially along the longitudinal axis of the bone (Fig. 7.3b). The proximal half of the cranial surface of the body presented with a flat surface (Fig. 7.6a). The radial tuberosity was prominent and relatively further distally located (Figs 7.5a and 7.6b). It had a longitudinal groove (Fig. 7.6b). The trochlea of the radius had three cranial grooves for the passage of tendons (Fig. 7.6c). Medially, it presented with a prominent crest (Fig. 7.6c and 7.6d). The ulnar notch was concave and elongated craniocaudally.

The ulna curved laterally along the longitudinal axis of the bone. The tuber olecrani was square (Figs. 7.5a and 7.7a). On the ML view of the elbow joint,

a thin straight radiopaque line was seen to run more or less parallel with the proximal margin of the tuber olecrani representing the physeal scar of the tuber olecrani (Fig. 7.5a). The medial coronoid process was prominent and rounded (Figs 7.5a and 7.7b). The anconeal process sloped from lateral to medial (Fig. 7.7b) with its lateral margin wrapped proximally against the lateral surface (Fig. 7.7a). The craniolaterally located radial notch was at the same level as the body of the ulna and consisted of a single articular facet (Fig. 7.7a). Just distal to the medial coronoid process, the body of the ulna presented with a deep narrow groove for the insertion of the *M. brachialis* (Fig. 7.7a).

The head of the ulna was well developed (Fig. 7.7c). The articular circumference was markedly elevated from the body of the ulna and formed an almost ninety degree angle with the styloid process (Figs 7.7c and 7.8). The styloid process was large and bulbous (Figs 7.7c and 7.8). On the ML view of the elbow joint, the physes of the tuber olecrani and proximal part of the radius were similar to those of the domestic cat and dog (Fig. 7.5c). The physes of the distal part of the radius and ulna appeared transverse similar to those of the domestic cat (Fig. 7.8c).

7.3.5 Carpus

The carpus consisted of seven carpal bones: the intermedioradial, ulnar, accessory, and the first, second, third and fourth carpal bones (Fig. 7.8a). The intermedioradial carpal bone was the largest carpal bone. Palmaromedially, it

presented with a tuberosity (Fig. 7.8a). Medially, the bone presented with an ovoid articular facet for the sesamoid bone of the *M. abductor digiti I longus*.

The palmarolaterally directed accessory carpal bone was prominent and almost the same size as the intermedioradial carpal bone (Fig. 7.8a). It had two articular surfaces for the ulnar carpal bone and styloid process of the ulna (Fig. 7.8). On the ML view of the carpus, the physis of the accessory carpal bone appeared sagittal similar to those of the domestic cat and dog (Fig. 7.8c).

The fourth carpal bone was the largest bone in the distal row (Fig. 7.8a). The third carpal bone was flattened mediolaterally and comma-shaped on the DPa view of the carpus (Fig. 7.8a). The second carpal bone was the smallest bone in the distal row and was fairly triangular (Fig. 7.8a). The first carpal bone was well developed and articulated distally with the first metacarpal bone (Fig. 7.8a).

7.3.6 Metacarpus and digits

Five metacarpal (MC) bones and digits were seen (Fig. 7.9). All MC bones were almost equally developed in terms of width (Fig. 7.9). The MC bones were widely spread and relatively short in relation to the length of the digits (Fig. 7.9). The first digit had only two phalanges: the proximal and distal phalanges. The other digits (II–V) had three phalanges: proximal, middle and distal phalanges (Fig. 7.9). The distal articular surface of the middle phalanx

was symmetrical and convex (Fig. 7.10a). The proximal articular surface of the distal phalanx was concave and parallel to the horizontal plane.

7.3.7 Sesamoid bones

A large sesamoid bone of the *M. abductor digiti I longus* was seen in all animals (Figs 7.8a and 7.10b). On the DPa view of the carpus, it was seen medial to the intermedioradial carpal bone (Fig. 8a). On the ML view of the carpus, it was not seen due to its superimposition on the carpal bones (Fig. 7.8b). Each metacarpophalangeal joint had paired proximal sesamoid bones on the palmar aspect (Fig. 7.9).

7.3.8 Other findings

In four and two animals a single and two small bones, respectively, were seen on the palmar aspect of the fifth MC bone on the ML view of the carpus (Figs 7.8b and 7.10c). On the DPa view of the carpus, the bones were poorly seen superimposed on the abaxial palmar aspect of the fifth MC bone (Fig. 7.8a).

Osteoarthrosis of the elbow (Fig. 7.11a) and carpus (Fig. 7.11b,c) were seen in two and three animals, respectively, greater than 9 years old. Two animals with elbow osteoarthrosis had concurrent osteoarthrosis of the carpus. Comparing the two joints, the elbow was most severely affected. Elbow osteoarthrosis was characterised by sclerosis of the trochlea notch, poor visualization of the medial coronoid process, thickening of the cranial cortex of the distal part of the humerus, and the presence of osteophytes dorsally on the anconeal process, the cranial aspect of humeroradial joint, around the

trochlea notch and the lateral epicondylar crest (Fig. 7.11a). Osteoarthrosis of the carpus was characterised by poor delineation of the carpal bones, osteophytes on the distal part of the radius and styloid process of the radius and enthesophytes on the lateral and medial margins of the bases of the metacarpal bones, distal part of the sesamoid bone for the *M. abductor digiti I longus*, lateral aspect of the fourth carpal bone and ulnar carpal bone (Fig. 7.11b,c).

7.4 DISCUSSION

Less cursorial animals inhabit high structured habitats such as dense forests, whereas cursorial animals inhabit more open terrain (Gonyea, 1978). The thoracic limb of less cursorial animals is capable of a greater range and variety of movements compared to cursorial animals (Hopwood, 1947). The difference in movements of the thoracic limb between these two groups of animals is a result of variation in their feeding habits and the environments in which they live (Hopwood, 1947; Gonyea, 1978). In the red panda, movement on and between the small terminal branches of trees is facilitated by a high degree of flexibility of the pectoral and pelvic girdles and limb joints (Roberts and Gittleman, 1984).

The wide scapula observed in the red panda accommodates well developed muscles, which stabilizes the shoulder joint against luxation. Fisher et al., (2009) reported stout tendons of insertion of the *M. supraspinatus* and *M. infraspinatus*, which stabilize the shoulder joint in the red panda. In arboreal

quadrupedal animals, the thoracic limb is frequently used in an abducted position (Roberts and Davidson, 1975). Therefore, the muscles which stabilize the shoulder joint are well developed (Roberts and Davidson, 1975).

The presence of a prominent large hamate process and the location of the insertion of the *M. infraspinatus* at the same level as the head of the humerus in the red panda, enhance the abduction function of the shoulder joint. Similar findings have also been reported in some African mammals (Hopwood, 1947; Taylor, 1974). The prominent large hamate process provides the origin of *M. deltoideus pars acromialis*, which abducts the shoulder joint (Fisher et al., 2009).

The presence of the large area for the origin of the *M. teres major*, well developed medial epicondyle, deep groove for the insertion of the *M. brachialis* and prominent further distally located radial tuberosity observed in the red panda, indicate the presence of strong flexor muscles of the thoracic limb. Strong flexor muscles of the thoracic limb are important in arboreal quadrupeds since the thoracic limb is frequently held in a flexed position during locomotion (Hopwood, 1947). *M. teres major* and *M. brachialis* flex the shoulder and elbow joints respectively (Fisher et al., 2009). The medial epicondyle provides the origin for the flexor muscles of the carpus and digits (Fisher et al., 2009). The radial tuberosity provides the insertion for the *M. biceps brachii*, which flexes the elbow joint (Fisher et al., 2009). The radial tuberosity was also found to be larger and located further distally in the

African palm civet (*Nandinia binotata*) a climbing species, which indicated the strength of m. biceps brachii in flexion of the elbow joint (Taylor, 1974).

The concave caudal surface of the trochlea humeri in the red panda increases the stability of the elbow joint when the joint is in a flexed position (Fleagle and Simons, 1995). The prominent medial trochlea lip counteracts the adducting forces at the elbow joint produced by the carpal and digital flexors when the antebrachium and manus are in a pronated position (Fleagle and Simons, 1995).

The oblique orientation of the olecranon fossa sloping from proximolateral to distomedial observed in the red panda indicates that the thoracic limb moves through an arch away from the parasagittal plane of the body during locomotion as in most feline species (Gonyea, 1978). This phenomenon most likely reflects an adaptation to the arboreal environment in which it lives. In felids, it was found that species which are exclusive forest dwellers had the greatest angle of inclination of the olecranon fossa compared to those who inhabit more open terrain (Gonyea, 1978).

The power to rotate the antebrachium, which is of a great importance to a climbing species (Hopwood, 1947) is also important as the manus is used as a prehensile organ for food manipulation e.g. grasping and bending bamboo to bring the leaves within the reach of the mouth (Roberts and Gittleman, 1984; Antón et al., 2006). In the red panda, the power to rotate the antebrachium was indicated by the presence of the following features: the

elliptically shaped head of the radius, stout and well developed body and head of the ulna, well developed muscles of supination and a craniolaterally located radial notch with a single articular facet at the same level as the body of the ulna (Taylor, 1974; Gonyea, 1978).

During pronation and supination the elliptically shaped head of the radius acts as a cam, which imparts to the radius' eccentric motion (Gonyea, 1978). The stout and well developed body and head of the ulna act as a pivot, which supports the radius during pronation and supination. The prominent lateral supracondylar crest provides the origin for the *M. brachioradialis*, which supinates the antebrachium (Fisher et al., 2009). A distinct flattening on the proximal half of the cranial surface of the radius accommodates the *M. supinator*, which supinates the antebrachium (Fisher et al., 2009). Additionally, the *M. abductor digiti I longus* assists in supination (Antón et al., 2006). The deep sited, cranial located radial notch with two articular facets restricts rotation of the radius (Taylor, 1974; Gonyea, 1978).

The palmarolaterally directed accessory carpal bone, large sesamoid bone for the *M. abductor digiti I longus* and widely spread MC bones indicate flexibility of the manus in the red panda, which is important for arboreal locomotion and food manipulation (Antón et al., 2006; Taylor, 1974). The palmarolaterally directed accessory carpal bone enables greater leverage to be exerted on the manus during ulnar deviation (Taylor, 1974). A large sesamoid bone for the *M. abductor digiti I longus* provides the insertion of the *M. abductor digiti I longus*,

which abducts the carpal joint and carpometacarpal joint of digit I (Fisher et al., 2009) and also supinates the manus (Antón et al., 2006).

Additionally the sesamoid bone of the *M. abductor digiti I longus* acts as a false-thumb for the grasping actions of the manus (Antón et al., 2006). Widely spread MC bones provide a large space and allow greater effectiveness of the muscles responsible for small movements of the digits (Taylor, 1974).

The presence of osteoathrosis (OA) in animals greater than 9 years old in this study without medical history of trauma suggests that the likely cause is primary OA. It is most likely that these two joints are subjected to more stress as a result of arboreal locomotion, however this warrants further investigation. A review of feline OA indicated that a greater proportion of animals reported with OA had no obvious cause, suggesting a primary OA (Lascelles, 2010).

The small bones located on the palmar aspect of MC V are likely sesamoid bones. However, in this study it was difficult to ascertain which muscle they are associated with. The symmetrical shape of the distal articular surface of the middle phalanx and the parallel orientation to the horizontal plane of the proximal articular surface of the distal phalanx observed in this study are different from felids (Gonyea and Ashworth, 1975) and indicated that the claws of the red panda are slightly (Taylor, 1974) to non retractile (Gonyea and Ashworth, 1975).

Morphology of the thoracic limb of the red panda evidenced by gross osteology and radiography indicated flexibility of the thoracic limb joints and well developed flexor and supinator muscles, which are important in arboreal quadrupedal locomotion. Species-specific differences exist in the normal gross osteology and radiographic anatomy of the thoracic limb. Knowledge of the normal gross osteology and radiographic anatomy of the thoracic limb of individual species is important for accurate interpretation and diagnosis of musculoskeletal diseases involving the thoracic limb.

7.5 ACKNOWLEDGEMENTS

The authors would like to thank the Organization for Women in Science for the Developing World (OWSD), Swedish International Development Cooperation Agency (SIDA), University of Pretoria, Johannesburg (JHB) and Bristol zoos for supporting this study. The National Museums of Scotland for supplying bone specimen. Dr. Georgina Cole, Ms. Fania Mohlala, sisters and animal handlers of the JHB zoo and Onderstepoort Veterinary Academic Hospital for their assistance during radiographic examination. Mrs. Charmaine Vermeulen and Mrs. Wilma Olivier of University of Pretoria for their assistance in photography and administrative work, respectively.

7.6 REFERENCES

Antón, M., M. J. Salesa, J. F. Pastor, S. Peigné, and J. Morales, 2006: Implication of the functional anatomy of the hand and forearm of *Ailurus fulgens* (Carnivora, Ailuridae) for the evolution of the 'false-thumb' in pandas. J. Anat. **209,** 757–764.

Carlsson, A., 1925: Über *Ailurus fulgens*. Acta. Zool. **6,** 269–305.

Fisher, R. E., B. Adrian, M. Barton, J. Holmgren, and S. Y. Tang, 2009: The phylogeny of the red panda (*Ailurus fulgens*): evidence from the forelimb. J. Anat. **215,** 611–635.

Fleagle, J. G., and E. L. Simons, 1995: Limb skeleton and locomotor adaptations of *Apidium phiomense*, an Oligocene Anthropoid from Egypt. Am. J. Phys. Anthropol. **97,** 235–289.

Gonyea, W. J., 1978: Functional implications of felid forelimb anatomy. Acta. Anat. **102,** 111–121.

Gonyea, W., and R. Ashworth, 1975: The form and function of retractile claws in the felidae and other representative carnivorans. J. Morph. **145,** 229–238.

Hopwood, A. T., 1947: Contributions to the study of some African Mammals-III. Adaptations on the bones of the forelimb of the lion, leopard and cheetah. J. Linn. Soc. Zool. **41,** 259–271.

IUCN, 2014: IUCN Red List of Threatened Species. Version 2014.3. Available at: http://www.iucnredlist.org (accessed on 18 November 2014).

Lascelles, B. D. X., 2010: Feline degenerative joint disease. Vet. Surg. **39,** 2–13.

Lynch, M., H. McCracken, and R. Slocombe, 2002: Hyperostotic bone disease in red pandas (*Ailurus fulgens*). J. Zoo. Wildl. Med. **33,** 263–271.

Nickel, R., A. Schummer, E. Seiferle, J. Frewein, H. Wilkens, and K. H. Wille, 1986: The Anatomy of the Domestic Animals. Berlin: Paul Parey.

Philippa, J., and E. Ramsay, 2011: Captive red panda medicine. In: Red panda Biology and Conservation of the First Panda (A. R. Glatston, ed.). London: Academic Press. pp. 271–285.

Preece, B., 2011: Red panda pathology. Red panda Biology and Conservation of the First Panda (A. R. Glatston, ed.). London: Academic Press. pp. 287–302.

Roberts, D., and I. Davidson, 1975: The lemur scapula. In: Lemur Biology (I. Tattersal and R. W. Sussman, eds). New York: Plenum Press. pp. 125–147.

Roberts, M. S., and J. L. Gittleman, 1984: *Ailurus fulgens*. Mamm. Species. **222,** 1–8.

Smallwood, J. E., and K. A. Spaulding, 2013: Radiographic anatomy of the appendicular skeleton. In: Textbook of Veterinary Diagnostic Radiology (D. E. Thrall, ed.). Missouri: Saunders Elsevier. pp. 224–251.

Taylor, M. E., 1974: The functional anatomy of the forelimb of some African Viverridae (Carnivora). J. Morph. **143,** 307–335.

Thrall, D. E., and I. D. Robertson, 2011: Atlas of Normal Radiographic Anatomy and Anatomic Variants in the Dog and Cat. Missouri: Elsevier Saunders.

7.7 TABLES

Table 7.1 Measurements of the scapula, humerus, radius and ulna in captive red pandas

Bone	Variable	Number of animals	Mean ± SD (cm)	Range (cm)
Scapula	Length[a]	3	7.00 ± 0.10	6.90 – 7.10
	Craniocaudal diameter[a]	3	6.32 ± 0.08	6.25 – 6.40
Humerus	Length[b]	5	11.58 ± 0.48	11.10 – 12.00
	Craniocaudal diameter[b]	5	1.12 ± 0.08	1.00 – 1.20
Radius	Length[b]	5	9.36 ± 0.93	8.20 – 10.80
	Craniocaudal diameter[b]	5	0.51 ± 0.02	0.50 – 0.55
Ulna	Length[b]	5	10.64 ± 0.99	9.00 – 11.50
	Craniocaudal diameter[b]	5	0.60 ± 0.07	0.50 – 0.70

[a]Measurements done on bone specimens

[b]Radiographic measurements not compensated for magnification

Table 7.2 Radiographic measurements not compensated for magnification of metacarpal bones and phalanges in captive red pandas

Bone	Number of animals	Length (Mean ± SD) cm	Range (cm)
MC I	6	1.58 ± 0.16	1.30 – 1.70
MC II	6	2.42 ± 0.13	2.20 – 2.50
MC III	6	2.93 ± 0.12	2.80 – 3.10
MC IV	6	3.17 ± 0.14	3.00 – 3.40
MC V	6	2.65 ± 0.12	2.50 – 2.80
P1 of digit I	6	1.20 ± 0.11	1.00 – 1.30
P1 of digit II	6	1.70 ± 0.13	1.50 – 1.80
P1 of digit III	6	1.98 ± 0.10	1.80 – 2.10
P1 of digit IV	6	3.17 ± 0.14	3.00 – 3.40
P1 of digit V	6	1.65 ± 0.08	1.60 – 1.80

MC, metacarpal; P1, proximal phalanx

Measurements of the carpal bones, middle and distal phalanges were not performed due to their oblique presentation

Table 7.3 Radiographic measurements not compensated for magnification of the sesamoid bones in captive red pandas

Sesamoid	Variable	Number of animals	Mean ± SD (cm)	Range (cm)
M. abductor digiti I longus	Length	6	0.32 ± 0.04	0.30 – 0.40
	ML diameter	6	0.40 ± 0.06	0.30 – 0.50
MCP digit I axial	Length	6	0.35 ± 0.05	0.30 – 0.40
MCP digit I abaxial	Length	6	0.32 ± 0.03	0.30 – 0.35
MCP digit II axial	Length	6	0.42 ± 0.04	0.40 – 0.50
MCP digit II abaxial	Length	6	0.38 ± 0.04	0.30 – 0.40
MCP digit III axial	Length	6	0.45 ± 0.05	0.40 – 0.50
MCP digit III abaxial	Length	6	0.50 ± 0.06	0.40 – 0.60
MCP digit IV axial	Length	6	0.49 ± 0.02	0.45 – 0.50
MCP digit IV abaxial	Length	6	0.47 ± 0.04	0.40 – 0.50
MCP digit V axial	Length	6	0.56 ± 0.05	0.40 – 0.50
MCP digit V abaxial	Length	6	0.43 ± 0.05	0.40 – 0.50

MCP, metacarpophalangeal; ML, mediolateral

7.8 FIGURES

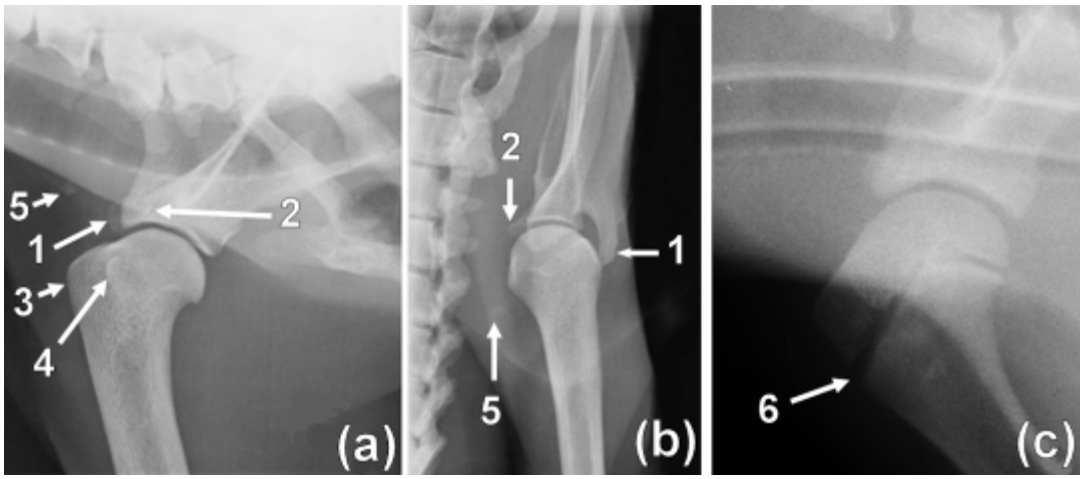

Fig. 7.1 Mediolateral (a, c) and CdCr (b) radiographs of the right shoulder joints of a 14.3-year-old male (a, b) and skeletally immature (c) red panda. (1) Hamate process, (2) coracoid process, (3) major tubercle, (4) minor tubercle, (5) rudimentary clavicle and (6) physis of the proximal humerus.

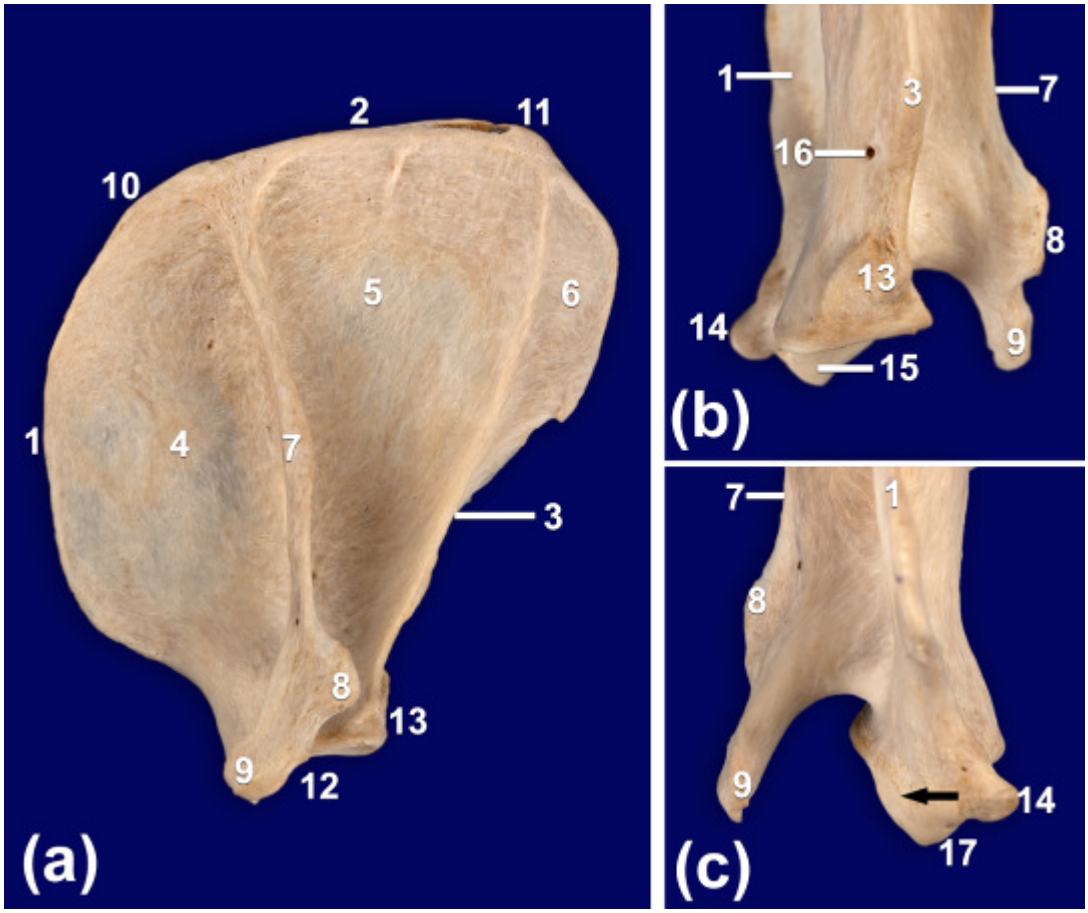

Fig. 7.2 Lateral (a), caudal (b) and cranial (c) views of bone specimen of the right scapula of an adult red panda. (1) Cranial margin, (2) dorsal margin, (3) caudal margin, (4) supraspinous fossa, (5) infraspinous fossa, (6) area for the origin of the *M. teres major*, (7) spine of the scapula, (8) suprahamate process, (9) hamate process, (10) cranial angle, (11) caudal angle, (12) ventral angle, (13) infraglenoid tubercle, (14) coracoid process, (15) glenoid cavity, (16) nutrient foramen and (17) supraglenoid tubercle, Black arrow: proximal extension of the articular surface of the glenoid cavity.

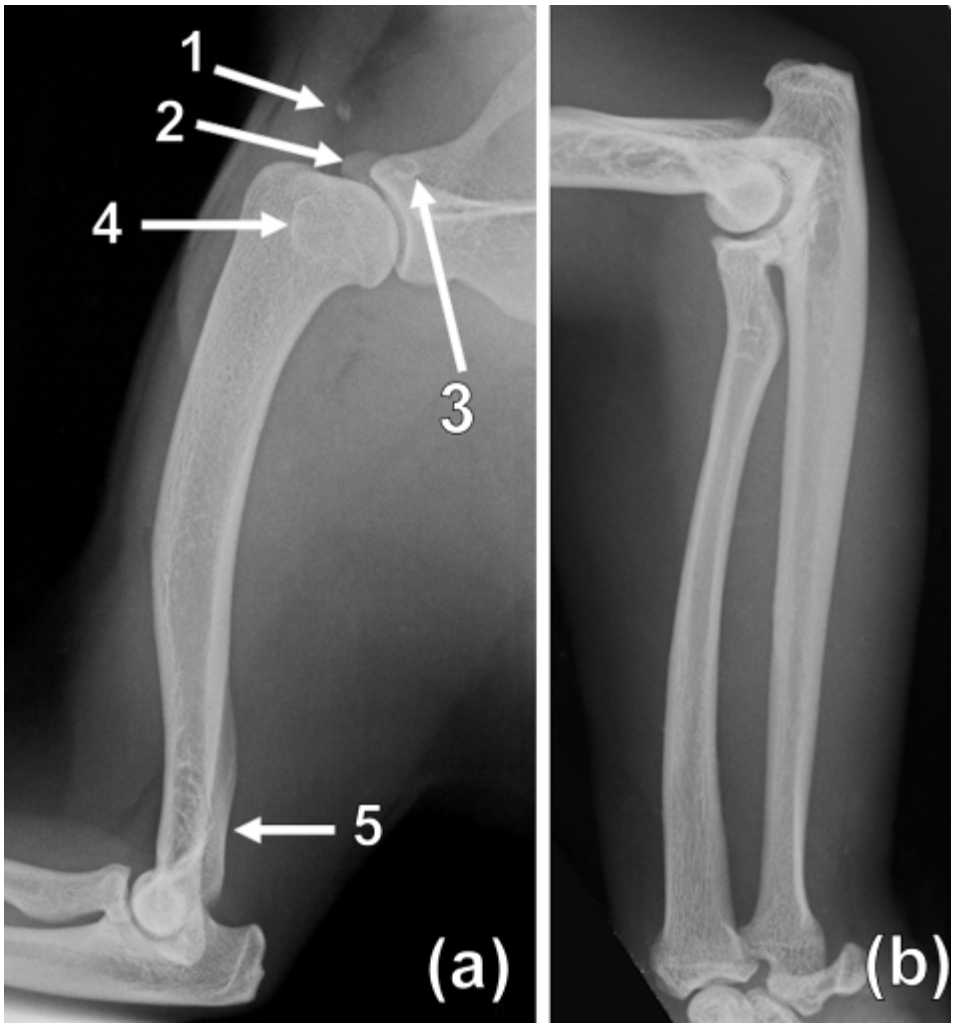

Fig. 7.3 Mediolateral radiographs of the right humerus (a) and radius and ulna (b) of 1.4-year-old (a) and 2.5-year-old (b) male red pandas. (1) Rudimentary clavicle, (2) hamate process, (3) coracoid process, (4) minor tubercle and (5) lateral supracondylar crest.

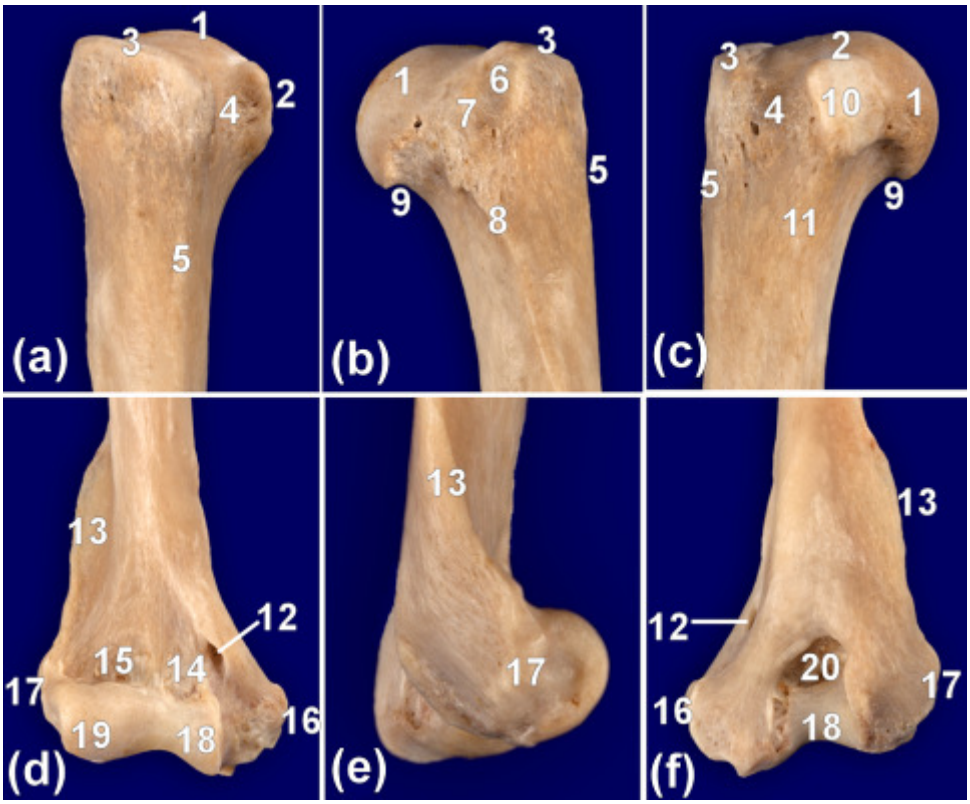

Fig. 7.4 Cranial (a, d), lateral (b, e), medial (c) and caudal (f) views of a bone specimen of the right proximal (a, b, c) and distal (d, e, f) humerus of an adult red panda. (1) Head of the humerus, (2) minor tubercle, (3) major tubercle, (4) intertubercular groove, (5) major tubercular crest, (6) *Facies m. infraspinati*, (7) area of insertion of the *M. teres minor*, (8) triceps muscle line, (9) neck of the humerus, (10) area of insertion of *M. subscapularis*, (11) crest of the minor tubercle, (12) supracondylar foramen, (13) lateral supracondylar crest, (14) coronoid fossa, (15) radial fossa, (16) medial epicondyle, (17) lateral epicondyle, (18) trochlea humeri, (19) capitulum humeri and (20) olecranon fossa.

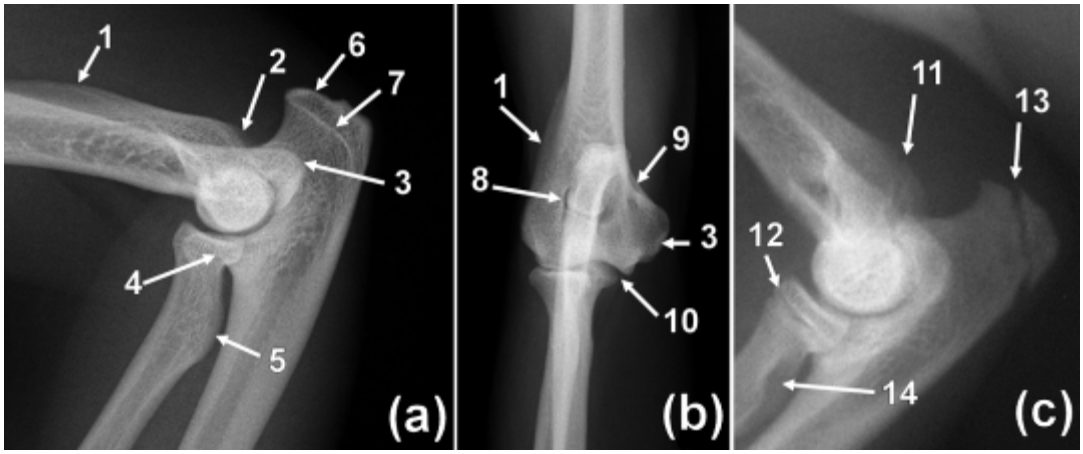

Fig. 7.5 Mediolateral (a, c) and CrCd (b) radiographs of right elbow joints of 1.4 year-old (a), 10.3 year-old (b) and skeletally immature (c) male red pandas. (1) Lateral supracondylar crest, (2) lateral epicondyle, (3) medial epicondyle, (4) medial coronoid process, (5) radial tuberosity, (6) tuber olecrani, (7) olecranon physeal scar, (8) olecranon fossa, (9) supracondylar foramen, (10) humeroulnar joint space, (11) distal physis of the humerus, (12) proximal physis of the radius, (13) tuber olecrani physis and (14) area of radiolucency as a result of a longitudinal groove on the radial tuberosity.

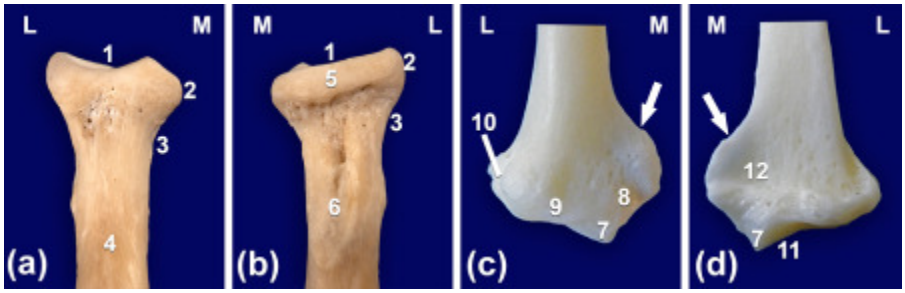

Fig. 7.6 Cranial (a, c) and caudal (b, d) views of bone specimens of the right proximal (a, b) and distal (c, d) radius of adult red pandas. (1) Articular fovea, (2) head, (3) neck, (4) flat surface for accommodation of *M. supinator*, (5) articular circumference, (6) radial tuberosity, (7) styloid process, (8) medial tendon groove, (9) middle tendon groove, (10) lateral tendon groove, (11) carpal articular surface and (12) area for the insertion of *M. pronator quadratus*. Note a prominent crest (c, d) for the insertion of the *M. brachioradialis* (white arrow).

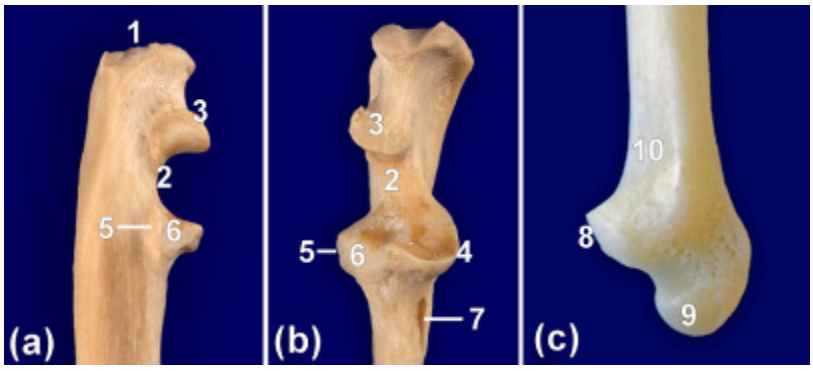

Fig. 7.7 Lateral (a), cranial (b) and medial (c) views of bone specimens of the right proximal (a, b) and distal ulna (c) of adult red pandas. (1) Tuber olecrani, (2) trochlea notch, (3) anconeal process, (4) medial coronoid process, (5) lateral coronoid process, (6) radial notch, (7) groove for insertion of *M. brachialis*, (8) articular circumference, (9) styloid process and (10) area for the origin of *M. pronator quadratus*.

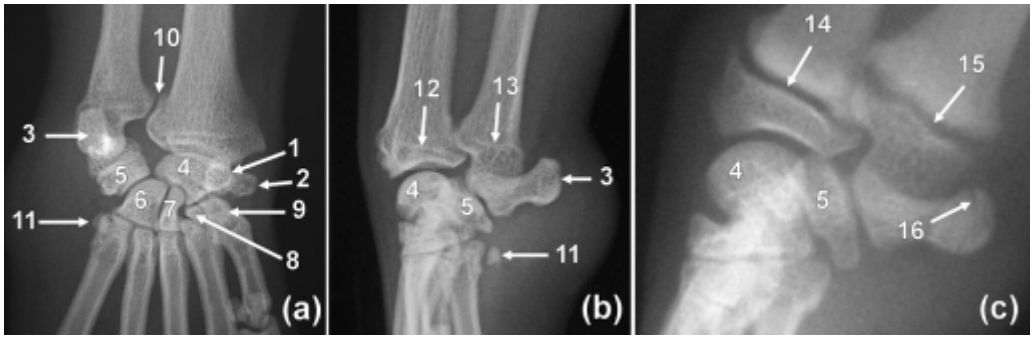

Fig. 7.8 Dorsopalmar (a) and mediolateral (b, c) radiographs of the right carpus of 1.4 year-old female (a, b) and skeletally immature (c) red pandas. (1) An ovoid area of increased mineral opacity representing the tuberosity on the palmar aspect of the intermedioradial carpal bone, (2) sesamoid bone for the *M. abductor digiti I longus*, (3) accessory carpal bone, (4) intermedioradial carpal bone, (5) ulnar carpal bone, (6) fourth carpal bone, (7) third carpal bone, (8) second carpal bone, (9) first carpal bone, (10) radioulnar articulation, (11) a small single bone on the palmar aspect of MC V, (12) distal physeal scar for radius, (13) distal physeal scar for ulna, (14) distal physis of the radius, (15) distal physis of the ulna, (16) accessory carpal bone physis.

Fig. 7.9 Dorsopalmar radiograph of the right manus of a 1.4 year-old female red panda. (1) Abaxial proximal sesamoid bone, (2) axial proximal sesamoid bone and (3) unguicular crest.

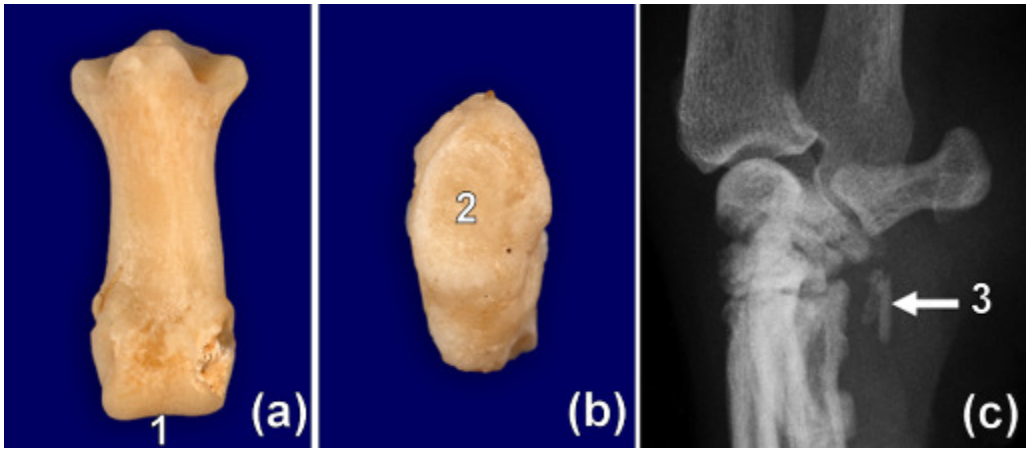

Fig. 7.10 (a) Dorsal and (b) lateral views of bone specimens of the middle phalanx and sesamoid bone for the *M. abductor digiti I longus*, respectively, of an adult red panda. (c) Mediolateral radiograph of the right carpus of 11.3-year-old male red panda. (1) Symmetrical and convex distal articular surface of the middle phalanx, (2) an ovoid articular facet for articulation with the intermedioradial carpal bone and (3) two small bones on the palmar aspect of the fifth metacarpal bone.

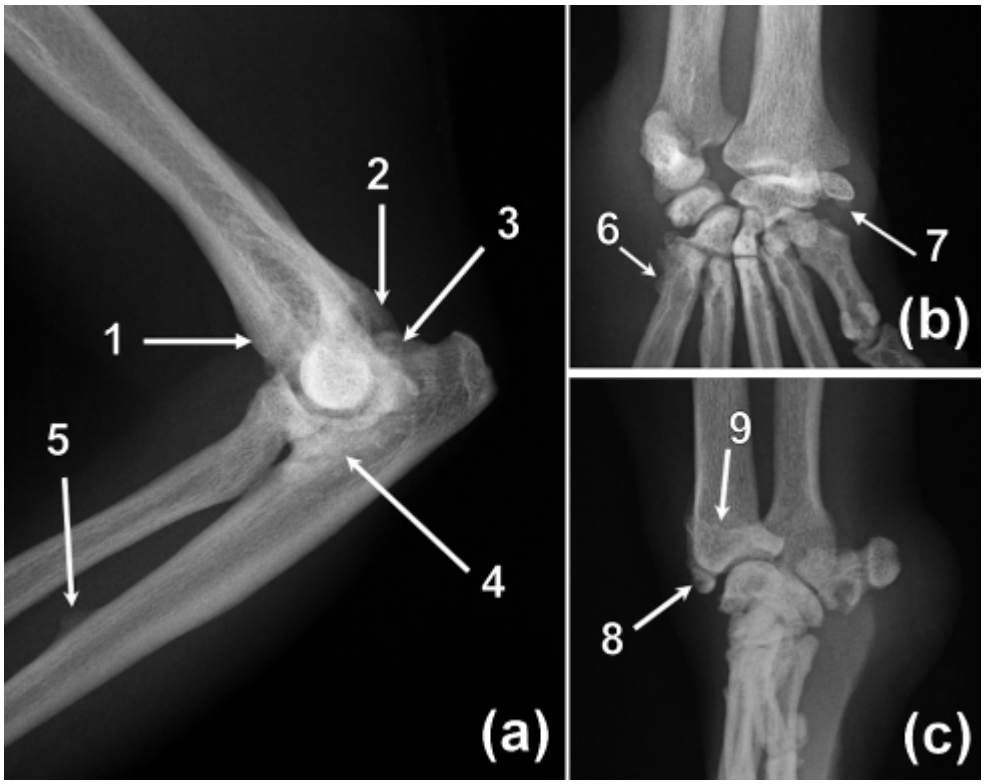

Fig. 7.11 Mediolateral (a, c) and dorsopalmar (b) radiographs of the right elbow joint (a) and carpus (b, c) of 9.6 year-old female (a), 11.3 year-old male (b) and 14.3 year-old male (c) red pandas. (a) Note the thickening of the cranial cortex of the distal part of the humerus (1), osteophytes on the lateral epicondylar crest (2) and dorsally on the anconeal process (3). Note also sclerosis of the trochlea notch (4), enthesophyte on the cranial aspect of the shaft of the ulna (5) and poor visualisation of the joint space compared to Fig. 7.5a. (b) Note the presence of enthesophytes on the lateral aspect of the base of the MC V (6) and distal part of the sesamoid bone for the *M. abductor digiti I longus* (7). Note the poor delineation of the carpal bones and bases of the metacarpals (Fig. 11b, c) compared to Fig. 7.8. (c) Note the presence of osteophytes on the distal part of the radius (9) and its styloid process (8).

CHAPTER 8

MORPHOLOGY OF THE PELVIS AND HIND LIMB OF THE RED PANDA (*AILURUS FULGENS*) EVIDENCED BY GROSS OSTEOLOGY, RADIOGRAPHY AND COMPUTED TOMOGRAPHY

8.1 INTRODUCTION

The red panda (*Ailurus fulgens*) is a quadrupedal arboreal animal primarily distributed in the Himalayas and southern China (Fisher et al., 2009). It is classified by the International Union for Conservation of Nature and Natural Resources (IUCN) as a vulnerable species (IUCN, 2014). The red panda is closely related to mustelids, procyonids and skunks (Groves, 2011).

Wild pandas weigh between 4.0 kg to 5.0 kg (Preece, 2011). In captivity the weight of adult males and females ranges from 3.7 kg to 6.2 kg (mean: 5.0 kg) and 4.2 kg to 6.0 kg (mean: 4.9 kg), respectively (Roberts and Gittleman, 1984). The head and body length ranges from 560 mm to 625 mm. The tail length ranges from 370 mm to 472 mm (Roberts and Gittleman, 1984).

The red panda lives in forests with bamboo understory at an altitude ranging from 1500 m to 4800 m (Srivastav et al., 2009). Trees provide sites for resting, sleeping, nesting and escaping from predators (Roberts and Gittleman, 1984;

Srivastav et al., 2009; Eriksson et al., 2010). Apart from trees they also prefer other elevated surfaces such as rocks (Roberts and Gittleman, 1984; Pradhan et al., 2001). Although the red panda spends most of its time in trees, it forages primarily on the ground (Roberts and Gittleman, 1984). Its diet is largely vegetarian, consisting primarily of bamboo leaves [80–90%] (Wei and Zhang, 2009). The average lifespan of the red panda in the wild is 8 years to 10 years, whereas in captivity it is 13.4 years (Heath and Platnick, 2008).

Diseases involving the musculoskeletal system such as avascular necrosis of the femoral head (Delclaux et al., 2002), hyperostotic bone disease (Lynch et al., 2002), osteoarthrosis (Philippa and Ramsay, 2011; Preece, 2011) and neoplasia such as squamous cell carcinoma (Preece, 2011) have been reported in the red panda.

Although radiography has been used as the first diagnostic imaging modality for musculoskeletal disease in the red panda (Delclaux et al., 2002; Lynch et al., 2002), computed tomography (CT) is an excellent imaging modality to evaluate bone (Ohlerth and Scharf, 2007). Compared to radiography, CT provides cross sectional images without superimposition and has superior tissue contrast. Therefore early bone changes can be detected (Ohlerth and Scharf, 2007). Further, post processing of images (multiplanar and three-dimensional reconstructions) is possible with CT (Kinns et al., 2011).

Normal osteology, radiographic and CT anatomy of the pelvis and hind limb is well documented in companion animals (Nickel et al., 1986; Samii et al., 2011;

Thrall and Robertson, 2011) and provides a reference for identification of skeletons and diagnosis of musculoskeletal diseases. Several authors have also documented the normal osteology, radiographic and CT anatomy of the pelvis and hind limb in wildlife species (Taylor, 1976; Silverman and Tell, 2005; de Araújo et al., 2013).

There are few reports on the normal gross osteology of the pelvis and hind limb of the red panda (Roberts and Gittleman, 1984; Fisher et al., 2008; Fisher, 2011) and to the authors' knowledge the normal radiographic and CT anatomy of the pelvis and hind limb has not been reported in this species. Interestingly, the red panda has been reported to descend head first by gripping the tree trunk medially with the feet (Roberts and Gittleman, 1984) indicating how well the hind limb is adapted for arboreal quadrupedal locomotion.

The objective of this study was to document the normal gross osteology, radiographic and CT anatomy and range of variation in the pelvis and hind limb of the red panda with the aim of helping identify lesions successfully.

8.2 MATERIALS AND METHODS

8.2.1 Animals

Nine captive adult red pandas (*Ailurus fulgens*) from the Johannesburg (JHB) zoo were radiographed in this study (Table 8.1). Six were males and three were females (Table 8.1). The minimum and maximum ages of the animals

were 1.4 years and 14.3 years, respectively (mean: 6.76 ± 4.96 years). The weight of the animals ranged from 3.7 kg to 5.96 kg (mean: 4.65 ± 0.78 kg). Of the nine animals, two were euthanased during the course of the study and were subjected to gross osteological study (Table 8.1). Bone specimens of a 3.5-year-old male red panda from the National Museum of Scotland were also used for gross osteological study (Table 8.1). This study was approved by the Animal Use and Care Committee (AUCC) of the University of Pretoria and Johannesburg Zoo Ethics and Research Committee.

8.2.2 Radiography

Radiography of the pelvis and right hind limb was performed in nine and seven animals, respectively, under general anaesthesia using a table top technique. Animals were radiographed during annual health examinations. In eight animals, a EVA-HF525 X-ray machine (Comed Medical System Co. Ltd, Kyunggi, Korea) was used at a source to image distance (SID) of 95 cm. An automatic X-ray film processor model CP-345 (ELK Corporation, Tokyo, Japan) was used. For the pelvis, a kVp range of 42–44 and 2.5 mAs was used with medium speed screen type film, Fuji medical X-ray films (Fujifilm Corporation, Tokyo, Japan) in combination with RAREX green regular intensifying screens (Okamoto manufacturing Co. LTD, Tokyo, Japan). For the hind limb, 46 kVp and 5 mAs was used with mammography films (UM-MA, Fujifilm Corporation, Tokyo, Japan) in combination with mamoray screens (Fujifilm Europe GmbH, Düesseldorf, Germany).

In the remaining animal, radiography was performed using a Siemens Polymat 50 (Siemens, Munich, Germany) X-ray machine at a SID of 100 cm. Images were obtained using a computed radiography (CR) unit (Fuji Axim FCR Capsula XL, Fujifilm Corporation, Tokyo, Japan). A kVp range of 48–60 and mAs range of 4–6 were used for the pelvis and hind limb.

8.2.3 Computed tomography

Computed tomography of the torso and the left hind limb was performed in one animal (Table 8.1) using a Siemens Emotion Duo CT scanner (Siemens Medical Systems, Forchheim, Germany). For the torso, 2 mm thick transverse slices were acquired from just cranial to the thoracic inlet to the ischiatic tuberosities at a kVp of 130 and 20 mAs using a soft tissue window (window width (WW) = 400 and window level (WL) = 40) and a medium kernel (B41s). For the hind limb, 1 mm thick transverse slices were acquired from just proximal to the stifle joint to the distal phalanges using a bone window (WW = 1400 and WL = 300) at a kVp of 130 and 30 mAs with a sharp kernel (B80s). A post processing, three-dimensional (3D) volume rendering technique was performed with a grey scale default.

8.2.4 Gross osteology

Bone specimens from three adult animals (National Museum of Scotland and two euthanased animals from the JHB zoo) were used (Table 8.1). Photographs of bone specimens from different views were obtained using a digital camera (CANON 5DMARK2, Canon Inc., Tokyo, Japan). A previous report (Fisher et al., 2008) on the myology of the pelvis and hind limb of the

red panda was used to locate the sites for origins and insertions of different muscles on bone specimens and their functions.

8.2.5 Bone measurements

Bone measurements of the pelvis and the right hind limb were performed on the radiographic images. The maximum lengths of bones were measured from the proximal to the distal extremities on the mediolateral (ML) view. For the metatarsal (MT) bones, phalanges and tarsal sesamoid bone, the maximum lengths were measured on the plantarodorsal (PlD) view of the pes. The craniocaudal (CrCd) and ML diameters were measured on the ML and PlD views, respectively. The CrCd diameters of the long bones were measured at the mid-diaphysis. For the sesamoid bones, the CrCd and ML diameters were measured as a maximum distance perpendicular to the length of the bone.

The maximum length of the pelvis was measured on the ventrodorsal (VD) view between two lines drawn transversely from the most cranial part of the right wing of the ilium and the most caudal part of the right ischium. The transverse diameter was measured on the VD view from one iliopectineal line to the other (O'Brien, 1978). Radiographic measurements were not compensated for magnification.

8.2.6 Statistical analysis

Data were analysed using Stat View© (SAS Institute Inc., Cary, NC, USA) statistical package. The mean, range and standard deviation (SD) were calculated. Data are expressed as mean ± SD and the range.

8.3 RESULTS

8.3.1 Pelvis

Gross osteology

The ilial wings were broad and the gluteal surface was directed slightly dorsolaterally (Figs 8.1a,b and 8.2a). When viewed from dorsally or ventrally, the ilial wings were almost parallel to each other (Fig. 8.1a,b). The body of the ilium and the major ischiatic notch were short (Figs 8.1a,b and 8.2a). The ventromedial surface of the ilium was wide (Fig. 8.1b). The origin for the *M. rectus femoris* presented with a rough surface (Fig. 8.2a). The pubic bone was L-shaped with wide cranial and caudal rami (Figs 8.1a,b and 8.2a). The pelvic symphysis was partially fused in two of the three bone specimens (Fig. 8.1a,b). The obturator foramina were triangular with rounded edges (Fig. 8.2a). The ischiatic tuberosities were not prominent (Fig. 8.1a). The ischiatic arch was deep and narrow (Fig. 8.1a). The grooves for the tendon of the *M. obturatorius internus* were prominent (Figs 8.1a and 8.2a).

Radiography and CT

On the VD view, the pelvic inlet was fairly rounded and the obturator foramina appeared fusiform (Fig. 8.1c). The body of the ischium was fairly straight and the ischiatic tuberosities were not prominent (Fig. 8.1c). On the right lateral (RL) view, the obturator foramina appeared triangular with rounded angles (Fig. 8.2b). The iliac crest was straight and the pelvic symphysis was short (Fig. 8.2b,c). A prominent os penis was seen in all male animals (Fig. 8.2b,c). Radiographic measurements are summarised in Table 8.2.

8.3.2 Femur

Gross osteology

Generally the femur was straight and slender. The head of the femur was spherical in shape and directed medially (Fig. 8.3a,b,c). It had a very prominent *Fovea capitis* (Fig. 8.3c). The major trochanter did not extend proximal to the head of the femur (Fig. 8.3a,b,c). The medially directed minor trochanter was prominent (Fig. 8.3a,b,c) and not connected to the major trochanter by an inter-trochanteric crest (Fig. 8.3b). The third trochanter was poorly developed and presented with a rough surface (Fig. 8.3a,b)

The medial and lateral ridges of the trochlea of the femur ran parallel to each other with the lateral ridge extending more proximally than its medial counterpart (Fig. 8.3d). The trochlea of the femur was wide and shallow (Fig. 8.3d). Medial and lateral to the proximal border of the caudal surface of the medial and lateral condyles, respectively, the distal part of the femur had fossae for the origin of the medial and lateral heads of the *M. gastrocnemius* (Fig. 8.3e,f). The articular facet for the lateral sesamoid bone of the *M. gastrocnemius*, further indicated as the lateral fabella, was visualised on bone specimens of two animals.

The lateral surface of the distal part of the femur had three fossae for the lateral collateral ligament and origin of the *M. popliteus* and *M. extensor digitorum longus* (Fig. 8.3f). The popliteal fossa was more pronounced than the extensor fossa (Fig. 8.3f). The medial surface of the distal part of the

femur had a fossa for the medial collateral ligament. The fossa for the medial collateral ligament was more prominent than its lateral counterpart.

Radiography

On the CrCd view, the major trochanter did not extend proximal to the head of the femur and the minor trochanter was prominent (Fig. 8.1c). The edge of the major trochanter ran distally (Fig. 8.1c). On the ML view, the shaft of the femur was long and slender (Fig. 8.4a). The cranial and caudal diaphyseal cortices of the femur were of almost uniform thickness (Fig. 8.4a). Radiographic measurements are shown in Table 8.2.

8.3.3 Stifle

Gross osteology, radiography and CT

The patella was similar to that seen in feline species with a pointed and elongated apex (Figs 8.5 and 8.6a). The lateral fabella was seen radiographically in 5/7 animals, whereas a medial fabella was not visualised radiographically in any animal (Fig. 8.5). The popliteal sesamoid bone was seen radiographically in 5/7 animals (Fig. 8.5). The trochlea of the femur was wide and shallow (Fig. 8.5g).

On the ML view, the caudal surface of the apex of the patella sloped from caudoproximal to craniodistal (Fig. 8.5a,b,c). The popliteal lymph node (Fig. 8.5a) and infrapatellar fat pad (Fig. 8.6b) were seen. The lateral fabella was mostly seen as ovoid elongated craniocaudally (Fig. 8.5c) and rarely angular or rounded (Fig. 8.5b). The popliteal sesamoid bone was large and located

just proximal to the condyles of the tibia and caudal to the inter-condylar eminence (Fig. 8.5a,c). It was ovoid elongated craniocaudally (Fig. 8.5a,c). The inter-condylar eminence and tibial tuberosity were not prominent (Fig. 8.5a,b,c).

On the CrCd view, the proximal border of the patella was fairly straight (Fig. 8.5d,e,f). The lateral fabella (Fig. 8.5f) and popliteal sesamoid bone (Fig. 8.5f) were ovoid. The popliteal sesamoid bone was mostly seen superimposed on the lateral condyle of the tibia (Fig. 8.5e) and rarely on the lateral joint space. The inter-condylar eminence was not prominent (Fig. 8.5d,e,f). Radiographic measurements are shown in Table 8.2.

8.3.4 Tibia and fibula

Gross osteology

The larger tibia and smaller fibula were unfused bones. The proximal articular surface of the tibia was located slightly caudally (Fig. 8.7b). The lateral condyle was slightly convex, whereas the medial condyle was concave. The inter-condylar eminence and tibial tuberosity were not prominent (Fig. 8.7a,b). The flat and ovoid caudolaterally located facies articularis fibularis of the tibia was prominent (Fig. 8.7b).

The cochlea grooves were shallow and the intermediate ridge was poorly defined. The medial malleolus was wide craniocaudally and presented with prominent grooves for the digital flexors. The facies articularis malleoli medialis sloped from lateral to medial (Fig. 8.7c,d). The lateral surface of the

distal part of the tibia had a distinct facet, the fibular notch, for articulation with the distal part of the fibula (Fig. 8.7c,d).

The head and lateral malleolus of the fibula were well developed (Fig. 8.7e,f). The head of the fibula had a distinct proximomedial facet (facies articularis capitis fibularis) for articulation with the proximal part of the tibia (Fig. 8.7e). The body of the fibula was less compressed transversely. The lateral malleolus had two distinct medially located articular facets, which were proximal and distal to each other (Fig. 8.7f). The distal articular facet (facies articularis malleoli lateralis) sloped from medial to lateral and was fairly flattened. The proximal articular facet, which articulated with the fibular notch of the tibia, was slightly concave (Fig. 8.7f).

Radiography

On the ML view, the body of the tibia was fairly straight with a thicker cranial cortex than the caudal cortex (Fig. 8.4b). The head and lateral malleolus of the fibula were bulbous (Fig. 8.4b). The body of the fibula appeared of almost uniform thickness (Fig. 8.4b). The cranial and caudal diaphyseal cortices of the fibula were of uniform thickness (Fig. 8.4b). The inter-osseous space was broad and ran the entire length of the crus (Figs 8.4b, 8.5 and 8.8). Radiographic measurements are shown in Table 8.2.

8.3.5 Tarsus

Gross osteology, radiography and CT

The tarsus consisted of seven tarsal bones namely: calcaneus, talus, central tarsal bone as well as first (T I) through fourth (T IV) tarsal bones (Fig. 8.8a). The calcaneus was the largest and longest bone located laterally in the proximal row of the tarsus (Fig. 8.8). The proximal half of the bone was narrow transversely, whereas the distal half was wide transversely with two processes. The medial process (sustentaculum tali) was wide, whereas the lateral process was pointed (Fig. 8.8a).

The dorsal surface of the calcaneus had three articular surfaces; the proximal, middle and distal articular surfaces. The proximal articular surface was the largest with a less convex articular surface, which articulated with the plantarolaterally located proximal articular surface of the talus. The dorsomedially located middle articular surface was slightly concave and articulated with the plantaromedially located middle articular surface of the talus, whilst the smallest distal articular surface was elongated mediolaterally.

The talus was the second largest bone and was located on the medial side of the proximal row of the tarsus (Fig. 8.8). The trochlea of the talus was shallow with a prominent lateral ridge and an almost flattened medial ridge (Fig. 8.8a). The head of the talus was elongated transversely. The plantar surface of the talus had three articular surfaces; the proximal, middle and distal ones. The plantarolaterally located proximal articular surface was the largest with a slightly concave articular surface. The plantaromedially located middle

articular surface had a slightly convex articular surface. The distal articular surface was the smallest and articulated with the distal articular surface on the dorsal surface of the calcaneus.

The central tarsal bone was the only bone located in the middle row (Fig. 8.8). It was elongated transversely and shortened longitudinally (Fig. 8.8a). The bone had prominent proximal and distal articular surfaces, which were concave and convex, respectively (Fig. 8.8a,b). The T IV was the most lateral bone, whereas the T I was the most medial bone in the distal row (Fig. 8.8a). The T I had a proximomedial articular facet for articulation with the tarsal sesamoid bone on the medial aspect of the distal row of the tarsus (Fig. 8.8a). The T II was the shortest bone longitudinally in the distal row.

In all animals, a large tarsal sesamoid bone was seen on the medial aspect of T I on the PID view of the pes (Fig. 8.8a). A distinct articulation was seen between the tarsal sesamoid bone and T I (Fig. 8.8a,c,d). The shape of the tarsal sesamoid bone varied. It was mainly seen as comma-shaped elongated longitudinally and rarely ovoid or angular. On the ML view, a focal radiolucent region was seen just distal to the calcaneus (Fig. 8.8b). On the PID view, the facies articularis malleoli medialis sloped from lateral to medial (Fig. 8.8a). The radiographic measurements of the tarsal sesamoid bone are shown in Table 8.2.

8.3.6 Metatarsus and digits

Gross osteology, radiography and CT

Five MT bones and digits were seen. The MT bones and digits were widely spaced (Fig. 8.8c,d). The lateral process of the base of the MT V was directed laterally (Fig. 8.8a,c,d). The heads of the MT bones were wider than the shafts. Digits II to V had proximal (P1), middle (P2) and distal (P3) phalanges, whereas digit I had only phalanges P1 and P3 (Fig. 8.8c,d). The distal articular surface of P2 was fairly symmetrical. P3 had a concave proximal articular surface, which was parallel to the horizontal plane. The unguicular crests were prominent (Fig. 8.8c). On the ML view, a small semicircular metatarsal sesamoid bone was seen on the plantar aspect of the pes caudal to the bases of the MT bones (Fig. 8.8b and Table 8.2). Paired (axial and abaxial) proximal sesamoid bones were seen on the plantar side of each metatarsophalangeal joint (Fig. 8.8c,d). Radiographic measurements are shown in Table 8.3.

8.3.7 Other findings

Fusion of the dorsal surface of the wing of the sacrum and ilium was seen in a 14.3-year-old animal (Fig. 8.1a). Unilateral lumbarisation of the first sacral vertebra was seen in a 10.3-year-old animal (Fig. 8.9a). Osteoarthrosis (OA) of the hip joint was seen bilaterally in a 11.3-year-old animal and was characterised by osteophyte formation around the neck of the femur and in the trochanteric fossa (Fig. 8.9d,e). Osteoarthrosis of the stifle joint was seen in a 9.6-year-old animal and was characterised by the presence of enthesiophytes on the apex of the patella and tibial tuberosity (Fig. 8.9b,c). In

the tarsus OA was seen in three animals older than 9-years and was characterised by poor delineation of the tarsal bones and bases of the MT bones (Fig. 8.9c). Fusion of the tibiofibular joint was seen in two animals above 10-years (Figs 8.5f and 8.9f).

8.4 DISCUSSION

The red panda is a quadrupedal arboreal animal spending most of its time in trees (Srivastan et al., 2009). Movement in trees is facilitated by a high degree of flexibility of the pelvic and pectoral girdles and limb joints (Roberts and Gittleman, 1984).

The more medially directed minor trochanter permits greater rotation of the femur and is associated with climbing ability (Taylor, 1976). The poorly defined intermediate ridge at the distal articular surface of the tibia and the less pronounced medial ridge of the trochlea of the talus facilitate supination of the foot (Taylor, 1976). Prominent medial and intermediate ridges of the talus and distal articular surface of the tibia, respectively, restrict the movement of the tibiotalar joint in flexion and extension for terrestrial locomotion (Taylor, 1976; Fleagle and Simons, 1995). Slightly concave and convex proximal and middle articular surfaces, respectively, on the plantar aspect of the talus, which articulate with the calcaneus, allow for greater mobility of the talocalcaneal joint (Taylor, 1976).

The laterally directed lateral process of the base of MT V most likely aids in the abduction of the foot and/or MT V as was speculated in climbing African Viverridae (Taylor, 1976). In a study, which involved African Viveridae (Carnivora), the lateral process of the base of the V was found to be directed laterally in climbing species, whereas in terrestrial species it was directed proximally (Taylor, 1976). The latter orientation permits very limited extension and flexion (Taylor, 1976), probably as an adaptation to a terrestrial environment. The widely spaced MT bones provide a large space for the effectiveness of the muscles, which are responsible for small movements of the digits (Taylor, 1974).

Unlike in the red panda, the medial ridge of the talus and intermediate ridge at the distal articular surface of the tibia are more prominent in the coati (*Nasua nasua*) (Martins et al., 2013). The coati lives both on the ground and in trees (McClearn, 1992). Although it can descend or ascend small trees and vines, it is primarily a terrestrial animal (Gompper and Decker, 1998). The coati is not a graceful climber (McClearn, 1992) and unable to fully reverse its hind foot during descending (McClearn, 1992; Gompper and Decker, 1998) as does the red panda.

The wide ventromedial surface of the ilium and the medially directed minor trochanter observed in this species are associated with climbing ability. The wide ventromedial surface of the ilium provides a large area for the origin of the *M. iliacus*, which inserts on the minor trochanter (Fisher et al., 2008). The

wide ventromedial surface of the ilium most likely indicates that the *M. iliopsoas* is powerful in this species.

The caudal ramus of the pubis provides the origin of the various adductors of the hind limb (Fisher et al., 2008). This wide ramus of the pubis observed in this species is similar to that of the coati (Martins et al., 2013) and most likely indicates the strength of these muscles in adduction of the hind limb. It is most likely that these muscles, together with the ability to supinate the foot play a greater role in the gripping action of the feet.

The shallow trochlea of the femur, the short widely spaced MT bones and the presence of a well-developed MT I observed in the red panda are adaptations to arboreal locomotion. The trochlea of the femur is well-developed and surrounded by high ridges in cursorial animals and those that rely on rapid or powerful knee extension (Taylor, 1976; Fleagle and Simons, 1995). Further, in cursorial species the MT bones are long and close to each other with MT I being reduced or absent (Taylor, 1976). In the coati (Martins et al., 2013) the MT bones are widely spaced and MT I is well-developed, similar to the red panda. This is because both the red panda and coati have the ability to climb trees.

A distinct articular facet between the distal parts of the tibia and fibula observed in this species is similar to the coati (Martins et al., 2013) and is associated with a plantigrade posture (Taylor, 1976). Plantigrade posture has been reported in the coati (Gompper and Decker, 1998). The fairly

symmetrical distal articular surface of P2 and the parallel orientation to the horizontal plane of the proximal articular surface of P3 observed in this species indicate that the claws are slightly (Taylor, 1974) to non-retractile (Gonyea and Ashworth, 1975).

The large ovoid popliteal sesamoid bone observed in this study appears similar to that of domestic cats (McCarthy and Wood, 1989). The absence of visualisation of the popliteal sesamoid bone on radiographic examination in some of the animals in this study is similar to a reported study in domestic cats (Arnbjerg and Heje, 1993). The medial fabella may not be visualised radiographically in domestic cats (Arnbjerg and Heje, 1993), which is also similar to our findings.

The tarsal sesamoid bone observed in the red panda provides the origin for the medial belly of the *Mm. flexores digiti I profundi breves* (Fisher et al., 2008). Therefore, the name 'medial sesamoid bone for the *Mm. flexores digiti I profundi breves*' is suggested. The tarsal sesamoid bone is also present in the coati (Martins et al., 2013).

The reason for existence and exact function of sesamoid bones is debatable (Mottershead, 1988). It is most likely that sesamoid bones enable tendons in which they are associated with to become fixed to an adjacent bony area, thus allowing the particular muscle involved to act in a specialized manner at certain times and for a specific purpose (Mottershead, 1988).

The focal radiolucent region seen just distal to the calcaneus in all animals on the ML radiographic view is a relative radiolucency as a result of less bone in this area (3D effect of bones) and should not be misinterpreted as osteolysis due to pathological conditions.

Osteoarthrosis of the hip joint observed in this study was characterised mainly by remodelling of the neck of the femur similar to dogs but different from domestic cats (Biery, 2006; Lascelles, 2010). In the latter species, it is characterised mainly by extensive remodelling and proliferative changes involving the craniodorsal acetabular margin and minimal remodeling of the neck of the femur (Biery, 2006; Lascelles, 2010). The normal pointed appearance of the patella in this species could make the decision of whether early enthesiophyte formation is present very difficult.

Radiographic measurements obtained in this study will be slightly increased due to magnification (Thrall, 2013). Object-film distance affects magnification more than focal spot-film distance. This is because the latter is usually kept constant. In clinical practice some parts of the patient are always farther from the film, which causes magnification. Increasing object-film distance increases magnification (Thrall, 2013). It was decided not to compensate for magnification in order to provide more useful data for clinical use, where compensation for magnification is also not applied.

The morphology of the pelvis and hind limb of the red panda indicated flexibility of the pelvis and hind limb joints as an adaptation to arboreal

quadrupedal behaviour. Further, this species possesses some unique anatomical features such as a tarsal sesamoid bone, a poorly defined intermediate ridge at the distal articular surface of the tibia, a laterally directed lateral process of the base of MT V, widely spaced MT bones and digits, and a well-developed MT I and digit I. Knowledge of the variations in the normal morphology of the pelvis and hind limb of different animal species is essential for successful identification of lesions and skeletons.

8.5 ACKNOWLEDGEMENTS

The authors would like to thank the Organization for Women in Science for the Developing World (OWSD), Swedish International Development Cooperation Agency (SIDA), University of Pretoria, Johannesburg (JHB) and Bristol Zoos for supporting this study. The National Museum of Scotland for supplying the bone specimen. Dr. Georgina Cole, Ms. Fania Mohlala, sisters and animal handlers of the JHB zoo and Onderstepoort Veterinary Academic Hospital for their assistance during anaesthesia, CT and radiographic examinations. Mrs. Charmaine Vermeulen of the University of Pretoria for photographic assistance and Mrs. Wilma Olivier of University of Pretoria for her assistance in administrative work.

8.6 REFERENCES

Arnbjerg, J., and N. I. Heje, 1993: Fabellae and popliteal sesamoid bones in cats. J. Small Anim. Pract. **34,** 95–98.

Biery, D. N., 2006: The hip joint and pelvis. In: BSAVA Manual of Canine and Feline Musculoskeletal Imaging (F. J. Barr and R. M. Kirberger, eds). Gloucester: UK. pp. 119–134.

de Araújo, F. A. P., N. F. Sesoko, S. C. Rahal, C. R. Teixeira, T. R. Müller, and M. R. F. Machado, 2013: Bone morphology of the hind limbs in two caviomorph rodents. Anat. Histol. Embryol. **42,** 114–123.

Delclaux, M., C. Talavera, M. López, J. M. Sánchez, and M. I. García, 2002: Avascular necrosis of the femoral heads in a red panda (*Ailurus fulgens fulgens*): possible Legg-Calve-Perthes disease. J. Zoo Wildl. Med. **33,** 283–285.

Eriksson, P., J. Zidar, D. White, J. Westander, and M. Andersson, 2010: Current husbandry of red pandas (*Ailurus fulgens*) in zoos. Zoo Biol. **29,** 732–740.

Fisher, R. E., 2011: Red panda anatomy. In: Red panda Biology and Conservation of the First Panda (A. R. Glatston, ed.). London: Academic Press. pp. 89–100.

Fisher, R. E., B. Adrian, C. Elrod, and M. Hicks, 2008: The phylogeny of the red panda (*Ailurus fulgens*): evidence from the hind limb. J. Anat. 213, 607–628.

Fisher, R. E., B. Adrian, M. Barton, J. Holmgren, and S. Y. Tang, 2009: The phylogeny of the red panda (*Ailurus fulgens*): evidence from the forelimb. J. Anat. **215,** 611–635.

Fleagle, J. G., and E. L. Simons, 1995: Limb skeleton and locomotor adaptations of *Apidium phiomense*, an Oligocene Anthropoid from Egypt. Am. J. Phys. Anthropol. **97,** 235–289.

Gompper, M. E., and D. M. Decker, 1998: *Nasua nasua*. Mamm. Species. **580,** 1-9.

Gonyea, W., and R. Ashworth, 1975: The form and function of retractile claws in the felidae and other representative carnivorans. J. Morph. **145,** 229–238.

Groves, C., 2011: The taxonomy and phylogeny of *Ailurus*. In: Red panda Biology and Conservation of the First Panda (A. R. Glatston, ed.). London: Academic Press. pp. 101–124.

Heath, T., and J. Platnick, 2008: Ailurus fulgens animal diversity web. Available at: http://animaldiversity.ummz.umich.edu/accounts/Ailurus_fulgens (accessed on 4 April 2013).

IUCN, 2014: IUCN Red List of Threatened Species. Version 2014.3. Available at: http://www.iucnredlist.org (accessed on 18 November 2014).

Kinns, J., R. Malinowski, F. McEvoy, T. Schwarz, and A. Zwingenberger, 2011: Special software applications in veterinary computed tomography. In: Veterinary Computed Tomography (T. Schwarz and J. Saunders, eds). UK: John Wiley & Sons Ltd. pp. 67–74.

Lascelles, B. D. X., 2010: Feline degenerative joint disease. Vet. Surg. **39,** 2–13.

Lynch, M., H. McCracken, and R. Slocombe, 2002: Hyperostotic bone disease in red pandas (*Ailurus fulgens*). J. Zoo Wildl. Med. **33,** 263–271.

Martins, G. S., E. R. Lopes, I. I. G. Taques, C. Y. Correia, Y. S. Meireles, N. C. M. R. Turbino, L. D. Guimarães, and P. B. Néspoli, 2013: Radiographic morphology of the skeleton, thorax and abdomen of coati (*Nasua nasua* Linnaeus, 1766). Pesq. Vet. Bras. **33,** 1137–1143.

McCarthy, P. H., and A. K. W. Wood, 1989: Anatomical and radiological observations of the sesamoid bone of the popliteus muscle in the adult dog and cat. Anat. Histol. Embryol. **18,** 58–65.

McClearn, D., 1992: Locomotion, posture and feeding behaviour of kinkajous, coatis and raccoons. J. Mamm. **73,** 245–261.

Mottershead, S., 1988: Sesamoid bones and cartilages: An enquiry into their function. Clin. Anat. **1,** 59–62.

Nickel, R., A. Schummer, E. Seiferle, J. Frewein, H. Wilkens, and K. H. Wille, 1986: The Anatomy of the Domestic Animals Vol. 1. Berlin: Springer-Verlag.

O'Brien, T., 1978: Normal radiographic anatomy of the abdomen. In: Radiographic Diagnosis of Abdominal Disorders in the Dog and Cat. Philadelphia: W. B. Saunders Company. pp. 9–47.

Ohlerth, S., and G. Scharf, 2007: Computed tomography in small animals-basic principles and state of the art applications. Vet. J. **173,** 254–271.

Philippa, J., and E. Ramsay, 2011: Captive red panda medicine. In: Red panda Biology and Conservation of the First Panda (A. R. Glatston, ed.). London: Academic Press. pp. 271–285.

Pradhan, S., G. K. Saha, and J. A Khan, 2001: Ecology of the red panda *Ailurus fulgens* in the Singhalila National Park, Darjeeling, India. Biol. Cons. **98,** 11–18.

Preece, B., 2011: Red panda pathology. In: Red panda Biology and Conservation of the First Panda (A. R. Glatston, ed.). London: Academic Press. pp. 287–302.

Roberts, M. S., and J. L. Gittleman, 1984: *Ailurus fulgens*. Mamm. Species. **222,** 1–8.

Samii, V., I. Gielen, E. Ludewig, W. M. Adams, I. Kiefer, H. vanBree, and J. Saunders, 2011: Joints. In: Veterinary Computed Tomography (T. Schwarz and J. Saunders, eds). UK: John Wiley & Sons Ltd. pp. 387–419.

Silverman, S., and L. A. Tell, 2005: Radiology of Rodents, Rabbits and Ferrets, An Atlas of Normal Anatomy and Positioning. St. Louis: Elsevier Saunders.

Srivastav, A., P. Nigam, D. Chakraborty, and A. K. Nayak, 2009: National Studbook of Red pandas *(Ailurus fulgens)*. New Delhi: Wildlife Institute of India, Dehradun and Central Zoo Authority.

Taylor, M. E., 1974: The functional anatomy of the forelimb of some African Viverridae (Carnivora). J. Morph. **143,** 307–335.

Taylor, M. E., 1976: The functional anatomy of the hind limb of some African Viverridae (Carnivora). J. Morph. **148,** 227–253.

Thrall, D. E., 2013: Introduction to radiographic interpretation. In: Textbook of Veterinary Diagnostic Radiology (D. E. Thrall, ed.), St. Louis: Saunders Elsevier. pp. 74–86.

Thrall, D. E., and I. D. Robertson, 2011: The pelvic limb. In: Atlas of Normal Radiographic Anatomy and Anatomic Variants in the Dog and Cat (D. E. Thrall and I. D. Robertson, eds). St. Louis: Elsevier Saunder. pp. 100–126.

Wei, F., and Z. Zhang, 2009: Family Ailuridae (red panda). In: Handbook of the Mammals of the World Vol. 1 Carnivores (D. E. Wilson and R. A. Mittermeier, eds). Barcelona: Lynx Edicions. pp. 498–503.

8.7 TABLES

Table 8.1 Sample population of red pandas used for gross osteology, radiography and computed tomography (CT)

Identification	Age (years)	Weight (kg)	Sex	Study
3323[a]	14.3	3.7	Male	Gross osteology, radiography and CT
4694[a]	11.3	3.87	Male	Gross osteology and radiography
5230	10.3	5.09	Male	Radiography
5542	9.6	4.65	Female	Radiography
8493	2.5	4.57	Male	Radiography
8680	1.4	3.97	Female	Radiography
8681	1.4	5.6	Male	Radiography
8678	2.08	4.48	Female	Radiography
6591	8	5.96	Male	Radiography
2004.71.2[b]	3.5		Male	Gross osteology

[a]Euthanased animals

[b]Bone specimens from the National Museum of Scotland

Table 8.2 Radiographic measurements, not compensated for magnification, of the pelvis, long bones and sesamoid bones of the right hind limb in captive red pandas

Bone	Variable	Number of animals	Mean ± SD (cm)	Range (cm)
Pelvis	Length	8	9.25 ± 0.21	8.90 – 9.50
	*T diameter	8	3.45 ± 0.22	3.20 – 3.70
Femur	Length	6	11.98 ± 0.37	11.50 – 12.50
	CrCd diameter	6	0.80 ± 0.06	0.70 – 0.90
Tibia	Length	6	11.52 ± 0.32	11.10 – 12.00
	CrCd diameter	6	0.78 ± 0.42	0.70 – 0.80
Fibula	Length	6	10.42 ± 0.33	10.00 – 10.90
	CrCd diameter	6	0.30 ± 0.00	0.30 – 0.30
Patella	Length	7	1.19 ± 0.02	1.15 – 1.20
	CrCd diameter	7	0.43 ± 0.05	0.40 – 0.50
Lateral fabella	Length	5	0.17 ± 0.07	0.10 – 0.25
	CrCd diameter	5	0.26 ± 0.15	0.10 – 0.40
Popliteal sesamoid	Length	5	0.21 ± 0.02	0.20 – 0.25
	CrCd diameter	5	0.39 ± 0.02	0.35 – 0.40
Tarsal sesamoid	Length	5	0.70 ± 0.17	0.60 – 1.00
	ML diameter	5	0.29 ± 0.02	0.25 – 0.30
Metatarsal sesamoid	Length	4	0.31 ± 0.09	0.20 – 0.40
	CrCd diameter	4	0.14 ± 0.03	0.10 – 0.15

*T, Transverse

Table 8.3 Radiographic measurement, not compensated for magnification, of length of short bones of the right hind limb in captive red pandas

Bone	Number of animals	Mean ± SD (cm)	Range (cm)
MT I	6	2.20 ± 0.13	2.00 – 2.30
MT II	6	3.08 ± 0.17	2.80 – 3.30
MT III	6	3.43 ± 0.18	3.10 – 3.60
MT IV	6	3.62 ± 0.19	3.30 – 3.80
MT V	6	3.37 ± 0.20	3.00 – 3.50
P1 of digit I	6	1.42 ± 0.08	1.30 – 1.50
P1 of digit II	6	1.68 ± 0.12	1.50 – 1.80
P1 of digit III	6	1.93 ± 0.08	1.80 – 2.00
P1 of digit IV	6	1.87 ± 0.10	1.70 – 2.00
P1 of digit V	6	1.47 ± 0.08	1.30 – 1.50
P2 of digit II	6	1.21 ± 0.08	1.10 – 1.30
P2 of digit III	6	1.25 ± 0.06	1.20 – 1.30
P2 of digit IV	6	1.27 ± 0.10	1.10 – 1.40
P2 of digit V	6	1.01 ± 0.13	0.80 – 1.20

MT, metatarsal; P1, proximal phalanx; P2, middle phalanx

8.8 FIGURES

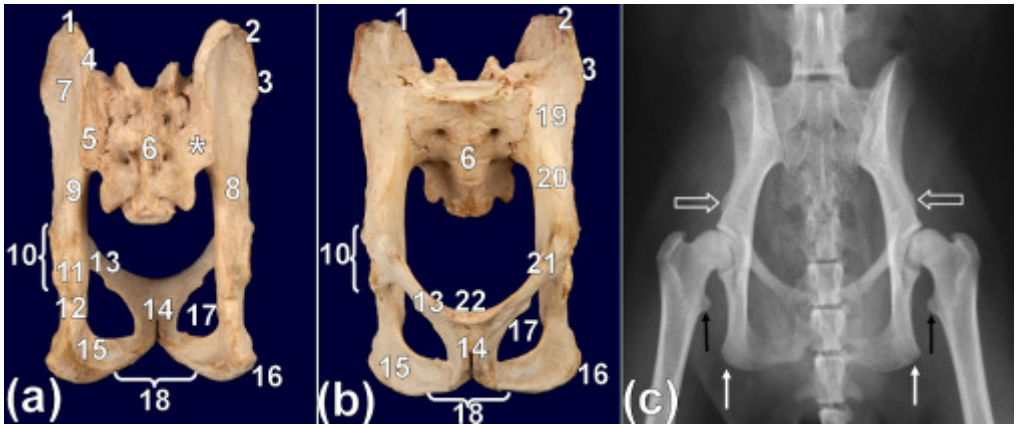

Fig. 8.1 Dorsal (a) and ventral (b) views of a bone specimen of the pelvis of a 14.3-year-old male red panda. (c) Ventrodorsal radiograph of the pelvis of a 2.1-year-old female red panda. Note the fusion of the dorsal surface of the wing of the sacrum and ilium (asterisk) (a) and the cranial part of the pelvic symphysis (a, b). The ventromedial surface of the ilium is wide (b). (c) The ilial wings are wide and the lateral area for the *M. rectus femoris* (open white arrows) and ischiatic tuberosities (white arrows) are less prominent. The prominent minor trochanters of the femur are pointed at by black arrows. (1) Iliac crest, (2) cranial ventral iliac spine, (3) caudal ventral iliac spine, (4) cranial dorsal iliac spine, (5) caudal dorsal iliac spine, (6) sacrum, (7) gluteal surface, (8) body of ilium, (9) major ischiatic notch, (10) acetabulum, (11) ischiatic spine, (12) groove for the tendon of the *M. obturatorius internus*, (13) pubic bone, (14) pelvic symphysis, (15) ischium, (16) ischiatic tuberosity, (17) obturator foramen, (18) ischiatic arch, (19) iliac surface, (20) arcuate line, (21) iliopubic eminence and (22) pecten of pubic bone.

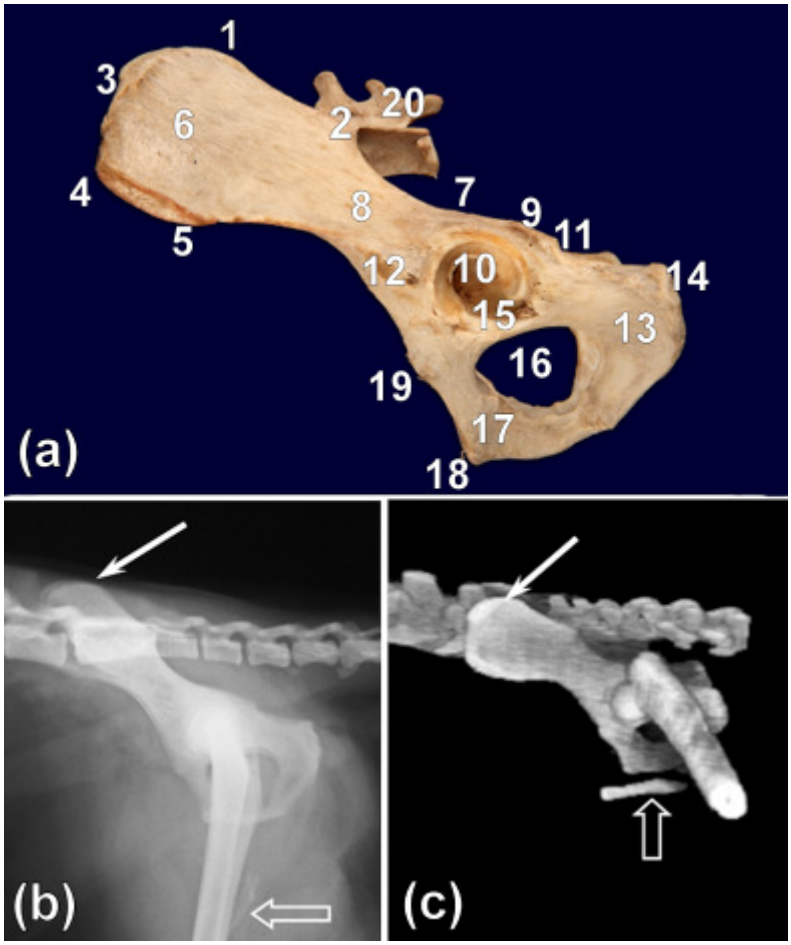

Fig. 8.2 Lateral view (a) of a bone specimen of the pelvis of a 14.3-year-old male red panda. Right-lateral radiograph (b) of the pelvis of an 8-year-old male red panda. Lateral view (c) of a 3D volume-rendered CT image (using a grey scale default) of the pelvis of a 14.3-year-old male red panda. Note the broad ilial wings (white arrows) and visualisation of the os penis (open white arrow). (1) Cranial dorsal iliac spine, (2) caudal dorsal iliac spine, (3) iliac crest, (4) cranial ventral iliac spine, (5) caudal ventral iliac spine, (6) gluteal surface, (7) major ischiatic notch, (8) body of the ilium, (9) ischiatic spine, (10) acetabulum, (11) groove for the tendon of the *M. obturatorius internus*, (12) lateral area for the *M. rectus femoris*, (13) ischium, (14) ischiatic tuberosity, (15) acetabular notch, (16) obturator foramen, (17) pubic bone, (18) pecten of pubic bone, (19) iliopubic eminence and (20) sacrum.

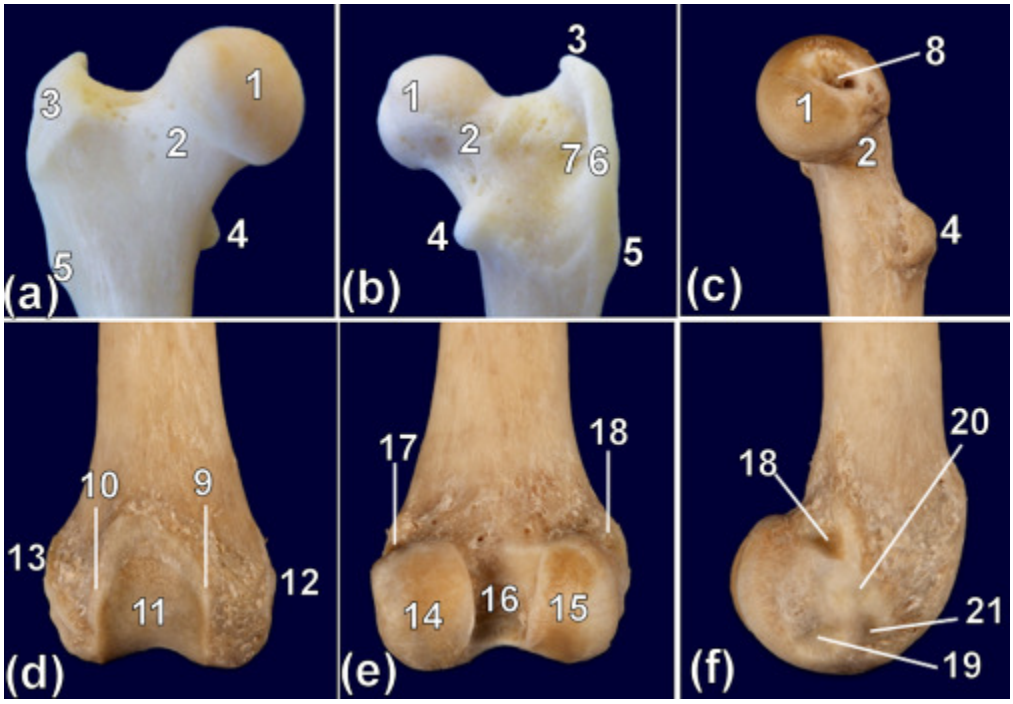

Fig. 8.3 Cranial (a), caudal (b) and medial (c) views of the proximal, and cranial (d), caudal (e) and lateral (f) views of the distal bone specimens of the femur of 3.5-year-old (a, b) and 14.3-year-old (c, d, e, f) male red pandas. (1) Head, (2) neck, (3) major trochanter, (4) minor trochanter, (5) third trochanter, (6) edge of the major trochanter, (7) trochanteric fossa, (8) *Fovea capitis*, (9) medial ridge of trochlea, (10) lateral ridge of trochlea, (11) trochlea, (12) medial epicondyle, (13) lateral epicondyle, (14) medial condyle, (15) lateral condyle, (16) inter-condylar fossa, (17) fossa for the insertion of the medial head of the *M. gastrocnemius*, (18) fossa for the insertion of the lateral head of the *M. gastrocnemius*, (19) popliteal fossa, (20) fossa for the lateral collateral ligament and (21) extensor fossa.

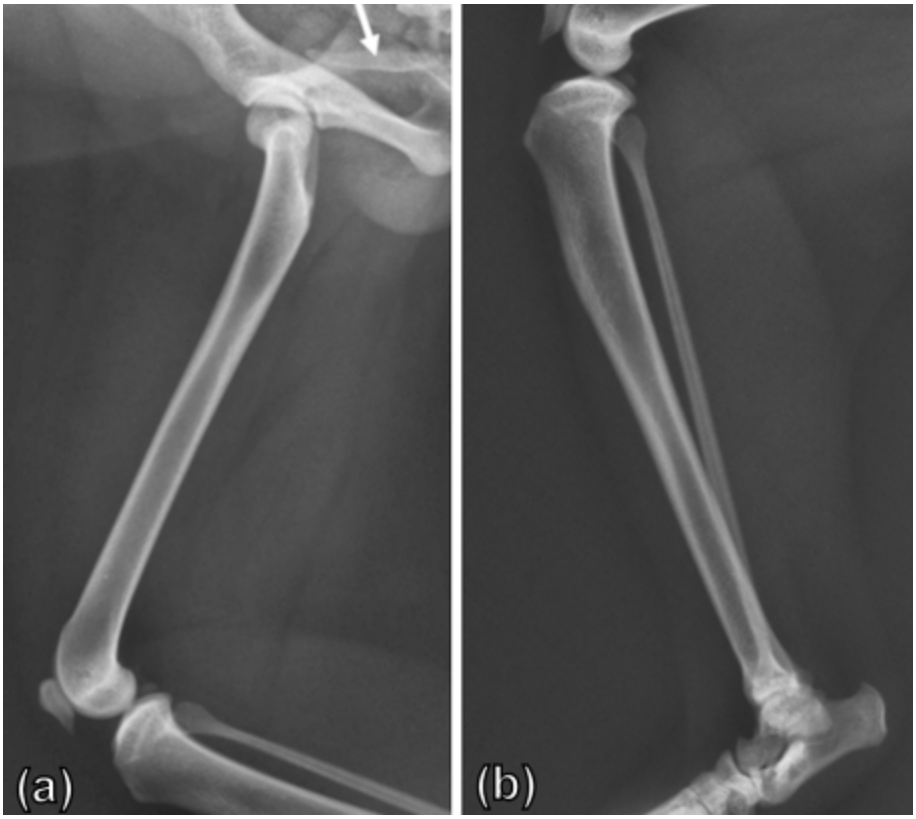

Fig. 8.4 Mediolateral radiograph of the right femur (a), tibia and fibula (b) of a 1.4-year-old male red panda. (a) The femur is slender with very symmetric thicknesses of the cranial and caudal diaphyseal cortices. The os penis is indicated by the white arrow. (b) Note the variation in thickness of the cranial and caudal diaphyseal cortices of the tibia and an almost uniform thickness of the cranial and caudal diaphyseal cortices of the fibula. The body of the tibia is curved cranially. Note also the bulbous appearance of the proximal and distal parts of the fibula.

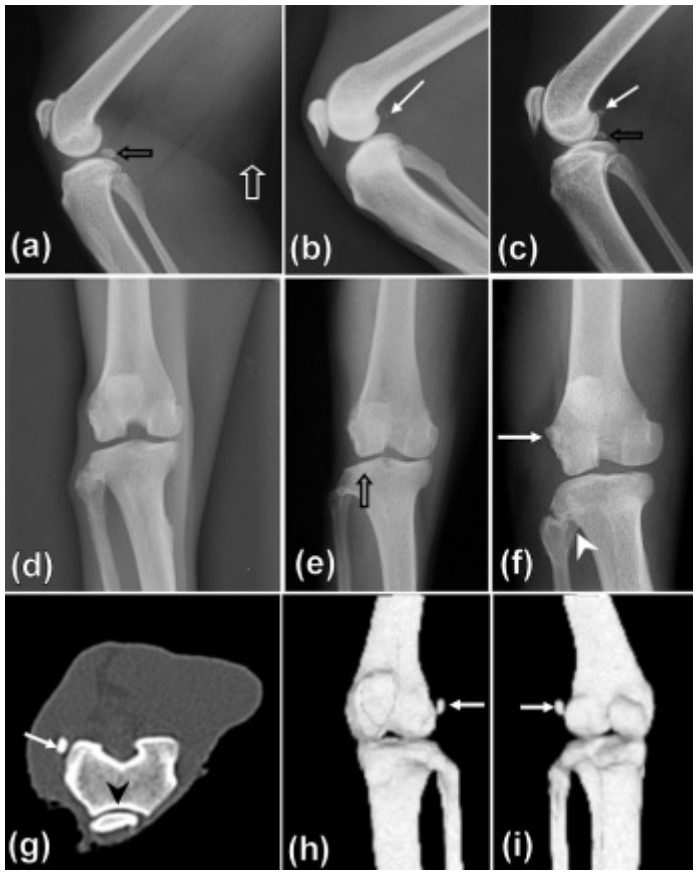

Fig. 8.5 Mediolateral (a, b, c) and CrCd (d, e, f) radiographs of the right stifle joint of 2.5-year-old (a), 14.3-year-old (b, d), 1.4-year-old (c, e) and 11.3-year-old (f) male (a, b, d, e, f) and female (c) red pandas. Computed tomographic images (g, h, i) of the left stifle joint of a 14.3-year-old male red panda. Transverse slice (g) displayed using a sharp (B80) kernel with a bone window (WW=2000; WL=400). Craniolateral (h) and caudomedial (i) views of the 3D volume-rendered CT image of a left stifle joint (using a grey scale default). Note the elongated and pointed apex of the patella, large popliteal sesamoid bone (open black arrows), and low projection of the tibial tuberosity and inter-condylar eminence. Note also the visualisation of the lateral fabella (white arrows) and popliteal lymph node (open white arrow). Note the lack of visualisation of the medial fabella in all animals. The popliteal sesamoid bone is poorly visualised superimposed on the lateral condyle of the tibia (e). Note also the ankylosis of the tibiofibular joint (white arrow head) (f) and the shallow trochlea of the femur (black arrow head) (g).

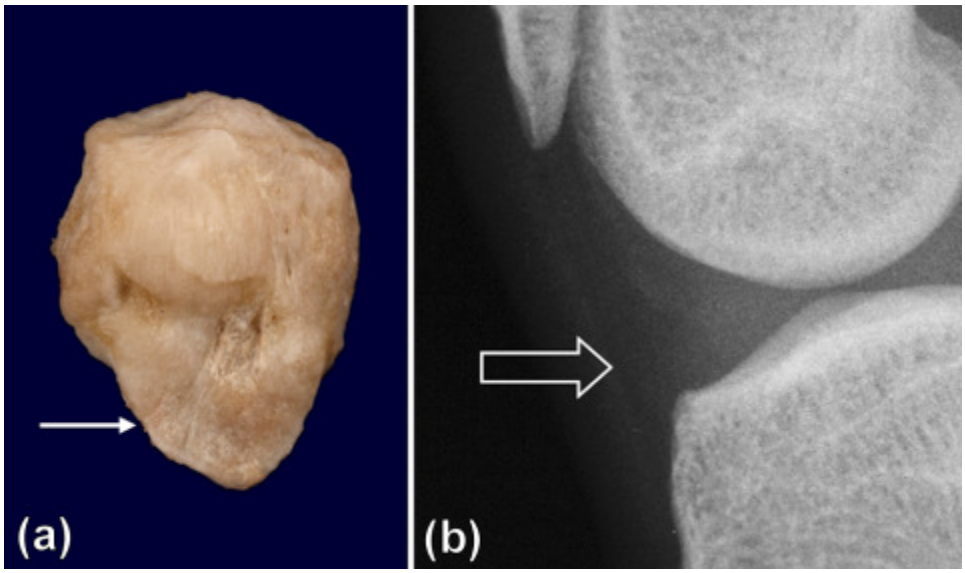

Fig. 8.6 Dorsal view (a) of a bone specimen of the patella of a 14.3-year-old male red panda. Close-up ML radiograph (b) of the right stifle joint of a 2.5-year-old male red panda. (a) Note the elongated and pointed apex of the patella (white arrow). (b) Note also the visualisation of the infrapatellar fat pad (open white arrow).

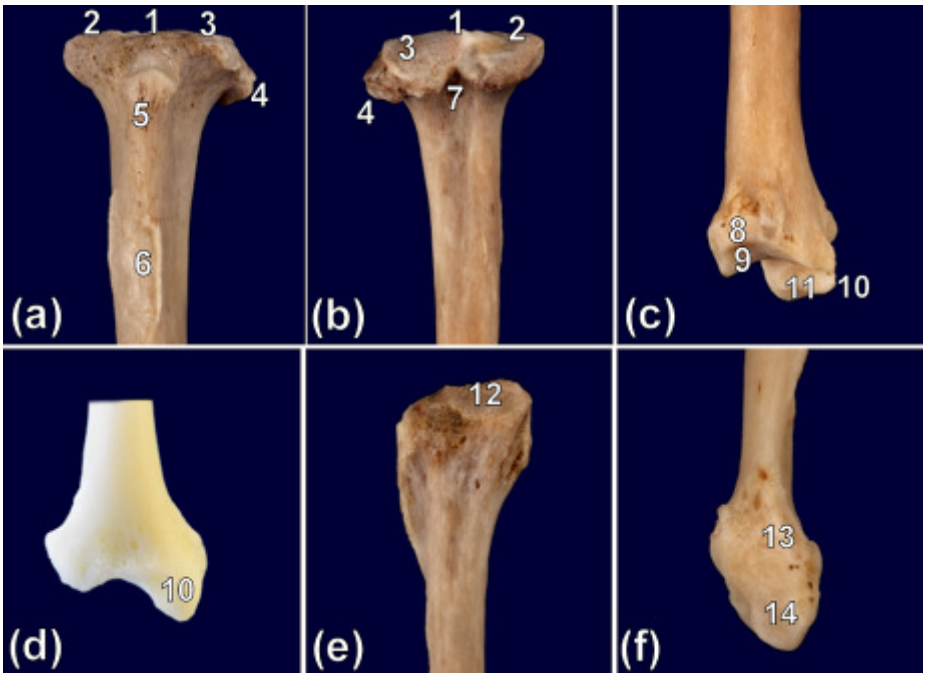

Fig. 8.7 Cranial (a, d), caudal (b) and caudolateral (c) views of the proximal and distal bone specimens of the tibia of an 11.3-year-old (a, b, c) and a 3.5-year-old (d) male red pandas. (e, f) Medial view of the proximal (e) and distal (f) bone specimen of the fibula of an 11.3-years-old male red panda. (1) Intercondylar eminence, (2) medial condyle, (3) lateral condyle, (4) facies articularis fibularis, (5) tibial tuberosity, (6) area for attachment of the *M. sartorius*, *M. gracilis* and *M. semitendinosus*, (7) popliteal notch, (8) fibular notch, (9) cochlea tibiae, (10) medial malleolus, (11) facies articularis malleoli medialis, (12) facies articularis capitis fibularis, (13) articular surface for the fibular notch of the tibia and (14) facies articularis malleoli lateralis.

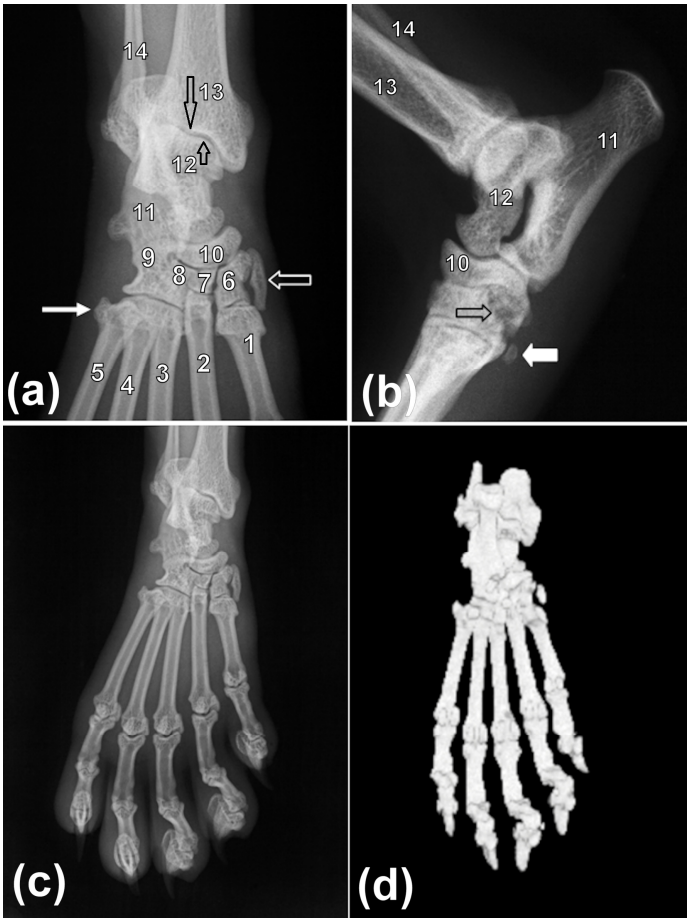

Fig. 8.8 Plantarodorsal (a, c) and mediolateral (b) radiographs of the right tarsus (a, b) and pes (c) of a 2.5-year-old male (a, c) and a 1.4-year-old female (b) red panda. Plantar view (d) of the 3D volume-rendered CT image of the left pes of a 14.3-year-old male red panda. (a) Note the low projection of the intermediate (long black open arrow) and medial (short black open arrow) ridges of the distal articular surface of the tibia and of the trochlea of the talus, respectively. Note also the laterally directed lateral process of the base of the MT V (white arrow) and the presence of a tarsal sesamoid bone (white open arrow). Note the sloping of the facies articularis malleoli medialis from lateral to medial. (b) Note also the presence of a small MT sesamoid bone on the plantar aspect of the bases of the MT bones (thick white arrow) and the wide talocalcaneal joint space. The focal radiolucent region seen just distal to the calcaneus (open black arrow) is normal and should not be confused with pathology. (c, d) Note the presence of paired axial and abaxial proximal sesamoid bones on each metatarsophalangeal joint and widely spaced MT bones and digits. (1) MT I, (2) MT II, (3) MT III, (4) MT IV, (5) MT V, (6) T I, (7) T II, (8) T III, (9) T IV, (10) central tarsal bone, (11) calcaneus, (12) talus, (13) tibia, (14) fibula.

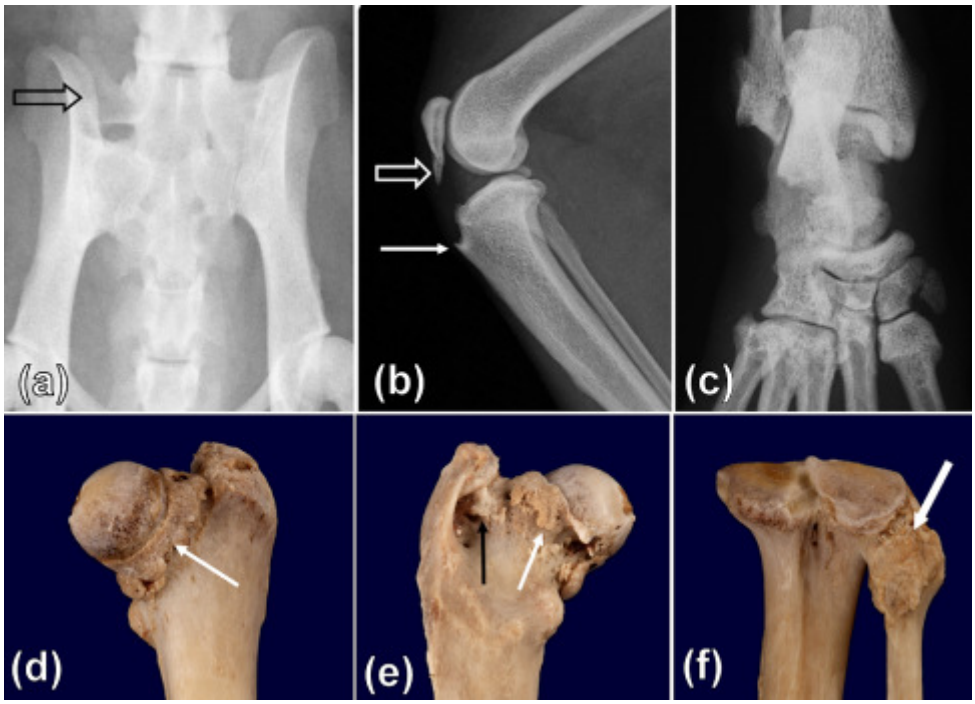

Fig. 8.9 Close-up VD radiograph of the pelvis of a 10.3-year-old male red panda (a), ML radiograph of the right stifle joint of a 9.6-year-old female red panda (b) and PlD radiograph of the right tarsus of a 14.3-year-old male red panda (c). Cranial (d) and caudal (e, f) views of bone specimens of the proximal femur (d, e) and fibula (f) of a 11.3-year-old male red panda. (a) Note the unilateral lumbarisation of the first sacral vertebra (open black arrow). (b) Note also the presence of enthesiophytes on the apex of the patella (open white arrow) and tibial tuberosity (white arrow). (c) Note the poor delineation of the tarsal bones and bases of the MT bones when compared to Fig. 8.8a. (d, e) Note also the presence of osteophytes at the femoral neck (white arrows) and in the trochanteric fossa (black arrow). (f) Note the ankylosis of the tibiofibular joint (thick white arrow).

CHAPTER 9

RADIOGRAPHIC THORACIC ANATOMY OF THE RED PANDA (*AILURUS FULGENS*)

9.1 INTRODUCTION

The red panda (*Ailurus fulgens*) is primarily distributed in the Himalayas and southern China (Fisher et al., 2009). It is classified as a vulnerable species by the International Union for Conservation of Nature and Natural Resources (IUCN 2014). The red panda is closely related to procyonids, mustelids and skunks (Groves, 2011). It is a species commonly kept in zoological gardens. The head and body length of the red panda ranges from 560 mm to 625 mm (Roberts and Gittleman, 1984). The mean weight of adult males and females in captivity is 5.0 kg (range: 3.7 kg–6.2 kg) and 4.9 kg (range: 4.2 kg–6.0 kg), respectively (Roberts and Gittleman, 1984).

The trachea of the red panda consists of 38 cartilage rings and it is 4.5 inches (11.43 cm) in length and 0.5 inches (1.27 cm) in average width (Flower, 1870). The cartilage rings are incomplete dorsally as described in domestic cats (Light, 1993) and dogs (Evans and de Lahunta, 2013). The trachea branches into two short principal bronchi: the left and right principal bronchi. The right principal bronchus is shorter and wider than the left principal bronchus (Flower, 1870). The right lung consists of four lobes i.e. the cranial,

medial, caudal and accessory lobes. The left lung consists of two lobes i.e. the cranial and caudal lobes (Flower, 1870).

Various thoracic diseases such as traumatic pericarditis (Zwart, 1989), right heart failure (Preece, 2011), hypertrophic cardiomyopathy (Gardner, 1985), dirofilariasis (Harwell and Craig, 1981; Preece, 2011), pleuritis (Preece, 2011; Zwart, 1989), tracheal obstruction (Preece, 2011), bovine tuberculosis (Philippa and Ramsay, 2011), anthracosis (Zwart, 1989), lung worm infestation (Preece, 2011), lung sarcoma (Philippa and Ramsay, 2011), and infectious and non-infectious pneumonias such as aspiration pneumonia, chronic fibrosing interstitial pneumonia and verminous pneumonia (Patterson-Kane et al., 2009; Philippa and Ramsay, 2011; Preece, 2011; Zwart, 1989) have been reported in the red panda.

Radiography is a non-invasive diagnostic imaging modality, which is used for diagnosis of various thoracic diseases (Suter, 1981; Fossum et al., 1989; Sullivan and Lee, 1989; Lobetti et al., 2001; Buchanan, 2004). It is commonly used as the first diagnostic imaging modality for thoracic diseases in animals. Knowledge of the normal radiographic thoracic anatomy of individual species is important for accurate interpretation and diagnosis of various thoracic diseases (Thrall, 2013). The normal radiographic thoracic anatomy of companion animals is well documented, which provides a reference for diagnosis of thoracic disease (Thrall and Robertson, 2011).

The aim of this study was to describe the normal radiographic thoracic anatomy of captive red pandas as a species-specific reference for routine health examinations and clinical cases. To the best of the author's knowledge this has not been published previously.

9.2 MATERIALS AND METHODS

9.2.1 Animals

Eleven adult captive red pandas (*Ailurus fulgens*) from the Johannesburg zoo, South Africa, without clinical evidence of thoracic disease were used in this study. The age of animals ranged from 1.4 years to 14.3 years (mean: 5.9 ± 4.6 years). Their minimum and maximum weights were 3.7 kg and 6.0 kg, respectively (mean: 4.7 ± 0.7 kg). Of the 11 animals, six were females and five were males. There was no significant difference (P = 0.38) in the mean age between male and female animals. The mean weight of male animals (5.06 ± 0.92kg) was higher than female animals (4.41 ± 0.41kg) although statistically not significant (P = 0.15). This study was approved by the Animal Use and Care Committee (AUCC) of the University of Pretoria and Johannesburg Zoo Research Committee.

9.2.2 Radiography

Radiography of the thorax was performed under general anaesthesia during annual health examinations. Animals were fasted for 8-12 hours but water was given *ad libitum* until shortly before anaesthesia. Anaesthesia was induced by intramuscular injection of medetomidine hydrochloride (Pfizer

Laboratories Ltd, Sandton, South Africa) and ketamine hydrochloride (Kyron Laboratories Ltd, Benrose, South Africa). Animals were intubated and anaesthesia maintained using isoflurane (Safeline Pharmaceuticals Ltd, Roodepoort, South Africa).

In 10 animals, radiography was performed using an EVA-HF525 (Comed Medical System Co. Ltd, Kyunggi, Korea) x-ray machine and a table-top technique was used. A source to image distance (SID) of 95 cm was used with a kVp range of 46-48 and 1.25 mAs. In 9 of the 10 animals, images were obtained by a conventional system. In the remaining animal (1/10) computed radiography (CR) (Vita LE®, Carestream Health Inc, New York, United States) was used. For the conventional system, an automatic x-ray film processor model CP-345 (ELK Corporation, Tokyo, Japan) was used with medium speed screen-type films (Fujifilm Corporation, Tokyo, Japan) in combination with RAREX green regular intensifying screens (Okamoto manufacturing Co. Ltd, Tokyo, Japan). Radiographic images were digitalized using a digital camera (CANON 5DMARK2, Canon Inc., Tokyo, Japan).

In 1 of the 11 animals, a Siemens polymat 50 x-ray machine (Siemens, Munich, Germany) was used at a kVp and mAs of 96 and 2, respectively. Images were obtained using a Fuji Axim FCR Capsula XL (Fujifilm Corporation, Tokyo, Japan) CR system. A bucky table grid of 8:1 was used at a SID of 107 cm. In all animals right lateral (RL) and dorsoventral (DV) views of the thorax were taken at the end of inspiration.

9.2.3 Radiographic evaluation

Visibility, shape and location of thoracic organs were recorded. The depth of the thorax (TDp) was measured on the RL view (Fig. 9.1) from the dorsocaudal border of the last sternebra (six) to the closest edge of the vertebral column (Litster and Buchanan 2000b). The width of the thorax (TW) was measured on the DV view (Fig. 9.2) as the maximum distance between the left and right pleural surfaces of the eighth ribs (Litster and Buchanan, 2000b).

The lengths of thoracic vertebral bodies and sternebrae (Fig. 9.1) were measured on the RL view from the mid-point of the cranial endplate to the mid-point of the caudal edge of the caudal endplate (Nelson et al., 2011). The heights of thoracic vertebral bodies and sternebrae (Fig. 9.1) were measured on the RL view along a line that extended between the cranioventral and craniodorsal borders of the vertebral body and sternebra (Nelson et al., 2011).

The vertebral heart score (VHS) was measured on the RL and DV views as previously described in domestic cats (Litster and Buchanan, 2000b). Cardiac long axis (CLA) and cardiac short axis (CSA) measurements on the RL (Fig. 9.1) and DV (Fig. 9.2) views were used to calculate the VHS on the RL and DV views (Litster and Buchanan, 2000b) as well as cardiothoracic ratios (Nelson et al., 2011).

The maximum diameter of the caudal vena cava (CVC) was measured on the RL view cranial to the diaphragm and caudal to the cardiac silhouette (Fig.

9.1). The diameter of the CVC was also compared to the length of the thoracic vertebral body (VL) above the tracheal bifurcation (Lehmkuhl et al., 1997). The width of the craniodorsal mediastinum (MDWd) was measured at the level of the third rib head (Fig. 9.2) (Young et al., 2013).

9.2.4 Data analysis

Data was analysed using Stat View® statistical package (SAS Institute, Cary, NC, USA). Mean, standard deviation and range were calculated. Student t-test was used to compare the mean age and weight between male and female animals as well as the means of VHS on RL view versus DV view. Statistical significance was accepted at $P \leq 0.05$. Data are expressed as mean ± standard deviation (SD).

9.3 RESULTS

9.3.1 Musculoskeletal system

Of the 11 animals, 10 had 14 thoracic vertebrae (Fig. 9.3) whereas one animal (female) had 15 thoracic vertebrae. The spinous processes of thoracic vertebrae were short and decreased in length from cranial to caudal (Fig. 9.3). The anticlinal vertebra was thoracic vertebra 11 (T11) in 10 of 11 animals and T10 in one animal (Fig. 9.3). Generally, the size of thoracic vertebral bodies increased from cranial to caudal (Fig. 9.3). Of the 11 animals, 10 had 14 pairs of ribs (Fig. 9.3) of which the last two pairs were floating. One animal had 15 pairs of ribs of which the last three pairs were floating.

The sternum was fairly straight (Figs 9.3 and 9.4). In all animals, it consisted of the manubrium sterni and six sternebrae (Figs 9.3 and 9.4). The mineralised xiphoid process was seen in 10/11 animals (Fig. 9.4a). In young animals, the mineralised xiphoid process was very small (Fig. 9.4a) or not seen at all (Fig. 9.4b). The length of sternebrae decreased from cranial to caudal (Fig. 9.4). Rudimentary clavicles were seen in 3 of the 11 animals (Fig. 9.5). Of the three animals with rudimentary clavicles, in one animal it was unilateral in the left shoulder joint. Radiographic measurements and findings of the thorax are reported in Tables 9.1–9.3.

9.3.2 Cardiovascular system

On the RL view, the ovoid cardiac silhouette was obliquely positioned and the long axis of the cardiac silhouette formed an acute angle with the thoracic spine (Fig. 9.3). The cardiac silhouette was more obliquely positioned and elongated in older animals. The cranial and caudal borders of the cardiac silhouette were located at the third rib and sixth intercostal space, respectively, in 8 of the 11 animals (Fig. 9.3). In the remaining three animals, the cranial and caudal borders of the cardiac silhouette were located at the level of the fourth and seventh ribs, respectively. The size of the cardiac silhouette ranged from three to three and a half intercostal spaces (Fig. 9.3). There was no cardiodiaphragmatic contact, except in one animal (5.6 kg).

On the DV view, the cardiac silhouette was ovoid and the apex was located in the left hemithorax (Fig. 9.5). Cardiodiaphragmatic contact was seen in 8 of the 11 animals (Fig. 9.5). In the heaviest animal (6 kg) the cardiac silhouette

was rounded and there was extensive cardiodiaphragmatic contact (Fig. 9.6). The cardiac silhouette was elongated in older animals. There was a significant difference (P = 0.0002) in the mean VHS obtained on the RL and DV views.

On the RL view, the dorsal border of the descending aorta was not clearly seen (2/11) (Fig. 9.3) or not seen at all (9/11). The aortic arch was elongated (redundant) in one 14.3-year-old animal. The caudal vena cava (CVC) was clearly seen in all animals (Fig. 9.3). On the DV view, the left margin of the descending aorta was seen in all animals (Fig. 9.5). Left bulging of the aortic arch was seen as a result of a redundant aorta in one animal. The CVC was seen clearly caudal to the cardiac silhouette in 3 of the 11 animals.

9.3.3 Respiratory system

On the RL view, the trachea was wide with mineralised cartilage rings in all animals (Fig. 9.3). It was aligned parallel to the thoracic spine and diverged ventrally from the thoracic spine from the level of the sixth or seventh thoracic vertebra caudally to the carina in six and five animals, respectively (Fig. 9.3). The caudal borders of the scapulae were superimposed over the trachea (Fig. 9.3). The carina was clearly seen (Fig. 9.3) in the majority of animals (10/11). The mean location of the carina with respect to intercostal space (ICS) and vertebra was 5.27±0.47 cm and 7.27±0.47 cm, respectively. In most animals (7/11), the pulmonary cupula ended at the caudal border of the first rib (Fig. 9.3) and rarely at the first intercostal space (3/11) or cranial border of the first rib (1/11). The diaphragmatic crura were frequently seen to be parallel (6/11) and less frequently superimposed (3/11) or diverged dorsally (2/11) (Fig. 9.3).

On the DV view, the trachea was running slightly to the right of the spine in all animals (Fig. 9.5). The left and right pulmonary cupulae didn't extend cranially beyond the second rib (Fig. 9.5). The caudoventral mediastinal reflection was seen in six of the 11 animals (Fig. 9.2). In all animals the craniodorsal mediastinum exceeded the width of the spine (Figs 9.5 and 9.6). The cranioventral mediastinal reflection was not seen in all animals. An early alveolar lung pattern was seen in one animal in the right hemithorax adjacent to the right cardiac margin (Fig. 9.6). No pleural fissure lines were observed. The diaphragm appeared as a single dome (Figs 9.5 and 9.6).

9.3.4 Other findings

Three animals (two females and one male) older than nine years had multiple areas of lateral and ventral spondylosis deformans with the caudal thoracic vertebrae being severely affected. The oesophagus and thoracic lymph nodes were not seen.

9.4 DISCUSSION

Thoracic anatomical structures of clinical importance in red pandas were seen and evaluated radiographically. The mean ratio of thoracic depth to thoracic width obtained in this study (0.82) indicates a normal thoracic conformation (Buchanan and Bücheler, 1995) similar to the coati (*Nasua nasua*) (1.05) (Martini et al., 2013). Variation in the number of ribs (14 to 15) and the presence of 14 pairs of ribs in the majority of animals observed in this study has also been reported in the coati (Martins et al., 2013). The number of

thoracic vertebrae observed in the majority of red pandas (14) is also similar to the coati. Most coati had 14 pairs of ribs (Martins et al., 2013) consistent with 14 thoracic vertebrae. In this study the anticlinal vertebra was mostly T11 and all animals had six sternebrae which is similar to the domestic cat and dog (Liabrés-Díaz et al., 2008). The fairly straight sternum resembles that of the coati (Martins et al., 2013) and the presence of two pairs of floating ribs is similar to the domestic cat (Liabrés-Díaz et al., 2008).

The presence of rudimentary clavicles in some red pandas is similar to domestic dogs (McCarthy and Wood, 1988; Cerny and Cizinauskas, 1995). The rudimentary clavicles should not be misinterpreted as dystrophic mineralization as a result of neoplasias, granulomas and abscesses (Barr, 2006). Multiple areas of ventral and lateral thoracic spondylosis are considered incidental findings. Similar changes have been observed in domestic cats (Kranenburg et al., 2012) and dogs (Kranenburg et al., 2011) and are less frequent and milder in the domestic cat.

The mean VHS of the red panda obtained from RL (8.34 ± 0.25) and DV (8.78 ± 0.34) views is intermediate between the values reported in the domestic cat (RL: 7.5 ± 0.3; DV: 8.1 ± 0.45) (Litster and Buchanan, 2000b) and dog (RL: 9.7 ± 0.5; DV: 10.2 ± 1.45) (Buchanan and Bücheler, 1995). However, it is slightly lower than the reported mean value in the adult coati (9.36 ± 0.75) (Martini et al., 2013). The significant difference in the mean VHS obtained on the RL and DV views in this study has also been observed in the domestic cat (Litster and Buchanan, 2000b) and dog (Buchanan and Bücheler, 1995).

The oblique position of the cardiac silhouette in this species is similar to the domestic cat (Buchanan, 2000). Further, the more obliquely positioned and elongated cardiac silhouette and redundant aortic arch, which were seen in older animals in this study, have also been observed in older domestic cats (Moon et al., 1993). These changes are not pathological and most likely associated with age-related changes in thoracic conformation (Johnson et al., 2008). Similar changes have also been reported in older captive maned wolves (*Chrysocyon brachyurus*) (Estrada et al., 2009).

Mineralisation of the tracheal rings, which was observed in all animals, should not be misinterpreted as an ageing change or incidental finding. It is a normal feature in this species. The presence of mineralisation of the tracheal rings in this species is similar to the coati (Martins et al., 2013). The superimposition of the scapulae over the trachea on the RL view, should not be misinterpreted as redundancy of the dorsal tracheal membrane since the tracheal rings of the red panda are also incomplete dorsally similar to the domestic cat and dog (Thrall and Robertson, 2011).

The parallel alignment of the trachea with the thoracic spine on the RL view, is a normal feature in this species and should not be misinterpreted as dorsal displacement of the trachea as a result of cardiomegally and mediastinal mass (Hayward et al., 2008). Parallel alignment of the trachea with the thoracic spine has also been seen in the normal Dachshund and Welsh corgi (Thrall and Robertson, 2011). The location of the trachea slightly to the right of the spine on the DV view is similar to the domestic dog (Hayward et al., 2008;

Thrall and Roberson, 2011). The lung pattern (early alveolar), which was observed in one animal is believed to be the result of RL recumbency causing gravity-dependent atelectasis. This is due to the fact that the lung pattern occurred in the heaviest animal and was located in the right hemithorax. Further, none of the animals used in this study had evidence of thoracic disease on clinical examination.

Variations exist in the normal radiographic anatomy of the thorax of different animal species. Knowledge of the normal radiographic anatomy of the red panda thorax should prove useful in the diagnosis of thoracic diseases in this species.

9.5 ACKNOWLEDGEMENTS

The authors would like to thank the Organisation for Women in Science for Developing World (OWSD), Swedish International Development Cooperation Agency (SIDA), University of Pretoria and Johannesburg zoo for supporting this study. Dr. Georgina Cole, Ms. Fania Mohlala, sisters and animal handlers of the Johannesburg zoo and Onderstepoort Veterinary Academic Hospital for their assistance during radiography. Mrs. Charmaine Vermeulen and Mrs. Wilma Olivier of the University of Pretoria for their assistance in photography and administrative work, respectively.

9.6 REFERENCES

Barr, F., 2006: Soft tissues. In: BSAVA Canine and Feline Musculoskeletal Imaging F. J. Barr, and R. M. Kirberger, eds). Gloucester: BSAVA, pp. 1–8.

Buchanan, J. W., 2000: Vertebral scale system to measure heart size in radiographs. Vet. Clin. North. Am. Small. Anim. Pract. **30,** 379–393.

Buchanan, J. W., 2004: Tracheal signs and associated vascular anomalies in dogs with persistent right aortic arch. J. Vet. Intern. Med. **18,** 510–514.

Buchanan, J. W., and J. Bücheler, 1995: Vertebral scale system to measure canine heart size in radiographs. J. Am. Vet. Med. Assoc. **206,** 194–199.

Cerny, H., and S. Cizinauskas, 1995: The clavicle of newborn dogs. Acta. Vet. Brno. **64,** 139–145.

Estrada, A. H., T. J. Gerlach, M. K. Schmidt, J. L. Siegal-Willott, A. L. Atkins, J. Van Gilder, S. B. Citino, and L. R. Padilla, 2009: Cardiac evaluation of clinically healthy captive maned wolves (*Chrysocyon brachyurus*). J. Zoo. Wildl. Med. **40,** 478–486.

Evans, H. E., and A. de Lahunta, 2013: The respiratory system. In: Miller's Anatomy of the Dog, 4th edn. St. Louis: Elsevier Saunders, pp. 338–360.

Fisher, R. E., B. Adrian, M. Barton, J. Holmgren, and S. Y. Tang, 2009: The phylogeny of the red panda (*Ailurus fulgens*): evidence from the forelimb. J. Anat. **215,** 611–635.

Flower, W. H., 1870: On the anatomy of *Ailurus fulgens*. Proc. Zool. Soc. London. **38,** 747–795.

Fossum, T. W., R. J. Boudrieau, and H. P. Hobson, 1989: Pectus excavatum in eight dogs and six cats. J. Am. Anim. Hosp. Assoc. **25,** 595–605.

Gardner HM (1985) Case: Hypertropic cardiomyopathy in a lesser panda. Proc Am Assoc Zoo Vet: 76

Groves, C., 2011: The Taxonomy and Phylogeny of *Ailurus*. In: Red Panda Biology and Conservation of the First Panda (A. Glatston, ed.). London: Academic Press, pp. 101–124.

Harwel, G., and T. M. Craig, 1981: Dirofilariasis in a red panda. J. Am. Vet. Med. Assoc. **179,** 1258.

Hayward, N., T. Schwarz, and C. Weisse, 2008: The trachea. In: BSAVA Manual of Canine and Feline Thoracic Imaging (T. Schwarz and V. Johnson, eds). Gloucester: BSAVA, pp. 213–227.

IUCN, 2014: IUCN Red list of threatened species. Version 2014.3. Available at: http://www.iucnredlist.org (accessed on 18 November 2014).

Johnson, V., K. Hansson, W. Maï, J. Dukes-McEwan, N. Lester, T. Schwarz, P. Chapman, and F. Morandi, 2008: The heart and major vessels. In: BSVA Manual of Canine and Feline Thoracic Imaging (T. Schwarz and V. Johnson, eds). Gloucester: BSVA, pp. 86–176.

Kranenburg, H. C., B. P. Meij, E. M. L. van Hofwegen, G. Voorhout, L. I. Slingerland, P. Picavet, and H. A. W. Hazewinkel, 2012: Prevalence of spondylosis deformans in the feline spine and correlation with owner-perceived behavioral changes. Vet. Comp. Orthop. Traumatol. **25,** 217–223.

Kranenburg, H. C., G. Voorhout, G. C. M. Grinwis, H. A. W. Hazewinkel, and B. P. Meij, 2011: Diffuse idiopathic skeletal hyperostosis (DISH) and spondylosis deformans in purebred dogs: A retrospective radiographic study. Vet. J. **190,** e84–e90.

Lehmkuhl, L. B., J. D. Bonagura, D. S. Biller, and W. M. Hartman, 1997: Radiographic evaluation of caudal vena cava size in dogs. Vet. Radiol. Ultrasound. **38,** 94–100.

Liabrés-Díaz, F., A. Petite, J. Saunders, and T. Schwarz, 2008: The thoracic boundaries. In: BSAVA Manual of Canine and Feline Thoracic Imaging (T, Schwarz and V. Johnson, eds). Gloucester: BSAVA, pp. 340–376.

Light, G. S., 1993: Respiratory system. In: Atlas of Feline Anatomy for Veterinarians (L. C. Hudson and W. P. Hamilton, eds). Philadelphia: WB Saunders, pp. 135–148.

Litster, A. L., and J. W. Buchanan, 2000a: Radiographic and echocardiographic measurement of the heart in obese cats. Vet. Radiol. Ultrasound. **41,** 320–325.

Litster, A. L., and J. W. Buchanan, 2000b: Vertebral scale system to measure heart size in radiographs of cats. J. Am. Vet. Med. Assoc. **216,** 210–214.

Lobetti, R. G., R. Milner, and E. Lane, 2001: Chronic idiopathic pulmonary fibrosis in five dogs. J. Am. Anim. Hosp. Assoc. **37,** 119–127.

Martini, A. C., Y. S. Meireles, S. Monzem, L. P. Vanconcelos, N. C. M. R. Turbino, M. A. A. Dahroug, D. Farias, P. B. Néspoli, G. F. Gonçalves, R. L. Souza, and L. D. Guimarães, 2013: Radiographic evaluation of the cardiac silhouette using the VHS method (vertebral heart score) in

young and adults coatis (*Nasua nasua*, Linneaus 1766) living in captivity. Semin. Ciênc. Agrár. **34,** 3823–3830.

Martins, G. S., E. R. Lopes, I. I. G. Taques, C. Y. Correia, Y. S. Meireles, N. C. M. R. Turbino, L. D. Guimarães, and P. B. Néspoli, 2013: Radiographic morphology of the skeleton, thorax and abdomen of coati (*Nasua nasua* Linnaeus, 1766). Pesq. Vet. Bras. **33,** 1137–1143.

McCarthy, P. H., and A. K. Wood, 1988: Anatomic and radiologic observations of the clavicle of adult dogs. Am. J. Vet. Res. **49,** 956–959.

Moon, M. L., B. W. Keene, P. Lessard, and J. Lee, 1993: Age related changes in the feline cardiac silhouette. Vet. Radiol. Ultrasound. **34,** 315–320.

Morgan, J. P., 1967: Spondylosis deformans in the dog: its radiographic appearance. Vet. Radiol. Ultrasound. **8,** 17–22.

Nelson, N. C., J. S. Mattoon, and D. E. Anderson, 2011: Radiographic appearance of the thorax of clinically normal alpaca crias. Am. J. Vet. Res. **72,** 1439–1448.

Patterson-Kane, J. C., L. M. Gibbons, R. Jefferies, E. R. Morgan, N. Wenzlow, and S. R. Redrobe, 2009: Pneumonia from Angiostrongylus vasorum infection in a red panda (*Ailurus fulgens fulgens*). J. Vet. Diagn. Invest. **21,** 270–273.

Philippa, J., and E. Ramsay, 2011: Captive red panda medicine. In: Red Panda Biology and Conservation of the First Panda (A. R. Glatston, ed.). London: Academic Press, pp. 271–285.

Preece, B., 2011: Red panda pathology. In: Red Panda Biology and Conservation of the First Panda (A. R. Glatston, ed.). London: Academic Press, pp. 287–302.

Roberts, M. S., and J. L. Gittleman, 1984: *Ailurus fulgens*. Mamm. Species. **222,** 1–8.

Sullivan, M., and R. Lee, 1989: Radiological features of 80 cases of diaphragmatic rupture. J. Small. Anim. Pract. **30,** 561–566.

Suter, P. F., 1981: The radiographic diagnosis of canine and feline heart disease. Compend. Contin. Ed. Small. Anim. **3,** 441–454.

Thrall, D. E., 2013: Introduction to radiographic interpretation. In: Textbook of Veterinary Diagnostic Radiology (D. E. Thrall, ed.). St. Louis: Saunders Elsevier, pp. 74–86.

Thrall, D. E., and I. D. Robertson, 2011: The thorax. In: Atlas of Normal Radiographic Anatomy and Anatomic Variants in the Dog and Cat. St. Louis: Elsevier, pp. 127–167.

Young, A. N., W. M. du Plessis, D. Rodriguez, and A. Beierschmidt, 2013: Thoracic radiographic anatomy in vervet monkeys (*Chlorocebus sabaeus*). J. Med. Primatol. **42,** 310–317.

Zwart, P. C., 1989: Contribution to the pathology of the red panda (*Ailurus fulgens*). In: Red Panda Biology (A. R. Glatston, ed). The Netherlands: SPB Academic Publishing, pp. 25–29.

9.7 TABLES

Table 9.1 Radiographic measurements (cm) of thoracic vertebrae in captive red pandas (*Ailurus fulgens*) not compensated for magnification

Vertebra	Variable	Number	Mean ± SD (cm)	Range (cm)
T1	Length	11	1.06 ± 0.06	1.00 – 1.15
	Height	11	0.56 ± 0.05	0.50 – 0.60
T2	Length	11	1.17 ± 0.05	1.10 – 1.25
	Height	11	0.60 ± 0.06	0.50 – 0.70
T3	Length	11	1.21 ± 0.06	1.10 – 1.30
	Height	11	0.65 ± 0.07	0.60 – 0.80
T4	Length	11	1.20 ± 0.05	1.10 – 1.30
	Height	11	0.66 ± 0.05	0.60 – 0.70
T5	Length	11	1.22 ± 0.06	1.10 – 1.30
	Height	11	0.66 ± 0.05	0.60 – 0.70
T6	Length	11	1.26 ± 0.05	1.20 – 1.30
	Height	11	0.72 ± 0.06	0.60 – 0.80
T7	Length	11	1.26 ± 0.05	1.20 – 1.30
	Height	11	0.74 ± 0.05	0.70 – 0.80
T8	Length	10	1.27 ± 0.05	1.20 – 1.30
	Height	10	0.74 ± 0.05	0.70 – 0.80
T9	Length	10	1.29 ± 0.07	1.20 – 1.40
	Height	10	0.78 ± 0.08	0.70 – 0.90
T10	Length	10	1.36 ± 0.07	1.20 – 1.45
	Height	10	0.810 ± 0.09	0.70 – 0.90
T11	Length	10	1.43 ± 0.09	1.30 – 1.55
	Height	10	0.92 ± 0.35	0.70 – 1.90
T12	Length	10	1.52 ± 0.09	1.40 – 1.65
	Height	10	0.82 ± 0.12	0.70 – 0.90
T13	Length	10	1.60 ± 0.09	1.40 – 1.75
	Height	10	0.86 ± 0.08	0.75 – 1.00
T14	Length	10	1.73 ± 0.11	1.50 – 1.85
	Height	10	0.99 ± 0.33	0.80 – 1.90
T15	Length	1	1.80 ± 0.00	1.80 – 1.80
	Height	1	0.80 ± 0.00	0.80 – 0.80

T, thoracic

Table 9.2 Radiographic measurements (cm) of sternebrae in captive red pandas (*Ailurus fulgens*) not compensated for magnification

Sternebra	Variable	Number	Mean ± SD (cm)	Range (cm)
S1	Length	11	1.48 ± 0.12	1.30 – 1.65
	Height	11	0.58 ± 0.06	0.50 – 0.70
S2	Length	11	1.46 ± 0.08	1.40 – 1.60
	Height	11	0.60 ± 0.08	0.50 – 0.70
S3	Length	11	1.41 ± 0.09	1.30 – 1.60
	Height	11	0.56 ± 0.05	0.50 – 0.60
S4	Length	11	1.32 ± 0.08	1.20 – 1.45
	Height	11	0.57 ± 0.05	0.50 – 0.60
S5	Length	11	1.19 ± 0.08	1.10 – 1.30
	Height	11	0.56 ± 0.08	0.40 – 0.70
S6	Length	9	0.92 ± 0.16	0.70 – 1.10
	Height	9	0.53 ± 0.11	0.40 – 0.70

S, sternebrae

Table 9.3 Radiographic findings and measurements of the thorax not compensated for magnification in captive red pandas (*Ailurus fulgens*)

Variable	Number	Mean ± SD	Range
TDp [cm]	11	7.53 ± 0.38	7.00 – 8.10
TW [cm]	11	9.17 ± 0.56	8.20 – 10.10
TDp: TW	11	0.82 ± 0.05	0.75 – 0.91
Anticlinal vertebra	11	10.91 ± 0.30	10.00 – 11.00
CLA (RL) [cm]	11	6.71 ± 0.35	6.20 – 7.50
CSA (RL) [cm]	11	4.56 ± 0.33	4.00 – 5.00
CLA (DV) [cm]	11	7.08 ± 0.24	6.70 – 7.30
CSA (DV) [cm]	11	4.79 ± 0.30	4.20 – 5.30
CLA(RL): TDp	11	0.89 ± 0.04	0.84 – 0.93
CSA (RL): TDp	11	0.61 ± 0.04	0.55 – 0.67
CLA (DV): TW	11	0.77 ± 0.04	0.70 – 0.83
CSA (DV): TW	11	0.53 ± 0.05	0.45 – 0.60
VHS (RL)	11	8.34 ± 0.25	8.00 – 8.90
VHS (DV)	11	8.78 ± 0.34	8.30 – 9.60
CVC diameter [cm]	11	0.85 ± 0.06	0.80 – 0.95
CVC: VL	11	0.67 ± 0.05	0.62 – 0.75
MDWd [cm]	11	2.34 ± 0.16	2.00 – 2.50
Carina			
ICS	11	5.27 ± 0.47	5.00 – 6.00
Vertebra	11	7.27 ± 0.47	7.00 – 8.00
Cranial crus (RL)	11	14.06 ± 0.69	12.6 – 14.7
Diaphragm (DV)	11	11.66 ± 0.46	11.00 – 12.40

TDp, thoracic depth; TW, thoracic width; CLA, cardiac long axis; CSA, cardiac short axis; VHS, vertebral heart score; RL, right lateral; DV, dorsoventral; CVC, caudal vena cava; VL, thoracic vertebral body length; MDWd, craniodorsal mediastinum width and ICS, intercostal space

9.8 FIGURES

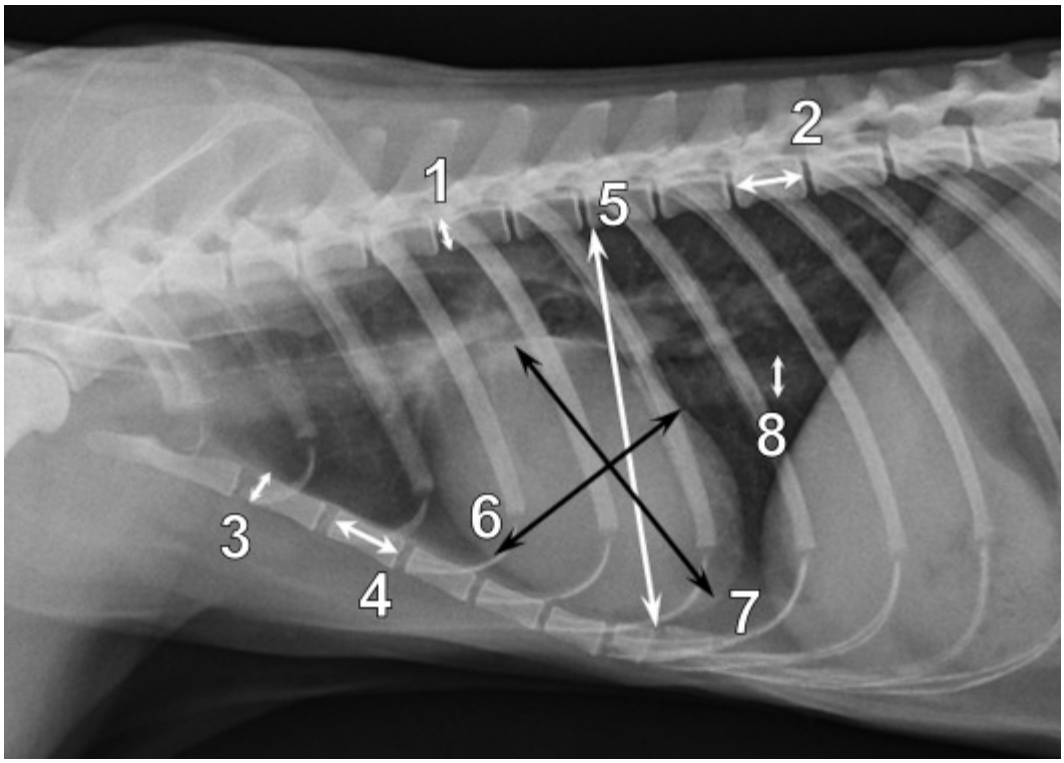

Fig. 9.1 Right lateral thoracic radiograph of a 10-year-old male (5.5 kg) red panda illustrating radiographic measurements. (1) Vertebral body height, (2) vertebral body length, (3) height of sternebra, (4) length of sternebra, (5) thoracic depth, (6) cardiac silhouette short axis measurement, (7) cardiac silhouette long axis measurement and (8) caudal vena cava diameter.

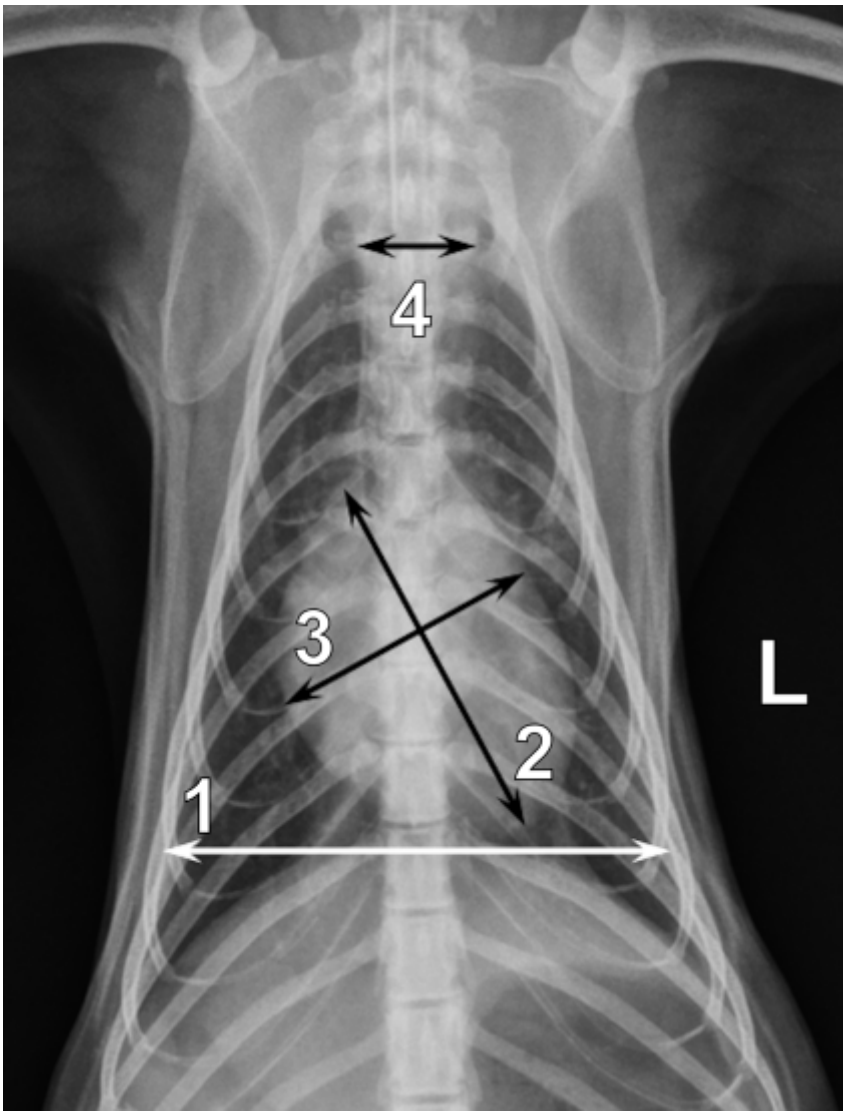

Fig. 9.2 Dorsoventral thoracic radiograph of a 10-year-old male (5.5 kg) red panda illustrating radiographic measurements. (1) Thoracic width, (2) cardiac silhouette long axis measurement, (3) cardiac silhouette short axis measurement and (4) width of the craniodorsal mediastinum. L, Left.

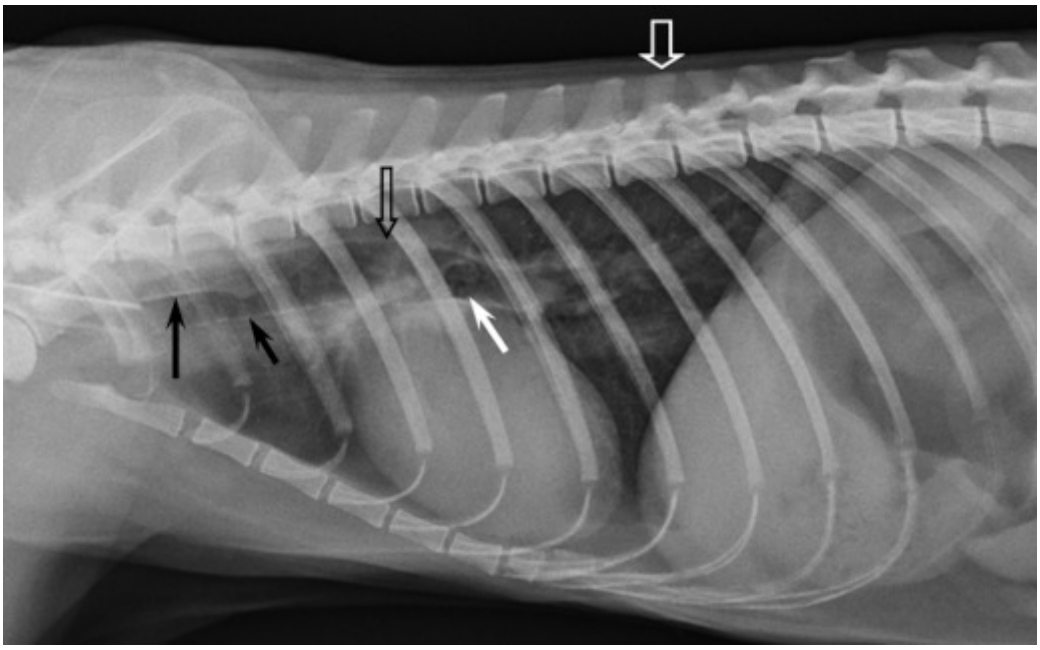

Fig. 9.3 Right lateral thoracic radiograph of a 10-year-old male (5.5 kg) red panda. Note the short spinous processes of the thoracic vertebrae and anticlinal thoracic vertebra number 10 (open white arrow). The sternum is fairly straight with six sternebrae. The large trachea with mineralised cartilage rings (short black arrow) is aligned almost parallel to the thoracic spine and diverges from the thoracic spine from thoracic vertebra six (open black arrow) caudally. Note also the superimposition of the caudal borders of the scapulae to the trachea (long black arrow) and clearly visible carina in the fifth intercostal space (white arrow). The ovoid cardiac silhouette is obliquely positioned occupying not more than three and half intercostal spaces.

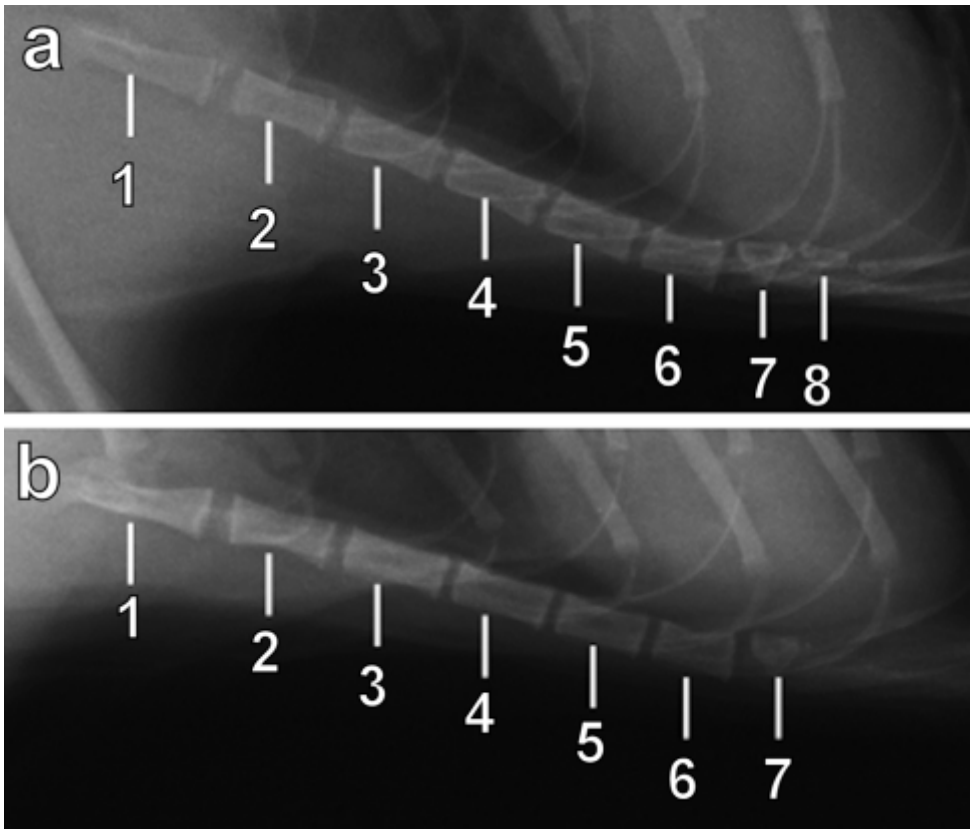

Fig. 9.4 Close-up of RL thoracic radiographs of the sternum of 1.4-year-old male (5.6 kg) (a) and female (4 kg) (b) red pandas. Note the visibility of a small mineralised xiphoid process in (a) and lack of visibility of the mineralised xiphoid process in (b). (1) Manubrium sterni, (2) first sternebra, (3) second sternebra, (4) third sternebra, (5) fourth sternebra, (6) fifth sternebra, (7) sixth sternebra and (8) xiphoid process.

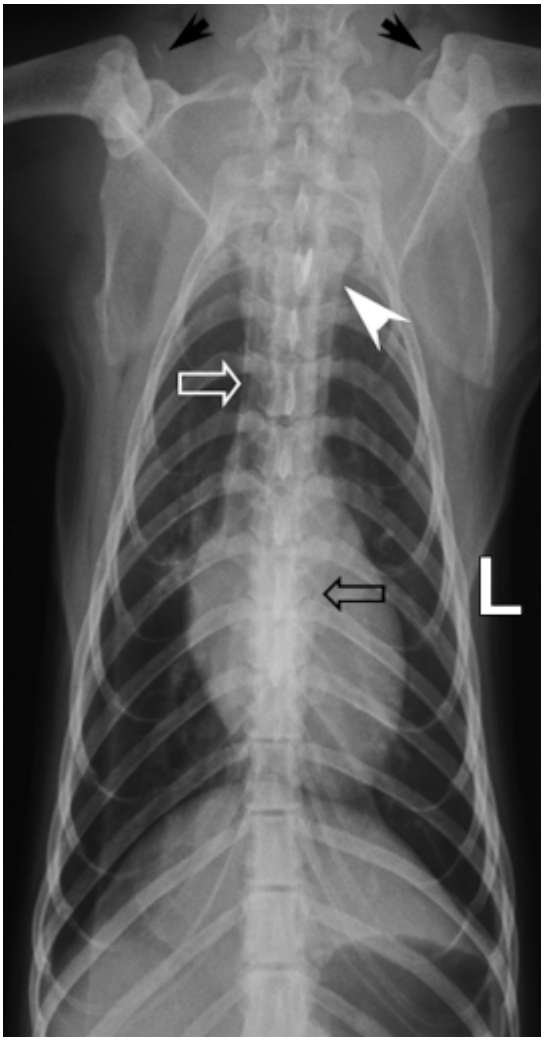

Fig. 9.5 Dorsoventral thoracic radiograph of a 1.4-year-old (5.6 kg) male red panda. Note the presence of the rudimentary clavicles (black arrows). The cardiac silhouette is ovoid and the apex is located in the left hemithorax. Note also the presence of minimal cardiodiaphragmatic contact. The trachea is positioned slightly to the right of the spine (open white arrow). The craniodorsal mediastinum is wider than the thoracic spine (white arrow head). The left margin of the descending aorta is indicated by an open black arrow. L, Left.

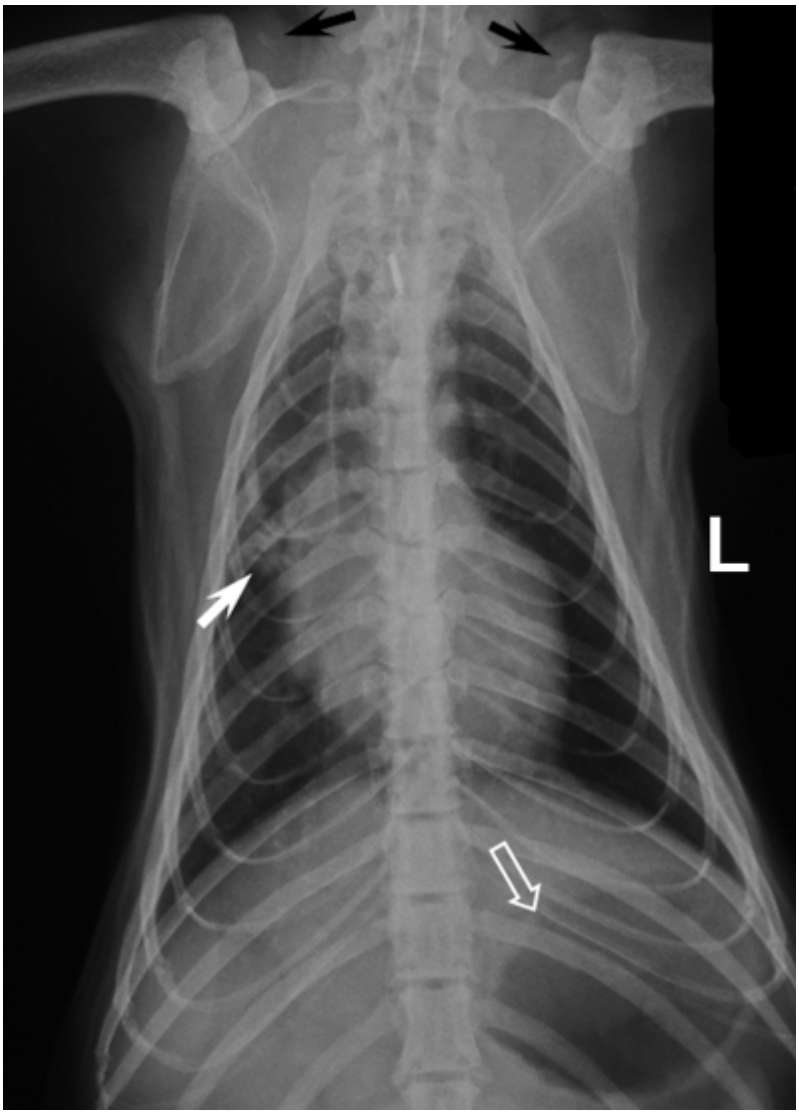

Fig. 9.6 Dorsoventral thoracic radiograph of an 8-year-old (6 kg) male red panda. The cardiac silhouette is rounded and there is extensive cardiodiaphragmatic contact. Note the presence of an early alveolar lung pattern (white arrow) in the right hemithorax adjacent to the right cardiac margin. Note also the presence of gastric gas in the fundus (open white arrow). The clavicles are indicated by black arrows. L, Left.

CHAPTER 10

RADIOGRAPHIC AND ULTRASONOGRAPHIC ABDOMINAL ANATOMY IN CAPTIVE RED PANDAS (*AILURUS FULGENS*)

10.1 INTRODUCTION

The red panda (*Ailurus fulgens*) is classified as a vulnerable species by the International Union for Conservation of Nature and Natural Resources (IUCN, 2014). It belongs to order; Carnivora, suborder; Caniformia, family; Ailuridae and genus; *Ailurus* (Wei and Zhang, 2009). The red panda is the only living species in the family Ailuridae (Wei and Zhang, 2009). It is closely related to procyonids, mustelids and skunks (Groves, 2011). The red panda is primarily distributed in southern China and Himalayas (Fisher et al., 2009). It feeds primarily on bamboo leaves or other vegetarian diet (Wei and Zhang, 2009).

The stomach of the red panda consists of a single chamber with a thick walled pylorus (Flower, 1870). The digestive tract is very short without a caecum and measures 8 feet and 8 inches (264.16 cm) in length from the pylorus to the anus (Flower, 1870). The lumen of the large intestine is slightly bigger than that of the small intestine (Carlsson, 1925) and the colon and rectum measure 18 cm in length (Carlsson, 1925). The elongated spleen is to the left of the stomach (Flower, 1870). The kidneys are not lobulated with the right kidney slightly more cranial than the left kidney (Flower, 1870).

The red panda is affected by abdominal diseases similar to those seen in domestic cats and dogs. Diseases involving the digestive system like gastric dilatation and volvulus (Neilsen et al., 2014), gastritis, gastric erosion and ulceration (Preece, 2011), intestinal obstruction (Preece, 2011), intestinal ulceration (Preece, 2011) and enteritis (Philippa and Ramsay, 2011) have been reported in this species. Further, liver diseases such as hepatitis, (Zwart, 1989), hepatic lipidosis (Montali et al., 1989) and neoplasia like hepatocarcinoma (Philippa and Ramsay, 2011) have also been documented.

Similar to the domestic cat, the red panda kidney is prone to physiological accumulation of fat and chronic renal disease (Zwart, 1989). Chronic renal disease occurs frequently in older red pandas and histopathology shows end-stage renal lesions similar to those seen in the domestic cat (Philippa and Ramsay, 2011; Preece, 2011). Other renal diseases, which have been documented in the red panda include nephritis, nephrosis, glomerulonephrosis, cystic dilation of tubules (Zwart, 1989), polycystic kidneys (Makungu et al., 2013) and papillary renal adenoma (Kummerfeld et al., 2008). Other abdominal diseases, which have been reported in the red panda are feline infectious peritonitis (Preece, 2011), splenitis (Zwart, 1989) and granulosa cell (ovarian) tumor (Philippa and Ramsay, 2011).

Knowledge of the normal radiographic and ultrasonographic abdominal anatomy of individual species is important for accurate interpretation and diagnosis of abdominal diseases. Normal radiographic (Thrall and Robertson, 2011) and ultrasonographic (Nyland and Mattoon, 2002) abdominal anatomy

of small animals is well documented, which provides guidance for evaluation and diagnosis of various abdominal diseases. Several authors have also reported the normal radiographic (Baitchman and Kollias, 2000; Wagner and Kirberger, 2005a; Martins et al., 2013) and ultrasonographic (Wagner and Kirberger, 2005b; Makungu et al., 2012; Ribeiro et al., 2013) abdominal anatomy of wild life species. The aim of this study was to describe the normal radiographic and ultrasonographic abdominal anatomy of captive red pandas as a species-specific reference.

10.2 MATERIALS AND METHODS

10.2.1 Animals

Ten adult captive red pandas without clinical evidence of abdominal disease from the Johannesburg zoo, South Africa (SA) and Bristol zoo, United Kingdom (UK) were used in this study. Radiography and ultrasonography were performed in nine and seven animals, respectively. Six animals were used for both radiographic and ultrasonographic studies. Of the nine animals used for the radiographic study, six were females and three were males. Their age ranged from 1.4 years to 11.6 years (5.06 ± 3.95 years). Their minimum and maximum weights were 3.97 kg and 6.98 kg, respectively, (5.04 ± 0.96 kg). Of the seven animals used for the ultrasonographic study, four were females and three were males. Their minimum and maximum ages were 2 years and 11.08 years, respectively, (5.50 ± 4.09 years). Their weight ranged from 3.96 kg to 5.96 kg (4.84 ± 0.65 kg).

Radiographic and ultrasonographic studies were performed under general anaesthesia during annual health examinations. Animals were fasted for 8–12 hours but water was given *ad libitum* until shortly before anaesthesia. Anaesthesia was induced by intramuscular injection of medetomidine hydrochloride (Pfizer Laboratories Ltd, Sandton, SA; Elanco Animal Health, Hampshire, UK) and ketamine hydrochloride (Kyron Laboratories Ltd, Benrose, SA; Fort Dodge Animal Health, Southampton, UK). All animals were intubated and anaesthesia maintained using isoflurane (Safeline Pharmaceuticals Ltd, Roodepoort, SA; Abbott Laboratories Ltd., Berkshire, UK). This study was approved by the Animal Use and Care Committee (AUCC) of the University of Pretoria.

10.2.2 Radiography

Right lateral (RL) and ventrodorsal (VD) views of the abdomen were taken at the end of expiration using a table top technique. In eight animals, an EVA-HF 525 (Comed Medical System Co. Ltd., Kyunggi, Korea) x-ray machine was used at a source to image distance (SID) of 95 cm. A kVp of 42 and 44 was used with 2.5 mAs. Images were obtained by either a computed radiography (CR) or conventional system. For the conventional system, medium speed screen type films (Fujifilm Corporation, Tokyo, Japan) were used with RAREX green regular intensifying screens (Okamoto manufacturing Co. LTD, Tokyo, Japan). Radiographs were obtained by an automatic x-ray film processor model CP-345 (ELK Corporation, Tokyo, Japan). For a CR, Vita LE (Carestream Health, Inc, New York, US) was used. In one animal, a Roentgen 703 (GEC Medical Equipment Ltd., Middlesex, UK) x-ray machine was used

at a 60 kVp and 3 mAs. A SID of 105 cm was used and images were obtained with computed radiography (CR) unit Regius Model 110 (Konica Minolta Medical and Graphic, INC., Tokyo, Japan).

10.2.3 Radiographic evaluation

Dorsoventral height of lumbar vertebral bodies (Fig. 10.1) was measured on the RL view at the cranial end-plate (Adams et al., 2010). The length of lumbar vertebral bodies (Fig. 10.1) was measured on the RL view at the dorsal margin of the vertebral body from the cranial end-plate to the caudal end-plate. For the second lumbar vertebra, the vertebral body length was also measured on the VD view (Fig. 10.2) from the cranial end-plate to the caudal end-plate along the sagittal plane of the vertebra (Eshar et al., 2013). Visibility, location, shape and number of abdominal organs were recorded.

The angle of the gastric axis (Fig. 10.1) was measured on the RL view, as the angle between the gastric axis and a line drawn along the ventral aspect of the thoracic (T) vertebrae T12 and T13 in six animals and T13 and T14 in three animals (Wagner and Kirberger, 2005a). The gastric axis is an imaginary line from the fundus through the body and pylorus (Seiler and Maï, 2009). The maximum external diameter of the small and large intestines was measured in cm (Fig. 10.1) and compared to the height of the second lumbar vertebral body on the RL view (Adams et al., 2010). The maximum external diameter of the large intestine was also compared to the length of the second lumbar vertebral body on the RL view (Wagner and Kirberger, 2005a). The length and width of the kidney were measured on the VD view (Fig. 10.2) and

compared with the length of the second lumbar vertebral body on the VD view (Wagner and Kirberger, 2005a; Eshar et al., 2013).

10.2.4 Ultrasonography

Abdominal ultrasonography was performed using a Landwind C40 (Shenzhen Landwind Industry Co Ltd, Shenzhen, China) ultrasound machine with a 7.5 MHz linear transducer. Animals were positioned in dorsal recumbency, the ventral abdominal area was clipped and ultrasound gel (Ultra Sound Gel, Portfolio Pharmaceuticals Ltd, Johannesburg, SA) was applied.

The length of the kidneys and wall thickness of the urinary bladder were measured on sagittal images. The maximum thickness of the spleen and height and width of the kidney were measured on transverse images. The wall thickness of the urinary bladder was measured at the midventral location. The gall bladder was evaluated in five animals and its wall thickness was measured on sagittal images of the liver at the middle of the near wall. All measurements were performed on frozen images with electronic callipers. The echogenicity of the right renal cortex was compared to that of the liver parenchyma, whereas the echogenicity of the left renal cortex was compared to the splenic parenchyma.

10.2.5 Data analysis

Data was analysed using Stat View® statistical package (SAS institute, Cary, NC, USA). Mean, range and standard deviation were calculated. Paired t-test was used to compare the mean length of lumbar vertebral bodies, length of

the second lumbar vertebral body on the RL and VD views and mean dimensions of the left vs. right kidney. Statistical significance was accepted at $P \leq 0.05$. Data is expressed as mean ± standard deviation (SD).

10.3 RESULTS

10.3.1 Musculoskeletal system

Of the nine animals, seven had six lumbar vertebrae (Fig. 10.3), whereas two animals had five lumbar vertebrae (Fig. 10.4). The spinous process of the lumbar vertebrae was short (Fig. 10.3). The mean length of lumbar vertebral bodies increased significantly ($P < 0.001$) from the first lumbar vertebra to the fourth lumbar vertebra (Table 10.1). There was no significant difference ($P = 0.62$) in the mean length of the fourth and fifth lumbar vertebral bodies (Table 10.1). The first lumbar vertebral body was the shortest, whereas the fifth lumbar vertebral body was the longest (Table 10.1). The mean length of the sixth lumbar vertebral body was significantly ($P = 0.0063$) lower than the mean length of the fifth lumbar vertebral body (Table 10.1). The mean length of the second lumbar vertebral body obtained on the RL view (1.95 ± 0.05 cm) was significantly ($P < 0.001$) higher than that obtained on the VD view (1.86 ± 0.06 cm). In eight animals, the sacrum had three fused segments (Fig. 10.3), whereas in one female animal it consisted of only two fused segments (Fig. 10.5).

A lumbosacral transitional vertebra was seen in one animal (Fig. 10.4). This animal with lumbosacral transitional vertebra had five lumbar vertebrae (Fig.

10.4). The os penis was seen in all male animals (Fig. 10.3 and 10.6). The os clitoridis was not seen. On the VD view, hypaxial muscles were conspicuous in heavy animals (Fig. 10.4). On the RL view, in heavy animals accumulation of a large amount of abdominal fat was seen in the retroperitoneal space and ventral to the liver (Figs 10.3 and 10.6). Osteoarthrosis of the vertebral articular facet and lumbosacral junction was seen in a female animal aged three years and a male animal aged 11 years, respectively, (Fig. 10.4). The animal with osteoarthrosis of the lumbosacral junction had also lumbosacral transitional vertebra.

10.3.2 Digestive system

On the RL view, the mean angle of the gastric axis was 63.22 ± 6.06º. The large intestine could be distinguished from the small intestine in all animals (Fig. 10.6). The contents of the descending colon had either soft tissue opacity, gas, gas and soft tissue opacity or gas and grainy faecal material (Figs 10.3 and 10.6). The mean diameter of the small intestine and ratio compared to the height of the second lumbar vertebral body was 0.88 ± 0.37 cm and 1.00 ± 0.41, respectively. For the large intestine, the mean diameter and ratio compared to the height and length of the second lumbar vertebral body was 1.79 ± 0.22 cm, 2.04 ± 0.33 and 0.92 ± 0.12, respectively.

On the VD view, the pylorus was located to the right of the midline and cranially to the fundus in 8/9 animals (Fig. 10.7). In one animal the pylorus was not visualised to the right of the midline (Fig. 10.5). Bunching of small intestines in the right central abdomen occurred in the two heaviest animals

weighing 6 kg and above (Figs 10.3, 10.6 and 10.8). The caecum was not identified in any view. Radiographic measurements for the gastrointestinal tract are shown in Table 10.2.

10.3.3 Lymphatic system

On radiographic examination, the spleen was prominent and was seen in all animals (Figs 10.4, 10.5, 10.7 and 10.8). On ultrasonography, the spleen was easily visualized and was either triangular (4/7) or fusiform (3/7) on transverse images surrounded by an echogenic capsule (Fig. 10.9a). It had a fine homogenous echotextured parenchyma. The mean splenic thickness was 1.42 ± 0.28 cm (Table 10.3). The thickness of the spleen was greater in older animals. All animals older than 8 years (three) had a splenic thickness of 1.7 cm and above. Animals less than 4 years had a maximum splenic thickness of 1.32 cm.

10.3.4 Urinary system

On the VD view, both kidneys were identified in eight of the nine animals (Figs 10.4 and 10.8). In six of the eight animals, the right kidney's caudal pole was positioned more cranial than the left kidney's caudal pole (Fig. 10.4). In the two heaviest animals (6 kg and above), the caudal poles of the left and right kidneys were at the same level (Fig. 10.8). The left kidney was seen more clearly than the right kidney (Figs 10.4, 10.7 and 10.8). On the RL view, the caudal pole of both kidneys was identified in six of the nine animals (Fig. 10.6). The right kidney's mean length in cm (P = 0.04) and ratio compared to

the length of the second lumbar vertebral body (P = 0.04) were significantly larger than for the left kidney.

Similarly, the right kidney's mean width (P = 0.73) and ratio compared to the length of the second lumbar vertebral body (P = 0.70) were larger than for the left kidney although statistically this was not significant. The urinary bladder was identified in three of nine animals. It was oblong and intraabdominal (Fig. 10.3). Radiographic measurements for the kidneys are shown in Table 10.2.

On ultrasonography, the non-lobulated kidneys were ovoid on sagittal and transverse images (Fig. 10.10). The kidney cortex was hyperechoic to the medulla (Figs 10.9b and 10.10). In all animals the right kidney was in close contact with the liver (Fig. 10.10). In 6/7 animals, the left kidney's cortex was isoechoic to the splenic parenchyma (Fig. 10.9b), whereas in one animal it was hyperechoic to the splenic parenchyma. The right kidney's mean length (P = 0.12) and width (P = 0.77) were larger than for the left kidney although this was not statistically significant (Table 10.3). The urinary bladder was seen in five of the seven animals. It was oblong with anechoic urine. The urinary bladder wall had a three-layered classical appearance as described in domestic cats and dogs. The mean thickness of the urinary bladder wall was 1.46 ± 0.36 mm (Table 10.3).

10.3.5 Glandular system

On the RL view, the liver was well contained in the ribcage (Fig. 10.3). Its caudoventral margin extended caudally beyond the costal arch in only three

animals. On ultrasonography, the liver parenchyma was either isoechoic (3/7) (Fig. 10.10) or hypoechoic (3/7) and rarely hyperechoic (1/7) to the right kidney cortex. The gall bladder contained anechoic content and was surrounded by an echogenic wall. The mean thickness of the gall bladder wall was 0.86 ± 0.18 mm (Table 10.3).

10.4 DISCUSSION

The presence of six lumbar vertebrae observed in the majority of animals in this species is similar to the sea otter (*Enhydra lutris*) (Stoskopf and Herbert, 1990) and river otter (*Lontra canadensis*) (Baitchman and Kollias, 2000) as well as to the coati (*Nasua nasua*). Since the coati had mostly six lumbar vertebrae cranial to the sacrum (Martins et al., 2013). Unlike the red panda, domestic cats and dogs have seven lumbar vertebrae (Nickel et al., 1986).

Variation in the number of lumbar vertebrae (five to six) observed in this species has also been reported in the coati (Martin et al., 2013). The number of fused sacral vertebrae (three) observed in the majority of animals in this study is similar to the sea otter (Stoskopf and Herbert, 1990), river otter (Baitchman and Kollias, 2000), coati (Martins et al., 2013), domestic cats and dogs (Nickel et al., 1986).

The occurrence of lumbosacral transitional vertebra observed in this species has also been reported in domestic dogs (Damur-Djuric et al., 2006; Flückiger et al., 2006; Lappalainen et al., 2012). In domestic dogs it is more prevalent in

German shepherd dogs and it has been postulated that this predisposes to premature disc degeneration leading to cauda equina syndrome (Damur-Djuric et al., 2006). The accumulation of abdominal fat ventral to the liver and the conspicuous hypaxial muscles, which were observed in heavy animals in this study have also been reported in obese domestic cats (Graham et al., 2007; Thrall and Robertson, 2011).

The prominent spleen in this species should not be misinterpreted as splenomegaly due to pathological conditions such as extramedullary haemopoiesis, passive congestion, diffuse neoplasia and inflammation, but facilitated easy visualization. A prominent spleen has also been reported in the sea otter (Stoskopf and Herbert, 1990) and river otter (Baitchman and kollias, 2000). On ultrasound, the homogenous, triangular spleen surrounded by an echogenic capsule is similar to the coati (Ribeiro et al., 2013), domestic cats and dogs (Mahoney, 2011).

The mean angle of the gastric axis obtained in this study (63.22 ± 6.06º) is lower than the reported angle in domestic cats (81.62 ± 12.33º) and dogs (85.71 ± 11.73º) (Lee and Leowijuk, 1982). The mean diameter of the small intestine obtained in this study (0.88 ± 0.37 cm) is within the reported range (< 1.2 cm) and close to the median value (1.1 cm) reported in domestic cats (Morgan, 1981; Adams et al., 2010). The mean ratio of the small intestinal diameter to the height of the second lumbar vertebral body observed in this study (1.00 ± 0.41) is lower than the median value (1.28) reported in domestic cats with no signs of gastrointestinal tract disease (Adams et al., 2010). The

disparity in the ratio of the small intestinal diameter to the height of the second lumbar vertebral body between the red panda and the domestic cat is due to the difference in the height of the second lumbar vertebral body in these two species.

For the large intestine, the mean diameter (1.79 ± 0.22 cm) and ratio compared to the height of the second lumbar vertebral body (2.04 ± 0.33) observed in this study are lower than the median values 2.4 cm and 2.79, respectively, reported in the domestic cats (Adams et al., 2010). However, the mean ratio of the large intestine compared to the length of the second lumbar vertebral body obtained in this study (0.92 ± 0.12) is similar to the reported values in domestic cats (1.13 ± 0.3) and dogs (1.05 ± 0.3) (Lee and Leowijuk, 1982).

The bunching of small intestines in the right central abdomen in the two heaviest animals has also been reported in obese domestic cats (Lee and Leowijuk, 1982; Graham et al., 2007) and should not be misinterpreted as an abdominal mass effect. The lack of visualization of the caecum in this species is different from domestic cats and dogs (Lee and Leowijuk, 1982). The caecum is also absent in the sea otter (Stoskopf and Herbert, 1990), river otter (Baitchman and Kollias, 2000) and coati (Carlsson, 1925).

The more cranial position of the right kidney compared to the left kidney observed in the majority of animals is similar to the sea otter (Stoskopf and Herbert, 1990), coati (Ribeiro et al., 2013), domestic cats and dogs (Feeney

and Johnston, 2007). The ultrasonographic appearance of the kidneys in this species, that is non-lobulated and ovoid with hyperechoic renal cortex compared to the medulla is similar to the coati (Ribeiro et al., 2013), domestic cats and dogs (Graham, 2011). The kidneys are multilobulated in the sea otter (Stoskopf and Herbert, 1990) and river otter (Baichman and Kollias, 2000). The isoechoic renal cortex in relationship to the splenic parenchyma observed in this study in the majority of animals is different from the reported study in the coati and in domestic cats and dogs. In the coati (Ribeiro et al., 2013) the spleen was reported to be hyperechoic to the renal cortex similar to domestic cats and dogs (Larson, 2009).

The mean length of the kidneys obtained from radiographic examination in this species (R: 4.20 cm; L: 4.04 cm) are within the reported range (3.8 – 4.4 cm) in domestic cats (Seyrek-Intas and Kramer, 2008). Furthermore the mean ratio of the kidney's length to the length of the second lumbar vertebral body in this species (R: 2.26; L: 2.16) is within the reported range (2.1 – 3.2) in domestic cats (Larson, 2009).

The ultrasonographic mean length measurements of the kidneys obtained in this study (R: 3.98 cm; L: 3.85 cm) are higher than the reported means in the coati (R: 3.06 cm; L: 3.03 cm) and are within the range (3.0 – 4.3 cm) reported in domestic cats (Larson, 2009). The difference in the mean length of the kidneys between this study and those reported in the coati is attributed to the difference in body weight. The mean weight of the coatis was reported to be 2.67 ± 0.54 kg (Ribeiro et al., 2013), which is lower than the mean weight of

the red pandas in this study (4.84 ± 0.65 kg). Kidney dimensions have been reported to increase with the weight of the animal (Barr et al., 1990).

The mean wall thickness of the urinary bladder obtained in this study (1.46 mm) is within the range (1.3-1.7 mm) reported in domestic cats (Finn-Bodner, 1995), which is higher than the reported mean (1.1 mm) in the coati (Ribeiro et al., 2013). However, the wall thickness of the urinary bladder depends on the degree of bladder distension (Geisse et al., 1997).

The caudal extension of the liver beyond the coastal arch observed in few animals in this study indicates that the liver is well contained within the ribcage. Variation in echogenicity of the liver parenchyma (hypoechoic to hyperechoic) in relationship to the right kidney's cortex is different from the reported study in the coati. In the coati the liver parenchyma was reported to be isoechoic to the renal cortex (Ribeiro et al., 2013). The hyperechoic renal cortex in relation to the liver parenchyma observed in three animals in this study is most likely the result of fat vacuoles in the cortical-tubular epithelium as explained in the domestic cat (Larson, 2009). The red panda kidney is also prone to physiological accumulation of fat like domestic cats (Zwart, 1989). The anechoic content of the gallbladder which is surrounded by an echogenic wall is similar to that of the coati (Ribeiro et al., 2013). The mean wall thickness of the gall bladder obtained in this study (0.86 mm) was within the reported range (0.4–0.9 mm) in domestic cats (Hittmair et al., 2001).

Species-specific differences exist in the normal radiographic and ultrasonographic abdominal anatomy. Knowledge of the normal radiographic and ultrasonographic abdominal anatomy of the red panda is important for accurate interpretation and diagnosis of abdominal diseases.

10.5 ACKNOWLEDGEMENTS

The authors would like to thank the Organisation for Women in Science for Developing World (OWSD), Swedish International Development Cooperation Agency (SIDA), University of Pretoria, Johannesburg and Bristol zoo for supporting this study. Drs. Georgina Cole, Kathryn Perrin, Ms. Fania Mohlala, sisters and animal handlers of the Johannesburg and Bristol zoos for their assistance during radiography and ultrasonography. Mrs. Charmaine Vermeulen and Mrs. Wilma Olivier of the University of Pretoria for their assistance in photography and administrative work, respectively.

10.6 REFERENCES

Adams, W. M., L. A. Sisterman, J. M. Klauer, B. M. Kirby, and T. L. Lin, 2010: Association of intestinal disorders in cats with findings of abdominal radiography. J. Am. Vet. Med. Assoc. **236,** 880–886.

Baitchman, E. J., and G. V. Kollias, 2000: Clinical Anatomy of the North American river otter (*Lontra canadensis*). J. Zoo. Wildl. Med. **31,** 473–483.

Barr, F. J., P. E. Holt, and C. Gibbs, 1990: Ultrasonographic measurement of normal renal parameters. J. Small. Anim. Pract. **31,** 180–184.

Carlsson, A., 1925: über *Ailurus fulgens*. Acta. Zool. **6,** 269–305.

Damur-Djuric, N., F. Steffen, M. Hässig, J. P. Morgan, and M. A. Flückiger, 2006: Lumbosacral transitional vertebrae in dogs: classification, prevalence and association with sacroiliac morphology. Vet. Radiol. Ultrasound. **47,** 32–38.

Eshar, D., J. A. Briscore, and W. Mai, 2013: Radiographic kidney measurements in North American pet ferrets (*Mustela furo*). J. Small. Anim. Pract. **54,** 15–19.

Feeney, D. A., and G. R. Johnston, 2007: The kidneys and ureters. In: Textbook of Veterinary Diagnostic Radiology (D. E. Thrall, ed.). Missouri: Saunders Elsevier. pp. 693–707.

Finn-Bodner, S. T., 1995: The urinary bladder. In: Practical Veterinary Ultrasound (R. E. Cartee, B. A. Selcer, J. A Hudson, S. T. Finn-Bodner, M. B. Mahaffey, P. L. Johnson, and K. W. Marich, eds). Philadelphia: William & Wilkins. pp. 200–235.

Fisher, R. E., B. Adrian, M. Barton, J. Holmgren, and S. Y. Tang, 2009: The phylogeny of the red panda (*Ailurus fulgens*): evidence from the forelimb. J. Anat. **215,** 611–635.

Flower, W. H., 1870: On the anatomy of Ailurus fulgens. Proc. Zool. Soc. London. **1870,** 752–769.

Flückiger, M. A., N. Damur-Djuric, M. Hässig, J. P. Morgan, and F. Steffen, 2006: A lumbosacral transitional vertebra in the dog predisposes to cauda equina syndrome. Vet. Radiol. Ultrasound. **47,** 39–44.

Geisse, A. L., J. E. Lowry, D. J. Schaeffer, and C. W. Smith, 1997: Sonographic evaluation of urinary bladder wall thickness in normal dogs. Vet. Radiol. Ultrasound. **38,** 132–137.

Graham, J. P., 2011: Kidneys and proximal ureters. In: BSAVA Manual of Canine and Feline Ultrasonography (F. Barr and L. Gaschen, eds). Gloucester: BSAVA. pp. 110–123.

Graham, J. P., C. R. Berry, and D. E. Thrall, 2007: Technical issues and interpretation principles relating to the canine and feline abdomen. In: Textbook of Veterinary Diagnostic Radiology (D. E. Thrall, ed.). St. Louis: Saunders. pp. 626–644.

Groves, C., 2011: The Taxonomy and Phylogeny of *Ailurus*. In: Red Panda Biology and Conservation of the First Panda (A. Glatston, ed.). London: Academic Press. pp. 101–124.

Hittmair, K. M., H. D. Vielgrader, and G. Loupal, 2001: Ultrasonographic evaluation of gallbladder wall thickness in cats. Vet. Radiol. Ultrasound. **42,** 149–155.

IUCN, 2014: IUCN Red list of threatened species. Version 2014.3. Available at: http://www.iucnredlist.org (accessed on 18 November 2014).

Kummerfeld, M., A. Knieriem, P. Wohlsein, M. Verlag, and H. Schaper, 2008: Osteomyelitis and papillary renal adenoma in a red panda (*Ailurus fulgens fulgens*). Dtsch. Tierarzti. Wochenschr. **115,** 421–425.

Lappalainen, A. K., R. Salomaa, J. Junnila, M. Snellman, and O. Laitinen-Vapaavuori, 2012: Alternative classification and screening protocol for transitional lumbosacral vertebra in German shepherd dogs. Acta. Vet. Scand. **54,** 1–10.

Larson, M. M., 2009: The kidneys and ureters. In: BSAVA Manual of Canine and Feline Abdominal Imaging (R. O'Brien and F. Barr, eds). Gloucester: BSAVA. pp. 185–204.

Lee, R., and C. Leowijuk, 1982: Normal parameters in abdominal radiology of the dog and cat. J. Small. Anim. Pract. **23,** 251–269.

Mahoney, P., 2011: Spleen. In: BSAVA Manual of Canine and Feline Ultrasonography (F. Barr and L. Gaschen, eds). Gloucester: BSAVA. pp. 100–109.

Makungu, M., W. M. du Plessis, M. Barrows, K. N. Koeppel, and H. B. Groenewald, 2012: Ultrasonographic abdominal anatomy of healthy captive caracals (*Caracal caracal*). J. Zoo. Wildl. Med. **43,** 522–529.

Makungu, M., W. M. du Plessis, M. Barrows, K. N. Koeppel, and H. B. Groenewald, 2013: Polycystic kidneys in the red panda (*Ailurus fulgens*). J. Zoo. Wildl. Med. **44,** 777–780.

Martins, G. S., E. R. Lopes, I. I. G. Taques, C. Y. Correia, Y. S. Meireles, N. C. M. R. Turbino, L. D. Guimarães, and P. B. Néspoli, 2013:

Radiographic morphology of the skeleton, thorax and abdomen of coati (*Nasua nasua* Linnaeus, 1766). Pesq. Vet. Bras. **33,** 1137–1143:

Montali, R. J., R. Wallace, L. G. Phillips Jr., M. Bush, M. Roberts, S. D. Crissey, K. J. Warnell, O. T. Oftedal, M. Edwards, and L. Rabin, 1989: Hepatopathy and hypercholesterolemia in red pandas associated with a diet change. In: Red Panda Pathology (A. R. Glatston, ed.). The Netherlands: SPB Academic Publishing. pp. 31–40.

Morgan, J. P., 1981: The upper gastrointestinal examination in the cat: normal radiographic appearance using positive contract medium. Vet. Radiol. Ultrasound. **22,** 159–169.

Neilsen, C., C. Mans, and S. A. Colopy, 2014: Gastric dilatation and volvulus in a red panda (*Ailurus fulgens*). Vet. Surg. **43,** 1001–1003.

Nickel, R., A. Schummer, E. Seiferle, J. Frewein, H. Wilkens, and K. H. Wille, 1986: The anatomy of the Domestic Animals. Berlin: Springer-Verlag.

Nyland, T. G., and J. S. Mattoon, 2002: Small Animal Diagnostic Ultrasound. Philadelphia: Saunders.

Philippa, J., and E. Ramsay, 2011: Captive red panda medicine. In: Red Panda Biology and Conservation of the First Panda (A. R. Glatston, ed.). London: Academic Press. pp. 271–285.

Preece, B., 2011: Red panda pathology. In: Red Panda Biology and Conservation of the First Panda (A. R. Glatston, ed.). London: Academic Press. pp. 287–302.

Ribeiro, R. G., A. P. A. Costa, N. Bragato, A. M. Fonseca, J. C. M. Duque, T. D. Prado, A. C. R. Silva, and N. C. Borges, 2013: Normal sonographic

anatomy of the abdomen of coatis (*Nasua nasua*, Linnaeus 1766). BMC. Vet. Res. **9,** 124.

Seiler, G., and W. Maï, 2009: The stomach. In: BSAVA Manual of Canine and Feline Abdominal Imaging (R. O'Brien, and F. Barr, eds). BSAVA, Gloucester, pp. 87–109.

Seyrek-Intas, D., and M. Kramer, 2008: Renal imaging in cats. Vet. Focus. **18,** 23–30.

Stoskopf, M. K., and D. Herbert, 1990: Selected anatomical features of the sea otter (*Enhydra lutris*). J. Zoo. Wildl. Med. **21,** 36–47.

Thrall, D. E., and I. D. Robertson, 2011: The abdomen. In: Atlas of Normal Radiographic Anatomy and Anatomic Variants in the Dog and Cat. St. Louis: Elsevier. pp. 169–206.

Wagner, W. M., and R. M. Kirberger, 2005a: Radiographic anatomy of the thorax and abdomen of the common marmoset (*Callithrix jacchus*). Vet. Radiol. Ultrasound. **46,** 217–224.

Wagner, W. M., and R. M. Kirberger, 2005b: Transcutaneous ultrasonography of the abdomen in the normal common marmoset (*Callithrix jacchus*). Vet. Radiol. Ultrasound. **46,** 251–258.

Wei, F., and Z. Zhang, 2009: Family Ailuridae (red panda). In: Handbook of the Mammals of the World Vol. 1 Carnivores (D. E. Wilson and R. A. Mittermeier, eds). Barcelona: Lynx Edicions. pp. 498–503.

Zwart, P. C., 1989: Contribution to the pathology of the red panda (*Ailurus fulgens*). In: Red Panda Biology (A. R. Glatston, ed.). The Netherlands: SPB Academic Publishing. pp. 25–29.

10.7 TABLES

Table 10.1 Radiographic measurement of the length and height in cm of lumbar vertebral bodies not compensated for magnification in captive red pandas

Vertebra	Number	Length RL Mean ± SD (Range)	Height RL Mean ± SD (Range)
L1	9	1.87±0.04 (1.80–1.90)	0.88±0.07 (0.79–1.00)
L2	9	1.95±0.05 (1.90–2.00)	0.91±0.06 (0.80–1.00)
L3	9	2.08±0.07 (2.00–2.20)	0.88±0.08 (0.80–1.00)
L4	9	2.18±0.08 (2.10–2.30)	0.87±0.08 (0.80–1.00)
L5	9	2.20±0.13 (2.00–2.40)	0.88±0.08 (0.80–1.00)
L6	7	2.09±0.14 (1.90–2.30)	0.86±0.08 (0.80–1.00)

RL, right lateral; L, lumbar vertebra

Table 10.2 Radiographic measurements of the gastrointestinal tract and kidneys not compensated for magnification in captive red pandas

Variable	Number	Mean ± SD	Range
Angle of gastric axis [º]	9	63.22±6.06	55.00–70.00
Small intestinal diameter [cm]	9	0.88±0.37	0.50–1.60
Small intestinal diameter: HL2	9	1.00±0.41	0.50–1.78
Large intestinal diameter [cm]	9	1.79±0.22	1.50–2.00
Large intestinal diameter: HL2	9	2.04±0.33	1.50–2.50
Large intestinal diameter: LL2	9	0.92±0.12	0.75–1.05
Left kidney			
Length [cm]	8	4.04±0.32	3.50–4.40
L:LL2	8	2.16±0.18	1.94–2.44
Width [cm]	7	2.24±0.17	2.12–2.60
W:LL2	7	1.19±0.12	1.10–1.44
Right kidney			
Length [cm]	7	4.20±0.36	3.80–4.70
L:LL2	7	2.26±0.20	2.03–2.61
Width [cm]	7	2.30±0.51	1.57–3.13
W:LL2	7	1.23±0.28	0.83–1.65

HL2, height of the second lumbar vertebral body; LL2, length of the second lumbar vertebral body, L:LL2, ratio of the kidney's length to length of the second lumbar vertebral body; W:LL2, ratio of the kidney's width to the length of the second lumbar vertebral body

Table 10.3 Ultrasonographic measurements of the spleen, kidneys, urinary and gall bladder in captive red pandas

Variable	Number	Mean ± SD	Range
Left kidney [cm]			
Length	7	3.85±0.27	3.50–4.23
Width	7	2.16±0.19	1.97–2.55
Height	7	1.88±0.26	1.59–2.38
Right kidney [cm]			
Length	7	3.98±0.33	3.49–4.54
Width	7	2.19±0.24	1.73–2.51
Height	7	1.78±0.19	1.60–2.13
Urinary bladder wall thickness [mm]	5	1.46±0.36	1.00–1.80
Splenic thickness [cm]	7	1.42±0.29	1.06–1.73
Gall bladder wall thickness [mm]	5	0.86±0.18	0.60–1.10

10.8 FIGURES

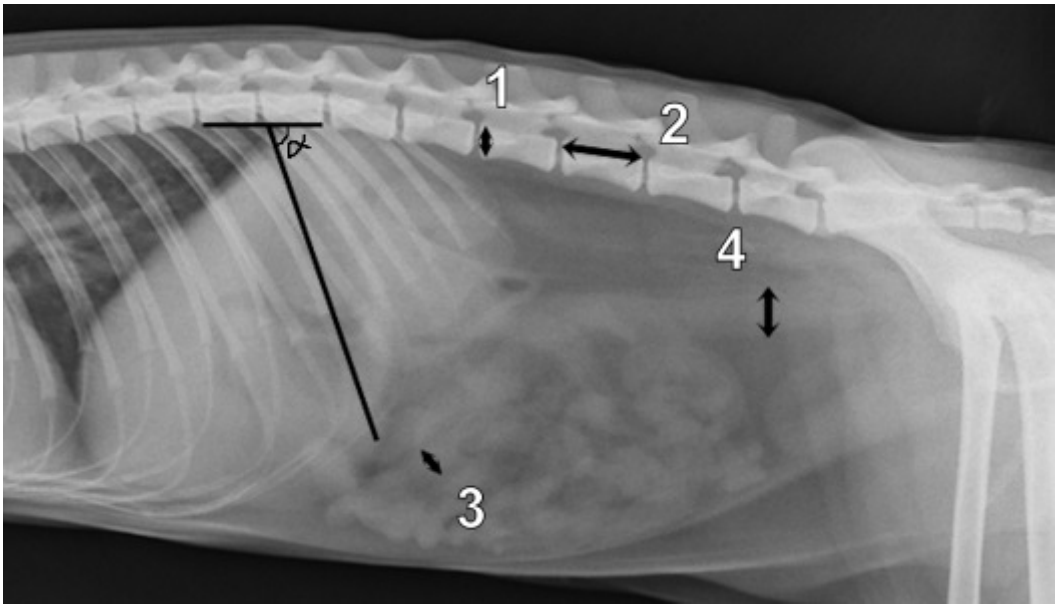

Fig. 10.1 Right lateral (RL) abdominal radiograph of a 2.5-year-old (7 kg) male captive red panda illustrating radiographic measurements. (1) Vertebral body height, (2) vertebral body length, (3) external diameter of the small intestine, (4) external diameter of the large intestine and α = angle of gastric axis.

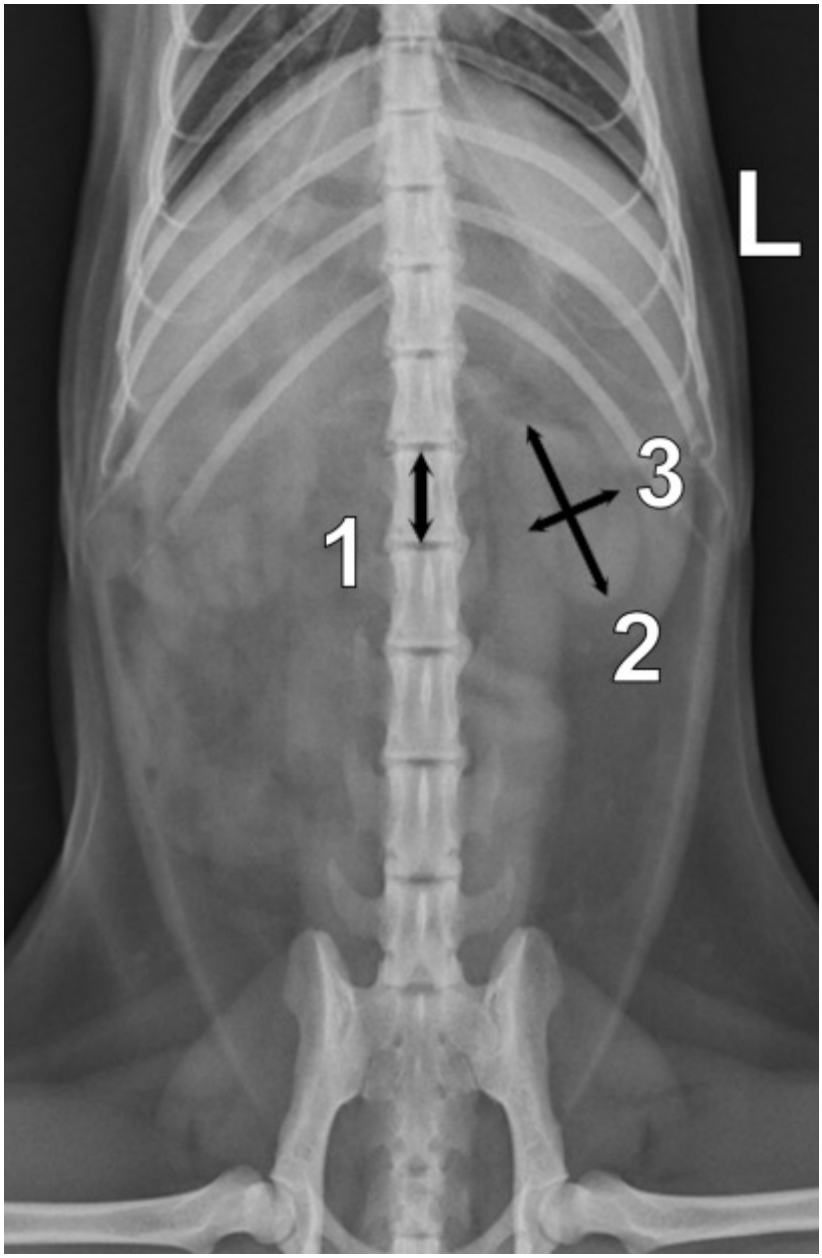

Fig. 10.2 Ventrodorsal (VD) abdominal radiograph of a 2.5-year-old (7 kg) male captive red panda illustrating radiographic measurements. (1) Vertebral body length, (2) length of the kidney and (3) width of the kidney. L, left.

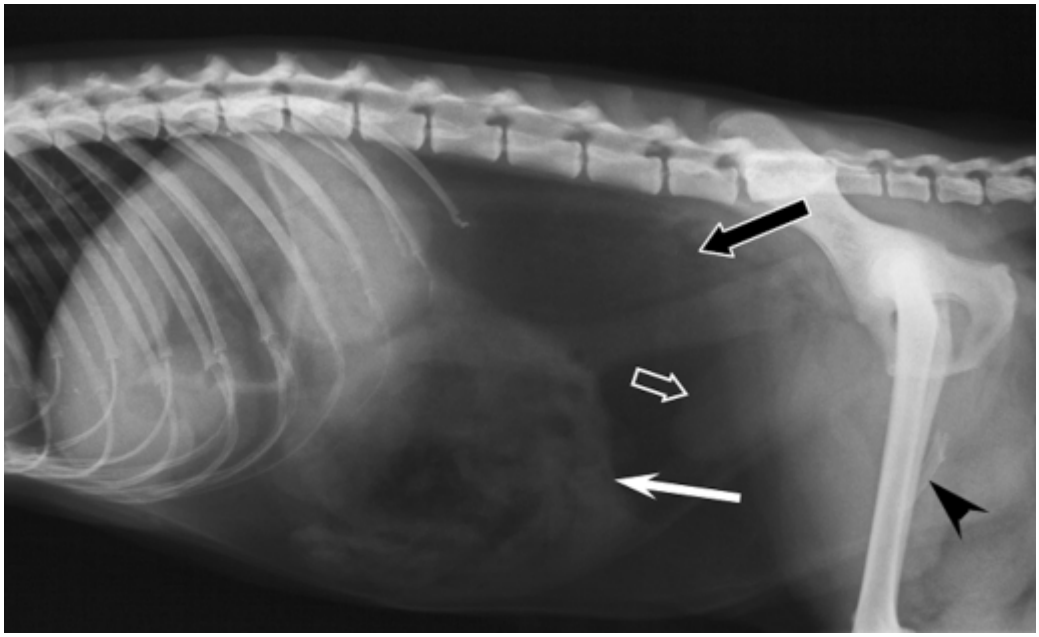

Fig. 10.3 Right lateral abdominal radiograph of an 8-year-old (6 kg) male captive red panda. Note the presence of six lumbar vertebrae with relatively short spinous processes and three fused sacral segments. Accumulation of large amount of fat is seen in the retroperitoneal space (black arrow) and the abdomen. The liver is well contained within the ribcage. Note also the bunching of small intestines in the central abdomen (white arrow). The urinary bladder (open white arrow) is oblong-shaped and intra-abdominal. Black arrow head shows the os penis.

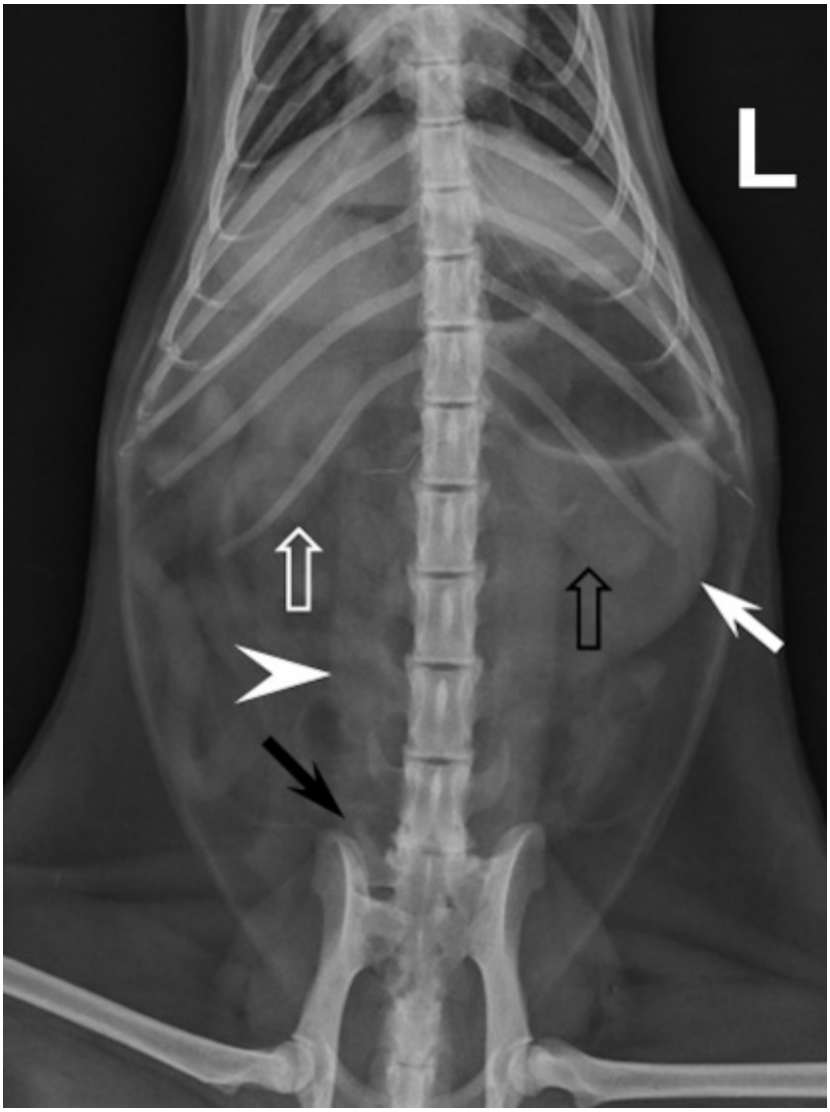

Fig. 10.4 Ventrodorsal abdominal radiograph of an 11.6-year-old (5.5 kg) male captive red panda. Note the presence of five lumbar vertebrae. Note also the lumbosacral transitional vertebra (black arrow) and osteoarthrosis involving the lumbosacral junction. The hypaxial muscles (white arrow head) are conspicuous and the spleen (white arrow) is prominent located lateral to the left kidney. The left kidney (open black arrow) is caudal to the right kidney (open white arrow). L, left.

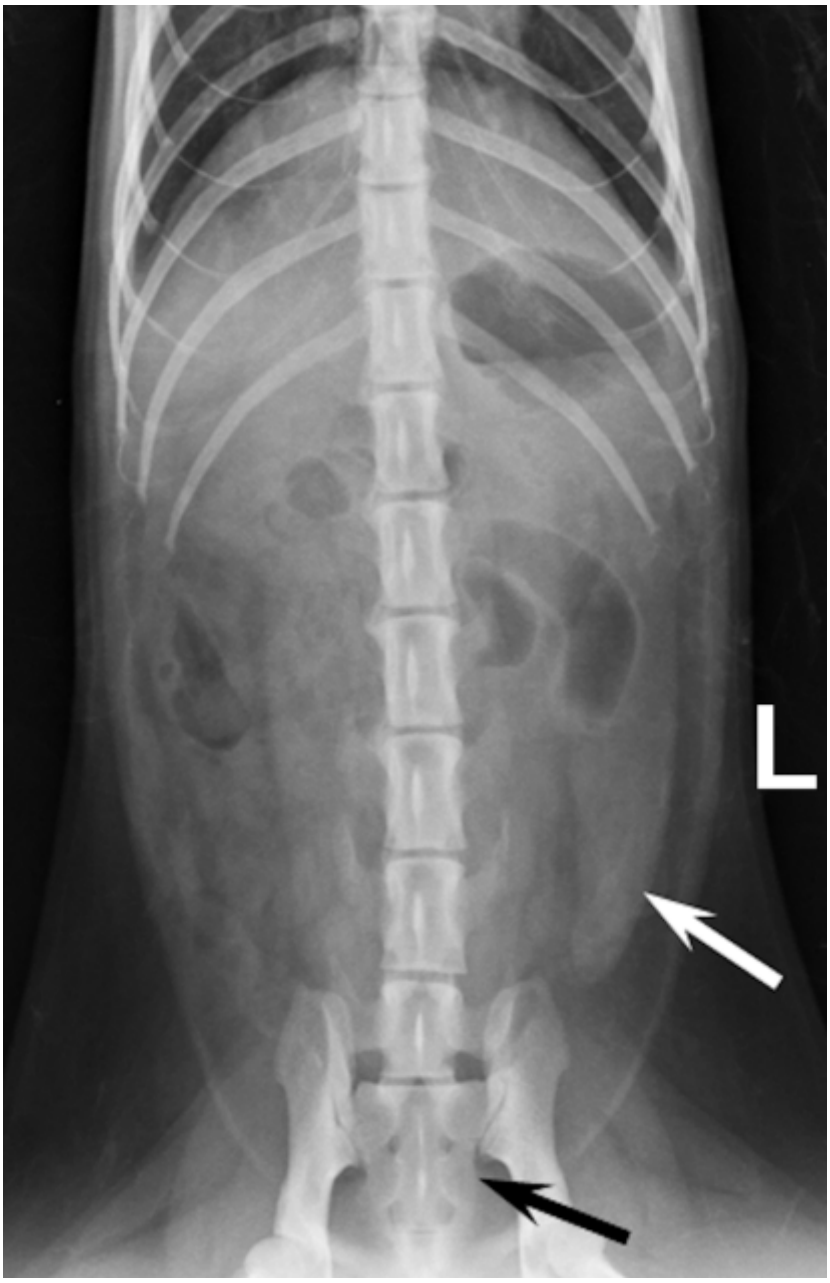

Fig. 10.5 Ventrodorsal abdominal radiograph of a 4-year-old (4.8 kg) female captive red panda. Note the presence of six lumbar vertebrae and two fused sacral segments (black arrow). Note also the presence of a prominent spleen (white arrow). L, left.

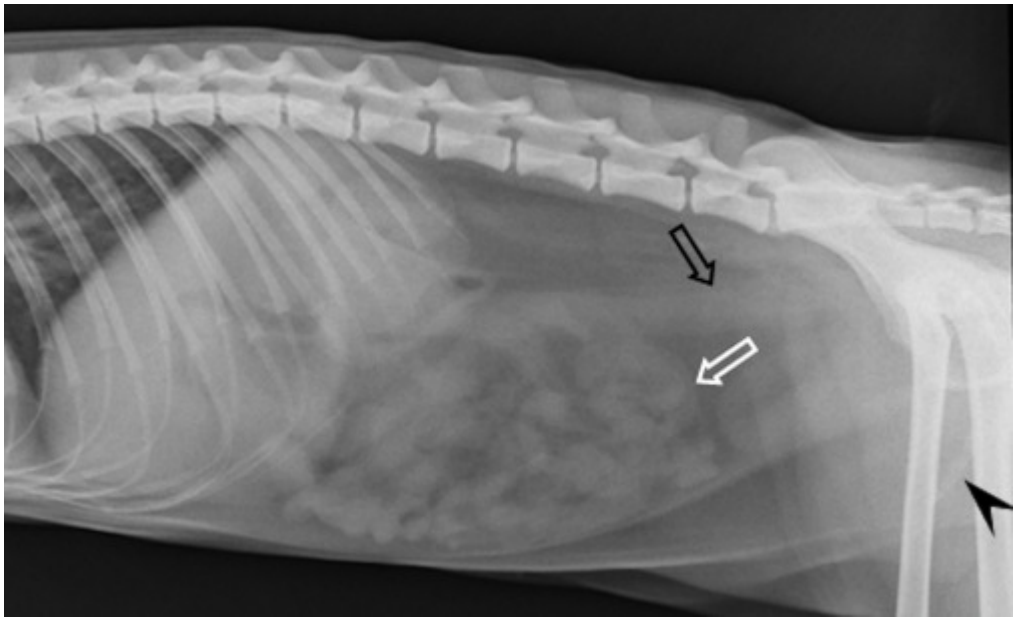

Fig. 10.6 Right lateral abdominal radiograph of a 2.5-year-old (7 kg) male captive red panda. Note the accumulation of fat in the retroperitoneal space and the abdomen. The oblong-shaped urinary bladder is located intra-abdominal. Descending colon (open black arrow), small intestines (open white arrow) and os penis (black arrow head).

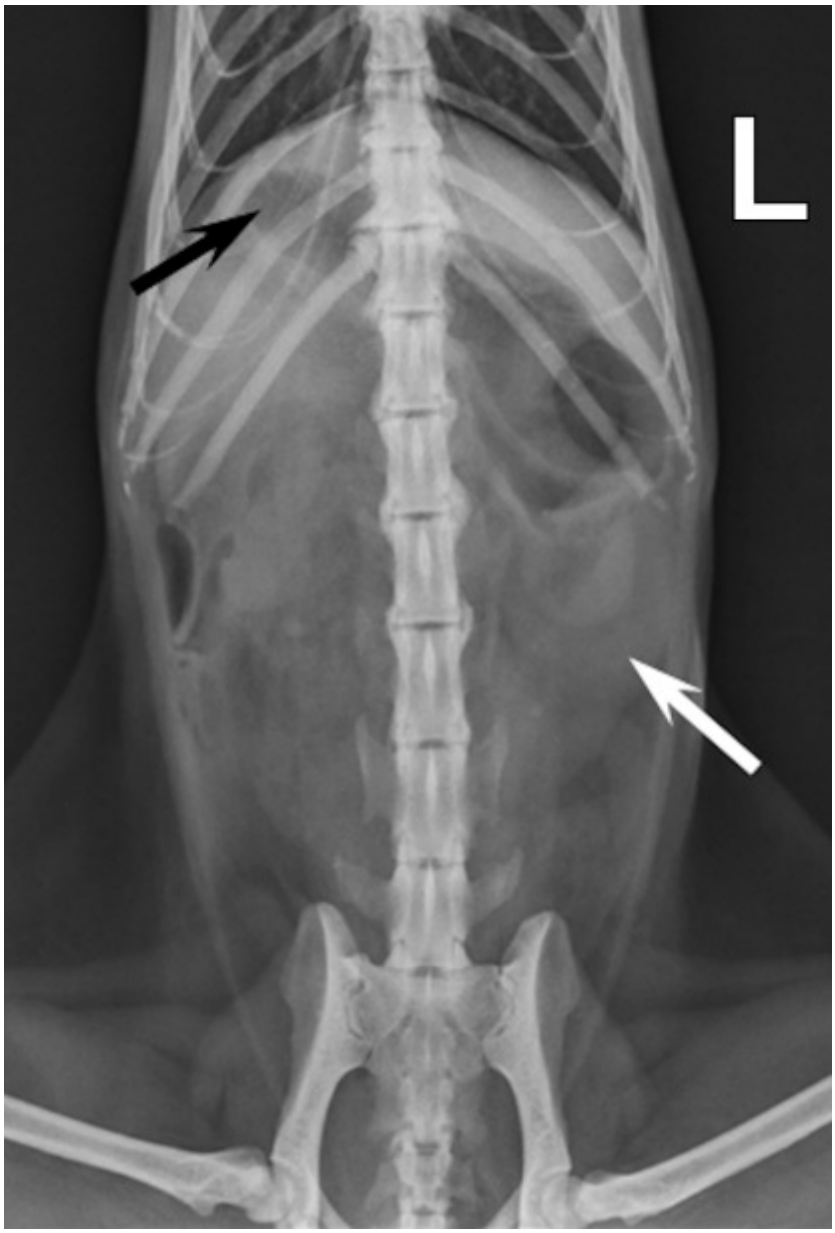

Fig. 10.7 Ventrodorsal abdominal radiograph of a 10.6-year-old (4.3 kg) female captive red panda. The pylorus (black arrow) is to the right of the midline and cranially to the fundus. The prominent spleen is shown by a white arrow. L, left.

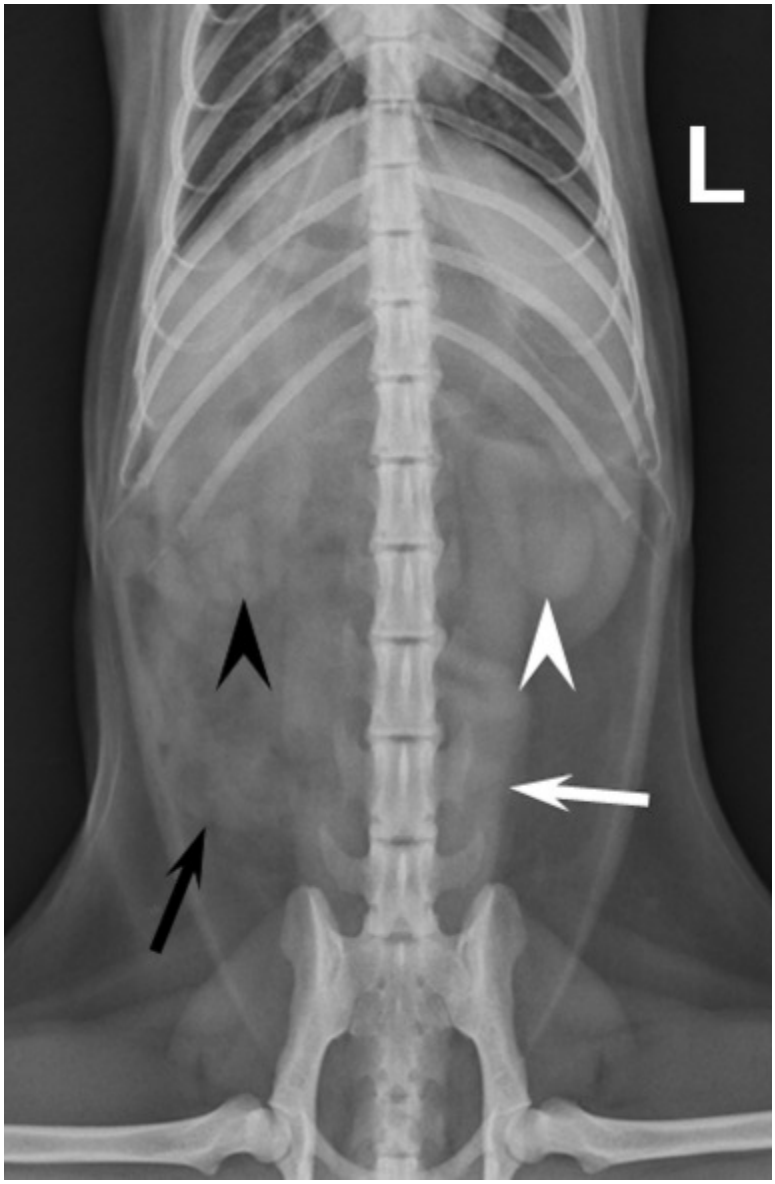

Fig. 10.8 Ventrodorsal radiograph of a 2.5-year-old (7 kg) male captive red panda. Note the bunching of small intestines (black arrow) in the right abdomen. The descending colon (white arrow) is superimposed on the hypaxial muscles. The left (white arrow head) and right (black arrow head) kidneys are at a similar level. Note also the prominent spleen lateral to the left kidney. L, left.

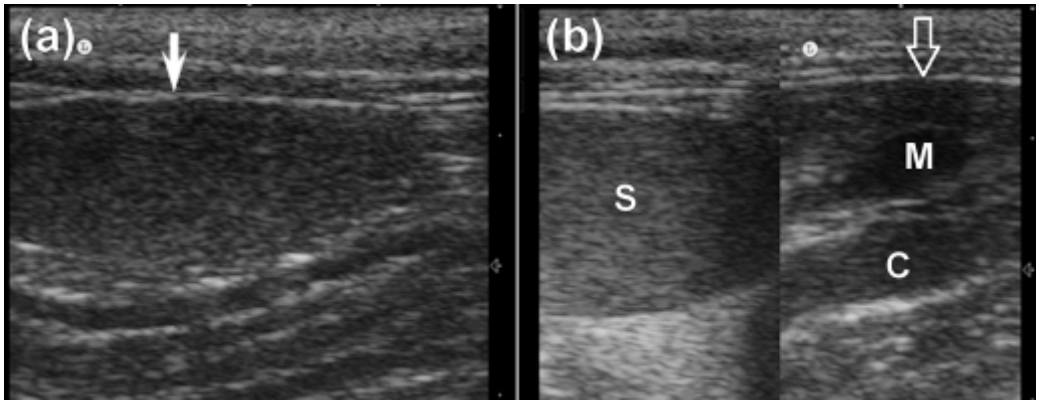

Fig. 10.9 (a) Transverse view of the spleen and (b) a split screen of transverse view of the spleen (S) and sagittal view of the left kidney (white open arrow) of a 2-year-old (4.9 kg) male captive red panda. (a) The spleen is fusiform with homogenous echotextured parenchyma surrounded by a thin echogenic capsule (white arrow). (b) Note the hyperechoic renal cortex (C) when compared to the medulla (M). The renal cortex (C) is isoechoic to the splenic parenchyma (S).

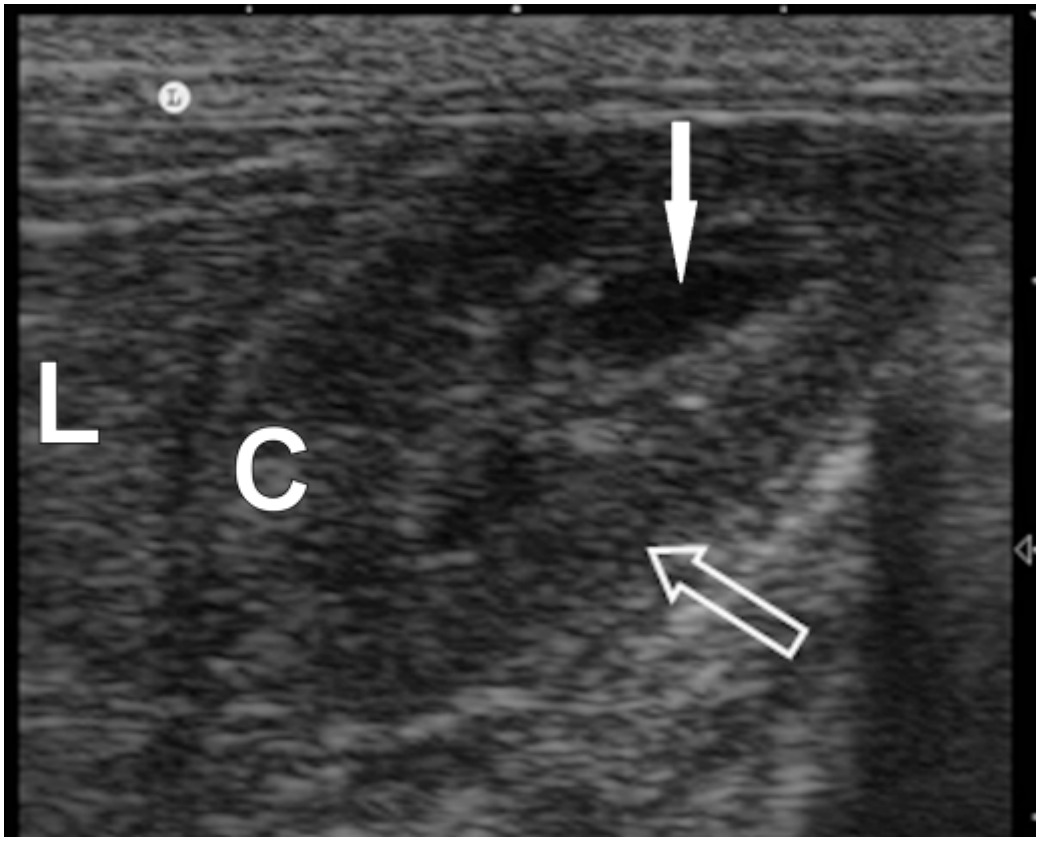

Fig. 10.10 Sagittal sonographic image of the right kidney (open white arrow) of a 2-year-old (4.5 kg) female captive red panda. The ovoid right kidney is in contact with the liver (L) and the right kidney cortex (C) is isoechoic to the liver parenchyma. Note the hypoechoic medulla (white arrow) in relation to the renal cortex (C).

CHAPTER 11

GENERAL DISCUSSION AND CONCLUSIONS

11.1 GENERAL DISCUSSION AND CONCLUSIONS

The morphology of the pelvis, thoracic and hind limb of the red panda and ring-tailed lemur support the presence of strong flexor and supinator muscles as well as flexibility of limb joints, which are important in arboreal quadruped locomotion. Such features included: the more medially directed minor trochanter, a poorly defined intermediate ridge at the distal articular surface of the tibia, an almost flattened medial ridge of the trochlea of the talus, widely spread metacarpal and metatarsal bones, the large area for the origin of the *M. teres major* and prominent medial epicondyle, lateral supracondylar crest, radial tuberosity and hamate process.

However, the scapula of the ring-tailed lemur is modified for both arboreal and terrestrial lifestyles. The narrow scapula of the ring-tailed lemur with a long dorsal margin and a short cranial margin allows rapid movement of the thoracic limb and at the same time provides an adequate area for insertion of the scapulovertebral muscles, which support the body weight and absorb the shock of the footfall at the end of a quadrupedal leap. Additionally, the pelvis and hind limb of the ring-tailed lemur showed locomotor adaptation for jumping. Such features included: an elongated central tarsal bone, a

prominent caudal ventral iliac spine and a tuberosity on the cranial surface of the patella.

The large sesamoid bone for the *M. abductor digiti I longus* observed in the red panda acts as a false-thumb for the grasping actions of the manus (Antón et al., 2006). The red panda has been observed to grasp and bend bamboo to bring the leaves within reach of the mouth (Roberts and Gittleman, 1984; Antón et al., 2006). The large sesamoid bone for the *M. abductor digiti I longus* is also present in coatis (*Nasua nasua*) (Martins et al., 2013) and giant pandas (*Ailuropoda melanoleuca*) (Endo et al., 1996).

The radiographic visualisation of a large ovoid popliteal sesamoid bone in the red panda was similar to that of domestic cats (McCarthy and Wood, 1989). Furthermore, the non-visualisation of the popliteal sesamoid bone on radiographic examination in some of the red pandas has also been reported in the domestic cat (Arnbjerg and Heje, 1993). In domestic cats (Arnbjerg and Heje, 1993) the medial fabella may not be visualised radiographically, which is similar to red pandas.

The presence of a tarsal sesamoid bone in the red panda is similar to the coati (Martins et al., 2013). In the red panda, the tarsal sesamoid bone provides the origin for the medial belly of the *Mm. flexores digiti I profundi breves* (Fisher et al., 2008). Therefore, the name 'medial sesamoid bone for the *Mm. flexores digiti I profundi breves*' is suggested. The tarsal sesamoid bone is absent in domestic cats and dogs (Nickel et al., 1986).

Several functions have been postulated for sesamoid bones and cartilages such as they alter the direction of pull of certain muscles, diminish friction and withstand pressure (Mottershead, 1988). However, the reason for their existence and exact function is debatable (Mottershead, 1988). It is most likely that sesamoid bones enable tendons in which they are associated with to become fixed to an adjacent bony area, thus allowing the particular muscle involved to act in a specialized manner at certain times and for a specific purpose (Mottershead, 1988).

As in other strepsirrhines (Osman Hill, 1953; Jouffroy, 1975), the central carpal bone was present in all skeletally mature ring-tailed lemurs. The central carpal bone is absent in other primates such as humans and in domestic cats and dogs (Nickel et al., 1986). The divergence of the first metacarpal and –tarsal bones further medially from the corresponding distal bones is related to the manus and pes being efficient grasping tools in non-human primates (Ankel-Simons, 2007).

The occurrence of the ossicle in the lateral meniscus and its location in ring-tailed lemurs is different from domestic cats (Whiting and Pool, 1984). In domestic cats the cranial horn of the medial meniscus is involved. In primates, the ossicle may involve the medial, lateral or both medial and lateral menisci (Ganey et al., 1994). In man, intrameniscal ossicles are very unusual, and are frequently positioned in the medial meniscus compared to the lateral meniscus (Le Minor, 1990). The cause of variation in the location of the ossicle within different species warrants further research.

In the Bengal tiger, the ossicle of the meniscus has been associated with running and jumping whereby the ossicle probably provides a mechanical fulcrum to accommodate the dynamic change in the shape of the meniscus during extension of the stifle (Ganey et al., 1994). The dynamic change of the shape of the meniscus distributes the load of the articulation through the meniscus, which reduces wear and fatigue of the articular surfaces of the femur and tibia (Ganey et al., 1994). This might also be true for the ring-tailed lemur since its locomotor habit involves branch running and springing (Ankel-Simons, 2007). The occurrence of an ossicle in the infrapatellar fat pad has not yet been described in healthy domestic and non-domestic animals.

The presence of an inter-phalangeal ossicle on the palmar and plantar aspect of the first digit in all healthy ring-tailed lemurs suggests that the ossicle is a normal anatomical finding in this species. Further studies are needed to determine the importance of the ossicle in the biomechanics of the first digit. In humans the ossicle is associated with development of biomechanical and clinical pathologies (Roukins and Hurless, 1996).

The brachial and antebrachial scent glands were only seen in male ring-tailed lemurs radiographically. The brachial scent gland is barely developed in female ring-tailed lemurs whereas the antebrachial scent gland is present in male and female ring-tailed lemurs (Wilson and Hanlon, 2010). Poor development of the antebrachial scent gland in female ring-tailed lemurs might explain why it was not seen radiographically in this study.

In the red panda osteoarthrosis (OA) of the carpus, tarsus, elbow, stifle and hip joint was seen in animals older than 9 years without history of trauma, which suggests that the likely cause is primary OA. A study on feline OA (Lascelles, 2010) indicated that the majority of animals reported with OA had no obvious cause, which also suggested a primary OA. Osteoarthrosis of the hip joint in the red panda was characterised mainly by remodelling of the femoral neck similar to dogs (Biery, 2006). In the domestic cat, it is characterised by minimal remodelling of the femoral neck and extensive remodelling and proliferative changes involving the craniodorsal acetabular margin (Biery, 2006; Lascelles, 2010).

The majority of red pandas had 20 thoracolumbar vertebrae (n = 11) and only one red panda had 19. Most red pandas with 20 thoracolumbar vertebrae had 14 thoracic and 6 lumbar vertebrae (n = 10) whereas only one red panda had 15 thoracic and 5 lumbar vertebrae. The red panda with 19 thoracolumbar vertebrae had 14 thoracic and 5 lumbar vertebrae. A transitional lumbosacral vertebra was observed in a red panda with 19 thoracolumbar vertebrae. Transitional lumbosacral vertebrae have also been reported in domestic dogs (Damur-Djuric et al., 2006).

Most of the thoracic organs and structures of clinical importance in the red panda were seen on radiographic examination. The mean ratio of thoracic depth to thoracic width obtained in the red panda indicated a normal thoracic conformation (Buchanan and Bücheler, 1995) similar to the coati (Martini et al., 2013). Rudimentary clavicles, which were observed in some red pandas,

have also been reported in dogs (McCarthy and Wood, 1988; Cerny and Cizinauskas, 1995). The more obliquely positioned and elongated cardiac silhouette and redundant aortic arch, seen in older red pandas should not be interpreted as pathological change, but as geriatric change (Johnson et al., 2008) and have also been reported in the domestic cat (Moon et al., 1993) and captive maned wolves (*Chrysocyon brachyurus*) (Estrada et al., 2009).

The prominent spleen on radiographic and ultrasonographic examination in the red panda should not be misinterpreted as splenomegaly due to pathological conditions such as extramedullary haemopoiesis, diffuse inflammation and neoplasia. A prominent spleen has also been reported in the sea otter (*Enhydra lutris*) (Stoskopf and Herbert, 1990) and river otter (*Lontra canadensis*) (Baitchman and Kollias, 2000). The echogenicity of the spleen in relation to the kidney cortex in red pandas in this study was isoechoic, which is different from the coati (Ribeiro et al., 2013), domestic cats and dogs (Mahoney, 2011). Bunching of small intestines in the right central abdominal position in obese red pandas should not be misinterpreted as a mass effect. It has also seen in obese domestic cats (Lee and Leowijuk, 1982; Graham et al., 2007). The radiographic visualisation of the os penis in male red pandas is similar to the coati (Martins et al., 2013).

The number of thoracolumbar vertebrae in the ring-tailed lemur ranged from 19 (n = 17) to 20 (n = 1). Most of the ring-tailed lemurs with 19 thoracolumbar vertebrae had 12 thoracic and 7 lumbar vertebrae (n = 14) and rarely had 13

thoracic and 6 lumbar vertebrae (n = 3). The ring-tailed lemur with 20 thoracolumbar vertebrae had 13 thoracic and 7 lumbar vertebrae.

Thoracic radiography in the ring-tailed lemur allowed visualisation of thoracic organs and structures of clinical importance. However during evaluation of thoracic radiographs careful inspection of the pericardial fat should be performed and ruled out to avoid exaggerated VHS measurements on the right lateral (RL) and dorsoventral (DV) views. Furthermore, prolonged lateral recumbency should be avoided during thoracic radiography in order to prevent lung patterns as a result of gravity-dependent atelectasis especially in heavy ring-tailed lemurs. The prominent craniodorsal mediastimum, which was seen in obese ring-tailed lemurs, should not be misinterpreted as pathological widening due to mediastinal masses (Thrall, 2007).

In obtaining abdominal radiographs in the ring-tailed lemur, careful collimation is important in order to ensure the entire diaphragmatic margin is included due to abdominal dominance in this species. Radiographic abdominal detail was excellent in the ring-tailed lemur and most organs of clinical importance such as the liver, spleen, stomach, intestines, kidneys and urinary bladder were evaluated. Identification of the small spleen mainly on the ventrodorsal (VD) view in the ring-tailed lemur is similar to domestic cats (Thrall and Robertson, 2011), and different from domestic dogs in which the spleen is normally seen on the VD and right lateral (RL) views (Thrall and Robertson, 2011). The initial difficulties in ultrasonographic identification of the spleen of ring-tailed lemurs are attributed to the small size and different echogenicity of the spleen in this

species when compared to the echogenicity seen in domestic cats and dogs where it is more echogenic than the renal cortex (Mahoney, 2011).

The radiographic visualisation of the os penis and os critoridis in male and female ring-tailed lemurs, respectively, has also been reported previously (Drea and Weil, 2008). The conspicuous hypaxial muscles in ring-tailed lemurs and red pandas are similar to the domestic cat (Thrall and Robertson, 2011) and should not be misdiagnosed as an abdominal mass. Measurements and ratios obtained from this study should prove useful in routine health examinations and in the diagnosis of diseases. Additionally, they can serve as baseline for future studies.

Species-specific differences exist in the normal gross osteology, radiographic and ultrasonographic anatomy of the ring-tailed lemur and red panda. Knowledge of the normal gross osteology, radiographic and ultrasonographic anatomy of the ring-tailed lemur and red panda is important for accurate interpretation and diagnosis of diseases during routine health examinations and clinical cases.

11.2 REFERENCES

Ankel-Simons, F., 2007: Primate Anatomy: An Introduction. Academic Press: Boston.

Antón, M., M. J. Salesa, J. F. Pastor, S. Peigné, and J. Morales, 2006: Implication of the functional anatomy of the hand and forearm of *Ailurus fulgens* (Carnivora, Ailuridae) for the evolution of the 'false-thumb' in pandas. J. Anat. **209,** 757–764.

Arnbjerg, J., and N. I. Heje, 1993: Fabellae and popliteal sesamoid bones in cats. J. Small. Anim. Pract. **34,** 95–98.

Baitchman, E. J., and G. V. Kollias, 2000: Clinical Anatomy of the North American river otter (*Lontra canadensis*). J. Zoo. Wildl. Med. **31,** 473–483.

Biery, D. N., 2006: The hip joint and pelvis. In: BSAVA Manual of Canine and Feline Musculoskeletal Imaging (F. J. Barr and R. M. Kirberger, eds). Gloucester: UK. pp. 119–134.

Buchanan, J. W., and J. Bücheler, 1995: Vertebral scale system to measure canine heart size in radiographs. J. Am. Vet. Med. Assoc. **206,** 194–199.

Cerny, H., and S. Cizinauskas, 1995: The clavicle of newborn dogs. Acta. Vet. Brno. **64,** 139–145.

Damur-Djuric, N., F. Steffen, M. Hässig, J. P. Morgan, and M. A. Flückiger, 2006: Lumbosacral transitional vertebrae in dogs: classification, prevalence and association with sacroiliac morphology. Vet. Radiol. Ultrasound. **47,** 32–38.

Drea, C. M., and A. Weil, 2008: External genital morphology of the ring-tailed lemur (*Lemur catta*): Females are naturally “masculinised”. J. Morphol. **269,** 451–463.

Endo, H., N. Sasaki, D. Yamagiwa, Y. Uetake, M. Kurohmaru, and Y. Hayashi, 1996: Functional anatomy of the radial sesamoid bone in the giant panda (*Ailuropoda melanoleuca*). J. Anat. **189,** 587–592.

Estrada, A. H., T. J. Gerlach, M. K. Schmidt, J. L. Siegal-Willott, A. L. Atkins, J. Van Gilder, S. B. Citino, and L. R. Padilla, 2009: Cardiac evaluation of clinically healthy captive maned wolves (*Chrysocyon brachyurus*). J. Zoo. Wildl. Med. **40,** 478–486.

Fisher, R. E., B. Adrian, C. Elrod, and M. Hicks, 2008: The phylogeny of the red panda (*Ailurus fulgens*): evidence from the hind limb. J. Anat. **213,** 607–628.

Ganey, T. M., J. A. Ogden, N. Abou-Madi, B. Colville, J. M. Zdyziarski, and J. H. Olsen, 1994: Meniscal ossification II. The normal pattern in the tiger knee. Skeletal. Radiol. **23,** 173–179.

Graham, J. P., C. R. Berry, and D. E. Thrall, 2007: Technical issues and interpretation principles relating to the canine and feline abdomen. In: Textbook of Veterinary Diagnostic Radiology (D. E. Thrall, ed). Saunders Elsevier: Missouri. pp. 626–644.

Johnson, V., K. Hansson, W. Maï, J. Dukes-McEwan, N. Lester, T. Schwarz, P. Chapman, and F. Morandi, 2008: The heart and major vessels. In: BSVA Manual of Canine and Feline Thoracic Imaging (T. Schwarz and V. Johnson, eds). BSAVA: Gloucester. pp. 86–176.

Jouffroy, F. K., 1975: Osteology and Myology of the Lemuriform Postcranial Skeleton. In: Lemur Biology (I. Tattersall and R. W. Sussman, eds). Plenum Press: New York. pp. 149–192.

Lascelles, B. D. X., 2010: Feline degenerative joint disease. Vet. Surg. **39,** 2–13.

Le Minor, J. M., 1990: Comparative morphology of the lateral meniscus of the knee in primates. J. Anat. **170,** 161–171.

Lee, R., C. Leowijuk, 1982: Normal parameters in abdominal radiology of the dog and cat. J. Small. Anim. Pract. **23,** 251–269.

Mahoney, P., 2011: Spleen. In: BSAVA Manual of Canine and Feline Ultrasonography (F. Barr and L. Gaschen, eds). BSAVA: Gloucester. pp. 100–109.

Martini, A. C., Y. S. Meireles, S. Monzem, L. P. Vanconcelos, N. C. M. R. Turbino, M. A. A. Dahroug, D. Farias, P. B. Néspoli, G. F. Gonçalves, R. L. Souza, and L. D. Guimarães, 2013: Radiographic evaluation of the cardiac silhouette using the VHS method (vertebral heart score) in young and adults coatis (*Nasua nasua*, Linneaus 1766) living in captivity. Semin. Ciênc. Agrár. **34,** 3823–3830

Martins, G. S., E. R. Lopes, I. I. G. Taques, C. Y. Correia, Y. S. Meireles, N. C. M. R. Turbino, L. D. Guimarães, and P. B. Néspoli, 2013: Radiographic morphology of the skeleton, thorax and abdomen of coati (*Nasua nasua* Linnaeus, 1766). Pesq. Vet. Bras. **33,** 1137–1143.

McCarthy, P. H., and A. K. Wood, 1988: Anatomic and radiologic observations of the clavicle of adult dogs. Am. J. Vet. Res. **49,** 956–959.

McCarthy, P. H., and A. K. Wood, 1989: Anatomical and radiological observations of the sesamoid bone of the popliteus muscle in the adult dog and cat. Anat. Histol. Embryol. **18,** 58–65.

Moon, M. L., B. W. Keene, P. Lessard, and J. Lee, 1993: Age related changes in the feline cardiac silhouette. Vet. Radiol. Ultrasound. **34,** 315–320.

Mottershead, S., 1988: Sesamoid bones and cartilages: An enquiry into their function. Clin. Anat. **1,** 59–62.

Nickel, R., A. Schummer, E. Seiferle, J. Frewein, H. Wilkens, and K. H. Wille, 1986: The Anatomy of the Domestic Animals Vol. 1. Springer-Verlag: Berlin.

Osman Hill, W. C., 1953: Primates (Comparative Anatomy and Taxonomy). I. Strepsirhini. University Press: Edinburgh.

Ribeiro, R. G., A. P. A. Costa, N. Bragato, A. M. Fonseca, J. C. M. Duque, T. D. Prado, A. C. R. Silva, and N. C. Borges, 2013: Normal sonographic anatomy of the abdomen of coatis (*Nasua nasua*, Linnaeus 1766). BMC. Vet. Res. **9,** 124.

Roberts, M. S., and J. L. Gittleman, 1984: *Ailurus fulgens*. Mamm. Species. **222,** 1–8.

Roukis, T. S., and J. S. Hurless, 1996: The hallucal interphalangeal sesamoid. J. Foot. Ankle. Surg. **35,** 303–308.

Stoskopf, M. K., and D. Herbert, 1990: Selected anatomical features of the sea otter (*Enhydra lutris*). J. Zoo. Wildl. Med. **21,** 36–47.

Thrall, D. E., 2007: Mediastinum. In: Textbook of Veterinary Diagnostic Radiology (D. E. Thrall, ed). Saunders Elsevier: Missouri. pp. 541–554.

Thrall, D. E., and I. D. Robertson, 2011: The abdomen. In: Atlas of Normal Radiographic Anatomy and Anatomic Variants in the Dog and Cat. Elsevier: St. Louis. pp. 169–206.

Whiting, P. G., and R. R. Pool, 1984: Intrameniscal calcification and ossification in the stifle joints of three domestic cats. J. Am. Anim. Hosp. Assoc. **21,** 579–584.

Wilson, D. N., and E. Hanlon, 2010: *Lemur catta* (Primates: Lemuridae). Mamm. Species. **42,** 58–74.